SURFACE STRESS SENSORS FOR CLOSED LOOP

LOW REYNOLDS NUMBER SEPARATION CONTROL

A dissertation submitted in partial fulfillment of the
requirements for the degree of
Doctor of Philosophy

By

CHRISTOPHER ROY MARKS
B.S.M.E., Michigan State University, 2001
M.S.M.E. Wright State University, 2006

_____

2011
Wright State University

WRIGHT STATE UNIVERSITY

SCHOOL OF GRADUATE STUDIES

<u>**June 13, 2011**</u>

I HEREBY RECOMMEND THAT THE DISSERTATION PREPARED UNDER MY SUPERVISION BY <u>**Christopher Roy Marks**</u> ENTITLED <u>**Surface Stress Sensors for Closed Loop Low Reynolds Number Separation Control**</u> BE ACCEPTED IN PARTIAL FULFILLMENT OF THE REQUIREMENTS FOR THE DEGREE OF <u>**Doctor of Philosophy.**</u>

J. Mitch Wolff, Ph.D.
Dissertation Director

Ramana V. Grandhi, Ph.D.
Director, Ph.D. in Engineering Program

Committee on Final Examination

Andrew Hsu, Ph.D.
Dean, Graduate School

J. Mitch Wolff, Ph.D.

Rolf Sondergaard, Ph.D.

James Menart, Ph.D.

Mark Reeder, Ph.D.

Joseph Shang, Ph.D.

ABSTRACT

Marks, Christopher, Roy. Ph.D. Department of Mechanical and Materials Engineering, Wright State University, 2011. Surface Stress Sensors for Closed Loop Low Reynolds Number Separation Control.

Low Reynolds number boundary layer separation causes reduced aerodynamic performance in a variety of applications such as MAVs, UAVs, and turbomachinery. The inclusion of a boundary layer separation control system offers a way to improve efficiency in conditions that would otherwise result in poor performance. Many effective passive and active boundary layer control methods exist. Active methods offer the ability to turn on, off, or adjust parameters of the flow control system with either an open loop or closed loop control strategy using sensors. This research investigates the use of a unique sensor called Surface Stress Sensitive Film (S3F) in a closed loop, low Reynolds number separation control system. S3F is an elastic film that responds to flow pressure gradients and shear stress along its wetted surface, allowing optical measurement of wall pressure and skin friction. A new method for installing the S3F sensor to assure a smooth interface between the wall and wetted S3F surface was investigated using Particle Image Velocimetry techniques (PIV). A Dielectric Barrier Discharge (DBD) plasma actuator is used to control laminar boundary layer separation on an Eppler 387 airfoil over a range of low Reynolds numbers. Several different DBD plasma actuator electrode configurations were fabricated and characterized in an open loop configuration to verify separation control of the Eppler 387 boundary layer. The open loop study led to the choice of a spanwise array of steady linear vertical jets generated by DBD plasma as the control system flow effecter. Operation of the plasma actuator resulted in a 33% reduction in section drag coefficient and reattachment of an otherwise separated boundary layer. The dissertation culminates with an experimental demonstration of S3F technology integrated with a control system and flow effecter for closed

loop, low Reynolds number separation control. A simple On/Off controller and Proportional

Integral (PI) controller were used to close the control loop.

Table of Contents

List of Figures

List of Tables

Nomenclature

C_d section drag coefficient

C_f skin friction coefficient

C_h Stanton number

C_p pressure coefficient

C_x axial chord length (meters)

d_a actual displacement (pixels)

d_e S3F tangential displacement error (pixels)

$\overline{d_e}$ filtered error signal (pixels)

d_i displacement at index i (pixels)

d_m mean displacement (pixels)

d_r reference displacement (pixels)

d_x S3F tangential displacement in the streamwise direction (pixels)

$\overline{d_x}$ filtered streamwise displacement (pixels)

d_y S3F normal displacement (pixels)

$e(t)$ error signal

E Energy consumption in an open loop configuration (Joules)

E_f Energy consumption with feedback flow control (Joules)

f_o S3F first natural frequency (Hz)

f_s sampling frequency (Hz)

h S3F thickness (meters)

i instantaneous current (Amps)

K_D derivative term gain

K_I integral term gain

K_P proportional term gain

L length

LS laminar separation location

m filter window size

P pressure or power (Pa or Watts)

Pr Prandtl number

P_t total pressure (Pa)

q dynamic pressure (Pa)

$r(t)$ reference signal

Re Reynolds number

t time (sec)

TR turbulent reattachment location

u local velocity or S3F displacement (m/s or px)

u_e local velocity (m/s)

$u(t)$ controller output signal

v instantaneous voltage

$/V/$ velocity magnitude

V_{in} inlet velocity (m/s)

w correlation window size (pixels)

x length scale or horizontal dimension

y vertical dimension

z spanwise dimension

Greek

α angle of attack (deg.)

β ratio of pressure gradient to shear stress (1/m)

δ boundary layer thickness

ε exposure time (sec.)

ε_b mean bias error (px)

ε_{RMS} RMS error (px)

η non-dimensional length in the airfoil normal direction

μ viscosity of air (kg/m·s)

μ_m shear modulus (Pa)

ρ density of air or S3F (kg/m^3)

τ_x shear stress in the streamwise direction (Pa)

τ_w wall shear stress (Pa)

φ variable of integration

Subscripts

in   inlet condition

w   value in the wake

Acknowledgements

My biggest thank you goes to my wife, Kristen. She has been my greatest supporter, runs our household, and raises our son Josh while working full-time! Every day I am amazed at the amount of work you can accomplish, and your breadth of knowledge! I look forward to the great times our family will have together. Thank you also goes to my parents and family who have supported me, and taught me the most important skills I use every day as an engineer from day one.

I would like to thank my advisor Dr. Mitch Wolff for his support and willingness to mentor me in this PhD effort, career, and life. I appreciate all the fruitful conversations we have had in your office over the extent of this work. I would also like to thank my supervisors while I worked at AFRL. Thanks to Dr. Rolf Sondergaard for his mentorship in the AFRL/RZ low speed wind tunnel facility. Your breadth of knowledge is amazing…thank you for sharing some of it with me. The generous support from Charles Stevens, and Dr. Sondergaard at AFRL/RZTT will never be forgotten. Dr. Rich Anthony is acknowledged for spending several late nights fabricating high quality plasma actuators with me!

Thank you to my dissertation committee members, Rolf Sondergaard, James Menart, Mark Reeder, and Joe Shang. I appreciate your willingness to take the time to advise and educate me with such busy schedules.

1. Introduction

The field of flow control is broad and encompasses systems with many different specific engineering objectives unique to a particular application, such as separation control, lift enhancement, and noise reduction. Even though specific applications have unique design goals, all flow control systems operate by altering the natural flow field around a wetted surface or object in order to obtain a performance improvement. Flow control systems are generally classified as either passive or active. Passive techniques are usually fixed to the surface of which the flow is being controlled. They have the benefit of being simple, but cannot be turned off. Examples of passive techniques include surface treatments like dimples, or vortex generators. Active control methods can be turned on and off, removing any penalty at off-design conditions, but require additional complexity and weight. Both an active flow control actuator and also a sensor are required. The added complexity of an active control system has no doubt limited their use to date. Significant research is under way in all areas of flow control, from actuators to sensors, to control logic for closed loop active control systems. In this work a new type of separation control sensor is investigated for use at low Reynolds number with the objective of using it to close the control loop in a separation control system.

1.1. Low Reynolds number fluid dynamics

Reynolds number is a non-dimensional parameter representing the ratio of inertial forces to viscous forces in a fluid, given by:

$$\mathrm{Re} = \frac{\rho U x}{\mu} \tag{1.1}$$

where x is the characteristic length. Equation (1.1) scales by a length parameter. For a fixed density, viscosity, and freestream velocity, e.g. two vehicles operating at the same flight

conditions, the Reynolds numbers increases as the size of the vehicle increases.   At high

Reynolds numbers, fluid inertial effects dominate; at low Reynolds number viscous effects (i.e.

boundary layer behavior) play a larger role.   The focus of this work is low Reynolds number

flows which are classified, as others have (see Lissaman 1983 and Gad-el-Hak 2000), to be flows

with Reynolds number between 10^4 and 10^6. At these conditions boundary layer behavior plays a

large role in aerodynamic losses of an object, and the transition process is more sensitive to free

stream disturbances and aberrations of the airfoil geometry (Mueller et al. 1983).
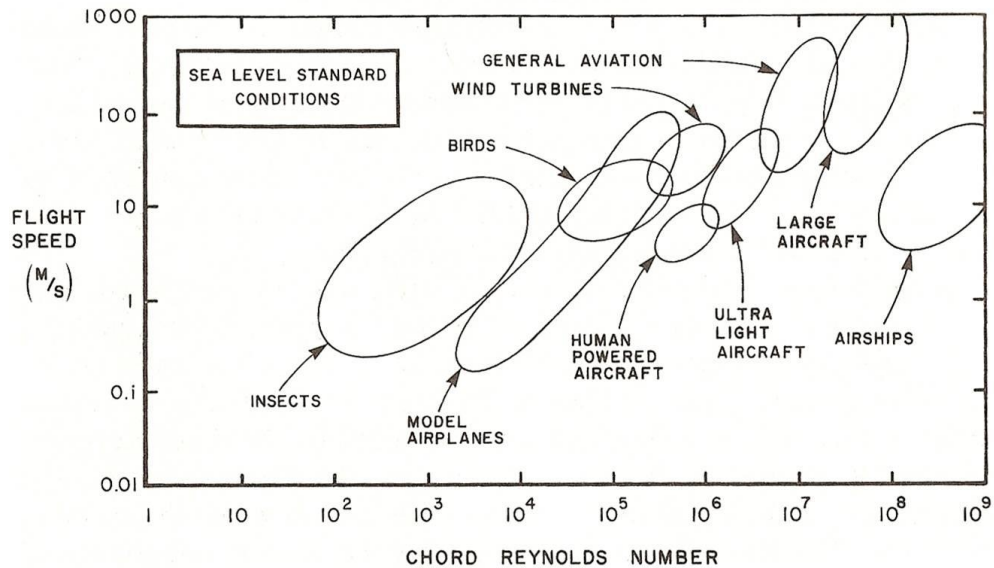
Figure 1.1 Flight Reynolds number spectrum at sea level (from Lissaman 1983).

In this range of Reynolds numbers, the maximum lift-to-drag ratio for smooth airfoils

decreases by two orders of magnitude as Reynolds number decreases (McMasters and Henderson

1980, Gad-el-Hak 2000). Turbomachinery components such as compressors, and low pressure

turbines also suffer a lapse in performance as Reynolds number decreases as shown in Figure 1.2.

According to Sharma (1998) the efficiency of LP turbines at take off conditions has steadily

increased over the last 25 years, but the same trend did not apply to LP turbines at cruise altitude

conditions. At cruise altitude, Reynolds number drops below 100,000 and in some cases below

25,000 (Bons et al. 2000, Sondergaard et al. 2002).   Considering that over a typical mission

(either military or civilian aircraft) the bulk of engine operation is at cruise altitude, improving

performance at these flight conditions is a priority. At such low Reynolds numbers, viscous

forces along the surface of the blades have a stronger effect on the fluid flow. An adverse

pressure gradient due to high aerodynamic loading coupled with low Reynolds flow has the

potential to separate flow over the suction surface of the blade. Flow separation is detrimental to

the efficiency of the turbine blade. A breakdown of LP turbine blade losses presented in Curtis et

al. (1997) indicated that the suction side surface of a LP turbine blade accounts for 60% of the

blade loss. Researchers have been developing methods of designing blades that increase the low

Reynolds number performance as well as methods of controlling the flow and improving

efficiency in conditions that would otherwise result in degraded performance.

    At low Reynolds number, separation, transition and reattachment can all occur within a short

distance and dramatically affect the performance of lifting surfaces (Gad-el-Hak 2000).

Depending on flow conditions, such as freestream turbulence, Reynolds number, surface

curvature, roughness, and pressure distribution, the boundary layer can remain laminar beyond

the minimum pressure location. The adverse pressure gradient beyond the minimum pressure
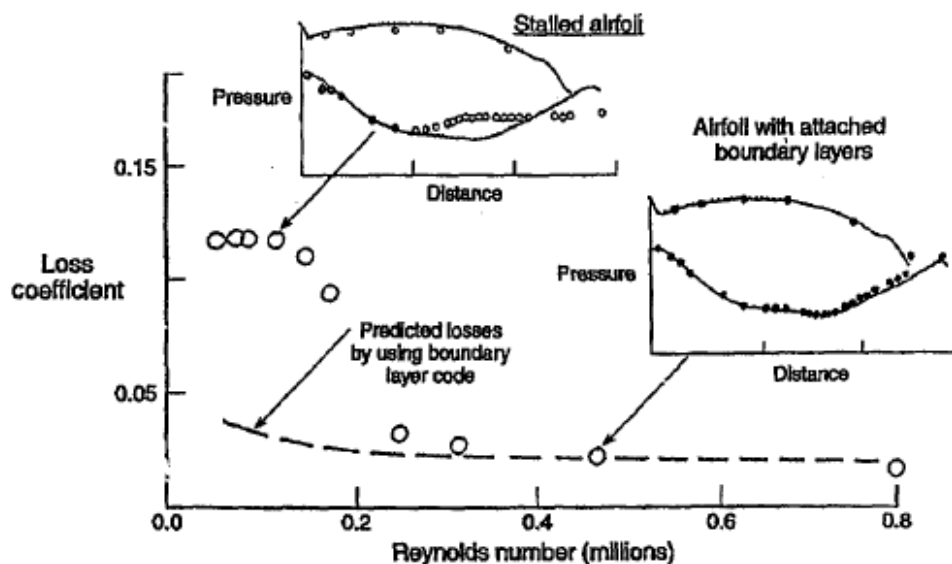
**Figure 1.2 High losses in LP turbine measured in a cascade at low Reynolds
number (from Sharma 1998).**

point on the suction surface can cause the laminar boundary layer to separate and become a free shear layer. When a laminar boundary layer separates, it rapidly undergoes transition to a turbulent flow (Lissaman 1983). The separated shear layer is unstable and depending on the Reynolds number and flow conditions, in some cases reattaches, forming a closed separation bubble. In other cases the free shear layer will remain separated over the remainder of the airfoil.

Mueller (1985) describes several types of flow behavior which result at low Reynolds number:

1. "Laminar separation occurring at
    a. high angle of attack and for which the separated boundary layer does not reattach, and the airfoil may be considered fully "stalled".
    b. low angles of attack in which the flow remains attached for a portion of the blade in which there is a favorable pressure gradient, but separates after the maximum thickness in the presence of an adverse pressure gradient.
2. Natural transition of the boundary layer to turbulent prior to reaching the surface of the blade in which there is an adverse pressure gradient. The transition of the laminar boundary layer near the leading edge to a higher energy turbulent boundary layer allows the boundary layer to remain attached. This behavior is accompanied by higher lift and lower overall drag coefficients.
3. An extension of the laminar separation case in which the separated laminar free shear layer may in some cases reattach shortly after separation, or more often may become turbulent and then reattach."

The description by Mueller was in the context of external flow such as those over aircraft airfoils, but a similar situation occurs in turbomachinery as well. In turbomachinery airfoil performance is also affected by three dimensional effects, periodic unsteadiness, and an adverse passage pressure gradient in compressors, and a favorable pressure gradient in turbines (Mayle 1991).

1.1.1. Laminar Separation Bubbles and Separation

As mentioned above, the presence of an adverse pressure gradient can lead to separation of the boundary layer from the surface. In this case the boundary layer becomes a separated shear layer. If conditions are right, the separated shear layer will transition to turbulent and reattach to the surface. The area between the separation point and reattachment point is referred to as a laminar separation bubble. Laminar separation bubbles have a large effect on the behavior of the boundary layer, and thus performance of an airfoil (Tani 1964). The diagram of Horton (1968) illustrates the characteristics of a closed reattaching laminar separation bubble. The description is of the mean flow structure, but in reality the structure is dynamic. Along the surface of the airfoil the shear stress will reach zero at the separation point. Downstream of the separation point is a region labeled dead-air. The flow is of course, not completely stagnant, but is the main recirculation area. This region has a relatively low, negative shear stress. At the downstream end of the laminar separation bubble is a region labeled reverse flow vortex. In this area the shear stress decreases further to a minimum before recovering to cross zero at the reattachment point. The scanning PIV measurements of Burgmann et al. (2006) of a SD7003 airfoil showed this reverse flow vortex can consist of several vortices with spanwise variation. The vortices under
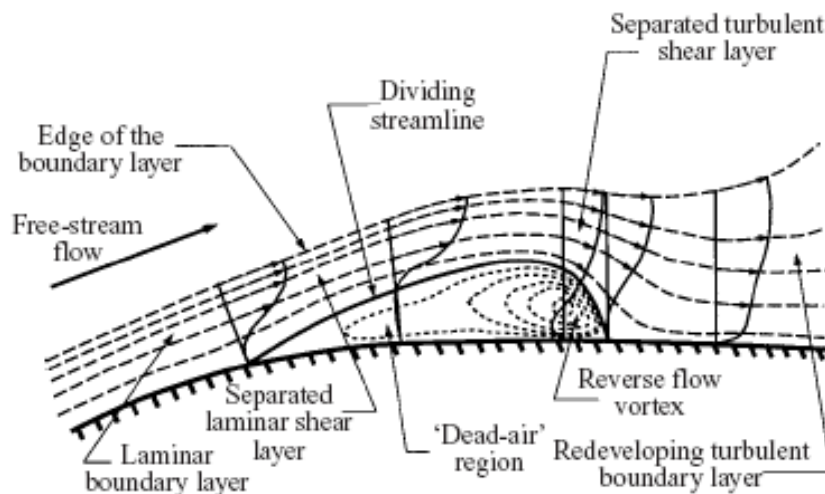
Figure 1.3 The time averaged flow structure of a laminar separation bubble (Horton 1968).

the right conditions burst from the separation bubble and travel downstream. There is a complex mutual interaction between vortex bursting and reattachment location via the pressure distribution (Bergmann et al. 2006).

A separation bubble is often described as long or short. Tani in his 1964 review of the subject explains that two types of bubbles should be distinguished by their effect on pressure distribution, and not on their length. A long bubble has a large affect on the pressure distribution, compared to that of an inviscid flow. The sharp pressure peak of an airfoil may be diminished or non-existent, significantly decreasing its lift. A short bubble has little effect on the peak pressure on the suction surface, which continues to increase as angle of attack is increased up to stall (Tani 1964).

Lin and Pauley (1996) point out that if the local Reynolds number is sufficiently high, boundary layer transition is caused by amplification of Tollmein-Schlichting instabilities. This is natural transition (viscous-type) of the attached boundary layer. Numerical simulations by Lin and Pauley suggest that if the boundary layer separates, Kelvin-Helmhotz (inviscid) instabilities will develop and cause the shear layer to rollup. They point out that it is expected that unsteadiness in the separation bubble will be dominated by large-scale vortex rollup and shedding, and not small-scale turbulence like many researchers often describe.

1.2. **Methods of flow control**

Gad-el-hak (2001a) defines flow control as "…the ability to manipulate a flowfield actively or passively to effect a desired change…" The control of low Reynolds number aerodynamic flows is of interest in many design domains such as air vehicles, turbomachinery, and wind turbines. Micro-air-vehicles (MAV) which have small length scales and operate at low flight speed present numerous low speed aerodynamic design challenges such as lift and control surfaces, thrust generation, and power plants (Gad-el-Hak 2001b).

Flow control is categorized as either passive or active, and active techniques can be further categorized as has been done by several groups (see Gad-el-Hak 2000, Wright et al. 2002). Gad-el-Hak divides active flow control into predetermined and reactive. Predetermined active flow control does not require sensors; however, the actuators are still turned on and off and for predetermined situations, either based on time or condition. Thus predetermined control is an open loop control strategy. Reactive flow control on the hand, requires a sensor to either provide feedback or on/off control of the sensor (Gad-el-Hak 2000).

Feedback control based systems consist of a flow effecter (or actuator), sensor, and control logic. The control strategy used with reactive flow control systems very considerably with regard to control logic complexity and synthesis of the model. Synthesis of the control system can range across physics based models, low-dimensional models, black-box models of the flow, and model free methods. Many physics based models are generated from solutions of the Navier-Stokes equations, however, the requirement of massive computing power to solve the equations limits their practical use (Henning and King 2007). Black-boxed based models describe simplified models developed by studying the input and output relationship of the plant (Brehm et al. 2006). Model-free controller synthesis for adaptive flow control shows promise in non-linear flow control environments since prior knowledge of the steady state input-output-map is not required (King et al. 2006 and Becker and King 2007).

Examples of low-dimensional models are Galerkin, and proper orthogonal decomposition (POD) based controllers (Henning and King 2007). POD is a technique used to identify the large scale motions of turbulent flows and is also known as Karhunen-Loeve decomposition. Lumley (1967) first applied POD to the study of turbulent flows (Pope 2008). It is based on orthogonal decomposition of the fluctuating velocity field, and a significant property of POD is that the first N modes of a POD contain more energy than any other orthogonal decomposition (Pope 2008).

The drawback of POD based analysis is that the optimal basis functions calculated are only optimal for certain flow conditions, which means they will change based on flow speed and

whether or not control is turned on (Gunes and Rist 2004; Gross and Fasel 2007). Glauser et al. (2004) and Pinier et al. (2007) describe the development of feedback control systems using proper orthogonal decomposition (POD) and modified linear stochastic measurement (mLSM) for control of separated flows. The methods described in Pinier et al. (2007) uses surface pressure measurements to estimate the first mode *global* POD coefficients and use them to demonstrate that the first mode is sufficient to use in a proportional feedback loop to control flow over a NACA 4412 airfoil. The use of global POD coefficients means the eigenfunctions have a greater "knowledge" of flow states, improving performance at different flow conditions.

An analytical approach to flow control is presented in the computational study of Alam et al. (2006). The method uses a distributed array of wall shear stress sensors; the wall shear stress distribution is viewed as the solution to a linear parabolic PDE with forcing. Two actuators on each end of the shear sensor provide separation and reattachment control via a feedback loop. The method was demonstrated computationally as a method to control separation of flow over a backward facing step.

If the system is relatively simple and has only one input and output, a mature class of control methods called proportional integral differential (PID) feedback controllers can be used. A PID controller has the general form:

$$u(t) = K_P e(t) + K_I \int e(t)dt + K_D \frac{de(t)}{dt}$$

where $u(t)$ is the controller output signal, and $e(t)$ is the error term equal to the difference between the reference $r(t)$ and the sensor $y(t)$ signal. K_P, K_I, and K_D are gains adjusted to tune the system response. K_P is the proportional gain and multiplication by the error results in adjustment of the controller output signal proportional to the amount of error. K_I is the integral gain and adjustment of K_I increases or decreases the controller output signal in proportion to the time history of error. K_D is the derivative term gain and is a prediction of future error. Variations of

this type of controller are systems that use only two of the elements making them PI or PD controllers.

Adjustment of the controller gain is done a variety a ways, often iteratively. The gain can be adjusted manually to obtain a stable response, or automatically based on a time response and desired output characteristics. In computational studies by Brehm et al. (2006) and Gross and Fasel (2007), control of laminar separation in a low pressure turbine cascade is simulated using a proportional differential (PD) feedback controller. Brehm et al. (2006) used one downstream pressure transducer as the input, and the control signal drove harmonic wall normal blowing. Values of K_P, K_D and other controller parameters were adjusted and set by defining an objective function and monitoring it as controller parameters were incrementally adjusted. Gross and Fasel (2007) compared the use of steepest decent algorithm versus simultaneous perturbation stochastic approximation (SPSA) demonstrating a self adaptive controller.

1.2.1. Recent Low Reynolds Number Research

A number of numerical and experimental studies have been carried out recently, with the focus on control of low Reynolds number laminar separation. Closed loop studies have been mostly limited to computational work as in the case of the Direct Numerical Simulation (DNS) study of Rist and Augstin (2006) on a flat plate, and the numerical work of Brehm et al. (2006), and Gross and Fasel (2007) applied to airfoils and LP turbine blades. Most control strategies employ an instability generating mechanism upstream of the separation point. The study by Rist and Augstin (2006) used a DNS analysis of a laminar separation bubble over a flat plate with an adverse pressure gradient to demonstrate the use of unsteady force to control laminar separation bubbles. Low amplitude boundary layer disturbances, mimicking suction or blowing, and generated at optimum frequencies control the size of the bubble by inducing earlier laminar-turbulent transition. The artificial, unsteady forcing generates instability waves that lead to spanwise vorticity which enhances wall-normal energy transfer, prior to full onset of turbulence.

9

Rist and Augustin recommend, based on linear stability theory (LST), that an actuator should not be placed in a region of favorable pressure gradient, but should be placed just upstream of the separation point, at an optimum neutral point based on linear stability theory. They used DNS to verify predictions from LST and found that even though transition is a nonlinear phenomena, most disturbance growth followed LST closely. The authors suggest that LST can be used as an effective method to estimate the effect of choosing different forcing frequencies (Rist and Augustin 2006).

Experimental studies using feedback control from a sensor signal often use simple controllers that trigger on an actuator when the sensor signal reaches a predetermined threshold value. The literature is dominated with feedback flow control methods that use a pressure signal to determine when to turn on a flow effecter. Patel et al. 2003 described an active stall control system using deployable vortex generators at Reynolds number of 6.0×10^5. The pressure signal from a pressure transducer sampled at 500 Hz was used to detect the onset of flow separation and trigger deployment of the vortex generators. A threshold value of the standard deviation of the pressure signal was determined and stored in onboard memory. Deployment of the actuators was based on comparing current standard deviation with the threshold values. In Patel et al. 2007 an additional method of using the pressure signal for flow control is described in experiments that use high bandwidth pressure sensors for feedback control of the flow over a NACA 0015 airfoil with plasma actuators located near the leading edge. The Amplitude Sense Peak and Control (ASPC) method uses a plasma actuator located at the leading edge that is cycled on and off as angle of attack is changed. The method takes advantage of experimental observation that the unsteady plasma actuator driving frequency is only detected in the pressure signals at an angle of attack that is just prior to separation , or at angles of attack in which separation would occur without flow control. This method enabled the authors to detect separation or the onset of separation.

Becker et al. 2007 uses the readings from two fast response pressure transducers to detect whether the flow state is attached or separated over the flap of a generic high lift airfoil

configuration. They infer the boundary layer state by the difference in the pressure coefficient calculated from the two pressure transducers. A separated flow case has a delta C_p of near zero, and a fully attached flow has a delta C_p significantly greater than 1.

An alternate way of measuring separation and reattachment regions is by surface shear stress. The surface shear stress is equal to zero at boundary layer separation and reattachment points. In regions of attached flow the shear stress is positive; in regions of separation the shear stress is negative. A sensor that can measure surface shear stress is a natural fit for separation control systems. Recently, Poggie et al. 2010 demonstrated the use of a shear stress sensitive sensor array in a large scale wind tunnel. An array of hot film sensors was used to detect stall and plasma actuators to reattach flow at a Reynolds number of 0.9 x 10^6 to 1.7 x10^6. When the hot-film signal exceeded a threshold value indicating the separation point was over the plasma actuator panel, the actuators were triggered on. Lack of the use of shear stress sensors for flow control is due to limited sensor technology that is mature, small scale, robust, and can be mounted to a surface in a clean manor. Shear stress sensors will be discussed further in the next section.

1.3. **Sensor Technology**

There are many different classes of flow control for different design conditions, each with different sensor and actuator needs. This fact makes it impossible to define a single set of requirements for all sensors in all aspects of active flow control (Wright et al. 2002).

Useful flow control sensors are shear stress, pressure, and temperature sensors. Pressure sensors can be point sensors as in the case of either diaphragm type, or piezoelectric, or field sensors as in the case of pressure sensitive paint (PSP). Piezoelectric transducers are typically smaller and have quicker response than the diaphragm type (Barlow et al. 1999). The small sizes of modern piezoelectric transducers make them a viable option as a flow control sensor if mounted flush to a surface with no tubing.   A group at Notre Dame has recently experimented

with using pressure transducers as stall detection sensors. Their technique uses frequency analysis of the pressure signal to detect flow separation. Both Fourier transforms based methods and wavelet transform techniques have been investigated (Bowles and Corke 2009). Several groups have also used microphones as sensor for flow control over a backward facing step.

Thermal based sensors for separation control take advantage of the Reynolds analogy, which states that wall shear and heat transfer rate are proportional:

$$\frac{C_h}{C_f} = f\left(\Pr, \frac{x}{L}, geometry\right) \tag{1.2}$$

where C_h is the Stanton number, and Pr is the Prandtl number (White 1991). The Stanton number is the non-dimensional wall heat transfer coefficient, and the Prandtl number is a non-dimensional ratio of viscous to thermal diffusion rates. For flat plate flow, with either turbulent or laminar boundary layer:

$$\frac{C_f}{C_h} = 2\Pr^{2/3} \tag{1.3}$$

In the presence of strong pressure gradient, this relationship breaks down (White 1991).

A shear sensor can be used as a flow control sensor in several ways. If the temporal resolution is high enough, frequency analysis of the sensor signal could indicate separation based on large fluctuations in shear (or power). The mean signal from an array of sensor could be used as indication of separation point based on wall shear stress magnitude (or direction for optical based sensors).

Shear stress measurement techniques can be divided into direct and indirect methods. Examples of direct methods are floating surface balances, surface stress sensitive film, and oil-film interferometry. These methods are called direct because the parameter being measured directly responds to skin friction (Liu et al. 2008). Indirect methods require an empirical or theoretical relation between a parameter measured by the sensor and shear stress. An example of

an indirect method is thermal based shear stress sensors which use the Reynolds analogy to relate wall heat transfer to wall-shear stress.

An early method to measure skin friction was described by Preston (1954) and utilizes a Pitot tube in the boundary layer and either a static port on the model surface or on a second probe. Preston originally describes its use to measure the skin friction in a turbulent boundary layer, but the probe can also be used in a laminar boundary layer with an equation provided by Bechert (1996). The accuracy of the technique is dependent on the logarithmic law of the wall, and requires a probe size that is much smaller than the boundary layer thickness.
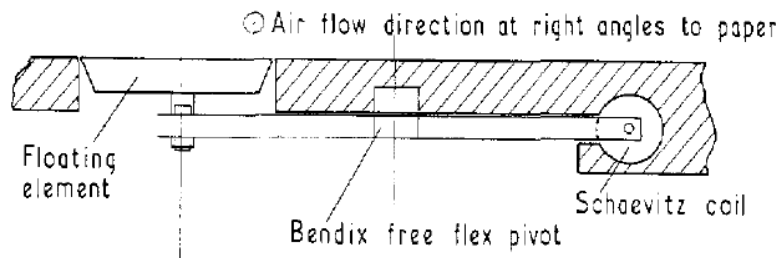
Figure 1.4 Example of skin friction force balance utilizing a floating surface element (Headley 1969).

Another method to measure skin friction described in Headley (1968) involves directly measuring skin friction with a measuring plate and balance, which is reported to date back to Schultz-Grunow in 1940. This method is shown in Figure 1.4, and of course, requires a large apparatus and correspondingly large test specimen. The other drawback of the technique is that it measures the integrated skin friction over a surface area, rather than a point measurement.

Another approach to the floating surface element was presented by Schmidt et al. (1988) who describe a micromachined floating-element sensor that uses a differential capacitor and integrated pair of matched transistors for readout. The prototype sensor featured a 500 μm x 500 μm floating element with overall chip dimensions of 4 mm x 5mm. The prototype had an on-chip sensitivity of 47 μV/Pa. A more recent development to the micromachined floating-element sensor was the use of integrated photodiodes, fabricated using wafer-bonding technology

(Padmanabhan et al. 1995). This new sensing scheme was developed after finding that environmental exposures impose high levels of drift on the capacitive readout shemes. The photodiodes measure in-plane displacement of a 120 μm x 120 μm x 7 μm floating element sensor. A reported shear stress sensitivity of 0.1 Pa and range of 0-5 Pa make them suitable for low shear stress boundary layers.

Tanner and Blows (1976) describes a method of measuring skin friction in air flows by the interferometric thickness measurements of silicone oil films flowing over body surfaces. The method is compared to the Preston tube method in Tanner (1977). The film is displaced over time due to the skin friction of the freestream gas flow, thus by measuring the change in thickness over time, skin friction can be deduced. The technique is more difficult to setup than Preston tube, but it useful for any boundary layer thickness, or state (laminar, transitional, turbulent).

Fernholz et al. (1996) gives a description of four measuring techniques: surface fence, wall hot wire, wall pulsed wire, and oil-film interferometry, with tabular comparison shown in Table 1.1. Each of the techniques are indirect with the exception of oil-film interferometry.

Table 1.1. Comparison of four skin-friction measuring techniques (from Fernholz et al. 1996)

	Surface fence	Wall hot wire	Wall pulsed wire	Oil-film interferometry
Measured quantity	Pressure difference	Heat transfer	Time of flight	Movement of fringes
Calibration necessary	Yes	Yes	Yes	No
Mean value	Yes	Yes	Yes	Yes
Temporal resolution	Unclear	> 10 kHz	$\simeq$ 20 Hz	No
Cross correlation	No	Yes	No	No
Spatial resolution				
Δx, Δz (mm)	< 1, 3	< 0.5, 0.5	1.5, 0.5	< 1, 1
Direction of τ_w	Yes	Yes	Yes	Possible
APG	Yes	Yes (but no instantaneous reverse flow)	Yes	Yes
Reverse Flow	Yes	No	Yes	Yes
FPG	Yes (but restricted)	Yes	Probably yes	Yes
Transitional flow	Unclear	Yes	Probably yes	Yes
Laminar flow	Yes	Yes	Probably yes	Yes
3D flow	Yes	Yes	Yes	Yes
Accuracy (estimated)	±4%	±4%	±4%	< ±4%

Wall shear stress can also be measured with wall mounted hot wire and hot-film probes. These probes can be used in experimental setups in which the conductivity of the fluid is higher

than the conductivity of the wall material. The benefits of hot-films are their high temporal resolution in contrast to only mean wall shear stress measurements by Preston tube.

Another device is the surface fence or sublayer fence in which a surface of height, not to exceed $H^+ \approx 5$, is placed in the viscous sublayer. The only measurement is the pressure difference upstream and downstream of the fence which requires a precision manometer or pressure transducer. Each fence requires a calibration procedure, with the skin friction being a function of pressure difference Δp. Reported accuracy of a surface fence is about $\pm 4\%$ (Fernholtz et al. 1996), but accuracy will likely decrease if the turbulent structure of the flow differs significantly from the calibration turbulent structure.

Montelpare and Ricci (2004) used a thermographic technique to locate local boundary layer separation phenomena. Their experimental work demonstrated the feasibility of using thermography for locating the laminar separation point and length of a laminar separation bubble on an Eppler 387 airfoil in a wind tunnel. They qualitatively located the bubble region visually based on the surface temperature, but required a quantitative technique to clearly identify the separation location and reattachment point. The local minimum and maximum of the first derivative of the temperature distribution was used to identify the separation point and length of the laminar separation bubble. The authors found that the separation and reattachment point agreed well with numerical and experimental locations, with separation point showing the best correlation.

A non-intrusive optical method to measure low values of wall shear stress was described by Gregory et al. in 2008. The technique builds upon the laser thermal tuft flow visualization method first reported in Baughn et al. (1995) and later patented by the U. S. Air Force (Rivir et al. 1999). The thermal tuft technique as used for flow visualization uses a laser to heat a spot on the surface immersed in a fluid flow. The surface which is coated with thermochromic liquid crystals changes temperatures and takes on a tuft shape as the heated air changes the surface temperature around the spot. The laser spot was ≈ 3 mm in diameter and the tuft points downstream. The

thermal tuft technique was used by Baughn et al. (1995) to obtain boundary layer separation location by noting that at the separation or reattachment point the tuft is circular, rather than tear dropped in the downstream direction. It was demonstrated in the early work that the thermal tuft could be used as a qualitative surface sensor, and Baughn et al. in (2006) reported that the length of the thermal tuft can be used to measure wall shear stress. Additional experimental and theoretical results are were reported in Gregory et al. in (2008) which confirmed the potential of the thermal tuft technique as a quantitative wall shear stress sensor especially at low values of shear stress less than 1 Pa. Gregory et al. (2008) reports that to date, the thermal tuft technique has only been used with steady laminar flow, and only to measure time averaged values due to the slow response of the heat transfer mechanism involved.

MEMS based separation control sensors have been proposed in a variety of packages. The most promising packaging consists of arrays of shear stress sensors mounted to flexible substrates with high spatial resolution. Most of these designs use thermal techniques to measure shear stress. Jiang et al. (2000) described a fabrication process that uses many of the techniques
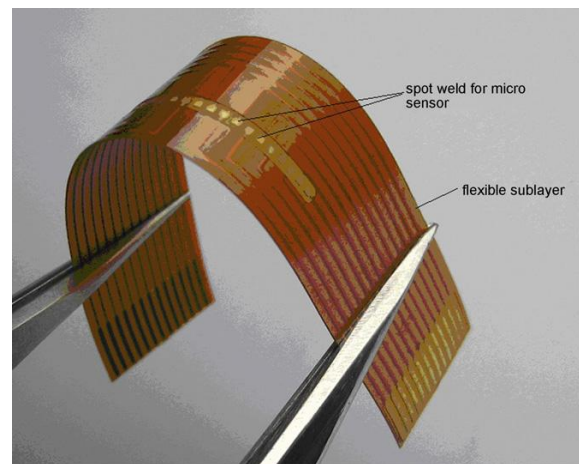
Figure 1.5 MEMS thin film sensor Liu et al. 2007.

used to fabricate integrated circuit (IC). They were able to create a flexible 80μm thick sensor array consisting of 100 vacuum-insulated diaphragm-type thermal shear-stress sensors inside a 1 cm x 3 cm area. Each sensor was on the order of 20 μm square.   The sensitivity of the sensors is about 100 mV/Pa. Measurements with sensor installed on the surface of a cylinder demonstrated that the sensor could be used for separation location detection.

Another MEMS array of thermal shear stress sensor is based on the principles of thermal anemometry shown in Figure 1.5. The flexible array of sensors consists of platinum thin film

resistors on a silicon nitride base. Current passes through the resistors which operate as constant current thermal anemometers with bandwidth of about 1 kHz. The sensors were shown to have the potential to accurately identify flow separation location around a cylinder based on mean or RMS sensor voltage output (Liu et al. 2007).

Another type of MEMS sensor in a cluster configuration was described by Kahng et al. (2000). The sensor cluster consists of local shear stress, pressure, and temperature on an airfoil. The shear sensor is heat transfer based, and is 300 microns square mounted on a flexible polyimide sheet. The reported typical sensitivity of the sensor is 150 mV/Pa.

Seifert and Melton (2004) describe a method they used to detect turbulent boundary layer separation using an array of hot film sensors. Their method of detecting separation utilizes analysis of the spectra from their wall mounted hot film sensors. The algorithm is based on the intermittent disappearance of high frequency content from the spectra as separation condition approaches.

Grobe and Schroder (2008) describe a shear stress measuring device based on micro-pillars or thin cylindrical beams that bend due to fluid forces against them. The pillars are made of an elastomer material and wall shear stress is obtained by relationship between pillar deflection and local surface friction. Diameters of the pillars are in the range of microns and an array of pillars offers the potential of high spatial resolution surface shear stress measurements. The height of the pillars is limited to the height of the viscous sublayer to ensure a linear relation between the wall shear stress and the near wall velocity gradient. Grobe et al (2006) report that intrusiveness of the sensor has been investigated using μPIV which has shown that the flow past the pillar is in the Stokes regime for typical low to moderate Reynolds number flows. There is only a local impact on the flow field in an area two to four diameter downstream of the pillar (Grobe et al. 2006). Typical lateral spacing of the pillars is 15-25 diameters (Grobe and Schroder 2008). In order to measure the mean and fluctuating components of shear, the dynamic characteristics of the pillars must be designed properly. Grobe and Schroder (2008) report the potential for

17

measurements at time scales on the order of a few kHz with properly designed pillars. The shear

stress is calculated ensuring the sensor is in the viscous sublayer where the mean velocity

gradient in turbulent flows can be approximated by a linear relationship between shear stress and

mean velocity gradient in the vicinity of the wall up to wall distances of $y \leq 7 \cdot y^{+}$ (Grobe and

Schroder 2008).

Gnanamanickam and Sullivan (2008) describe a similar optical based wall shear stress sensor

to that of Grobe and Schroder. Their shear stress sensor employs a micro pillar array made from

silicone rubber that is glued to the surface of a wall bounded flow. The micro pillars extend into

the viscous sublayer and deflect an amount proportional to the wall shear stress. They state that if

silicone based rubber is used as the pillar material, the resonant frequency of the pillars are on the

order of 100 kHz. Research investigating spacing of the micro pillars to eliminate interference is

ongoing. Micropillar based shear stress sensors will be susceptible to surface contamination

which will need to be further investigated. Regardless, micropillar based sensors show promise

as spatial shear stress sensors with high temporal resolution that will be required for controlling

turbulent flows.

A sensor capable of measuring surface shear stress field with high spatial resolution has been

under development by Innovative Scientific Solutions Inc. The technology is called Surface

Stress Sensitive Film (S3F). S3F is an optical sensor that uses a low shear modulus elastomeric

film that is inherently sensitive to both surface tangential stress (shear) and pressure gradient.

Optical measurements of markers on the surface of the film and embedded luminescent molecules

are used to determine the tangential stress and pressure gradient on the film. S3F has been used

to measure surface stresses in a variety of aerodynamic (e.g. Fonov et al. 2006) and

hydrodynamic (Crafton et al. 2008) flows. The system requires an illumination source, image

acquisition system, and processing system.

S3F was used extensively in this work, and a detailed background and discussion of S3F is

included in the experimental arrangement shown in Section 2.3.3 of this document.

1.4. **Actuation methods**

Passive techniques have the benefit of consuming no power or mass flow, but are "active" during all operating conditions. For this reason passive control application requires careful consideration and design in order to obtain the best performance over all operating conditions. Active flow control techniques on the other hand offer a flow control mechanism that can be turned on or off as needed. The disadvantage is their consumption of power or core mass flow, potentially reducing the benefit of the device. The best active flow control methods will consume a minimal amount of power compared to net performance improvements. The most efficient control schemes will always be operational as it was pointed out by Pinier et al. (2007) that it is more energy efficient to keep flow attached, than to reattach separated flow.

Researchers have been investigating the use of both passive and active flow control techniques to mitigate low Reynolds number flow separation for many years. Many of the techniques have shown large performance improvement in open loop configurations. With the intent of improving low pressure turbine blade efficiency at low Reynolds number Lake et al. (1999) investigated the use of surface dimples and v-grooves as a passive flow control technique on the suction side surface of a Pack-B LP turbine blade. Surface treatments have the same effect as dimples on golf balls, used to decrease drag at their flight Reynolds number of $\approx 10^5$ (White 1999). The increased surface roughness enhances momentum transfer between the boundary layer and freestream leading to earlier transition to turbulence, decreasing or eliminating the effects of flow separation. The experiments of Lake et al. (1999) demonstrated a 58% decrease in loss coefficient at low Reynolds number using dimples. The drawback of surface treatments is a negative parasitic effect at higher Reynolds number. Bons et al. (2000) and Sondergaard et al.

(2002) have investigated the use of both steady and unsteady vortex generator jets, which would provide the ability to control flow only when beneficial and remove the parasitic effect at off-design conditions. Vortex generating jets (VGJs) function by ejecting a small jet of air from the blade surface at a skewed angle to the freestream, thus generating streamwise vortices. VGJs have received a large amount of attention as a turbomachinery flow control mechanism because they are believed to be relatively straightforward to implement in a turbine engine. High pressure (HP) turbines utilize film cooling techniques that use bleed air ejected from the surface of the turbine blade, and employing VJGs could be an extension of this technology. Both steady VGJs (Sondergaard, et al. 2002) and pulsed VGJs (Bons et al. 2001; 2008) have beems investigated experimentally. Investigations with steady blowing have shown a reduction in blade wake pressure loss between a factor of two and three. Pulsed VGJs offer the greatest promise with lab tests showing that mass flow requirements are almost negligible and an order of magnitude less than steady VGJs (<0.01% of core mass flow) (Bons et al. 2001). Experimental work indicated that the mechanism of control has to do with the starting and ending transitions of the pulsing cycle rather than the injected stream itself (Bons et al. 2001). Sondergaard et al. 2002 investigated the potential to reduce the LP turbine blade count by increasing blade spacing using VGJs to maintain attached boundary layers. Over the Reynolds number levels investigated, 25,000-75,000, the authors found they could maintain design level wake pressure loss with pitch settings of 150% of design pitch. This demonstrates the potential for decreasing blade count in future LP turbines, or removing existing stages when flow control techniques are used.

As the ability to fabricate precision devices of increasingly smaller sizes has continually improved, a new field of multidisciplinary study known as Micro Electro Mechanical Systems (MEMS) has emerged. MEMS devices show promise as flow control sensors, and actuators, especially in the field of relaminarization since MEMS devices can be fabricated on the order of turbulent length scales. For low speed flows this is on the order of hundreds of microns and of tens of milliseconds (Kumar et al. 1999). Kumar et al. in 1999 describe MEMS zero mass flux

vortex generators developed by Jacobson (1995) and shown in Figure 1.6. The piezoceramic devices consists of cantilevers that expand and contract to create counter-rotating vortices, and when operated continuously forms a continuous jet. The size of the device is on the order of a dime and aligns flush with a surface for zero drag penalty.

Synthetic jet actuators generated by small flush mounted surface devices have been investigated for separation control of external flows (Smith et al. 1998; Amitay et al. 1998; Amitay et al. 1999), and internal flows (Amitay

Figure 1.6 MEMS zeros mass flux vortex generator from Kumar et al. (1999).

et al. 2000). The topic has been reviewed in Glezer and Amitay (2002). They function by providing an alternating suction and blowing force at the wall produced typically by an oscillating diaphragm over a cavity embedded in the wall. Using only the working flow, they produce a train of vortices whose interaction with the cross flow creates a synthetic jet. When operated at high actuation frequencies, they can produce a "virtual" surface shape change which can be used in flow control applications. Synthetic jets have also been generated by using plasma actuators, which have no moving parts, with an annular electrode configuration by Santhanakrishnan and Jacob (2008), and more recently in a linear arrangement by Santhanakrishnan et al. (2009). The use of dielectric barrier discharge (DBD) plasma actuators for flow control have been investigated for a variety of flow control applications, see Corke et al. (2005), and has become a popular research topic because they offer a low power, on demand active flow control method.

The following section discusses DBD plasma actuators and their potential use for flow control in more detail.

1.4.1. Dielectric Barrier Discharge plasma actuators

Several projects have been undertaken to demonstrate that DBD plasma actuators can be used for low Reynolds flow control.   The focus of this section is a brief background of DBD plasma actuators that have been presented in the literature for flow control applications. Common and alternate electrode configurations are discussed, as well as application of DBD plasma actuators for low Reynolds separation control around LP turbine blades.

1.4.1.1.   DBD Plasma Actuator Background and Overview

A simple schematic of an asymmetric configuration of DBD is shown in Figure 1.7. This configuration has been studied significantly in recent literature.

1.	Exposed electrode	4.	Ac voltage source
2.	Encapsulated electrode	5.	Induced velocity
3.	Dielectric	6.	Plasma discharge area
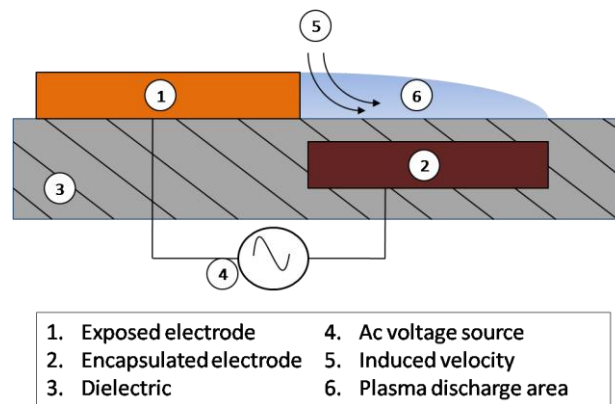
Figure 1.7. Asymmetric configuration of DBD plasma actuator.

The encapsulated electrode is typically grounded and the voltage potential is alternated between positive and negative. Typically high voltage AC is applied to the electrodes with voltage amplitudes of several kV_{p-p} to tens of kV_{p-p} and frequencies from around 1 kHz to tens of kilohertz.

In the case of the surface DBD, examination of the voltage and current (Pons et al. 2005), and optical measurements (Enloe et al. 2004a, 2004b, 2006) have both indicated that the plasma in the electrode gap is generated through a succession of microdischarges, randomly distributed in time and space (Moreau 2007). Moreau gives a simple explanation for the discharge mechanism known as the Townsend mechanism. Moreau's explanation is paraphrased here; under an applied electric field, the electrons located in the electron gap accelerate towards the anode and ionize

Figure 1.8 Ionization of neutral particles (as described in Moreau 2007).

the gas by collisions with neutral particles. An electron avalanche develops due to the multiplication of electrons as they move towards the anode, colliding with neutrals, releasing more electrons (Figure 1.8). A discharge current is then created, which is unique to the type of discharge present (i.e. corona, DBD) (Moreau 2007).

For detailed information and background on the physics of the plasma discharge, readers should refer to other papers (e.g. Enloe et al. 2004a, 2004b, 2006), the topical review paper by Fridman et al. (2005) and a paper by Moreau (2007).

The generation of an induced velocity by the DBD and its low power requirement make it a viable candidate for flow control applications. An electrostatic force (Enloe 2004b):

$$\vec{F} = \rho_e \vec{E} = -(\varepsilon_0/\gamma_D^2)\phi\vec{E} \tag{1.4}$$

acts on the charged species located in the plasma which results in an electric wind in the form of a wall jet. In equation 1.4, ρ_e is the net charge density, E is the electric field, ε_0 is the permittivity of free space, and γ_D is the debye length. The thrust produced by the force has been reported to be in the range of 10 mN or less (Enloe et al. 2006). The induced air flow can be several meters per second, but larger velocities have been generated (Moreau 2007). The induced velocity and power have both been observed to be proportional to $V_{app}^{7/2}$ (Enloe et al. 2004a). An induced

velocity and low power requirement are what make a DBD a viable candidate for low speed flow
control applications.
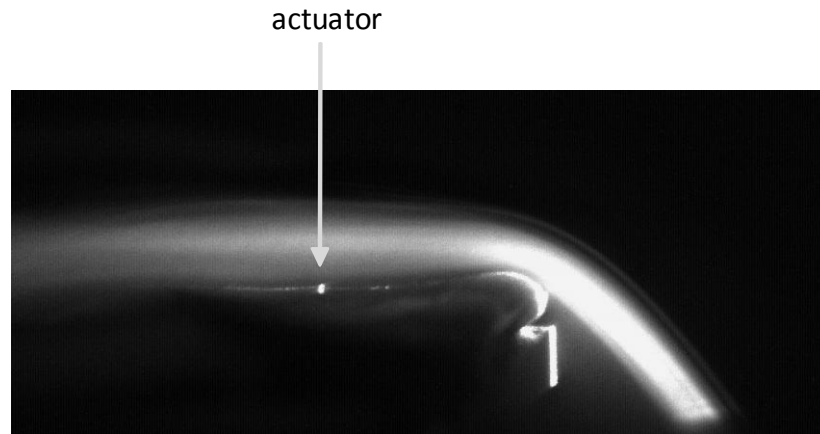
actuator

a.) Power off
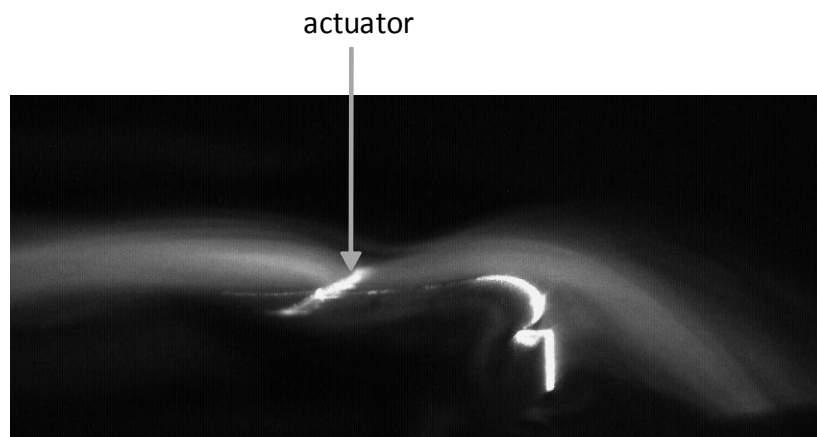
actuator

b.) Power on

**Figure 1.9. Visualization of the induced velocity generated by a DBD
plasma actuator single asymmetric electrode configuration. Top image:
actuator off. Bottom image: actuator on. Flow is from left to right.**

1.4.1.2. Alternate DBD Plasma Actuator Configurations

A majority of fundamental research and application of DBD plasma actuators for flow control

have utilized the linear asymmetric electrode arrangement illustrated in Figure 1.7. This

configuration generates an induced velocity in the form of thin wall jet over the buried electrode.

Figure 1.9 shows flow visualization of the induced velocity generated by a linear asymmetric electrode arrangement. The images are of a plasma actuator operating on a benchtop. The flow here is generated by the fog formed from dropping dry ice in water. The fog is naturally flowing over the plasma actuator from left to right in the images. The plasma has the effect of pulling the fog towards the buried electrode and ejecting in the form of a thin tangential wall jet. This configuration is effective at reenergizing the boundary layer by transferring momentum from the freestream to the boundary layer. The height of the jet is typically only several millimeters above the surface (Pons et al. 2005). This configuration was used experimentally by Huang et al. (2006) to reattach and decrease the length of a separation bubble over the Pack-B airfoil. The jet was oriented downstream along the surface of the airfoil just upstream from separation adding momentum to the boundary layer with the objective of overcoming the adverse pressure gradient aft of the negative pressure peak. Huang et al. concluded the actuator acted as a turbulent trip, promoting earlier transition to a turbulent boundary layer. A nearly analogous computational study by Rizzetta and Visbal (2007) found the same steady actuator configuration mounted facing upstream more effective then the downstream facing plasma actuator. They predicted that the upstream jet created a local small scale separation and subsequent formation of vorticity and turbulent mixing. It should be noted that both Huang et al. and Rizzetta and Visbal investigated pulsed configurations in their studies and found them to be more effective while using less power. Their performance gain was attributed to the generation of more coherent spanwise vortical structures that transferred high momentum fluid from the outer boundary layer to the blade surface (Huang et al. 2006, Rizzetta and Visbal 2007).

As alternatives to the asymmetric electrode arrangement several researchers have proposed different electrode configurations with the objective of improved control authority. The objective of alternative electrode configurations over the traditional linear plasma jet is generation of induced jets with three dimensionality and vorticity for enhanced boundary layer control. Longitudinal vortices generated by vortex generators are known to be efficient at eliminating or

reducing boundary layer separation by increasing cross-stream mixing of streamwise momentum (Johnston et al. 1990). Roy and Wang (2009) have proposed horseshoe and serpentine electrode configurations in a numerical study that showed promise for generating induced flows with three-dimensionality.

Plasma synthetic jet configurations have been proposed in both annular (Jacob et al. (2005), Santhankrishnan and Jacob (2007)) and linear configurations (Santhanakrishnan and Jacobs (2008), Santhanakrishnan et al (2009), Sherman (1998)). Santhanakrishnan and Jacobs experimentally studied both a steady and pulsed annular arrangement. Steady operation behaved like a synthetic jet in crossflow, and pulsed operation formed multiple counter-rotating vortex rings. Linear plasma synthetic jets were experimentally and numerically studied by Santhanakrishnan et al. (2009) in quiescent air using PIV. The researchers found similar findings as the annular array in that steady operation resulted in a zero-mass flux jet, and unsteady operation resulted in counter-rotating vortical structures. They also found a low peak velocity located close to the actuator compared to the higher velocities observed with traditional synthetic jets.

Porter et al. (2008, 2009) investigated improving upon the linear plasma synthetic jet by modifying the shape of the buried electrode to produce spanwise variation or "waviness" in the normal jet. They create spanwise waviness in the vertical jet by removing portions of the buried electrode (either diamond or square shapes) at specified spatial frequency. This limits the extent of the plasma to areas in which the bottom electrode has not been removed creating spanwise variation in the body force. They found that their electrode arrangements had the ability to generate vertical jets with spanwise spatial variation (Porter et al. 2009).

Jet vectoring is another interesting approach to generating increased vorticity and mixing by controlling the direction of the jet produced by linear plasma synthetic jets. Variations of jet vectoring have been suggested by Porter et al. (2008, 2009), Bolitho and Jacobs (2008), and Sherman (1998). The work of Porter et al. is very interesting in that they vary the voltage applied

to each of the two exposed electrodes that form a linear plasma synthetic jet. They demonstrate ≈ +/- 60 degrees of jet directional control by varying the voltage between exposed electrodes. In addition they demonstrate oscillation of the jet by frequency modulation, greatly expanding the design space of linear plasma synthetic jets.

1.5. **Current Study**

The objective of this research is to investigate the feasibility and technological challenges associated with using a new type of sensor in a closed loop separation control system. The sensor is based on surface stress sensitive film (S3F) technology which is sensitive to both surface shear stress and pressure gradient. Wright et al. in their 2002 paper outline two important challenges that must be addressed to use discrete sensors in flow control applications:

1. development of accurate, durable shear stress sensors

2. integration of a high-density sensor suites into aerodynamic surfaces.

This research has addressed both challenges by investigating the use of a new type of shear stress sensor technology for use as a sensor in a flow control system. This work focuses on several specific objectives:

1. Obtain the experimental suction surface Cp and boundary layer behavior of an Eppler 387 (E387) airfoil model at low Reynolds number over a range of small angles of attack that result in laminar boundary layer flow separation.

2. Study a new method of surface stress sensitive film installation over a curved surface to reduce the effect of the film on the boundary layer and surface being studied.

3. Compare several different dielectric barrier discharge plasma actuator geometries for low Reynolds number separation control on the E387 airfoil model.

4. Develop a first generation closed loop low Reynolds number separation control system using S3F as the separation control sensor.

This work culminates with an experimental demonstration of a separation control system comprised of an S3F sensor and linear vertical jets generated by dielectric barrier discharge (DBD) plasma actuators as the flow control mechanism.

2. Methodology

This chapter discusses the methodology used to complete this research. In order to reach the end goal of demonstrating S3F in a closed loop separation control system, several major milestones were completed:

- wind tunnel setup and modification

- fabrication and initial testing of airfoil models in a small scale wind tunnel

- development and testing of high sensitivity S3F based wall shear stress sensor

  - S3F based sensor system design – packaging & experimental arrangement

  - S3F development and fabrication by ISSI Inc., Dayton, OH

  - S3F testing in the AFRL/RZ wind tunnel, WPAFB, OH

- development of the actuator and flow control method (open loop experiments)

- detailed development of closed loop control method – software and hardware

Each of these milestones will be discussed in relevant sections of this chapter.

2.1. Experimental Facility

This research was performed at the Air Force Research Laboratory (AFRL) Propulsion Directorate's Low Speed Wind Tunnel (LSWT) facility located at Wright-Patterson Air Force Base, Ohio. The LSWT facility is comprised of two wind tunnels, the first is a large, variable angle linear cascade facility primarily used for aerodynamic investigation of turbomachinery components. The 2-D linear cascade has been used in numerous previous efforts (see for example Sondergaard et al. 2002; Bons et al. 2002; McQuilling 2007). The tunnel features a variable angle test section that is 0.85m tall by 1.22m wide at the inlet and typically houses 6-7 linear turbine blades with an axial chord of 17.8 cm. An optional turbulence generation grid can be used to increase the freestream turbulence up to a maximum of approximately 12%. A recent

upgrade to the facility has included the development, installation, and characterization of a unique, internally mounted, periodic wake generator which has been described in Nessler et al. (2009a; 2009b).

A second, straight test section wind tunnel was relocated to the LSWT facility to use in this effort. The wind tunnel is referred to as the Developmental Wind Tunnel (DWT). The DWT has good optical access, and an airspeed range of 4.5 – 65 m/s generated with a 7.5 kW electric motor. The inlet has a series of flow straighteners and turbulence-reducing screen followed by a 9.5:1 contraction providing an advertised turbulence level of less than 0.2%. The test section dimensions are 30.5 cm x 30.5 cm x 61 cm.
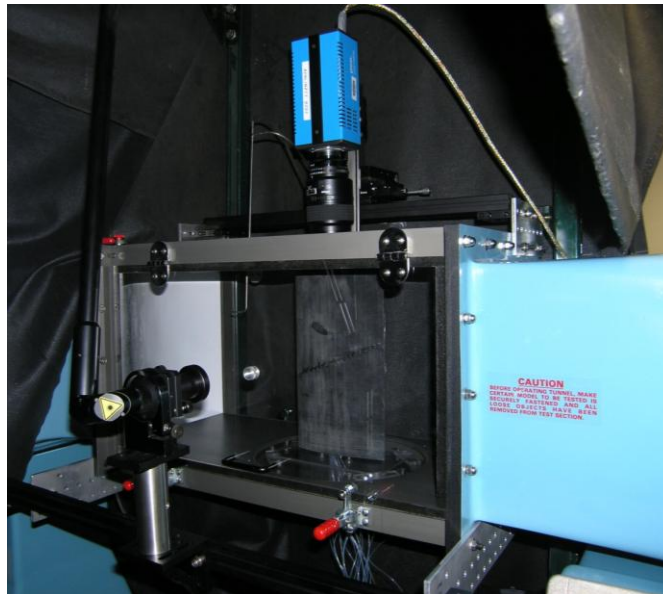
Figure 2.1 Airfoil 1 mounted in the DWT test section and setup up for PIV, flow visualization, and C_p measurements.

In order to complete the experiments in this research, several modifications to the wind tunnel were made. The bottom of the wind tunnel had an aluminum disk insert for mounting models or a sting. This metal disk was replaced with a clear acrylic disk to provide optical access from below, and lower mounting holes for the airfoil. An optical table was positioned in front of the wind tunnel section to mount equipment and isolate it from wind tunnel vibration. Four

mounting plates were fabricated and added to the top and bottom of the wind tunnel test section.

The lower mounting plates were extended out from under the test section to create a cantilevered

mounting. An optical plate was attached to the cantilevered mount. The two optical mounting

plates provided both a surface that was disconnected and free from wind tunnel motion, and one

that was rigidly attached to the wind tunnel test section. The PIV laser and S3F lamp power

supply were mounted on the optical table, and the S3F lamp, S3F camera, and sheet forming laser

lenses were mounted to the optical plate fixed to the wind tunnel test section.   Several traverses

were used around the test section.   A microtraverse controlled by a custom Labview VI was used

to position instruments in the wake of the test specimen. A manual traverse that moved in the

wind tunnel longitudinal direction was located above the test section and used to mount a camera.

Another manual traverse was mounted on the optical board and used to position either a camera

or laser sheet.

1. Floating optical table
2. Cantilevered mounted optical board
3. Side traverse (manual)
4. Wake traverse (computer cntrl.)
5. Upper traverse (manual)
6. Laser safety curtain
7. Articulating laser arm
8. Class 4 laser
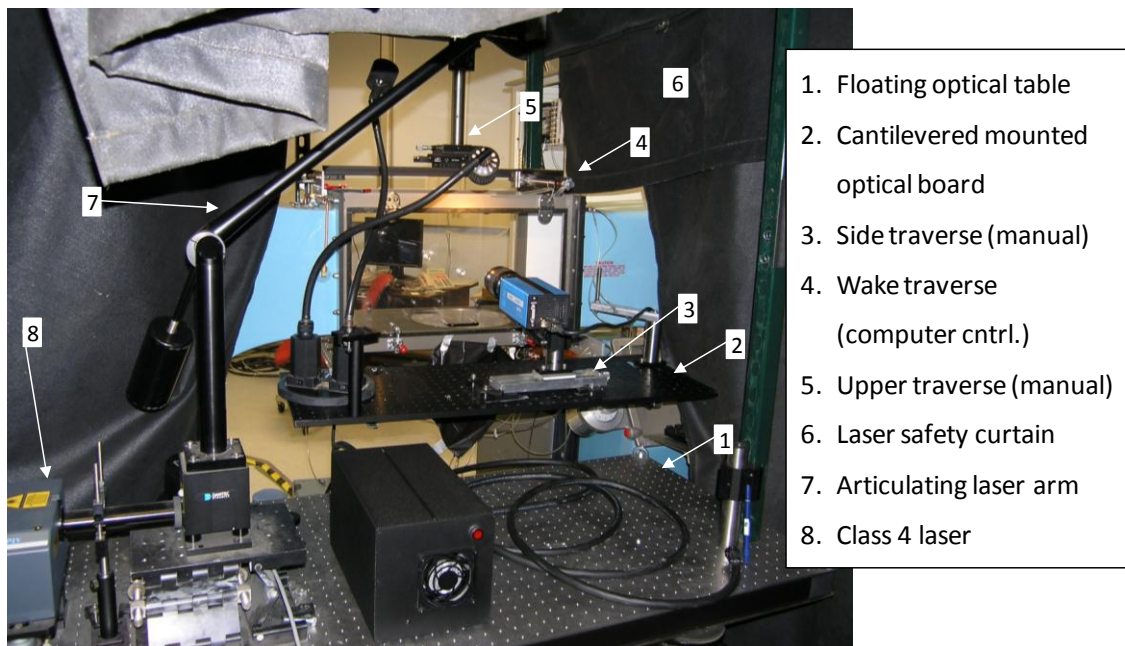
Figure 2.2 Modifications to wind tunnel

2.1.1. Data acquisition

A precompiled Labview application was provided with the wind tunnel to set the motor speed. In order to measure the wind tunnel freestream velocity and other parameters a National Instruments data acquisition rack was set up. The rack consisted of a PXI-1010 chassis with the cards shown in Table 2.1.   A MC-4SA Servo amplifier system and NI PXI-7344 motion controller was used to control a National Aperature MM4M-EX200 micro traverse. The micro traverse was mounted over a downstream slot which enabled wake traverses.

Table 2.1 PXI-1010

Device	Description	Function
PXI-8335	MXI-3 Interface	Interface to PC, 1.5 Gbit/s serial data rate
PXI-7344	Motion Controller	Control of microtraverse
PXI-5052E	Multifunction I/O	16 bit, 333 kS/s digitization of analog SCXI signals
SCXI-1121		Pressure Signal Acquisition

2.2. **Airfoil**

A generic low Reynolds number airfoil called the Eppler 387 (E387) was used in this work to make the research basic and applicable across design domains. Selig and McGranahan (2004) reported that the airfoil geometry was originally designed for model sailplanes in the 1960s by Richard Eppler, but has also been used to compare one low speed wind tunnel facility with another. For this reason the airfoil is well represented in literature and has been tested in numerous wind tunnel facilities such as those at: Princeton, NASA Langley, and the University of Illinois at Urbana-Champaign.   In addition to experimental data, several researchers have performed computational studies, both RANS and DNS, using the Eppler 387 airfoil.

The Eppler 387 airfoil has been extensively tested at the University of Illinois at Urbana-Champaign and results have been presented in several reports. A 2004 report by Seilig and McGranahan focused on the use of the blade geometry as a wind turbine, presented aerodynamic force measurements. The group at UIUC tested the blade at a range of low Reynolds numbers from 100,000 to 500,000. Researchers at NASA Langley (McGhee et al. 1988) also tested the blade at low Reynolds numbers down to 60,000. Both facilities report a mean separation bubble on the suction surface at a Reynolds number of 100,000 and zero degree angle of attack. The NASA Langley data provides pressure coefficient as well as laminar separation location and turbulent reattachment location identified from oil flow visualization.
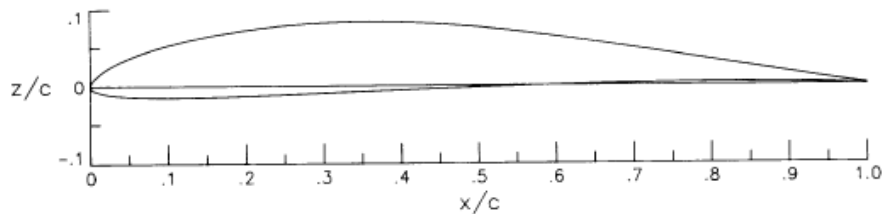
Figure 2.3. Eppler 387 airfoil section shape. (from McGhee et al. 1988)

Figure 2.4 shows pressure coefficient data taken in the NASA Langley tunnel at a Reynolds number of 100,000, and at angles of attack from -3 to +2 degrees. The pressure coefficient indicates laminar boundary layer separation at an angle of attack of -3 degrees, with turbulent reattachment near the trailing edge as angle of attack is increased to -2 degrees and above. Reattachment location moves upstream as angle of attack is increased. Figure 2.5 and Figure 2.6 show pressure coefficient at angles of attack of 0 degrees and 2 degrees overlaid with oil flow visualization indicated laminar separation and turbulent reattachment locations. For the larger angle of attack, the length of the separation bubble has decreased slightly as angle of attack increased. The separation point has moved forward as angle of attack increased. Based on the measurements at UIUC and NASA Langley the E387 was chosen because of laminar separation

33

on the suction surface at small angles of attack. The Langley data taken at a Reynolds number of

60,000 indicated laminar flow separation at angles of attack near zero. The experiments reported

in this work were in the range of Re = 1.5×10^5 to 5.0×10^4, so both a laminar separation bubble

and non-reattaching boundary layer separation were possible by adjusting the wind tunnel speed

with the angle of attack fixed. Both of these low Reynolds flow phenomena have been observed

in previous LP turbine investigations in the AFRL/RZ LSWT linear cascade at roughly the same

freestream velocities. This allowed previous work using S3F, in terms of film sensitivity, to be

directly applicable to the present study. It will also make scaling the experiments for future

studies in the large linear turbine cascade tunnel easier.

Several researchers have performed computational studies on the E387 airfoil geometry to

test numerical methods of simulating unsteady low Reynolds number flows over airfoils. Lin and

Pauley (1996) performed a computational study using an unsteady 2D incompressible Navier-

Stokes equation code. They found that periodic vortex shedding occurred at each Reynolds
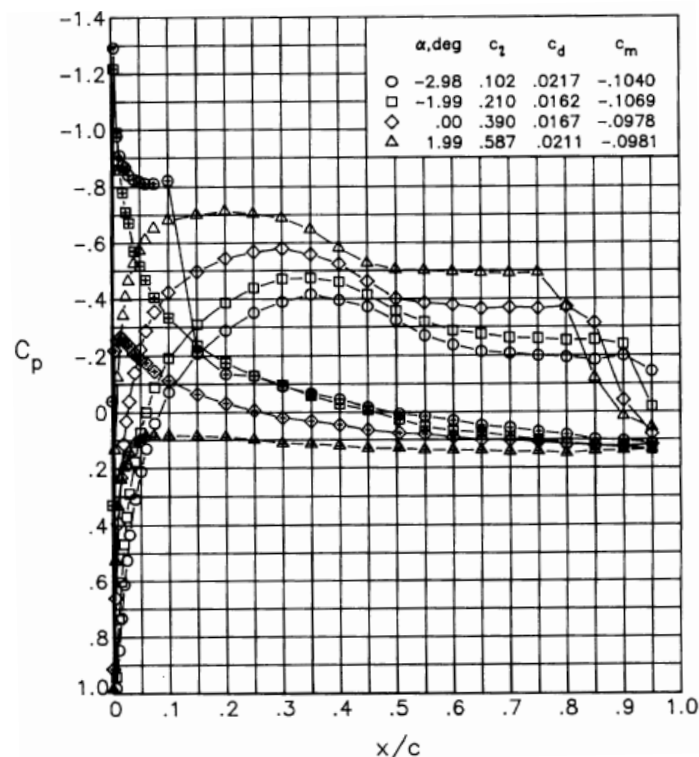
Figure 2.4 Eppler 387 Pressure Coefficient at Re = 100,000 (from McGhee et al. 1988).

number they studied, 6 x 10^4, 1 x 10^5, and 2 x 10^5 at several small angles of attack. The results

from Lin and Pauley lead them to suggest that two dimensional large-scale structures in the form

of vortex shedding control the laminar separation bubble and omnipresent small-scale turbulence

plays only a secondary role. Hall and Mohseni (2007) and Sahin, Hall, and Mohseni (2008) also

performed numerical studies on the flow around the Eppler 387 airfoil. In the first paper the

authors presented results using a time-accurate, three-dimensional, finite element based code,

with no turbulence model. Calculations were performed at a Reynolds number of 6.0 x 10^4 and at

various angles of attack. Surface pressure coefficient and surface shear stress was presented at

angles of attack of 2, 4, and 6 degrees. The second paper by Sahin, Hall and Mohseni in 2008

present DNS simulation of the flow around the Eppler 387. Computations were made at a
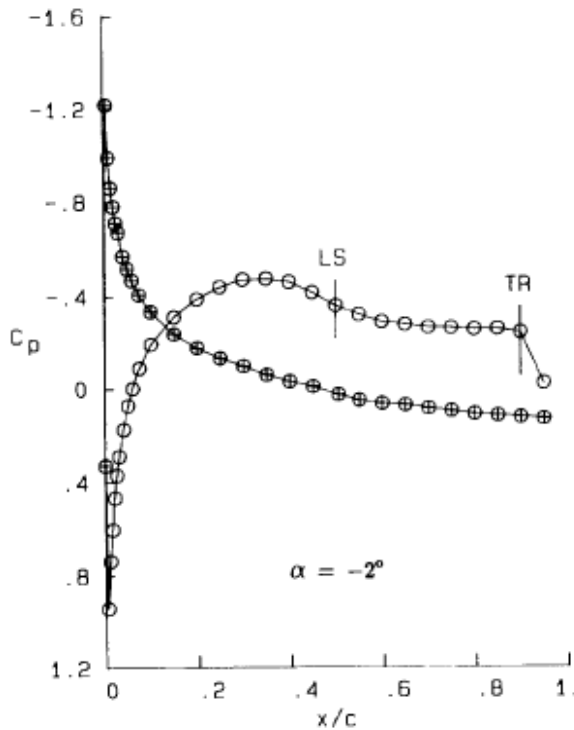
Figure 2.5. Pressure coefficient data at -2° angle of attack with laminar separation and turbulent reattachment point identified by oil flow visualization (from McGhee et al. 1988).
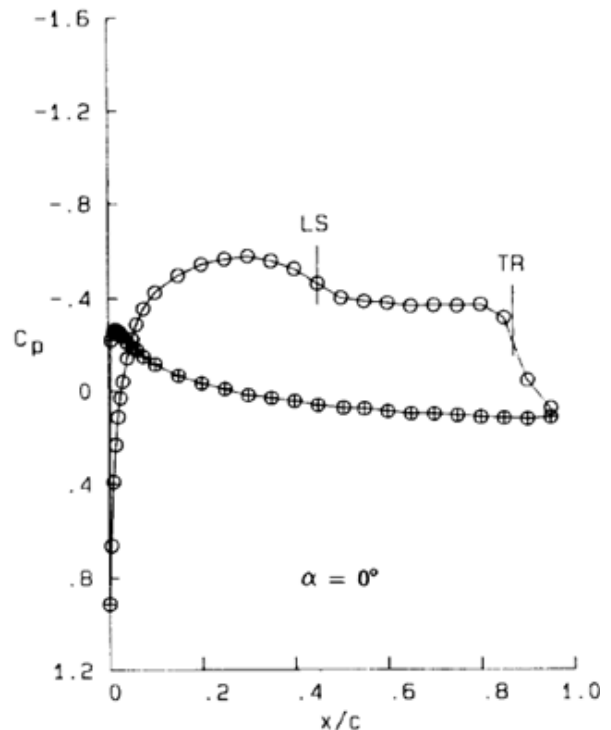
Figure 2.6. Pressure coefficient data at zero angle of attack with laminar separation and turbulent reattachment point identified by oil flow visualization (from McGhee et al. 1988).

Reynolds number of 6.0 x 10^4, using both three dimensional and two-dimensional DNS. The authors indicate that the two dimensional simulations indicated a large, abrupt decrease in surface pressure just before reattachment as was found in other numerical studies. The three dimensional simulation agreed with the experimental data by McGhee et al. in that the size of the abrupt decrease was smaller. This was attributed to the lack of spanwise flow structure in the two-dimensional simulation, as the three dimensional simulation indicated the formation of half-moon type vortices in the laminar shear layer, with no regular spanwise structure. The vortices were observed to interact with each other and burst into the freestream causing a momentum exchange between the airfoil boundary layer flow and freestream. They report these findings were consistent with experimental observations by Bergmann et al. (2006) who used scanning PIV to investigate the spanwise structure and dynamics of the roll-up of vortices within the separation bubble of the SD7003 airfoil.

An axial chord length of 16.51 cm (6.5 inches) was chosen for the experiments since the inlet velocity at the Reynolds numbers being investigated was inside the operating range of the wind tunnel and agrees well with velocities over a LP turbine blade in previous experiments using S3F. The airfoil models were rapid prototyped out of a mixture of ABS and Polycarbonate and were mounted across the full height of the wind tunnel and fixed at the top and bottom.

2.2.1. Wind tunnel models

Two different test articles were fabricated, both with the E387 airfoil geometry. The first airfoil was an unmodified E387 airfoil, and the second airfoil had a cavity formed in the suction surface in which a removable S3F carrier was mounted, these are referred to as Airfoil 1 and Airfoil 2. An end cap was attached to the top end of each airfoil with two screws. The end cap had a circular extrusion that extended into a hole in the top wall of the wind tunnel test section. A bolt held the top of the airfoil to the wind tunnel wall, and two screws at the bottom end of the airfoil rigidly fixed the airfoil in the test section.

The S3F carrier that was installed in Airfoil 2 was 3D printed out of a mixture of ABS and

polycarbonate and was very flexible due to its 1.3mm maximum thickness. The flexibility of the

carrier enabled it to conform to the curvature of the airfoil suction surface. The leading edge of

the S3F carrier and corresponding cavity on the airfoil were notched. This provided a secure,

tight, and smooth interface along the interface between the S3F carrier and airfoil suction surface.

Each carrier was hand sanded to ensure a tight fit into the airfoil cavity. Early tests used spray

adhesive to attach the S3F carrier to the airfoil. Adhesive did not prove to be a reliable method to

attach the S3F carrier because of small amounts of S3F residue left on the bottom of the S3F

carrier during filling of the S3F cavity. Instead the notch at the leading edge of the S3F carrier

and two small, countersunk screws placed at approximately $C_x = 90\%$ were used to reliably

secure the S3F carrier to the airfoil. Drawings of Airfoil 2 are shown in Figure 2.7 and Figure

2.8.
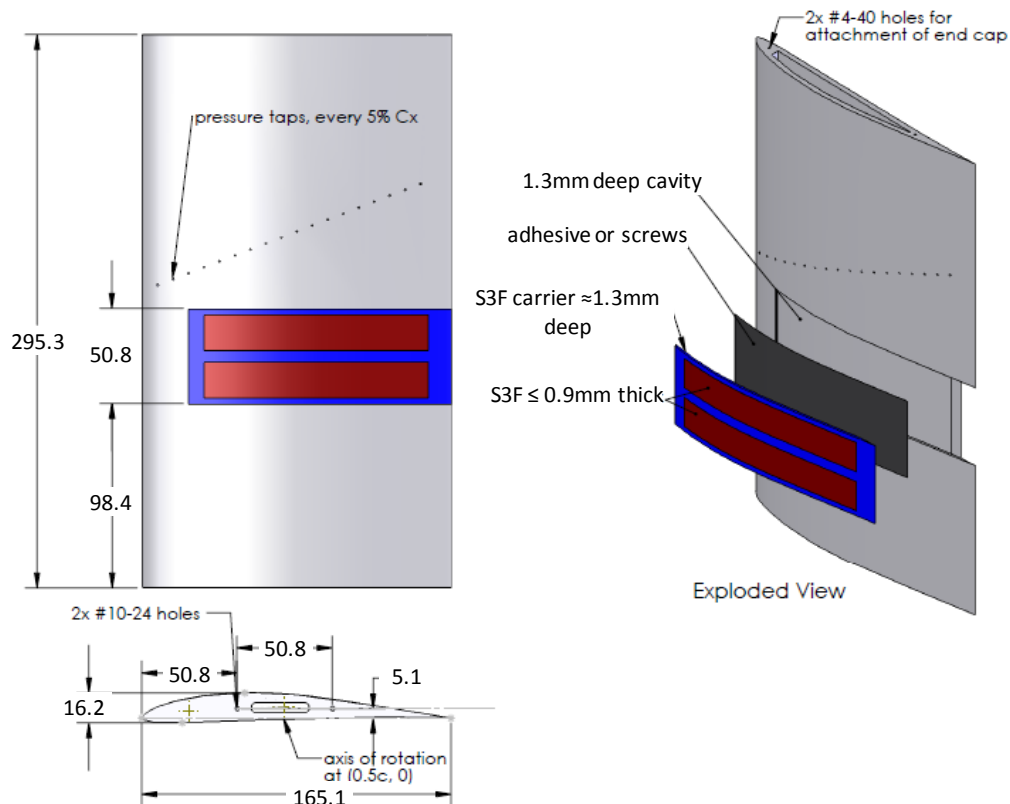
Figure 2.7 Drawing of Airfoil 2 showing the pressure tap locations and S3F location (all dimensions in millimeters).
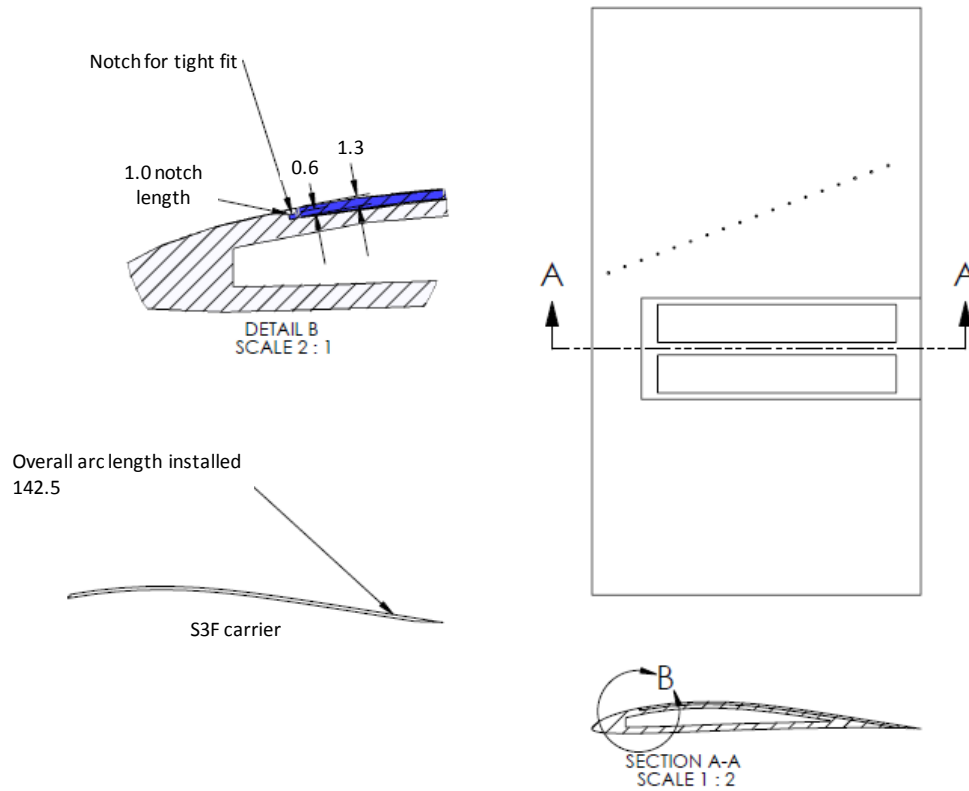
Figure 2.8 Drawing showing S3F carrier installation on Airfoil 2 (dimensions in mm).

2.3.   **Experimental Techniques**

This section explains the experimental methods used to acquire pressure data, particle image velocimetry, flow visualization, and S3F data.   A detailed background and explanation of the S3F method is provided.

2.3.1. Pressure Measurements

Pressure measurements were used to calculate the inlet velocity, surface pressure coefficient and drag. Two LabVIEW VIs were created, one to obtain static surface pressures to calculate pressure coefficient, and one to measure the pressure in the airfoil wake to calculate drag. While LabVIEW software automated the entire drag measurement process, the C_p measurements

required human intervention to adjust a manual pressure selector valve to choose the correct pressure port when prompted by Labview.

Pressure taps located every 5% axial chord on the suction surface of each model, starting from 5% chord to 90% chord, were placed during printing of the airfoil models. The pressure tap holes were purposely printed undersized and then manually enlarged during the plumbing process. Pressure taps had an internal diameter of 0.91 mm and were staggered in the spanwise direction to reduce the chance for imperfections of upstream taps to contaminate the downstream tap measurements. The pressure lines of Airfoil 1 were completely enclosed inside the body of the airfoil and exited through a hole at the bottom of the wind tunnel. During testing of the S3F method the hollow cavity in Airfoil 2 was filled in an effort to stiffen the model. This meant the pressure lines could not be passed through the inside of the airfoil. Instead the pressure lines were run along the pressure side of the airfoil and covered with a smooth layer of tape. Even though the pressure lines were extremely small diameter, this method modified the pressure surface geometry and effected the flow field. This will be discussed further in the section on airfoil characterization.

An array of AllSensor low pressure transducers were used for pressure measurements with nominal 0.05% and maximum 0.25% linearity full scale. A mounting plate, shown in Figure 2.9, with three 0-125 Pa (31.1 Pa/V) and three 0-249 Pa (62 Pa/V) pressure transducers was fabricated and mounted under the wind tunnel. The mounting plate included 5V supply voltage distribution and BNC connectors for signal transmission to the NI data acquisition rack. The 0-125 Pa transducers were used for wake pressure measurements and inlet dynamic pressure measurements. The 0-249 Pa transducer was used for C_p measurements. A barometer and thermometer were located on site to measure atmospheric conditions.
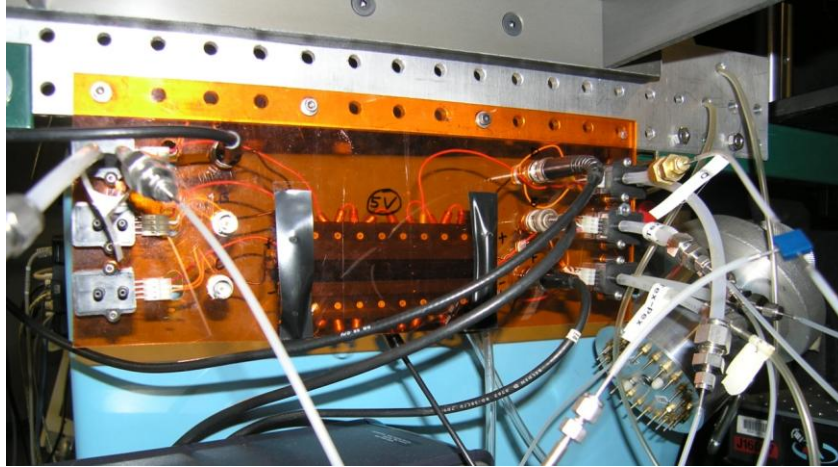
Figure 2.9 Pressure transducer mounting plate.

2.3.1.1.   Pressure Coefficient Measurements

The upstream static and total pressures were measured via a Pitot-static probe located 101 mm ($\approx 2/3\ C_x$) upstream from the leading edge of the airfoil. The pressure taps were plumbed to a manual selector valve and then to the pressure transducer mounting plate. Static pressure was calculated using:

$$Cp = \frac{P_i - P_{t,in}}{q_{in}} \tag{2.1}$$

with no corrections. P_i is the pressure at the each pressure tap, $P_{t,in}$ is inlet total pressure, and q_{in} is the inlet dynamic pressure. Pressure tap locations used on each airfoil are shown in Table 2.2. Check marks in the table indicate locations where measurements were made. The locations on Airfoil 2 between 25% and 35% axial chord listed as "blocked" indicate tap location that were covered up when plasma actuators were installed on the airfoils.

Table 2.2 Pressure tap locations.

	Tap Location - C_x%								
	5	10	15	20	25	30	35	40	45
Airfoil 1	√	√	√	√	√	√	√	√	√
Airfoil 2	-	-	-	-	Blocked	Blocked	Blocked	√	√
	50	55	60	65	70	75	80	85	90
Airfoil 1	√	√	√	√	√	√	√	√	√
Airfoil 2	√	√	√	√	√	√	√	√	√

Data was acquired at a 1000 Hz sampling frequency and the mean pressures over the sampling period were used in the calculation of C_p. Typically, data was recorded for a minimum of 4 seconds at each port, with a 9 second settling time before the start of recording at the next measurement location. This method provided very repeatable pressure coefficient measurements.

Uncertainty in the C_p measurements is nominally 1.5% at the pressure minimum, and 3.1% in the trailing edge area at Re = 5×10^4. At Re = 1.0×10^5 uncertainty in C_p is nominally 0.5% at the pressure minimum and 1.1% in trailing edge area.

2.3.1.2. Drag Measurements

Drag was calculated by wake traverses using the method of Jones (Goett, 1939):

$$C_d = \frac{2}{C_x} \int^W \frac{\sqrt{P_{T,w} - p_w}}{\sqrt{P_{T,in} - p_{in}}} \left(1 - \frac{\sqrt{P_{T,w} - p_{in}}}{\sqrt{P_{T,in} - p_{in}}} \right) dz \tag{2.2}$$

using a Pitot-static probe located in a slot $0.5 C_x$ downstream from the trailing edge. No corrections were applied to the data. Uncertainty in the drag measurements, omitting errors related to the probes, is less than 1%.

2.3.2. Particle Image Velocimetry & Flow Visualization

The modern digital 2D PIV technique has developed into a method that is quite common in experimental fluid dynamic laboratories. Fluid velocity fields can be obtained relatively quickly, with high spatial resolution, using a non-intrusive optical measurement method. Four main pieces of equipment are required: a high power laser, digital camera, flow seeder, and control and post processing software. The beam from a high power laser is formed into a thin laser sheet to illuminate a two dimensional cross section of fluid flow seeded with light scattering particles. A digital camera records the light scattered from the particles in two consecutive exposures. The time between the exposures is short, and set based on the velocity of the flow being measured and

the size of the field of view. Cross correlation methods are used to determine the particle

displacement in individual regions across the entire field of view. The fluid velocity across the

entire field of view is then calculated using local particle displacement divided by the time

between the two consecutive exposures.
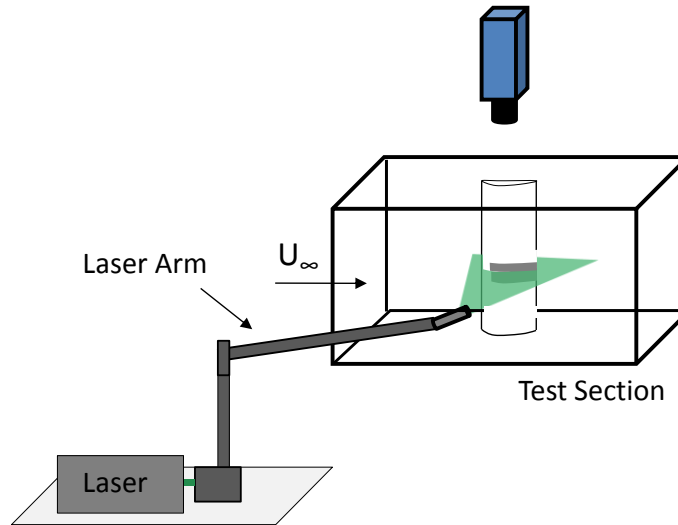
Figure 2.10 General PIV Experimental Arrangement

2.3.2.1. PIV Experimental Setup

A New Wave Solo - 120 dual-head Nd:YAG laser capable of dual 120 mJ pulses was used

for flow illumination. The laser beam was transmitted from the laser aperture to the wind tunnel

test section using a Dantec articulating laser arm. A Dantec sheet forming optics module was

mounted to the end of the articulating arm and used to form a thin laser sheet with 1 mm nominal

thickness. The laser sheet was positioned to cut through a cross section of the airfoil span at the

edge of the S3F film. A pulse generator was used to control system timing which was set to 10

Hz. The time between consecutive exposures was a function of flow velocity and optical

magnification factor. A high resolution, PCO 1600 camera with 1600 x 1200 pixel resolution

was used to acquire images.

Instantaneous and ensemble averaged flow fields were calculated using Dantec Flowmanager processing software. Multi-pass adaptive cross correlation was used to analyze the images with interrogation domains of 128, 64, and 32 pixels with a 50% overlap.

PIV experiments in the LSWT linear cascade have used fog from a theatrical fog generator for flow seeding, but that method proved unacceptable in the smaller DWT. Two issues precluded the use of the fog generator in the DWT: condensation on the airfoil leading edge and inadequate room ventilation to remove fog generator odor. Different clean seeding methods for PIV have been investigated by Reeder et al. (2009) and inspired the use of water particles generated by a commercial boiler. A Sussman MBA9 9kW electric boiler was used to generate steam that was directed into the inlet of the wind tunnel (See Figure 2.11). The steam was injected approximately 1-2 meters upstream of the inlet. A separate tank and water pump provided a virtually endless supply of water to the boiler. This seeding method worked nearly analogous to the propylene/water fog generator except that a much higher laser power setting was required for adequate illumination. Flow visualization images were acquired with the same setup as the PIV technique.

The PIV technique is very useful for obtaining high spatial resolution fluid velocity fields, but the method is not without limitations. General limitations of the technique encountered in this work were:

1. Laser reflection makes it difficult to obtain fluid velocity very close to the airfoil surface. Measurements were generally limited to greater than 1mm from the wall.

2. The time between consecutive exposures must be set to one value, but the actual flow field may have large velocity gradients. The experimenter must choose a time delay that provides adequate particle displacement (generally on the order of 10 pixels) in the region of greatest interest. In the separated flows measured in this work the delay time had to be set long enough to enable some measurement of the flow in the separated regions as well as freestream.

3. It is sometimes a challenge to get flow seeding reliably in the field of view. It is also difficult to reliably get seeding in regions of separated flow. If the seeding is inadequate in the separated regions the velocity will measure zero and potentially bias calculations in neighboring regions.

Figure 2.11 Flow seeding equipment.

2.3.2.2. Benchtop DBD Plasma Actuator Flow Visualization

Several different DBD plasma actuator electrode configurations were fabricated and tested in an effort to improve flow effecter control authority over the traditional asymmetric DBD plasma actuator electrode arrangement. A simple method to visualize the induced velocity of each arrangement on a bench top in quiescent flow was devised and used to compliment wind tunnel data.

A schematic of one flow visualization arrangements is shown in Figure 2.12. The plasma actuators were fixed to a Nylon sheet using adhesive transfer tape. The laser beam from a Class 3A laser diode was expanded into a sheet and used to illuminate planes across the plasma actuator. A small plastic container was filled with a mixture of water and dry ice that created a fog that was naturally pumped through a tube and out a series of orifices. The end of the tube was set up so that the fog would flow across the plasma actuator. Various digital camera and lens combinations were used to capture the plasma on and plasma off images showing the wall jets generated by each plasma actuator arrangement.
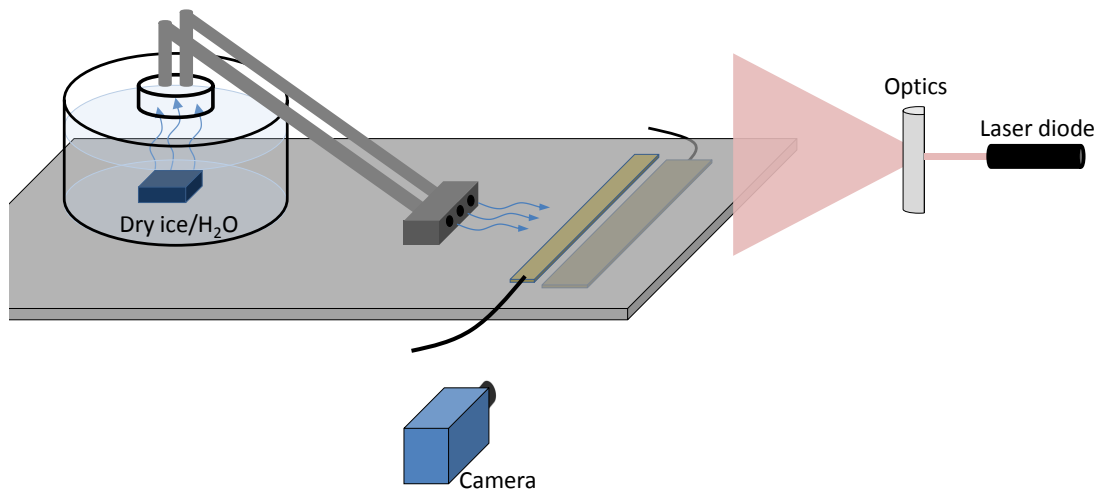
Figure 2.12 Benchtop plasma actuator flow visualization diagram.

2.3.3. The S3F Method

The S3F method uses an elastic film designed and manufactured by ISSI Inc. to measure wall pressure and wall shear stress in fluid flows. The film has two types of sensors; the first is used to measure normal force (pressure) on the film by a fluorescent probe embedded in the S3F. The second consists of markers distributed across the surface of the film. Marker displacement under load from the fluid flow is recorded using a digital camera and compared to a flow-off image to

determine film tangential displacement field. Recently Fonov et al. 2010 used stereo

photogammetry to measure and reconstruct the deformed S3F surface which enables

measurement of normal and tangential displacement using only cross correlation techniques.

Once the S3F deformation field is measured, the normal and tangential wall forces can be

calculated from the film displacement by solving an inverse elasticity problem using FEA (Fonov

et al. 2006).
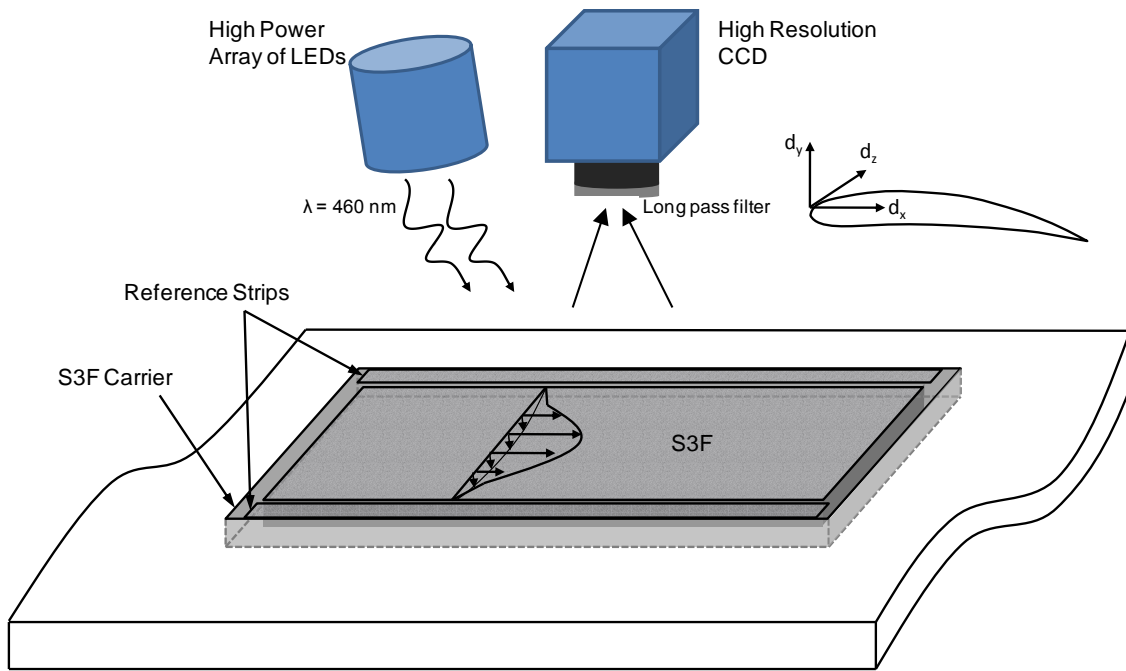
Figure 2.13. S3F Experimental Setup

Through analysis of the response of S3F using both experimental and analytical techniques

ISSI has determined that with spatial loading frequencies (thickness/contact surface) below 0.1,

film response can be modeled mathematically by (from Crafton et al. 2010):

$$d_X = \frac{h}{\mu_m}\left(\tau_X - \frac{h}{2}\frac{\partial P}{\partial x}\right) \qquad d_Y = \frac{h}{\mu_m}\left(\frac{h^2}{3}\frac{\partial^2 P}{\partial x^2} - \frac{h}{2}\frac{\partial \tau_X}{\partial x}\right) \qquad (2.3)$$

In Equation (2.3), the surface normal (d_y) and tangential (d_x) reaction of the film is written in

terms of the film thickness (h), shear modulus (μ_m), tangential stress (τ_x), and normal stress (P).

46

These equations give insight into designing a film to have a higher response to shear than pressure, or vice-versa. The tangential reaction of the film is a function of tangential stress and pressure gradient scaled by thickness. A thin film will have a higher relative response to shear forces than to pressure gradients. Conversely, a thicker film will show a higher response to pressure forces over shear forces (Crafton et al. 2010). Equation (2.3) was derived by ISSI Inc. based on the theory of elasticity and observed response of S3F to various surface forces (Fonov et al. 2011).

Another important insight from Equation (2.3) is that in the presence of small pressure gradients, shear stress is linearly related to tangential displacement. This key attribute was used in this work to develop the separation control sensor and will be discussed further in Sections 2.4 and 3.4.3.

The frequency response of the S3F is described by ISSI Inc. with a simple mass-spring-damper model that assumes the film is purely elastic (Crafton et al 2008). The first natural frequency of tangential oscilliation of the film is calculated by:

$$ f_0 = \frac{1}{2\pi} \sqrt{\frac{\mu_m}{\rho h^2}} \qquad (2.4) $$

The film frequency response is thus a function of shear modulus (μ_m), density (ρ), and thickness (h), which enables the frequency response to be adjusted in the range of 0.3 to 10 kHz (Crafton et al. 2008).

S3F has been fabricated with a shear modulus as low as 8 Pa and as high as several thousand Pascal, and thickness from 0.1mm to 1mm (Crafton et al. 2008). The ability to fabricate S3F with wide ranges of material properties allows a film to be fabricated with response characteristics that are designed for a particular flow environment using Equations 2.2-2.3.

Quantifying and improving upon the sources of uncertainty of S3F measurements is an on-going effort. Crafton et al. (2010) identified the dominant error sources of shear stress

measurement to be tangential displacement and film thickness. Experiments using fully

developed channel flow resulted in skin friction measurements with an error of about 6% full

scale (Crafton et al. 2010.).

Several methods are used by ISSI Inc. to obtain film properties, and each of these

measurements has a direct effect on skin friction and pressure measurements. The film thickness

is measured either by optical absorption, or an ultrasonic or capacitive thickness gage. Crafton et

al. (2010) estimates the accuracy of these thickness measurement devices to be about 1 μm plus

1% of the reading. ISSI uses two different methods to measure the shear modulus of the S3F.

One method is by static loading, the other is by dynamic loading. The static loading method

involves determination of the shear modulus by measuring the displacement of a small load

applied to the film surface as the system is rotated. An example of this method is shown in

Figure 2.14. The second approach uses dynamic modeling in which an oscillating tangential load

is applied to the film and the frequency is varied until the displacement amplitude reaches a

maximum. The frequency obtained using this technique is the first tangential natural frequency

of the film and the shear modulus is calculated using the equation shown in Figure 2.15. ISSI

estimated the uncertainty in shear modulus to be ± 10% for the ultra low shear modulus films

used in this work.

An additional error source when using S3F is the stability of the film properties. Crafton et al.
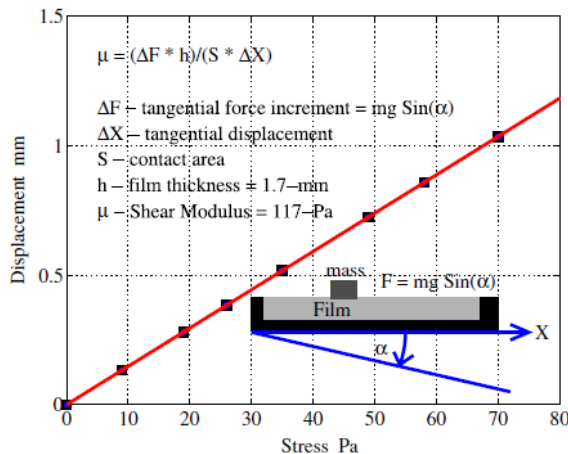
Figure 2.14 S3F calibration by static loading (from Crafton et. al 2008)
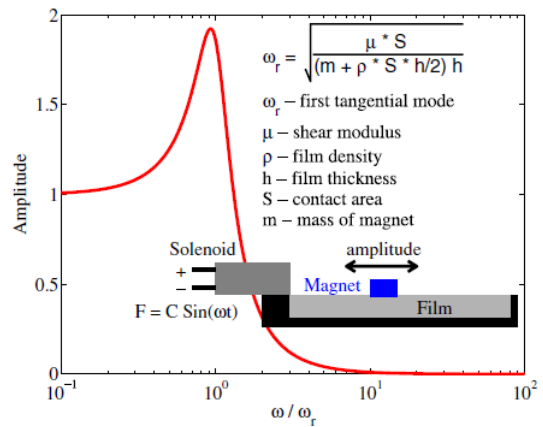
Figure 2.15 S3F calibration by dynamic loading (from Crafton et. al. 2008).

(2008) reported a significant change in shear modulus over the first day as the polymer initially cured. From day 1 to 10 the shear modulus changed 0.21% per day and experimental results indicated that over the remaining 118 day period the shear modulus change per day decreased even further.

The use of S3F at low Reynolds number, and in sea level air flows can push the limits of the technique (McQuilling 2007). Experiments using S3F have been reported in several studies found in open literature. Crafton et al. (2008) used the film for skin friction measurements in a hydrodynamic setting at high Reynolds number. Experiments were undertaken with a point sensor design installed in the wall of a water tunnel at Penn State University. The point sensor was packaged into a 76mm diameter plug inserted into the tunnel test section window. The S3F filled a 30 mm diameter x 1 mm diameter cavity. The bottom of the cavity was made of glass and below the glass window were LEDs for illumination and a CCD camera.

Figure 2.16 shows a picture of the point sensor concept as well as response of the film. The film was used in a zero pressure gradient boundary layer, so the film was designed for a large response to shear force versus normal force. The response plot shows that there is a non-uniform response along the edges of the sensor, but is uniform in the center up to approximately four film thicknesses from the boundary. Their work confirmed that the film displacement is linearly related to skin friction when the pressure gradient is negligible. The S3F skin friction measurements agreed with drag balance measurements with 5% rms difference, for one of the sensors used. The other sensor saw a larger deviation thought to be bias error. Source of error as pointed out by Crafton et al. (2008) are uncertainties in material properties, stability of the polymer, and experimental error sources caused by movement of the camera versus film over a series of data runs. In the work of McQuilling (2007, 2008a, 2008b), markers were added below the film and around the film in order to provide a reference channel for canceling out movement of the camera and optical system versus the film. The markers were fixed to the model, so any movement of the markers during the flow-on and flow-off images is associated with movement

between the model and the camera and are cancelled out. McQuilling (2007) used the film to study the flow over the suction surface of a low pressure turbine blade at low Reynolds number. The work of McQuilling (2008a) demonstrated the potential of S3F in flow velocities below 7 m/s. It was found that the sensitivity of the film was critical due to an order of magnitude variation of shear stress gradients from leading edge to trailing edge in the streamwise direction. McQuilling et al. (2008b) demonstrated the use of S3F applied to a L2F highly loaded LP turbine blade in a linear cascade to establish the separation location for CFD transition model validation. The studies by McQuilling et al. (2007; 2008b) demonstrated the potential of S3F for identification of flow features along the suction side surface of a blade at low velocity and also identified measurement uncertainties that need further investigation.
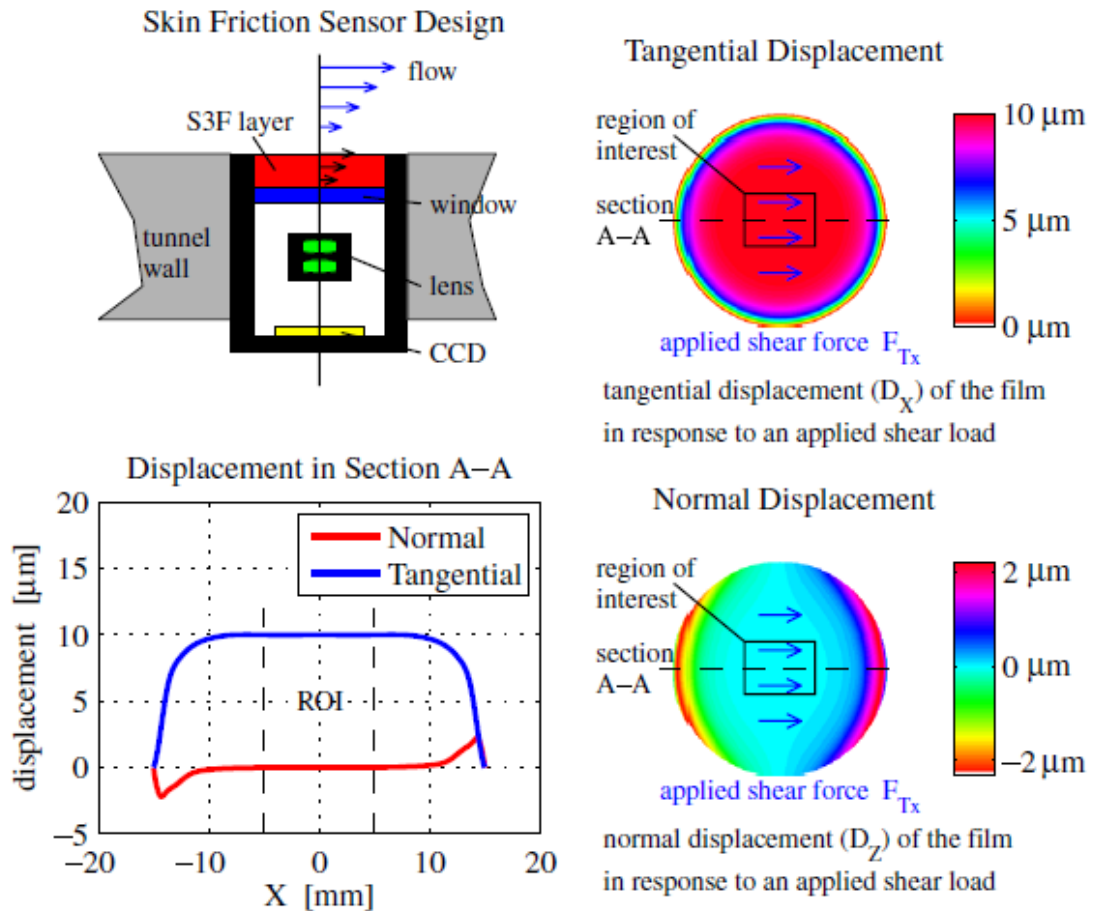
Figure 2.16 Design and response of S3F point sensor used by Crafton et al. (2008).

Two different applications of S3F film resulted in two different shear stress profiles along the surface of the blade. Sensitivity to tunnel vibration and deformation of the turbine blades in the wind tunnel was identified as a potential source of uncertainty with the technique (McQuilling 2008b).

Separate from fabrication and design of the film itself, another difficulty with the S3F technique is ensuring that S3F is cleanly mounted on the test article and that it does not affect the boundary layer or characteristics of the flow it is being used to study. The installation method could influence the pressure and skin friction over the surface. If the film is applied externally to an object (e.g. glued on) and not placed in a relief, the film will increase the thickness or shape of the object, which in turn will modify the pressure distribution. The film roughness may also affect the skin friction and transition point in the boundary layer if it differs in roughness from the base surface.

Previous studies have touched on the intrusiveness of the sensor. McQuilling (2007) applied S3F in a cavity along the suction surface of a LP turbine blade and irregularities in the data were observed that may have been due to disturbance of the flow by the S3F not being perfectly flat or flush with the blade surface. Measurements on the L1A LP turbine profile in the summer of 2009 compared the separation and reattachment location indentified from S3F measurements with the suction surface pressure profile measured using pressure taps at a different spanwise location. The reattachment and separation location indicated by shear measurement agreed within several percent of the chord with the pressure tap data.

An objective of this research was to improve the way S3F is installed on curved surfaces. S3F has been installed to surfaces by spraying, gluing, and filling a cavity.
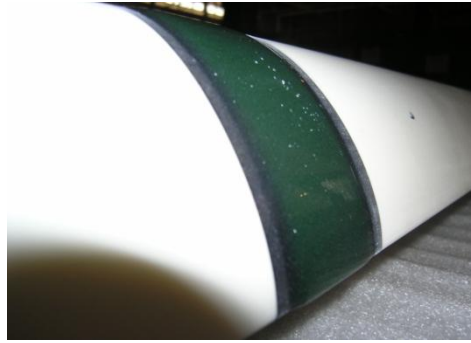
a.)
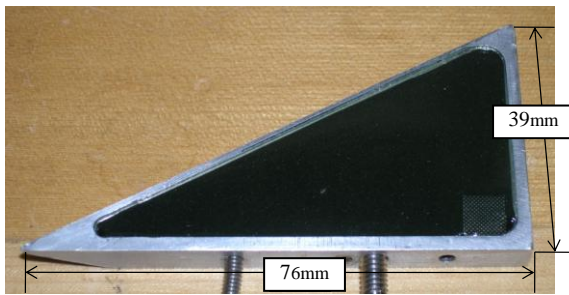
b.)
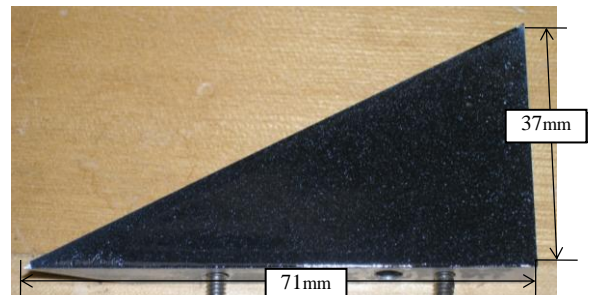
c.)

Figure 2.17 Samples of S3F applied by a.) gluing to a surface , b.) filling a cavity, c.) spray-on with an airbrush.

Forming the S3F in a cavity has worked well, but is difficult when the surface is curved. To simplify installing S3F on curved surfaces, a new method has been developed and demonstrated. Rather than forming the S3F in a cavity on the curved surface, it is formed in a flexible flat plate prior to installation onto the airfoil. The flat plate is referred to as the S3F carrier. In our experiments the S3F carrier was rapid prototyped with a single cavity, then lightly sanded for a smooth fit into a cavity on the suction surface of the airfoil as is shown in the drawing of Figure 2.8 and the photo in Figure 2.18. The S3F carrier was painted black prior to being filled with S3F to reduce reflection of light. The S3F carrier was filled with S3F at ISSI Inc. then installed in the airfoil and held in place with two flat head screws near the trailing edge.

Figure 2.18 Example of S3F carrier filled and installed on Airfoil 2.

The S3F experimental arrangement is shown in Figure 2.13. S3F was installed along the
suction surface of the E387 as was shown in Figure 2.7. Images were acquired with a
commercial, high resolution CCD camera (PCO 4000) with a resolution of 4008 x 2680 pixels. A
Nikkor 200 mm f4 lens with long pass filter was fitted to the camera and rigidly fixed to the wind
tunnel test section. A Novatron flashlamp with flash-on time on the order of several hundred
microseconds, and an ISSI Inc. high power LED lamp (460 nm wavelength) was used to
illuminate the S3F. The Novatron flashlamp provided a high intensity light source, but repetition
rate was limited to 0.33 Hz. The high power LED lamp can be operated in steady mode or high
speed pulsed mode driven by an external signal generator and was used in the closed loop control
experiments.

Images were transferred to CPU RAM over a high speed Cameralink interface (255 MB/s)
via a NI PCIe-1429 image acquisition board. A Labview based software program controlled
image acquisition and calculated film displacement using single pass cross-correlation. Frame
rate (sampling speed) and exposure was controlled by a Quantum Composer 9300 Pulse
generator. A slower, but potentially more accurate image analysis software program (ISSI Inc.)
was available to calculate S3F displacement for comparison with the Labview based software.

2.4. **Sensor System**

A general description and background on the S3F method was given in Section 2.3.3. This section focuses on the use of S3F in a separation control system, specifically in the experimental conditions of this research.

2.4.1. System Design Considerations

S3F is naturally sensitive to both pressure gradient and shear stress, however; in low pressure gradients Crafton et al. showed that film tangential response is essentially uncoupled from pressure gradient (Crafton et al. 2008). This implies that tangential displacement itself can be used as a direct indicator of shear stress direction and magnitude. Exploiting the direct relationship between S3F tangential displacement and shear stress enables the use of S3F as a separation sensor. The data from an S3F sensor could be analyzed and used in a separation control system in several ways that will be discussed in later sections.

In this investigation the tangential S3F displacement is used directly as a separation sensor output signal. Several factors put a limit on sensor speed: illumination intensity, camera frame rate, image processing speed, film response, and experimental setup. The factors are not independent of one another.

Image processing speed was set by the system hardware and image processing algorithm. The camera frame rate was limited by image sensor resolution and magnification factor required to sense film displacement. A high resolution camera was required to achieve adequate film displacement, which had a maximum resolution frame rate of only 5 fps. The intensity of the pulsed light source set a minimum exposure time of approximately 40ms.

The determination of appropriate S3F material properties for a given application is a trade-off between film displacement, frequency response, and pressure gradient effects. Equation (2.3) implies that for a given surface load, thinner films have a higher response to shear stress than

pressure gradient. Thinner films also have a higher frequency response, but lower overall tangential film displacement. The optics system must provide a large enough magnification so that film displacement is detectable and uncertainty acceptable. In this proof of concept research effort the light source and camera were mounted external to the test article as shown in Figure 2.19. A better packaging concept for an S3F based sensor for flow control is currently being analyzed by ISSI Inc. Any useful sensor package for flow control will need to include an integrated method to measure film displacement rather than an external camera and light source. In this experiment, the length scale of the airfoil, target experimental Reynolds number, and properties of air required that a very sensitive S3F, with high magnification factor be used. Ultimately, a miniaturized version of the discrete skin friction sensor system similar to the description in Crafton et al. (2008) would be a more useful package when integrated into an aerodynamic surface. This type of sensor would be useful in a variety of aerodynamic systems, with potential for using thinner films, higher frequency response, and increased sensor sampling speed. Unfortunately a discrete, small form factor sensor package that would fit on an airfoil was not available in time for this research.
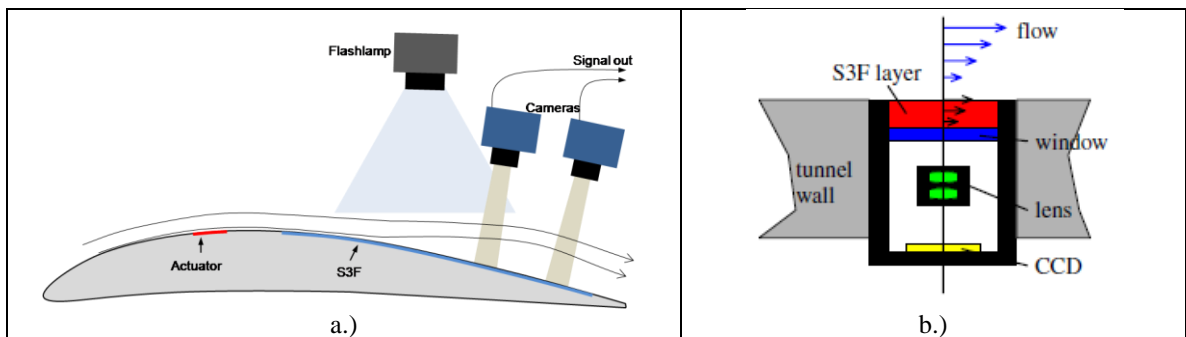
Figure 2.19 a.) Prototype S3F Separation Sensor used in current study. b.) Discrete S3F based skin friction sensor from Crafton et al. (2008)

The shear stress on the surface of the airfoil is low, on the order of 1 Pa. Figure 2.20 gives estimates of tangential film response for a 1 Pa shear stress with a 100 Pa/m pressure gradient over a range of S3F thicknesses and shear modulus calculated using Equation (2.3). The film must have an extremely low shear modulus (< 100 Pa) to provide adequate tangential

displacement on the order of 1 px. Ultra low shear modulus S3F refers to S3F with shear modulus approximately 100 Pa or less. A high resolution camera and high focal length lens was required to obtain a high image magnification factor. Image field of view height was on the order of 15mm, magnification factor >100 px/mm, and film thickness 0.9mm enabling measurement of displacements on the order of tens of microns.

Figure 2.21 shows S3F frequency response versus thickness and shear modulus. Ultra low shear modulus S3F has a frequency response as high as 500 Hz if thin films are used, and lower frequency response around 50 Hz if thicker films are used.   Another factor that effects S3F instantaneous measurements is film response to load changes, and image exposure time. As exposure time increases the wind on image is capturing marker track over time rather than a crisp image of instantaneous marker position. A comparison of marker appearance with a 100ms exposure and 50 ms exposure is shown in Figure 2.22.   The longer exposure time results in more markers blurring which adds noise to the cross correlation calculation and also potentially changing the cross correlation peak shape, affecting the accuracy of the peak finding method.
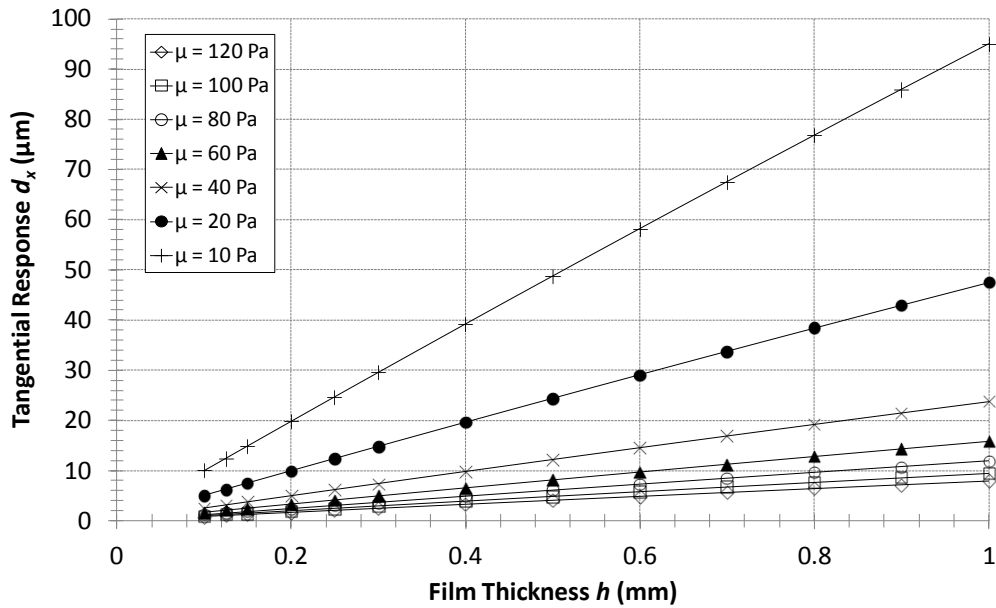
Figure 2.20 S3F tangential displacement for a 1 Pa surface shear stress and 100 Pa/m pressure gradient.
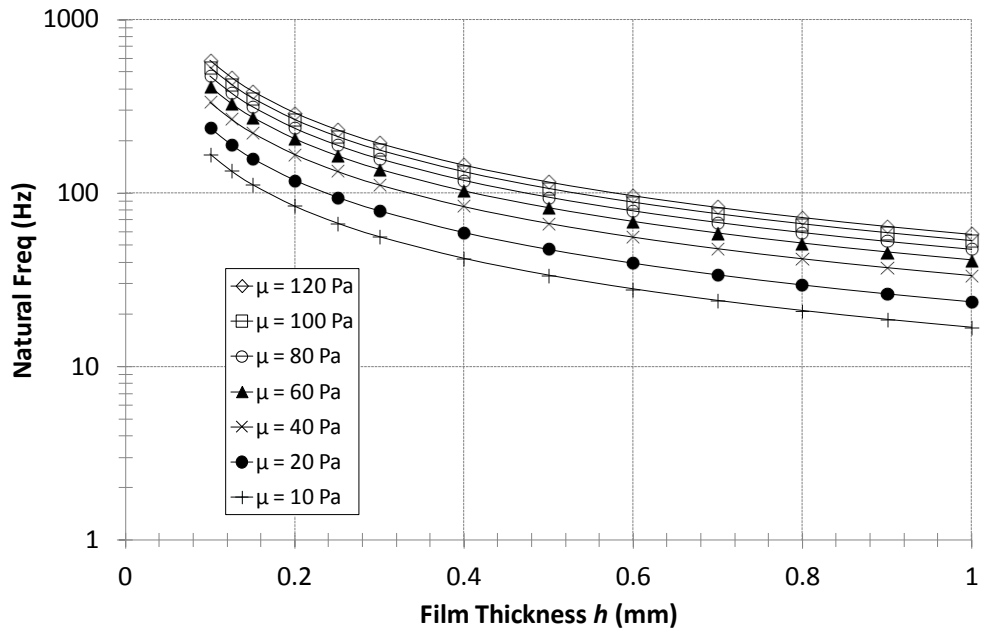
Figure 2.21. S3F frequency response.
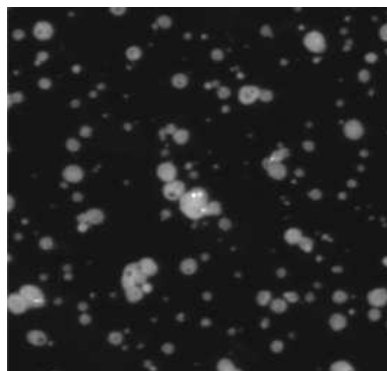
a.)
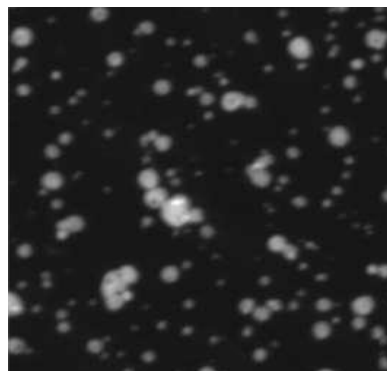
b.)
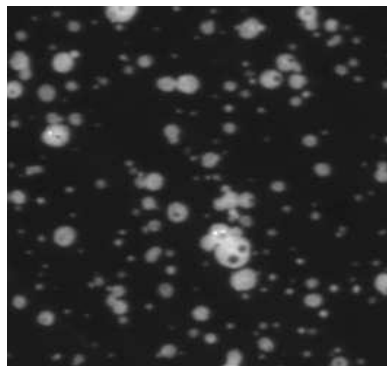
c.)
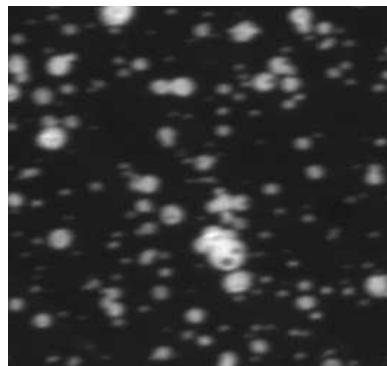
d.)

Figure 2.22 Effect of exposure time on image quality. Image a) wind-off, 50ms b.) wind-on 50ms c.) wind-off 100ms d.) wind-on 100ms

The S3F based separation sensor assumes that pressure gradient is low and the S3F tangential displacement is an indicator of surface shear stress direction and magnitude. In reality the pressure gradient over the surface of the airfoil also contributes to tangential film displacement introducing spatial error into the sensor signal. The error is dependent on film properties, pressure gradient, and shear stress. Figure 2.23 shows the error associated with assuming the film tangential displacement is linearly related to shear stress *only,* in the presence of a pressure gradient. β is the ratio of pressure gradient in Pa/m to shear stress in Pa. For thin films the error is below 10 percent even with a high pressure gradient to shear stress ratio. At higher film thicknesses, even a moderate loading ratio will result in significant local error.
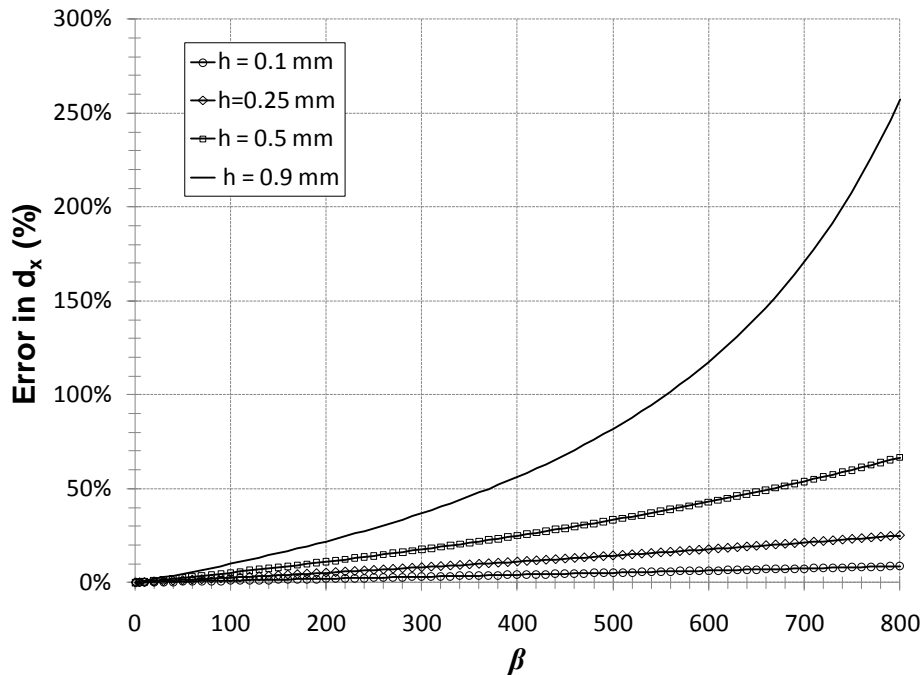
Figure 2.23. Error in tangential displacement when ignoring pressure gradient for various film thicknesses and shear stress.

2.5. Signal Analysis

Film tangential displacement is determined by calculating the shift of particles in the "wind-on" and "wind-off" images. Since the objective here is to use S3F as a separation control sensor

the image processing speed was essential. Two dimensional cross-correlation was chosen for its

relative simple digital implementation and efficiency compared to other techniques.
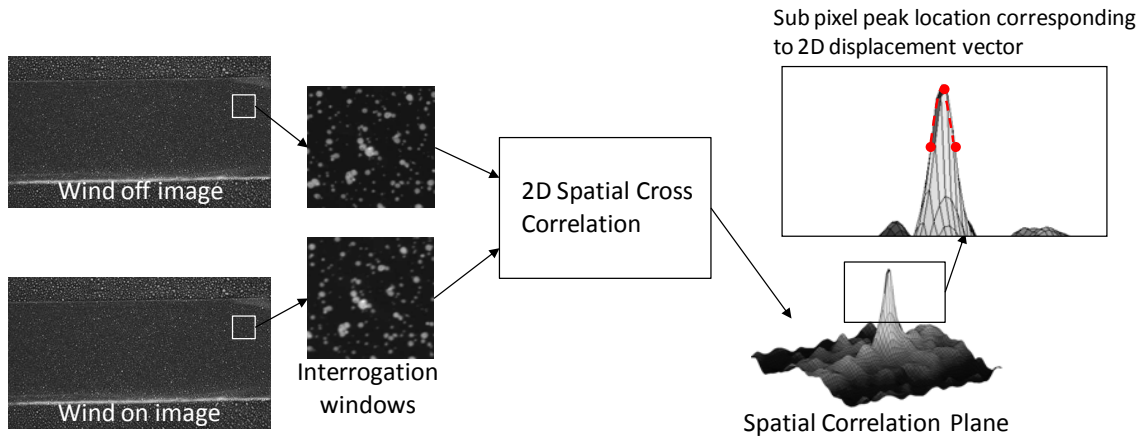
Figure 2.24 Two dimensional film displacement calculation using cross correlation.

The two images are divided into interrogation regions of size $N \ x \ N$ each containing an

adequate number of markers. Image correlation can be accomplished using statistical methods or

frequency based methods.   Frequency based methods are much quicker requiring $O[N^2 log_2 N]$

operations compared to $O[N^4]$ for statistical based methods (Raffel et al. 2007). Since processing

speed was critical in this application frequency domain based cross-correlation was used.

In practice the frequency based process is outlined in Figure 2.25. The FFT of the two regions

are calculated, complex conjugate multiplication of the two Fourier coefficients, then inverse FFT

results in a cross-correlation plane. The plane has dimensions N x N equivalent to the original

interrogation region.
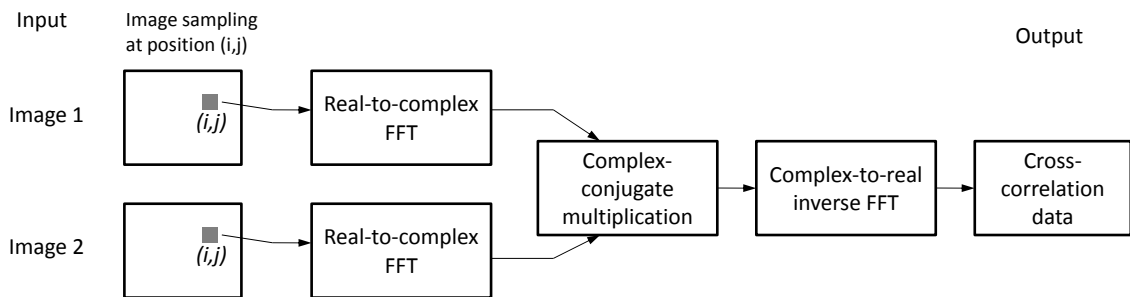
Figure 2.25 Implementation of cross-correlation using fast Fourier transforms (from Raffel et al. 2007)

The mean particle displacement is located at the maximum value in the correlation plane which is located at an integer value. Many methods have been proposed to locate particle displacement to sub-pixel accuracy. Displacement location to sub-pixel accuracy was achieved by using a three point Gaussian curve fitting function around the correlation peak (Willert and Gharib, 1991; Huang et al. 1997):

$$x = x_0 + \frac{\ln R_{x_0-1,y_0} - \ln R_{x_0+1,y_0}}{2 \cdot \ln R_{x_0-1,y_0} + 2 \cdot \ln R_{x_0+1,y_0} - 4 \cdot \ln R_{x_0,y_0}} \tag{2.5}$$

$$y = y_0 + \frac{\ln R_{x_0,y_0-1} - \ln R_{x_0,y_0+1}}{2 \cdot \ln R_{x_0,y_0-1} + 2 \cdot \ln R_{x_0,y_0+1} - 4 \cdot \ln R_{x_0,y_0}} \tag{2.6}$$

Several key system parameters significantly influence processing speed and accuracy. Most noticeably marker size and density places a bound on interrogation window size. Smaller interrogation window sizes result in a faster processing speed, but are only possible when SNR is high, and particle diameters and densities are appropriate. Increasing marker density increases the probability of valid displacement detection, and marker diameter affects displacement uncertainty with simulations indicating that diameters between 2-3 pixels are optimum (Raffel et al. 2007).

2.6. **Signal Preprocessing**

The additional processing times associated with multi-pass and other advanced processing techniques are not acceptable for the current study because of the additional time required to process the data with each additional pass. For this study only one pass is used, but several methods of improving the signal to noise ratio and reducing errors were evaluated: bias correction, thresholding, and correlation multiplication.

In order to better understand the impact of each of these signal enhancement methods 500 interrogation windows were analyzed. The interrogation windows were generated from a sample image of the fluorescent paint marker pattern taken with the same camera and optical

arrangement used in the actual experiments. Marker displacement was artificially generated by shifting one image a distance d_a in image processing software.

The mean bias error ε_b and RMS error ε_{RMS} were calculated. Bias error was calculated using:

$$\varepsilon_b = d_m - d_a \tag{2.7}$$

where d_m is the sample mean displacement, and d_a is the actual displacement. The RMS error was calculated as the standard deviation of the sample displacements:

$$\varepsilon_{RMS} = \sqrt{\frac{1}{N}\sum_{i=1}^{N}(d_i - d_m)^2} . \tag{2.8}$$

Sources of mean bias error include systematic errors having to do with the calculation of displacement vectors, such as inadequate curve fit for sub-pixel peak detection. This type of error is systematic. Random errors are due to a number of factors such as improper marker distribution, non-uniform illumination and reflection from markers, and camera noise (Huang et al. 1997).

The use of Fourier transforms assumes the signal is periodic, when in reality it is not. Bias correction corrects for the assumption of periodicity. As the wind-on image is shifted in relation to the wind-off (template) image, only a fraction of the signal contributes to the actual correlation value resulting in displacement biased to a lower magnitude. This can be overcome by applying a weighting function to the correlation plane. The method outlined in Raffel et al. (2007) was used to correct for bias. A weighting function was generated by convolving the image sampling function with itself. The weighting function was then divided out of the correlation plane. Correcting for bias in the correlation plane increased the mean displacement decreasing the overall mean error with little effect on the RMS error. Bias correction was used in the signal analysis code because of the reduction in error with little additional processing time.

Thresholding of the image signal was accomplished by defining a lower threshold value τ, and regions of the image that were below the threshold were forced to zero. The main objective of thresholding is to remove background noise from the images. In addition to removing

61

background noise, large markers with smaller signal values were effectively decreased in size, essentially acting as a filter. Increasing threshold value reduced the RMS error at values above d_a = 0.5 px, but the trend was little to no improvement in mean bias error.

Correlation multiplication (Hart et al. 2000) involves multiplying the correlation planes of two adjacent, partially overlapped interrogation windows. As long as the displacement gradient is small, this multiplication has the effect of reducing noise and amplifying the correlation peak. For this simple investigation two adjacent correlation planes offset by 50% were multiplied with each other. The calculation of an extra correlation plane has the negative impact of essentially doubling the time it takes to calculate one displacement vector.

Single pass correlation of 500 interrogation windows with markers artificially shifted provides an estimate of the uncertainty due correlation calculation. Figure 2.26 compares the effect of thresholding, correlation multiplication, and a combination of thresholding and correlation multiplication with a standard 2D cross-correlation. Correlation multiplication by itself shows a definite improvement in mean bias error at all sub-pixel displacements, and a bias towards lower magnitudes at displacements larger than one pixel compared to the baseline. Correlation multiplication decreases the RMS error, and in combination with thresholding decreases the RMS error by 50% or more at displacements greater than one pixel. For sub-pixel marker displacement thresholding resulted in a decrease in RMS error, but an increase in mean bias error.
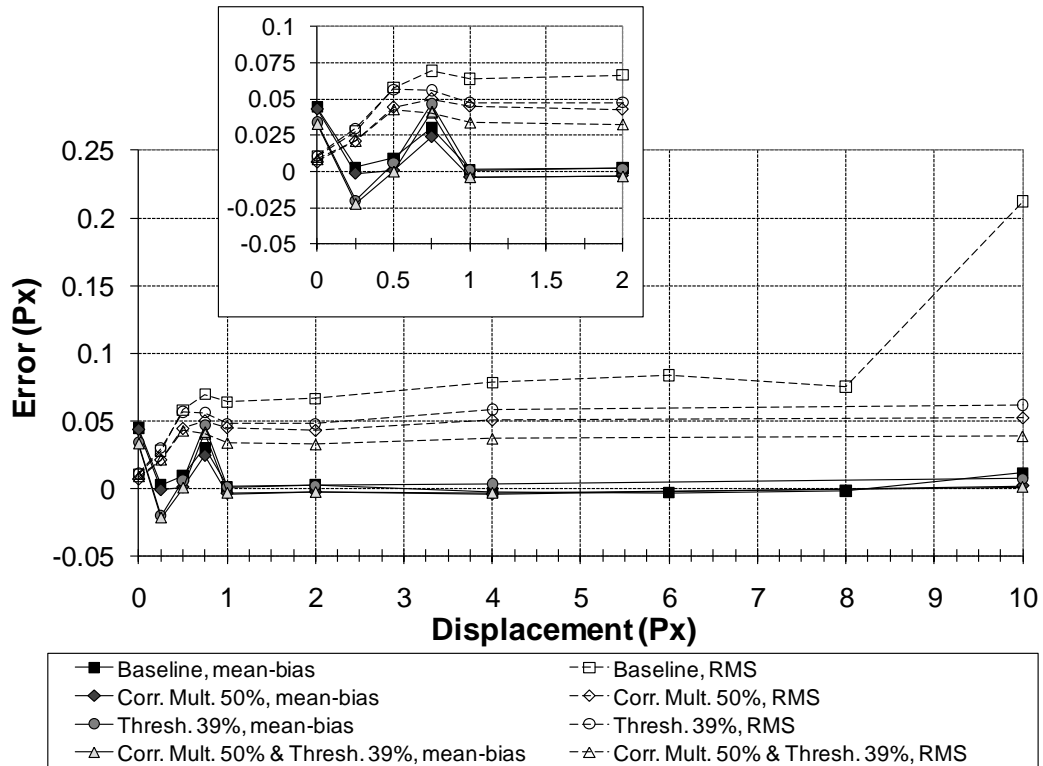
Figure 2.26 Comparison of noise reduction processing techniques.

The plot of Figure 2.27 gives mean and RMS error for subpixel and integer marker displacement using correlation multiplication which is equivalent to the method used in the separation control system software. Peak error is at sub-pixel displacement with nearly 9% ε_{rms} and 3.2% ε_b. Both types of errror significantly decrease as displacement increases up to a marker displacement of 10 pixels.

Figure 2.28 compares error in the displacement calculation using two different correlation window sizes. RMS error is higher for the smaller interrogation windows size. Bias error is higher for the larger interrogation window size at sub-pixel displacement, with comparable, very small amount of error at integer displacements.

Other sources of error in the displacement calculation include airfoil movement relative to the camera. Airfoil motion was compensated for by calculating the displacement of markers just above and below the S3F. The top and bottom region of markers were rigidly fixed to the airfoil. The displacement of the airfoil itself was subtracted from the calculated S3F displacement along

63

the midspan using 2D interpolation.   An investigation into the uncertainty associated with correcting for airfoil movement was undertaken by installing a flat plate with markers into the cavity of the airfoil in which the S3F carrier was installed. Images of marker displacement with the wind tunnel on were recorded and displacement analyzed using ISSI Inc. hybrid cross correlation/optical flow software, then correcting for displacement using the method described above in Matlab. Marker displacement after correction for airfoil motion should have resulted in zero displacement. The analysis indicated that second order curve fits of airfoil motion in the streamwise direction worked better than linear or third order curve fitting. First order curved fits were used in the spanwise (vertical) direction. Analysis indicated a mean displacement error of approximately +/- 0.015 pixels could be obtained using averages of 25, 50, and 100 images. This is an estimate of the accuracy of the airfoil rotation correction method.
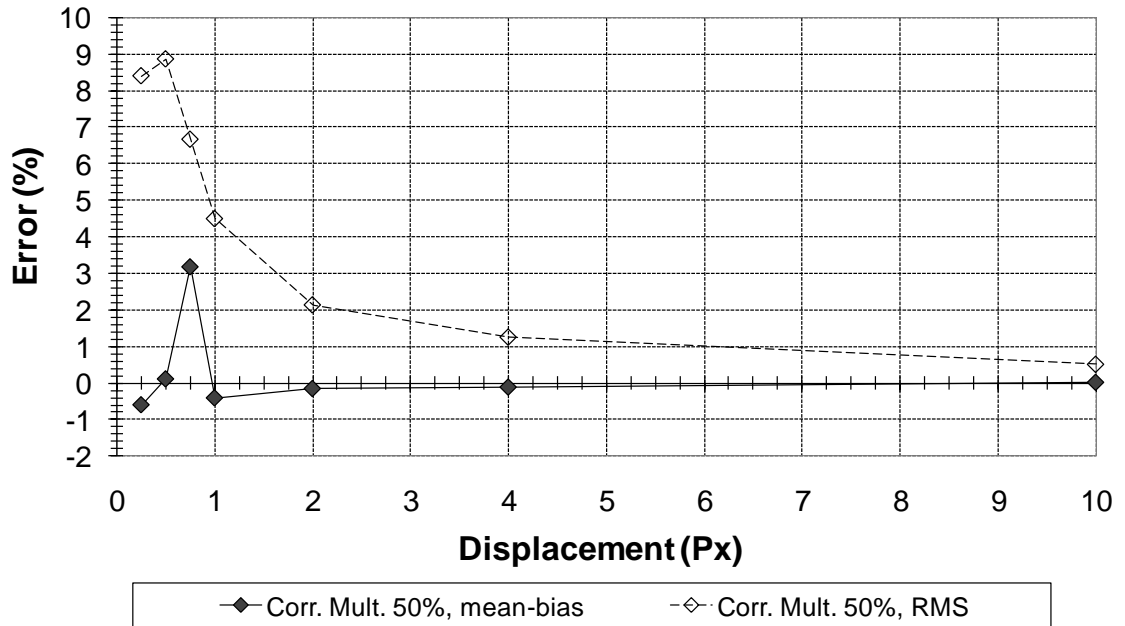
Figure 2.27 Percent error of single pass correlation using correlation multiplication with 50% overlap.
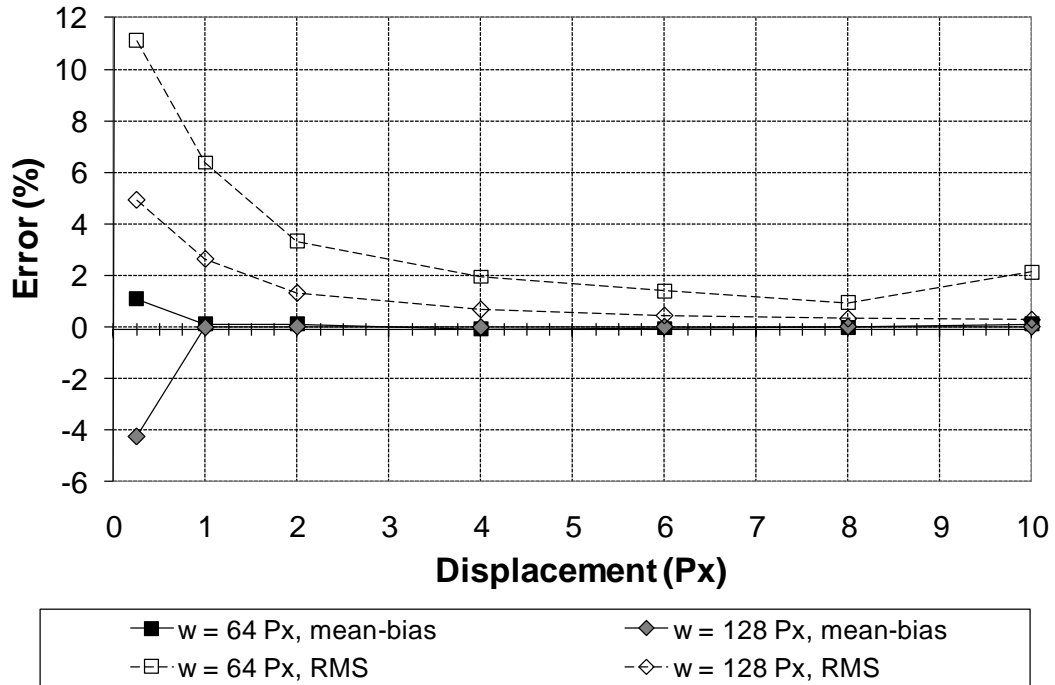
Figure 2.28 Comparison of error in displacement calculation using single pass cross correlation for two different interrogation region sizes.

2.7. **Separation Control System Software**

A custom LabVIEW virtual instrument was developed to read and analyze images of the S3F, record wind tunnel conditions, send plasma actuator control signals, and execute the closed loop separation control system logic. The film tangential displacement was calculated using frequency domain, single pass cross correlation described in Sections 2.5 and 2.6. A screenshot of the Labview separation software GUI is shown in Figure 2.29, and a top level system diagram of the system is shown in Figure 2.30.
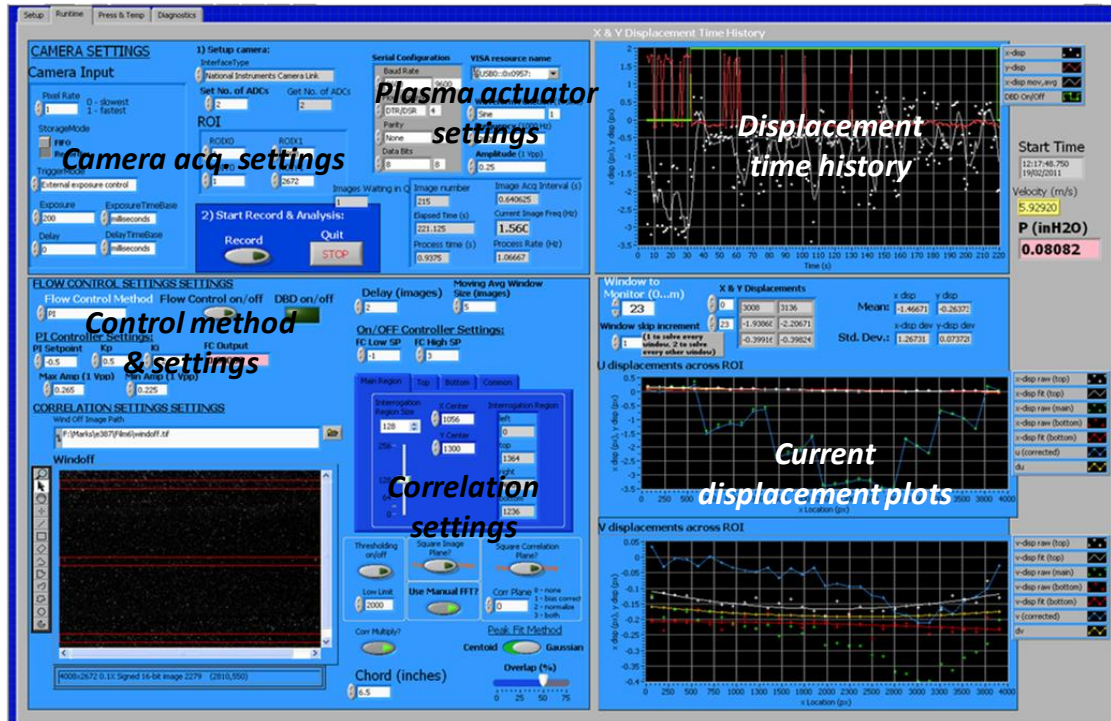
Figure 2.29 Screenshot of Separation Control Software GUI.

The software GUI can be described as having seven different functional areas. Each area is labeled in Figure 2.29 with the exception of the screen in which the pressure transducer and thermocouple data acquisition parameters are input. The region labeled *Camera acq. settings* is where PCO camera specific parameters such as region of interest, exposure control, and number of ADCs, are input. *Plasma actuator setting* is the region where variables associated with the plasma actuator signal are input. The control method and variables associated with each particular control method are contained in the area labeled *Control method and settings*. *Correlation settings* contains input parameters for the cross correlation method and correction methods, such as interrogation region size, and regions of interest settings. On the right side of the screen are plots that are updated in real time after each calculation of film displacement. The top plot is the time history of film displacement at the monitoring point. The bottom plot is film displacement across the entire view, at the top, bottom, and middle regions of interest. The data displayed in each plot is saved to the hard drive after each run.
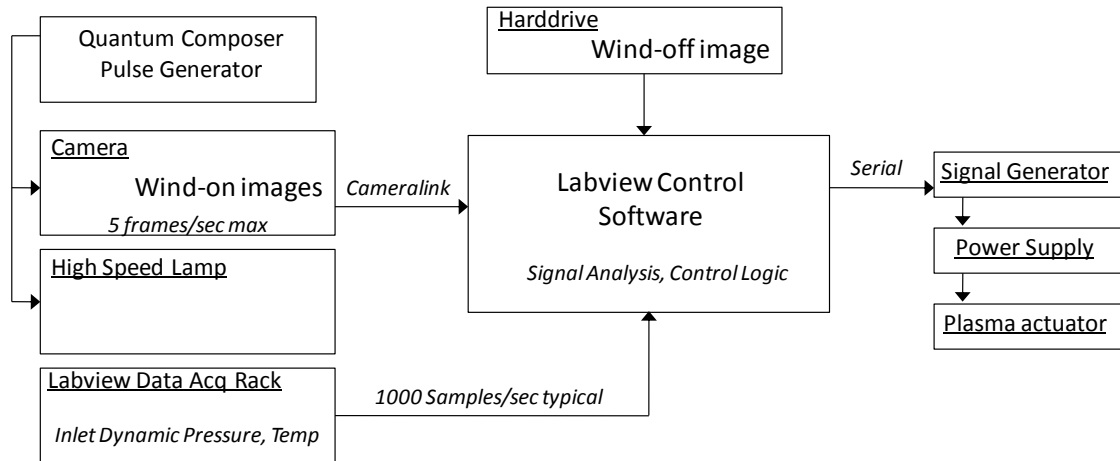
Figure 2.30 Top level system diagram.

The top level system diagram shows signal sources, paths, and interaction between the

equipment used in the separation control system. A flow chart of command and control system

logic pertaining to control of the plasma actuator executed during each time step is shown in

Figure 2.31. Two different control methods were implemented in the code: On/off control and PI

control. The wind-off image is recorded prior to execution of the separation control code. Upon

execution of the separation control code, and during initialization of variables, the regions of

interest in the wind-off image are loaded into computer RAM. This occurs only once during

initial execution of the software. The wind-on images are transferred to the computer

immediately after each exposure using camera FIFO protocol via a high speed Cameralink

interface.   A high resolution PCO 4000 scientific camera that has 4008 x 2600 pixel CCD image

sensor was used in the experiments to obtain high magnification rates required to detect film

displacement. While the PCO 4000 provided high resolution, low noise data, the features of the

camera limited frame rate and processing speed.   Data representing each image was large and

can only be transferred to computer RAM as 16 bit data. The camera had the ability to only

record a portion of the image sensor array by defining one region of interest.   Because the motion

of the airfoil relative to the camera needs to be calculated and corrected for during each exposure,

three different regions of interest were required: a top region just above the S3F, a middle region

along the mid span of the S3F, and a bottom region just below the S3F. Since only one region of interest can be designated with the PCO 4000, the full image data was transferred to the computer RAM upon each exposure. The use of a high resolution camera with the ability to transfer 8bit image data and multiple regions of interest, rather than the entire image, would increase the sampling rate over the system described and used in this work.
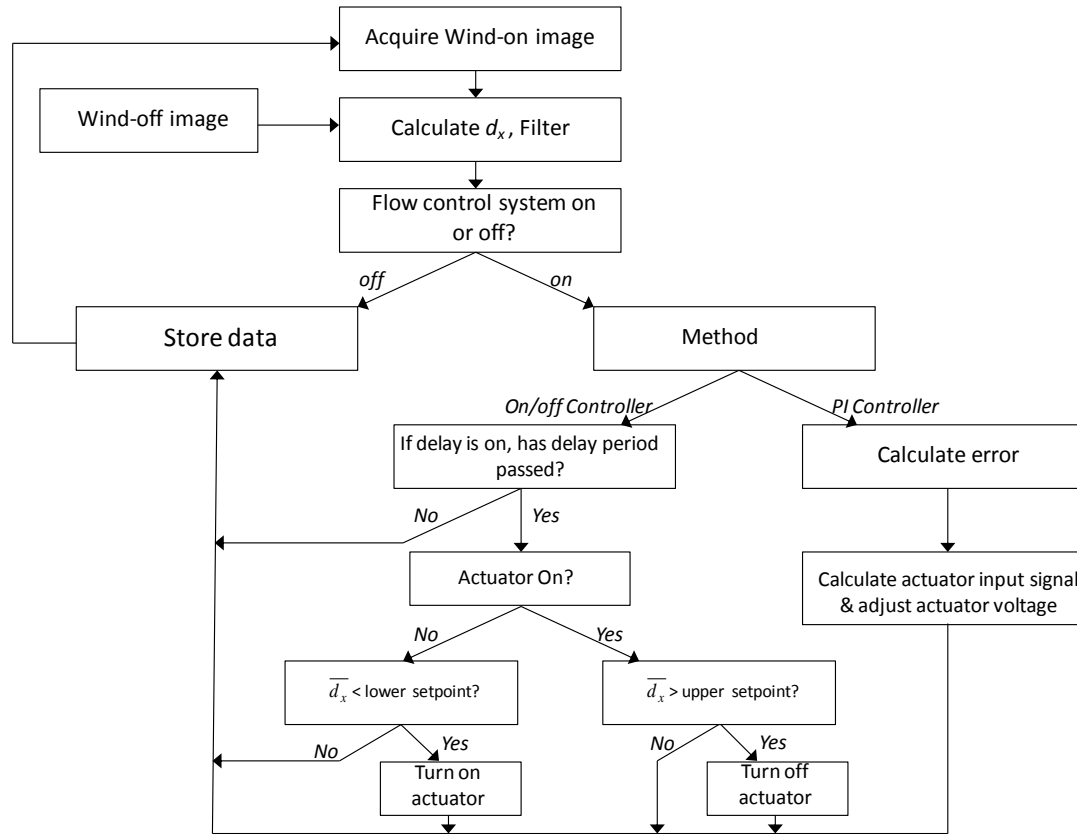
Figure 2.31 Command and control system software flow chart.

Sampling speed was limited by the experimental setup and hardware, ultimately set by the high resolution camera and illumination requirements to approximately 3 Hz. Sampling rates were typically kept to 0.5-2.5 Hz and were sufficient for experimental setup and control method used. The most appropriate way to increase the sensor system speed is by creating a miniature discrete sensor package similar to Figure 2.19b which would improve system speed by:

1. Increasing the frame rate by using lower resolution image sensors

2. Eliminate the need for airfoil/camera motion correction

3. Decrease the illumination intensity required.

In addition, a real time processor using GPUs optimized to perform the FFTs required for cross correlation would increase processing speed and allow the use of more accurate multi-pass algorithms that achieve higher accuracy.

Figure 2.32 shows a typical mean displacement field near the suction surface trailing edge calculated by both the ISSI Inc. software which uses a hybrid optical flow/cross correlation method, and by single pass cross correlation. The ISSI Inc. image processing algorithm uses phase correlation to estimate displacement to an integer value, and then an optical flow based method to estimate the displacement to sub integer (pixels) levels (Fonov et al. 2004). It was reported that the hybrid approach is similar to the method proposed by Cheng-Yuan et al. (1998) (Fonov et al. 2004). At a Reynolds number of $Re = 1.0 \times 10^5$, Figure 2.32 clearly shows a reattachment region with a definite zero crossing location at approximately C_x=94% using both image analysis techniques. The hybrid optical flow/cross correlation method results in larger overall displacement magnitude and a more continuous signal when displacements are small near the zero crossing point. The smoother displacement signal calculated by the hybrid optical flow/cross correlation software is not surprising due to a multi-pass approach and spatial filtering. The mean biasing is evident in the single pass cross correlation signal in regions of near zero displacement. At the lower Reynolds number, peak displacement of the single pass cross correlation agrees well with the ISSI Inc. software calculation, but between 83% C_x and 94% C_x where the displacement is near zero, the single pass cross correlation method results in a signal that oscillates about zero. S3F in a filled cavity will show edge effects in an area approximately three to four film thicknesses from the edges (Crafton et al. 2008), and the edge of this region has been highlighted with a dark dashed line in Figure 2.32.
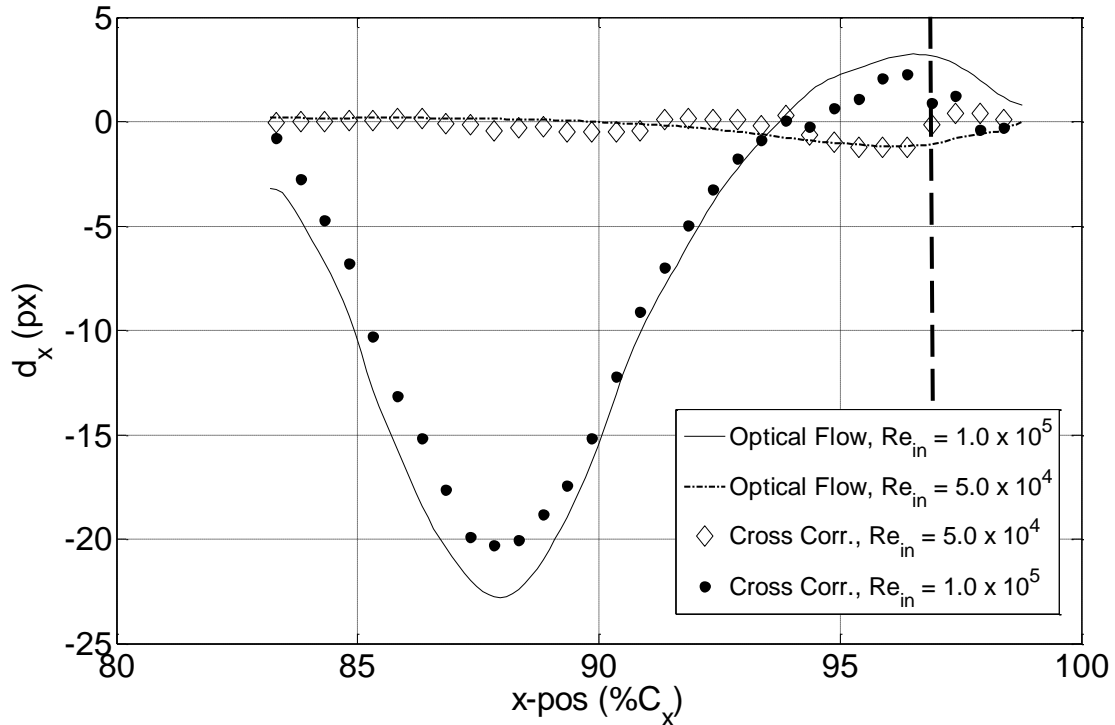
Figure 2.32. Comparison of mean streamwise displacement, ε = 200ms, Fs=1 Hz, correlation multiplication on.

S3F #6 had an estimated first natural frequency of 16 Hz, meaning signals at frequencies greater than twice the natural frequency would be significantly filtered out. Depending on damping characteristics, the film could also oscillate if loaded at a frequency near the natural frequency. Film displacement was also dependent on exposure time since longer exposure resulted in larger particle blurring as is seen in the raw images of Figure 2.22. A comparison of mean displacement field with exposure times of 50ms – 200ms is shown in Figure 2.33. The longer exposure time resulted in an 8% increase in peak displacement at an exposure of 200ms versus 50ms. The zero crossing location varied by less than $0.5\%\,C_x$, but the longer exposure image crossed zero at more than one location, indicating larger error in the correlation calculation. This could be due to mean bias error due to inadequate sub-pixel peak fitting. A minimum exposure time of 40ms was used for flow control experiments because it provided adequate marker illumination with the high speed S3F LED lamp.
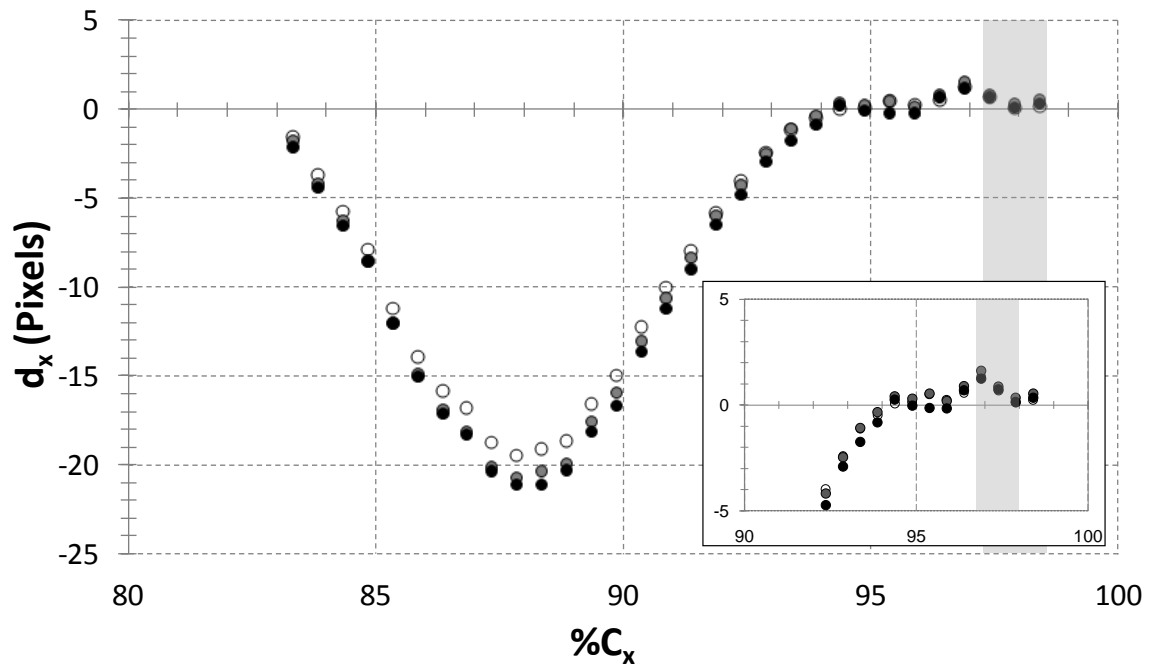
<figure>
○ ε = 50ms, w = 128px   ● ε = 100ms, w = 128px   ● ε = 200ms, w = 128px

Figure 2.33 Effect of exposure time on calculated mean displacement, Re = 1.0x10^5, 100 samples using single pass cross correlation.
</figure>

3. Airfoil Characterization

Airfoil characterization involved determining the behavior of the unmodified and modified airfoils in the AFRL/RZ low speed wind tunnel. This was accomplished by comparing suction surface C_p, drag, and PIV images with data from other facilities. Suction surface C_p was measured on the unmodified Airfoil 1 to determine an angle of attack that produced laminar boundary layer separation. The criteria for choosing angle of attack were:

- low angle of attack to minimize flow blockage
- laminar separation with and without reattachment in the Reynolds number ranged studied ($1.5 \times 10^5 - 5 \times 10^4$).

Included in this chapter are the experimental measurements on each airfoil and a comparison of PIV measurements on a clean version of Airfoil 2 compared with S3F installed on Airfoil 2.

3.1. Airfoil 1

The objective of this baseline dataset was to obtain the pressure coefficient on the suction surface of the rapid prototyped model and compare it with inviscid distribution to identify approximate separation and reattachment locations. Data was taken at angles of attack between 2.5° and -1.5° in order to determine an angle of attack that resulted in a laminar boundary layer separation on the suction surface.

Suction surface pressure coefficients at various low angles of attack are presented in Figure 3.1 - Figure 3.5 at Reynolds numbers of 1.5×10^5, 1.4×10^4, and 6.0×10^4. Experimental results measured in the AFRL/RZ DWT compared to XFOIL inviscid solution, and experimental measurements by McGhee et al. (1988) taken in the NASA Langley low turbulence wind. For angles of attack in which no NASA experimental data was available, the closest angle of attack to that used at AFRL was included in the plot for reference. The XFOIL airfoil analysis code was

used to obtain inviscid surface pressure distributions to compare with measured surface pressure coefficients. XFOIL was developed by Mark Drela of MIT in 1986. It is an open source airfoil design and analysis software capable of inviscid or viscous solutions. The inviscid solution uses a linear-vorticity stream function panel method in which the equations are closed with an explicit Kutta condition. Karman-Tsien compressibility correction is included, valid up to sonic conditions (Drela and Youngren 2001).

Figure 3.1 and Figure 3.2 show the suction surface pressure distribution at small angles of attack with Re = 1.0 x 10^5 and Re = 6 x 10^4. The laminar boundary layer separation is evident by the plateau in pressure coefficient in the area of C_x = 45-55%. The separation point moves upstream as angle of attack is increased. At the higher Reynolds number of 1.0 x 10^5 the boundary layer reattaches at angles of attack greater than -1.5°. As angle of attack increases the reattachment point moves upstream.
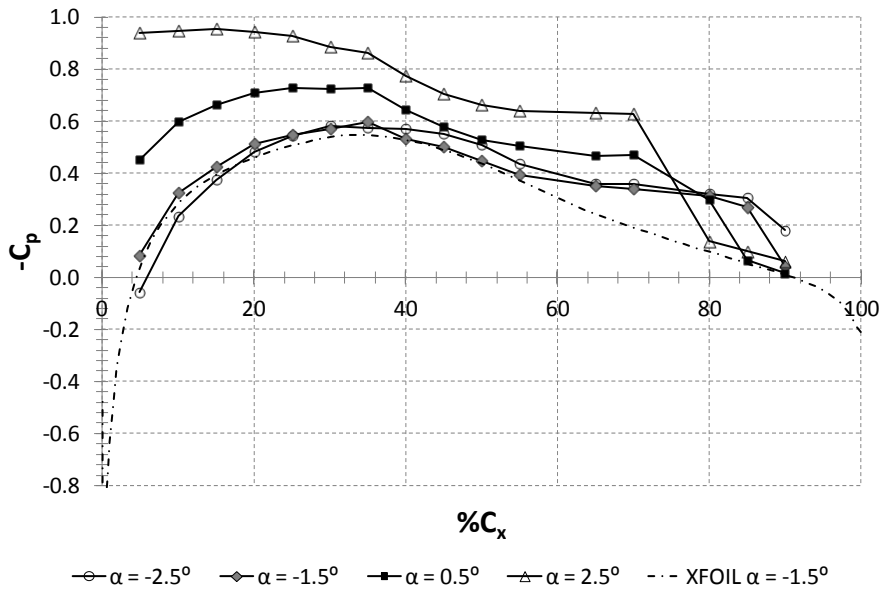
Figure 3.1 Suction surface C_p at small angles of attack, Re = 1.0 x 10^5.

At the lower Reynolds number of 6 x 10^4 the boundary layer separates in the area of C_x = 45-55% with the separation point moving upstream as angle of attack increases. The boundary layer does not appear to reattach until angles of attack larger than 0.5°.
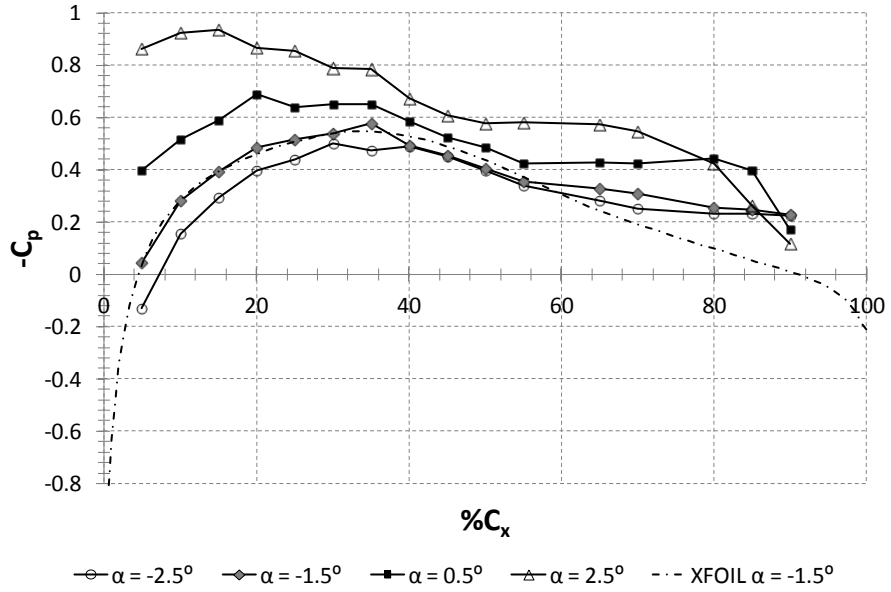
Figure 3.2 Suction surface C_p at small angles of attack, Re = 6 x 10^4.

Figure 3.3 compares data taken in the AFRL/RZ LSWT facility Developmental Tunnel with measurements in the NASA Langley wind tunnel from McGhee et al. (1988) at a Re = 1.0 x 10^5. In general, the loading was higher in the AFRL/RZ DWT and closer to the inviscid loading predicted in XFOIL, except in the region of laminar boundary layer separation.
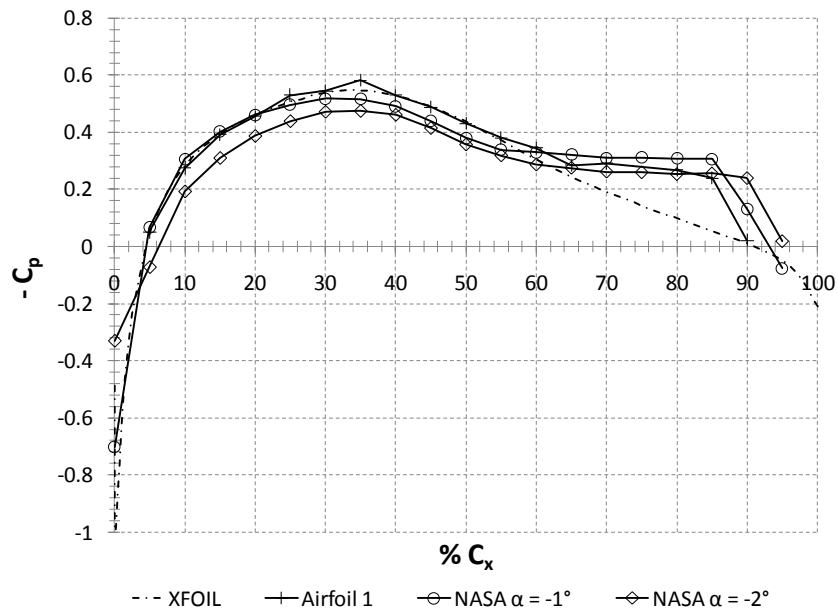
Figure 3.3 Comparison of NASA Langley measurements compared with AFRL/RZ LSWT measurements at $\alpha = -1.5°$, Re = 1 x 10^5.

Figure 3.4 compares data taken in the two facilities at a Reynolds number of 1.0×10^5. The trend is similar to the lower Reynolds number data. The AFRL/RZ DWT data has a higher loading than the data from McGhee et al. The data taken in the DWT has lower loading than predicted in XFOIL, but higher than the data in McGhee et al.

a.) α = 0.5°

b.) α = 2.5°
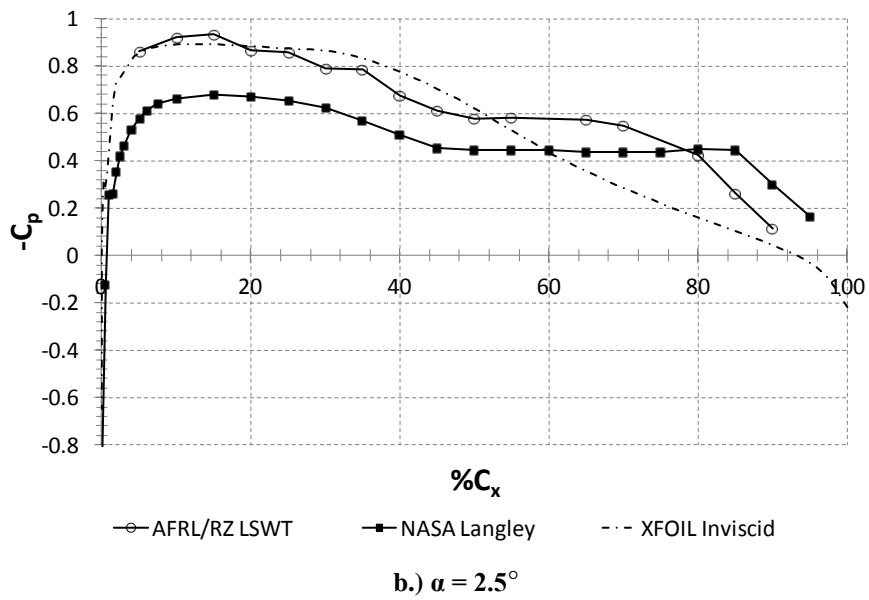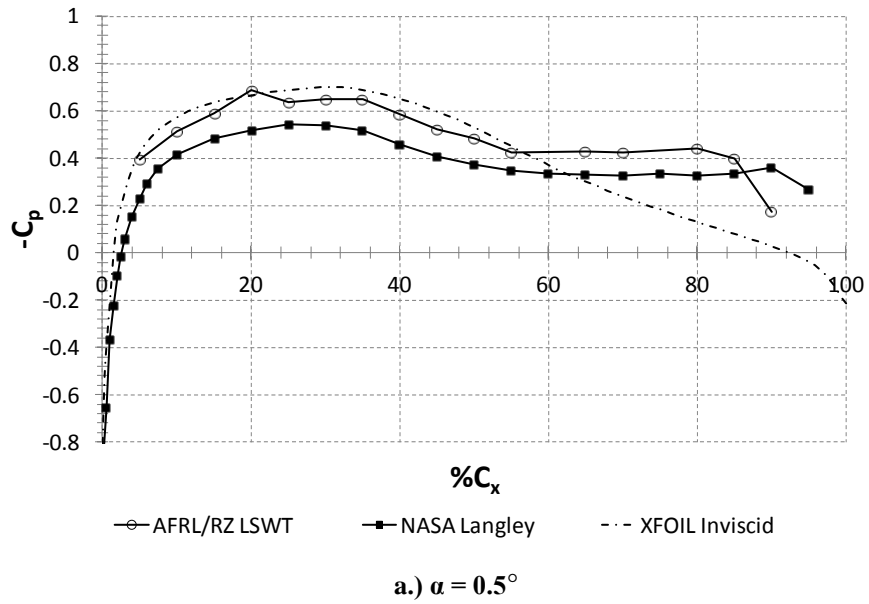
Figure 3.4 Suction surface pressure distribution compared to NASA Langley at Re = 6.0 x 10⁴ and small angles of attack.

The pressure distributions are obviously effected by boundary layer separation and deviations from the inviscid profile were used to estimate separation and reattachment locations (listed in Table 3.1). The pressure coefficient measurements on Airfoil 1 were jagged and not smooth along the chord. This was most profound at $C_x = 20\%$ and 35%. Testing indicated that this variation was not due the sampling period, as the measurements were repeatable. It is assumed that the measurement anomalies were due to irregularities at the pressure ports or the internal pressure tubing.

The baseline C_p data indicated that an angle of attack of -1.5° would provide the desired boundary layer behavior on the suction surface: the presence of a separation bubble at Reynolds number of 1.0×10^5, and separation without reattachment at a Reynolds number of 6.0×10^4. These two conditions allowed ample testing of the separation control system, both in an open loop configuration, and a closed loop configuration.

Table 3.1. Summary of approximate separation reattachment location on Airfoil 1 based on C_p measurements.

Reynolds Number	Angle of attack	Approx. separation location (C_x)	Approx. reattachment location (C_x)
1.0×10^5	-1.5°	55%	90%
6.0×10^4	-1.5°	55%	None

Figure 3.5 shows the suction surface pressure coefficient on Airfoil 1 over a Reynolds number range of 1.5×10^5 to 6×10^4, and $\alpha = 1.5°$. The plot shows that the separation point does not move significantly with Reynolds number, but reattachment moves upstream as Reynolds number increases. Airfoil loading increases as the Reynolds number increases and the extent of separation is reduced.
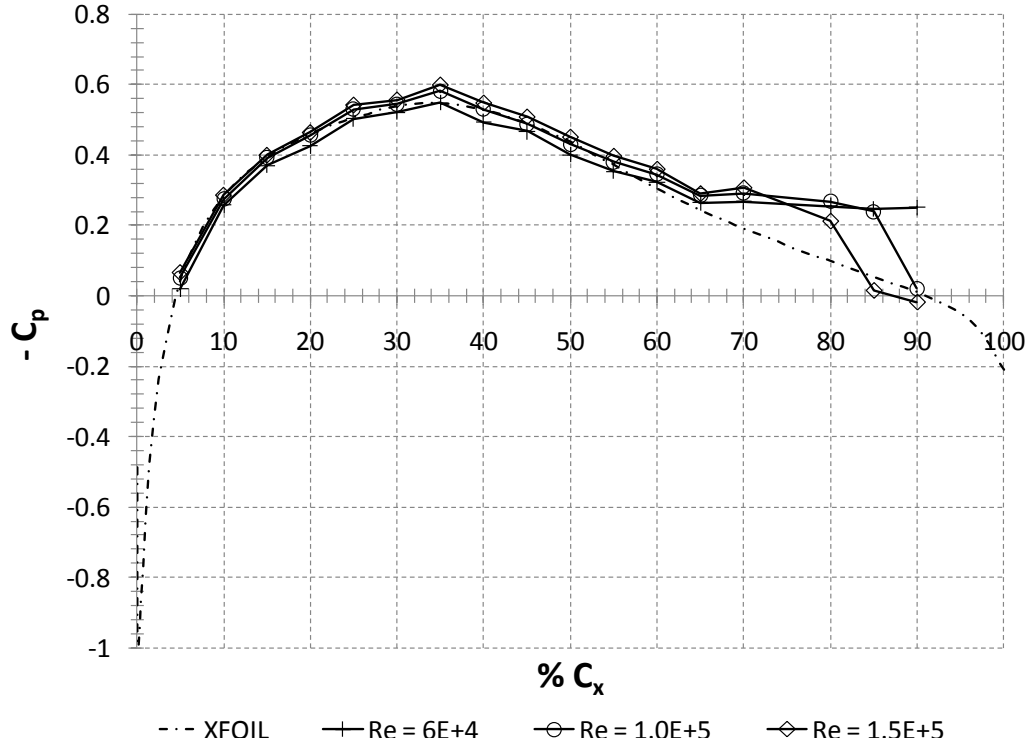
Figure 3.5 Airfoil 1 suction surface C_p at α = -1.5° and various Reynolds numbers.

3.2. **Airfoil 2**

The airflow around Airfoil 2 was expected to be different than Airfoil 1 due to the addition of

pressure lines along the pressure side of the airfoil.   In this section C_p measurements are

compared to the measurements of Airfoil 1 in the AFRL/RZ DWT facility. Drag measurements

between Airfoil 1 and Airfoil 2 are compared with measurements in other facilities, and PIV over

the suction surface of Airfoil 2 with and without S3F installed is compared.

3.2.1. C_p measurements

C_p measurements over the suction surface of Airfoil 2 at Reynolds numbers of Re=1.5x10^5,

1.0x10^5 and 6x10^4 are show in Figure 3.6. This data was obtained with a "clean" airfoil, meaning

that no S3F or plasma actuators were installed. A flat plate was installed in the cavity in which

S3F is typically installed. The inviscid suction surface profile is shown as well for comparison.

The peak loading at each Reynolds number is higher than the inviscid profile. Airfoil 2 Cp data is smoother along the chord direction than was observed in Airfoil 1. As Reynolds number decreases peak loading on the suction surface decreases, resulting in a decrease in lift. At each Reynolds number laminar flow separation occurs at approximately C_x=55%. Reattachment points vary for each Reynolds number tested. At the highest Reynolds number the reattachment point is at C_x = 85%. After the reattachment point the pressure coefficient again plateaus and deviates from the inviscid value indicating either separation at the trailing edge or erroneous data. This phenomenon did not occur on Airfoil 1. At a Reynolds number of 1.0×10^5 the plateau beginning at C_x=55% is sharp with transition in the area of C_x=80%, then recovering to the inviscid profile at C_x=90%. At the lowest Reynolds number the boundary layer separates, but it is unclear whether reattachment occurs near the trailing edge due to lack of pressure taps beyond C_x=90%.
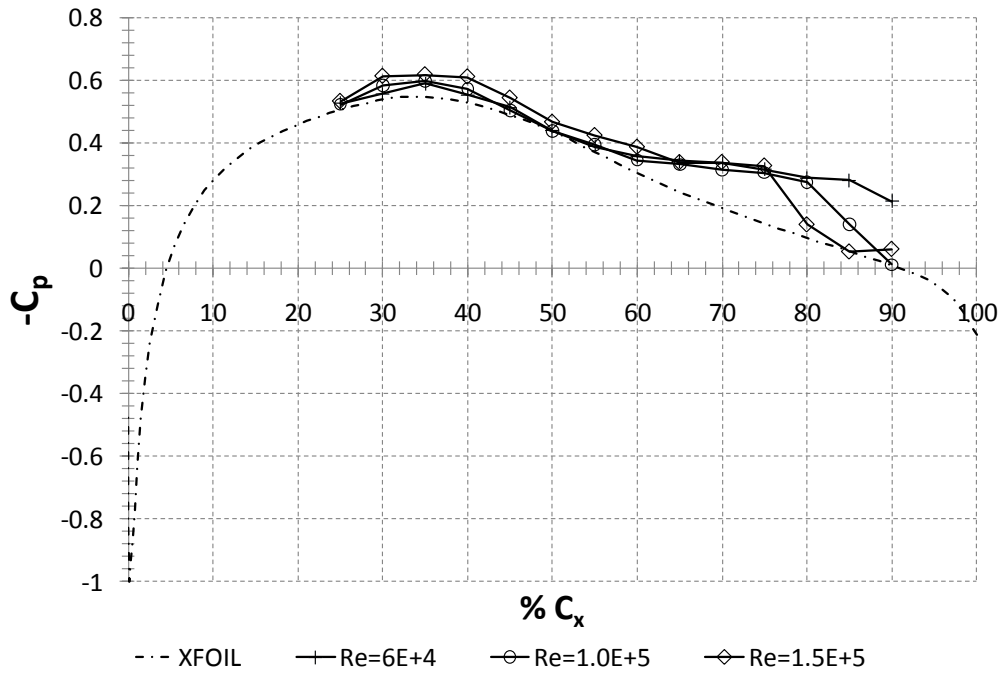
Figure 3.6 Airfoil 2 suction surface C_p at various Reynolds numbers.

The comparison of Airfoil 1 and Airfoil 2 shown in Figure 3.7 indicates that the laminar separation of Airfoil 2 is different than Airfoil 1, both in transition and reattachment location. It is difficult to determine from the C_p plots exactly where the separation and reattachment points

78

are, but it appears Airfoil 2 separates slightly upstream from the Airfoil 1 separation point with a

higher peak loading. Both airfoils reattach by $C_x = 90\%$ with Airfoil 2 transitioning further

upstream.
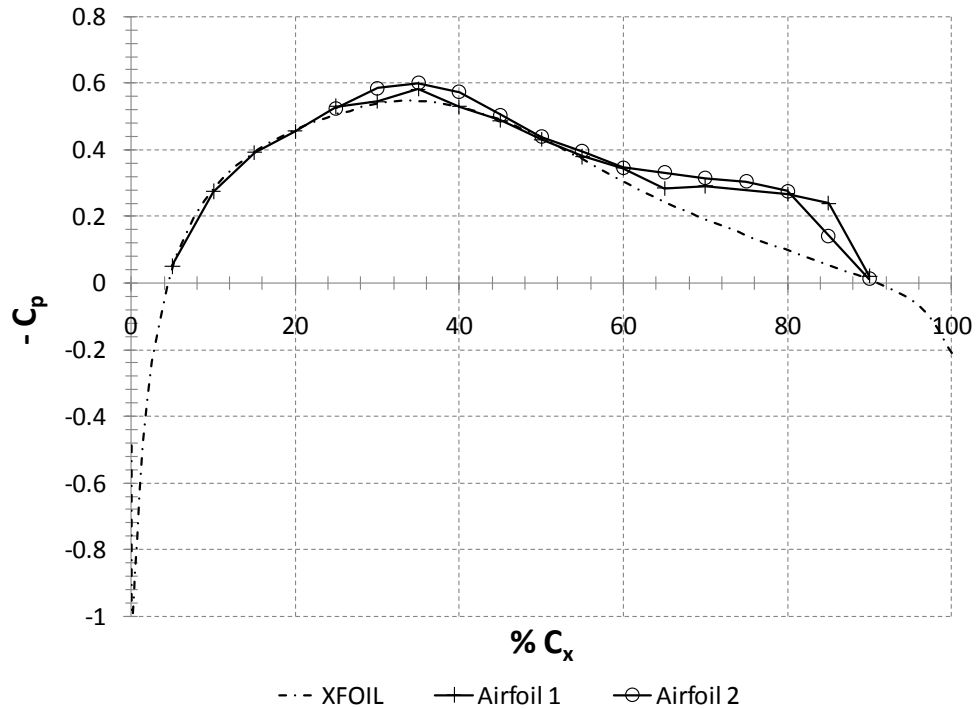
Figure 3.7 Comparison of Airfoil 1 and Airfoil 2 suction surface C_p at Re = 1.0x10^5.

3.2.2. PIV – No S3F Installed

Baseline PIV was taken on the modified airfoil with a flat plate installed in the S3F mounting

cavity as shown in Figure 3.8. Data was taken at three different inlet Reynolds numbers: 1.5x10^5,

1.0 x 10^5, 6 x 10^4. Data shown here were taken with four different camera views and assembled

together into one plot extending from approximately 42% C_x to 100% C_x. Each individual view

had a magnification factor of 54.85 px/mm resulting in a 29.2 x 21.9mm field of view. A

minimum of 250 images were used to calculate the mean flowfield.
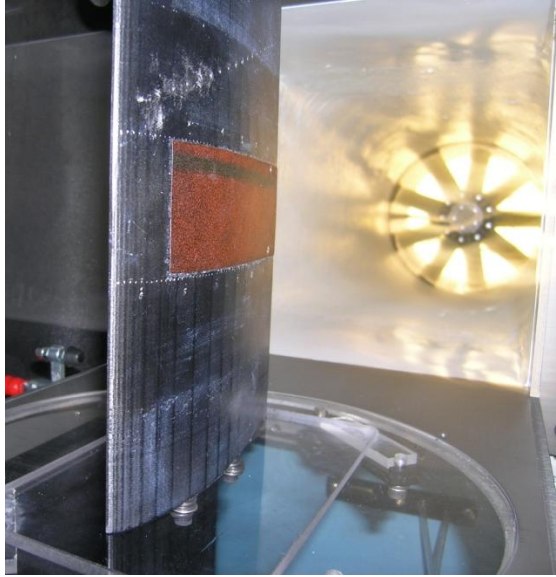
**Figure 3.8 Flat plate mounted in the S3F
cavity of Airfoil 2.**
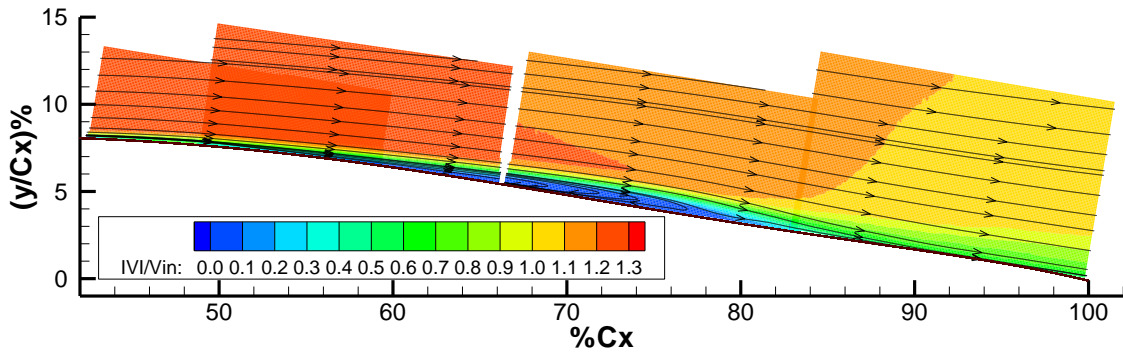
Figure 3.9 Airfoil 2, Flat plate installed, Re = 1.5 x 10^{5}
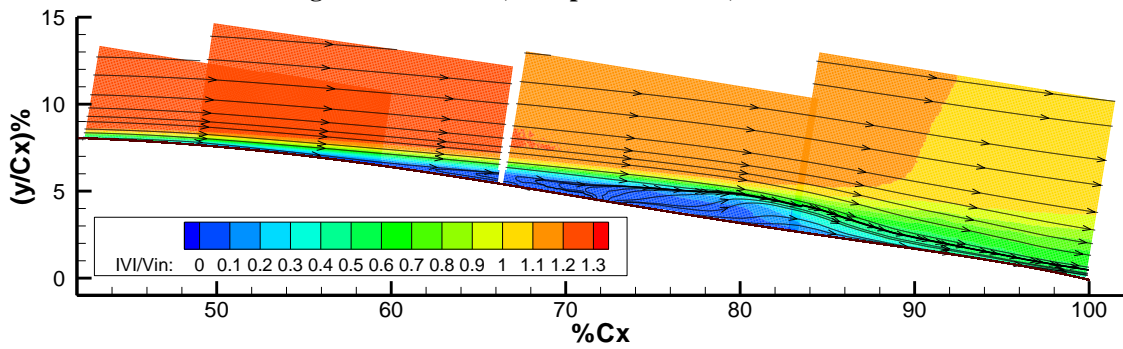
Figure 3.10 Airfoil 2, Flat plate installed, Re = 1.0 x 10^{5}
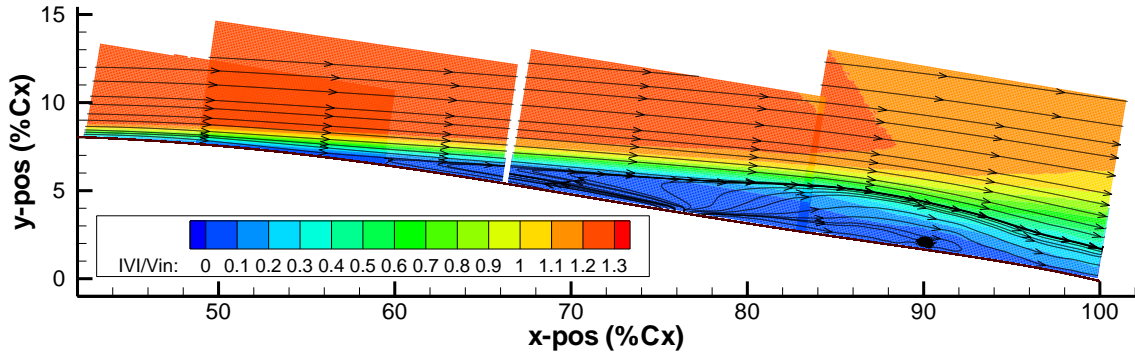
Figure 3.11 Airfoil 2, Flat plate installed, Re = 6 x 10^4

The mean PIV fields shown in Figure 3.9-Figure 3.11 provide more precise identification of the separation and reattachment locations compared to C_p measurements. A summary of the mean reattachment and separation points on Airfoil 2 is shown in Table 3.2. It is obvious that the higher spatial fidelity PIV data allows for a more precise determination of boundary layer behavior. The PIV data indicates that there is a small shift upstream in the separation location at the lowest Reynolds number. Mean separation bubble length increased as Reynolds number decreased. At the highest Reynolds number tested the reattachment point is at approximately C_x=82% and shifts downstream as Reynolds number is decreased. It was not obvious from the C_p data, but the mean flow does reattach just prior to the trailing edge at the lowest Reynolds number tested. The C_p data at Re = 1.5 x 10^5 at C_x=90% decreased creating a plateau that implied separation near the trailing edge. No trailing edge separation was observed in the PIV data.

Table 3.2 Comparison of approximate mean separation and reattachment locations on Airfoil 2

Inlet Reynolds Number	Separation		Reattachment	
	C_p	PIV	C_p	PIV
1.5 x 10^5	55%	56%	85%	82%
1.0 x 10^5	55%	56%	90%	86%
6 x 10^4	55%	54%	Unknown	97%-99%

In order to better understand the boundary layer behavior at the lowest Reynolds number $Re = 6 \times 10^4$, five instantaneous PIV velocity fields at the trailing edge are shown in Figure 3.12.
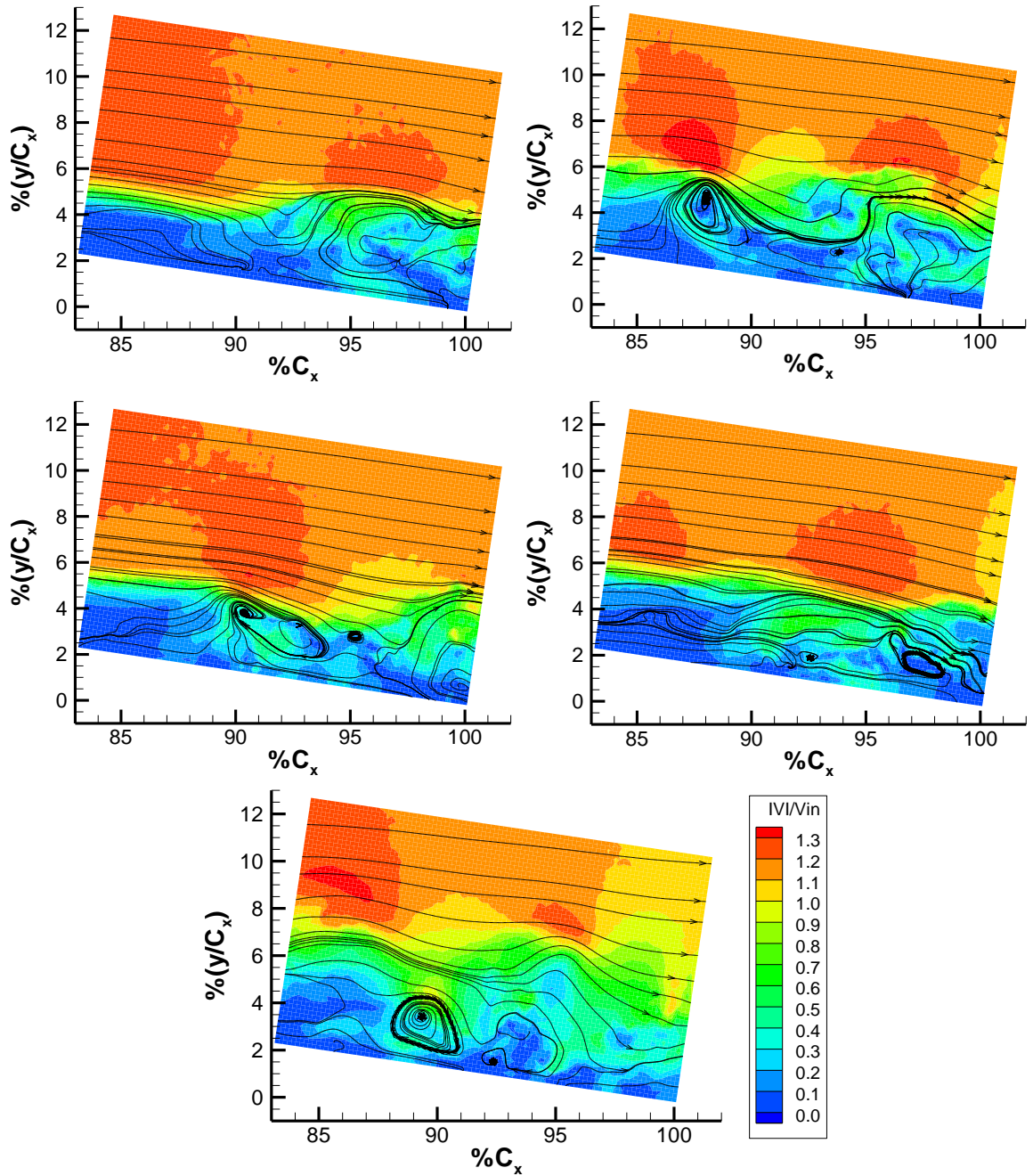
Figure 3.12 A sample of five instantaneous velocity fields in the trailing edge region at $Re = 6 \times 10^4$

Vortex shedding of the separated shear layer results in large vortices that develop and travel along the suction surface. Selected instantaneous PIV images in Figure 3.12 show that the shear

layer behavior is complex. The boundary layer near the trailing edge cannot be labeled reattached or separated unless considering time averaged data.

Examining the instantaneous velocity fields of Figure 3.12 shows that in some instances the shed vortex remains coherent and laminar, with areas that have begun to break down and transition to turbulence; in other instances the vortices are larger and appear to have merged. The large eddies, which are on the order of $4\% C_x$ had a large instantaneous effect on the flowfield and on boundary layer thickness. The unsteady numerical study of Lin and Pauley (1996) agreed with the PIV observations. Their study of the Eppler 387 at Re = 6.0 x 10^4 at a 4 degree angle of attack showed periodic shedding downstream of the separation point. Vortex pairing occurred at locations downstream of the separation point, where the shed vortices interacted and merged into one. Vortex pairing is believed to be due to the adverse pressure gradient which slows the leading vortex and allows the trailing vortex to close on the leading vortex and ultimately merge (Winert and Browand 1974; Lin and Pauley 1996).

3.2.3. Drag Measurements

Drag was measured by a wake traverse along the span of the airfoil. The installation of the pressure lines along the pressure surface resulted in better C_p measurements than on Airfoil 1, but at the cost of spanwise variation in drag. The addition of pressure tubing along the pressure side of the airfoil is clearly seen in the plot of drag along the span shown in Figure 3.13. Variation in losses is most significant on the pressure side of the airfoil in the region where the pressure tubes exit from the airfoil surface.
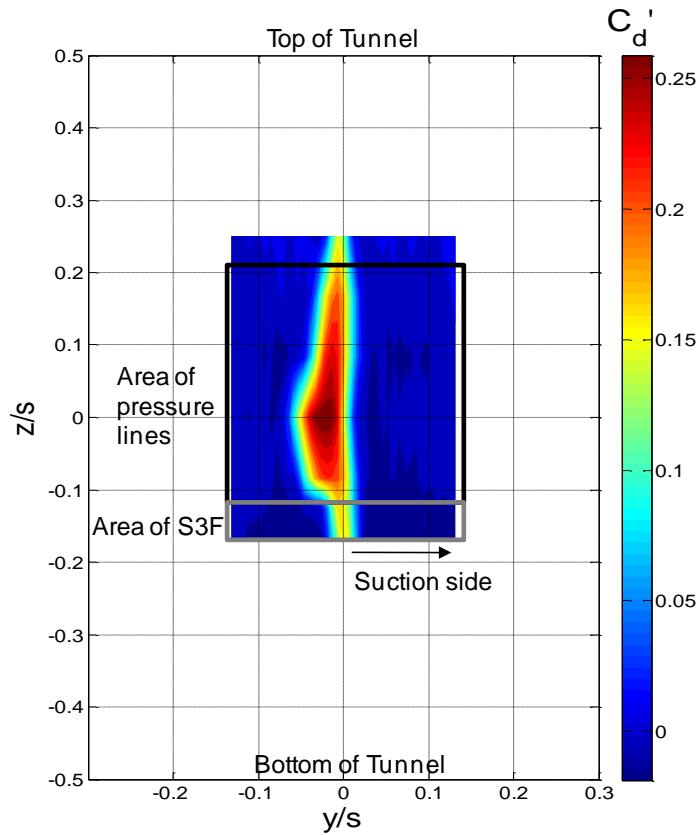
Figure 3.13 Spanwise variation in wake due to pressure lines on Airfoil 2, Re = 1.0 x 10^5.

The pressure tubes were covered with a piece of tape in order to make them more streamline with

the flow (Figure 3.14). All measurements presented in this paper were obtained on the suction

side of the airfoil where spanwise variation is less significant.
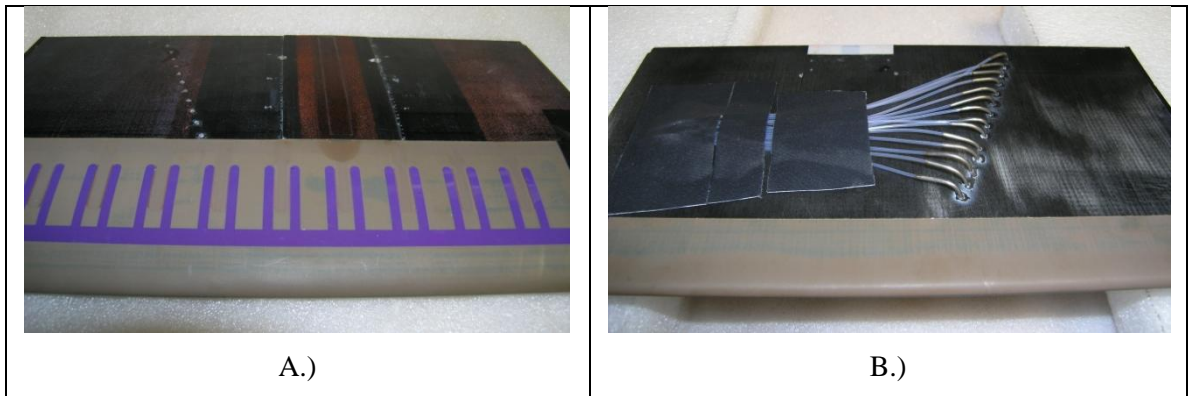
Figure 3.14 Images of Airfoil 2 A.) suction side surface and B.) pressure side surface with plasma actuator installed.

Figure 3.15 shows the wake velocity deficit in the region of the airfoil with S3F installed from z/s = -0.13 to -0.17 indicating the spanwise variation is minimal, especially on the suction surface ($y/s > 0$). This is the region in which S3F, PIV, and flow visualization images were recorded. Even with the spanwise variation in drag, the airfoil was considered to be adequate for the flow control experiments since laminar separation still existed as expected on the suction surface.
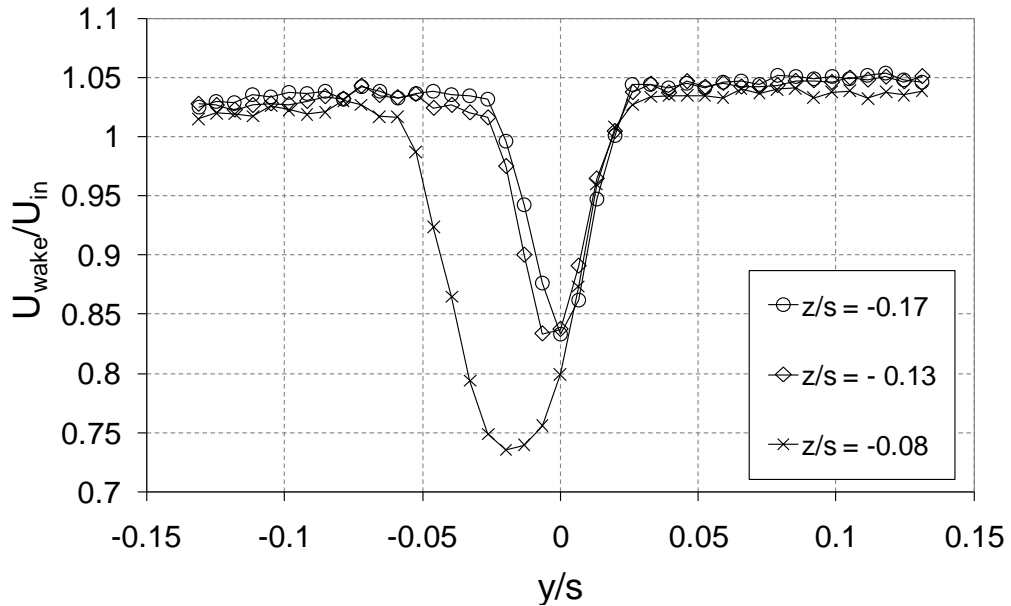
Figure 3.15 Wake velocity deficit in the area of S3F and PIV measurements at Re = 1.0 x 10^{5}.

A comparison of drag coefficient in the area of the S3F and PIV measurements is shown in Figure 3.16. There is a significant spread in data between all facilities. Section drag measured on Airfoil 1 at Re = 1.0 x 10^{5} is between the drag values measured at NASA Langley and U. of Illinois. Data from each facility was significantly lower than the U. of Stuttgart data. As expected Airfoil 2, which had pressure tubing exposed on the pressure side of the airfoil, had a higher drag coefficient at the lowest Reynolds number compared to Airfoil 1, but surprisingly not significantly higher than the value measured at the U. of Stuttgart.
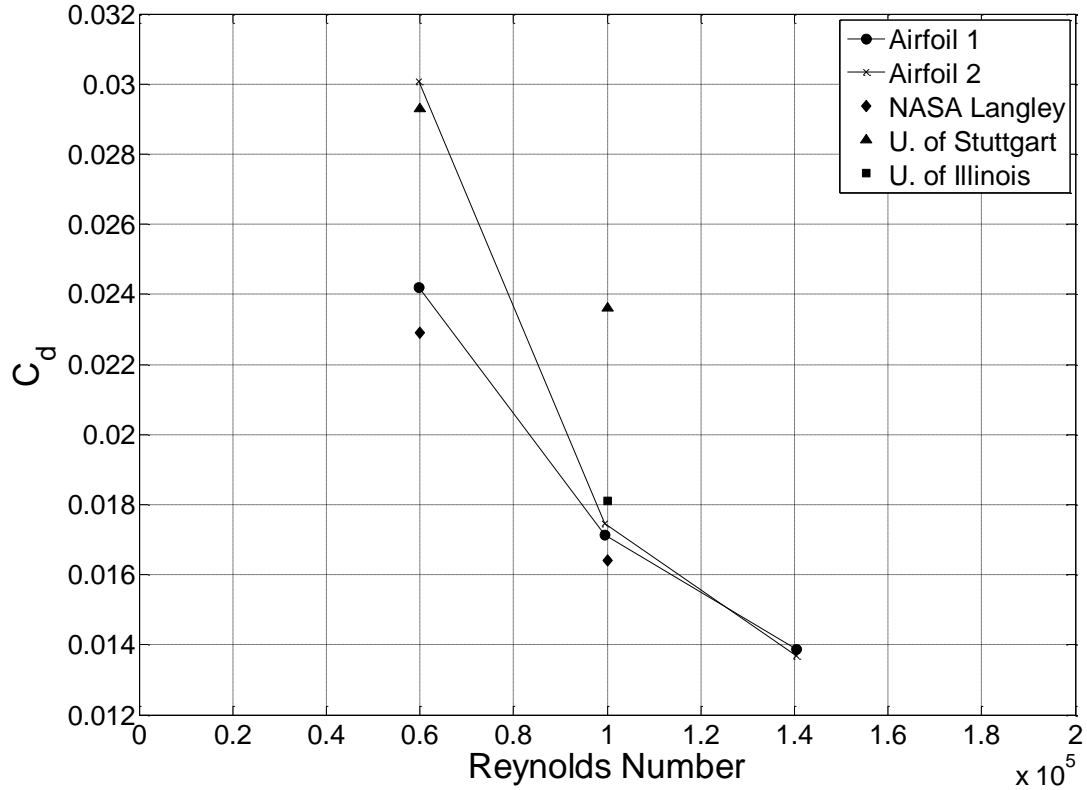
Figure 3.16 Comparison of drag measurements of Airfoil 2 compared to other facilities. Measurements were at z/s = -0.13 in area of S3F and PIV.

3.2.4. Summary

C_p measurements were taken on Airfoil 1 at several small angles of attack to determine an appropriate angle of attack for the separation control experiments. The measurements indicated that laminar separation occurred in the AFRL/RZ DWT consistent with measurements in the NASA tunnel, but that loading was slightly higher in the DWT. At α = 1.5° laminar separation could be obtained by varying Reynolds number. C_p measurements were recorded for Airfoil 2 and indicated that installation of the pressure lines along the pressure surface changed the reattachment point compared to Airfoil 1. Airfoil 2 did however, exhibit laminar boundary layer separation and reattachment on the suction surface consistent with the unmodified version of the E387 at the same angle of attack and Reynolds numbers. PIV data was recorded on Airfoil 2 in order to determine mean separation and reattachment points with better spatial resolution. Drag

measurements on both Airfoil 1 and Airfoil 2 were compared to E387 data from other facilities. Airfoi1 1 drag measurements were within the spread of data taken at other facilities. Airfoil 2 drag did not vary considerably from Airfoil 1 except at the lowest Reynolds number recorded, where drag was 25% higher on Airfoil 2, than Airfoil 1.

3.3. Clean Installation of S3F on Airfoil 2

PIV was used to obtain velocity field measurements in the area of the S3F and compared to PIV without the S3F installed in order to investigate whether the new method of S3F attachment significantly affected boundary layer behavior. The new S3F installation method was described in Section 2.2.1. The focus of the comparison was at Reynolds numbers of 1.0 x 10^5 and 6.0 x 10^4. This section also includes a comparison of mean velocity measurement with a plasma actuator installed on the airfoil to gage if either the S3F or plasma actuator had a significant effect on the boundary layer.

To simulate an airfoil with no S3F installed, the cavity was filled with a black flat plate. Mean velocity data for this case was shown in Section 3.2.2. S3F carriers were 3D printed with a single cavity, then lightly sanded for a smooth fit into a cavity on the suction surface of the airfoil. The S3F carrier was painted black prior to being filled with S3F to reduce reflection of light. The S3F carrier was filled with S3F at ISSI Inc. then installed in the airfoil and held in place with two flat head screws near the trailing edge.
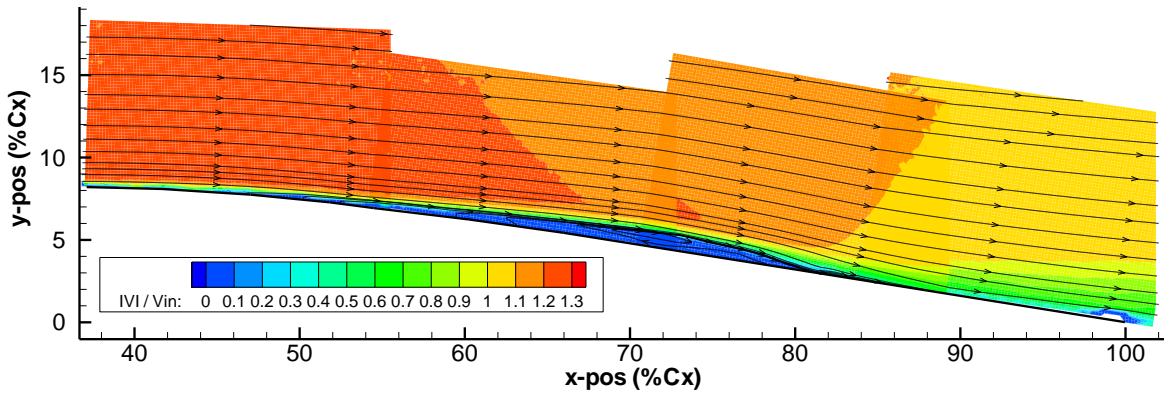
Figure 3.17 Airfoil 2, S3F #4, Re = 1.5 x 10^5
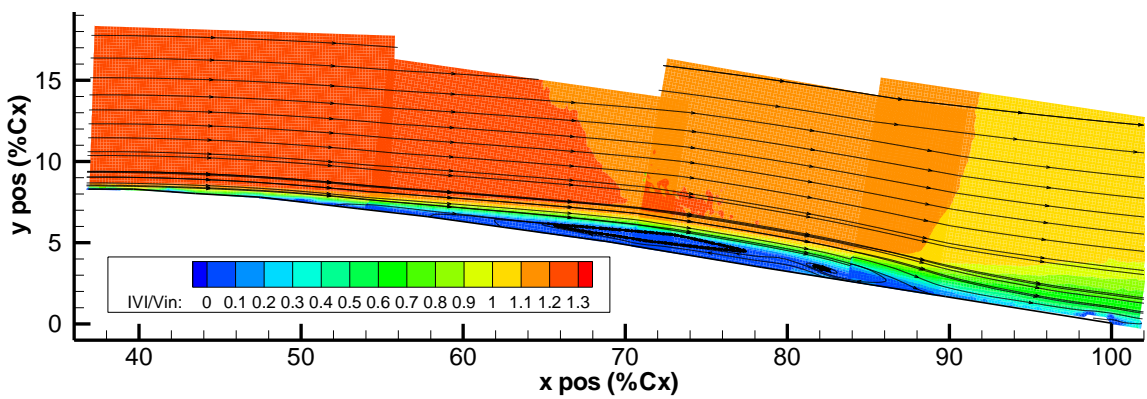
Figure 3.18 Airfoil 2, S3F #4, Re = 1.0 x 10^5
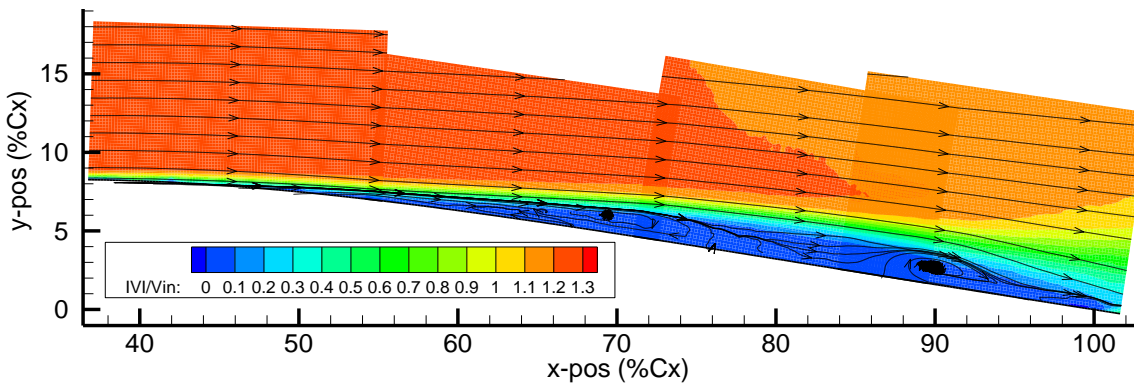
Figure 3.19 Airfoil 2, S3F #4, Re = 6 x 10^4

Mean non-dimensional velocity fields over the suction surface of Airfoil 2 with S3F #4

installed are shown in Figure 3.17 through Figure 3.19. The laser sheet was aligned with the top

edge of the S3F. Streamlines have been overlaid on the plots in order to visualize the flow field.

At the highest Reynolds number tested Re = 1.5 x 10^5 the boundary layer separates at

approximately C_x=54%. A thin mean laminar separation bubble extends to approximately

C_x=82%. At Re = 1.0 x 10^5 the separation bubble is thicker and extends to approximately

C_x=89%. Streamlines in the separation bubble indicate a clockwise recirculation until C_x≈78%,

followed by a second vortex at the trailing edge of the mean separation bubble with a core at

C_x=82%. This mean vortex is most likely an indication of the location in which vortices that that

have rolled up in the separated shear layer shed from the rear of the separation bubble. At a Re =

6 x 10^4 the extent of separation is nearly to the trailing edge of the airfoil. The mean streamlines

show a more complex shape. It appears that a main recirculation region forms under the

separated shear layer. Near the trailing edge a vortex is located with a core at C_x= 90%. The PIV

data implies that even at Re = 6 x 10^4 there is mean boundary layer reattachment near the trailing

edge of the airfoil, with a strong reverse flow vortex centered about C_x= 90%.

Mean velocity profiles normal to the airfoil surfaces are shown in Figure 3.20 through Figure

3.23. The figures compare velocity profiles measured on Airfoil 2 with and without (clean) the

S3F installed. Also included in the figures is data taken with a plasma actuator installed on the

airfoil. This data is labeled "DBD" in the figures and has been included to give perspective into

the change due to installation of the S3F compared to changes due to adding flow effecter to an

airfoil.

a.)   b.)
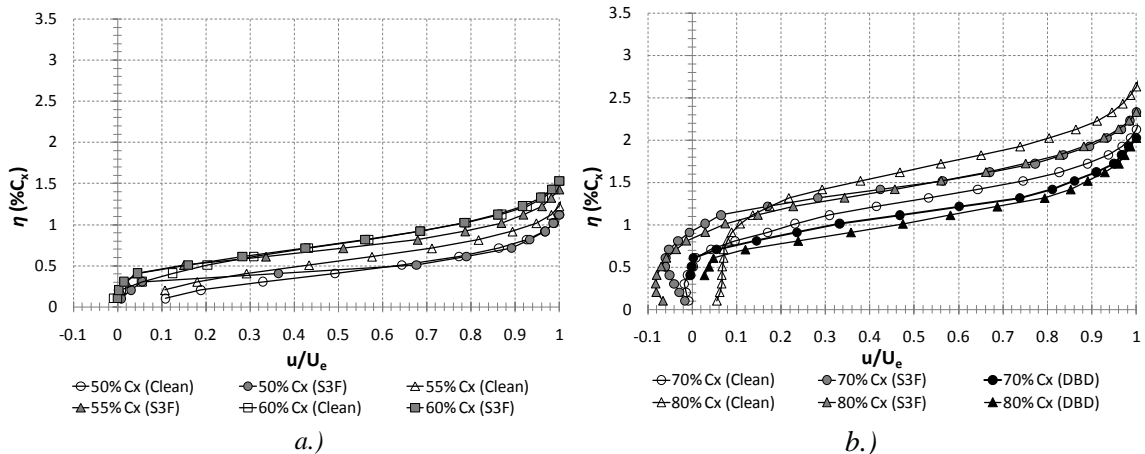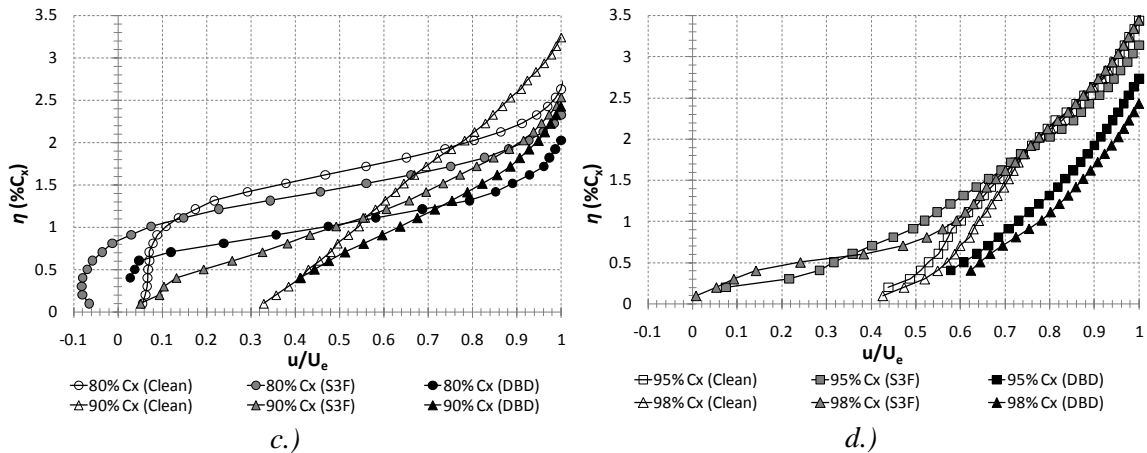
Figure 3.20 Suction surface boundary layer profiles with and without S3F installed, Re = 1.0x10^5.

Figure 3.20 shows mean boundary layer profiles normal to the airfoil. At upstream positions near the separation point (Figure 3.20a), the boundary layer has an inflection point very near the airfoil surface due to an adverse pressure gradient. The airfoil with S3F installed had a thicker, fuller boundary layer. It is interesting note that beyond the separation point, by C_x=60%, the boundary layer thickness is nearly equal for both cases. The separation point appears to be slightly further upstream when the S3F is installed. No data was available near the separation point with plasma actuator installed. It should be noted that the laminar boundary layer thickness in the region of separation is very thin relative to the size of the image field of view. The uncertainty could be quite high owing to the large velocity gradient between the free stream and the near wall flow. Mean velocity profiles in the region of the separation bubble are shown in Figure 3.20b. There is significant spread in the boundary layer height between the three cases shown. In general, the boundary layer is thicker when the plasma actuator is not installed. The velocity profiles at C_x=80% without the airfoil installed is positive without reverse flow near the wall. This could be erroneous data as it would imply the mean boundary layer has reattached. By C_x=90% the boundary layer has reattached for each case. The boundary layer is much thicker without S3F or the plasma actuator installed through the trailing edge. Near the trailing edge at

C_x=95%-98% the boundary layers are fuller and resemble turbulent boundary layers. When the plasma actuator is installed the boundary layer has the smallest thickness and fullest profile.

Boundary layer thickness has been plotted in Figure 3.21 and compared to predictions for a flat plate laminar boundary layer by Blasius, and 1/7th power law turbulent boundary layer prediction. The Blasius prediction for boundary layer thickness agrees with PIV obtained mean velocity data up to the separation point near 55% axial chord. The boundary layer thickness grows rapidly after separation. In the region of turbulent reattachment at C_x=90%, and to the trailing edge, the boundary layer thickness is higher for the clean airfoil. This is implies transition to turbulence occurs further downstream for the clean case, compared to the cases with S3F and a plasma actuator installed. In summary, both the S3F and the plasma actuator had the effect of decreasing boundary layer thickness downstream of the laminar separation point. Installation of the plasma actuator had the largest overall effect on boundary layer thickness at Re = 1.0 x 10⁵.
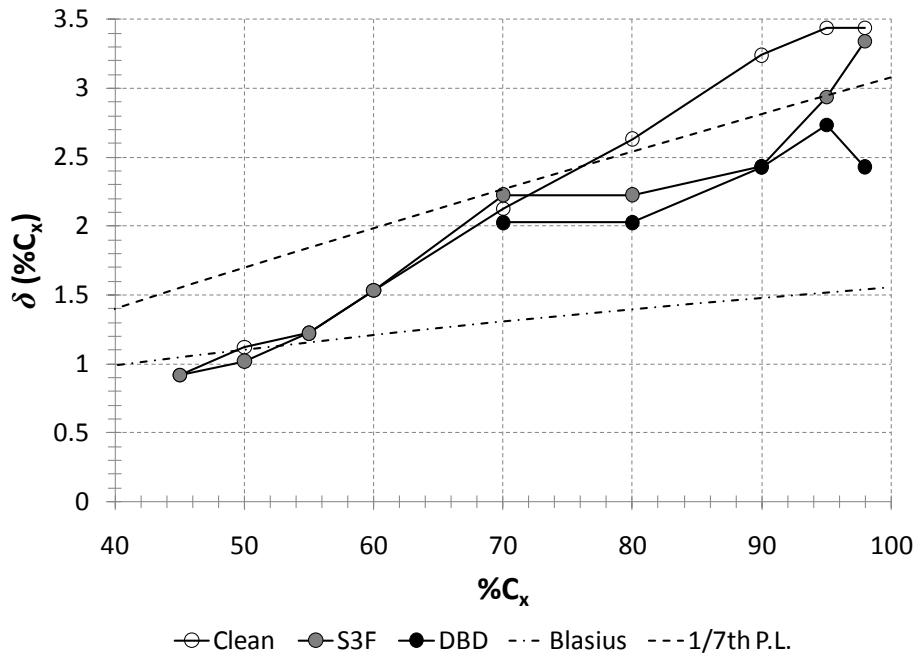
Figure 3.21 Boundary layer thickness with and without S3F installed, Re = 1.0x10⁵.

η (%C$_x$)

-0.1 0 0.1 0.2 0.3 0.4 0.5 0.6 0.7 0.8 0.9 1
u/U$_e$

○ 50% Cx (Clean)   ● 50% Cx (S3F)   △ 55% Cx (Clean)
▲ 55% Cx (S3F)   ⊞ 60% Cx (Clean)   ■ 60% Cx (S3F)

η (%C$_x$)

-0.1 0 0.1 0.2 0.3 0.4 0.5 0.6 0.7 0.8 0.9 1
u/U$_e$

○ 70% Cx (Clean)   ● 70% Cx (S3F)   ● 70% Cx (DBD)
◇ 80% Cx (Clean)   ◆ 80% Cx (S3F)   ◆ 80% Cx (DBD)

η (%C$_x$)

-0.1 0 0.1 0.2 0.3 0.4 0.5 0.6 0.7 0.8 0.9 1
u/U$_e$

○ 80% Cx (Clean)   ● 80% Cx (S3F)   ● 80% Cx (DBD)
◇ 90% Cx (Clean)   ◆ 90% Cx (S3F)   ◆ 90% Cx (DBD)

η (%C$_x$)

-0.1 0 0.1 0.2 0.3 0.4 0.5 0.6 0.7 0.8 0.9 1
u/U$_e$

○ 95% Cx (Clean)   ● 95% Cx (S3F)   ● 95% Cx (DBD)
△ 98% Cx (Clean)   ▲ 98% Cx (S3F)   ▲ 98% Cx (DBD)
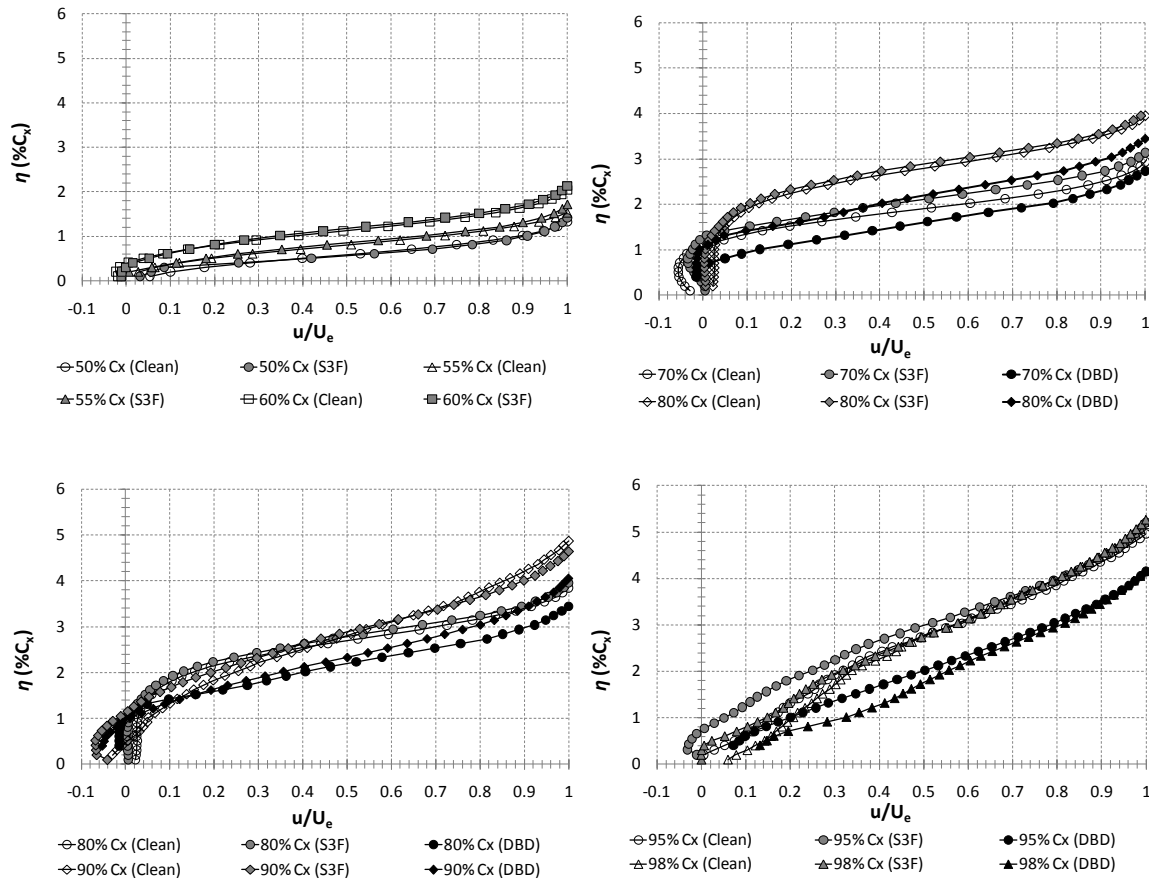
Figure 3.22 Suction surface boundary layer profiles with and without S3F installed, Re = 6 x 10^4.

Figure 3.22 shows the surface normal velocity profiles at Re = 6 x 10^4. Near the separation point the boundary layer profiles are very similar. Laminar boundary layer separation has occurred by C_x=60%. Boundary layer thickness has nearly doubled by C_x=80%. The near wall velocity is nearly zero, but each case shows a small positive velocity. This could be due to a mean bias in the measurement due to lack of reliable seeding in this region of very low velocity. At C_x=90% each profile has a negative velocity near the wall indicating that the mean boundary layer is separated. The reattachment point varies between all three cases. When the plasma actuator was installed the mean boundary layer reattachment occurred upstream of C_x=95%. With the S3F installed the boundary layer does not appear to reattach until approximately

C_x=98%, slightly downstream of the clean case. Mean boundary layer thickness is shown in Figure 3.23.

The installation of the S3F had a much smaller effect on boundary layer thickness at Re = 6 x 10^4, compared to the higher Reynolds number. On the other hand, the plasma actuator decreased boundary layer thickness by approximately 20%. Boundary layer thickness was not far off from the Blasius prediction up to the separation point. The $1/7^{th}$ power law prediction did not compare well to the boundary layer thickness near the trailing edge of the airfoil.
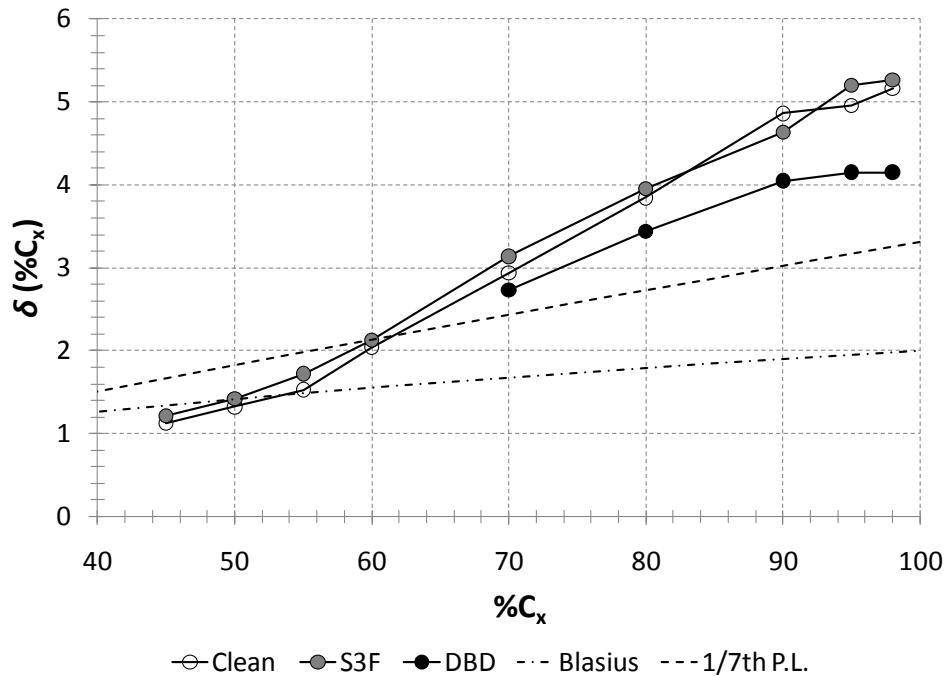
Figure 3.23 Boundary layer thickness with and without S3F installed, Re = 6 x10^4.

3.3.1. Summary

Comparisons of mean boundary layer thickness and velocity profiles using 2D-PIV have been made for three cases: Clean, S3F installed, and Plasma actuator installed. At both Reynolds numbers, installation of the plasma actuator had the largest effect on boundary layer thickness compared to installation of the S3F. Boundary layer thickness up to the laminar separation

location was consistent with Blasius's prediction for a flat plate boundary layer, at both Reynolds numbers. In the trailing edge region at Re = 1.0 x 10^5 the boundary layer thickness was in the range of $1/7^{th}$ power law prediction for a turbulent boundary layer. At the lower Reynolds number of 6 x 10^4 the $1/7^{th}$ power law prediction for boundary layer thickness was much lower than the actual boundary layer thickness calculated from PIV data. This agrees with instantaneous PIV velocity measurements that showed large coherent vortices along the trailing edge of the airfoil, rather than a developed turbulent boundary layer.

3.4. **S3F Development**

A total of six different S3F formulations summarized in Table 3.3 were fabricated and installed on Airfoil 2 over the period of this research. Frequency response was approximated using Equation (2.4) and shear modulus measurements were provided by ISSI Inc. The method used to measure such low shear modulus was improved over the course of the work by S3F #5 ISSI Inc. reported the uncertainty in the shear modulus measurement was +/-10%.

Table 3.3 S3F Properties

Version	Shear Modulus (Pa)	Mag Factor (px/mm)	Thickness (mm)	Freq. Response (Hz)	Notes
S3F #1	110	97	0.6	93	TiO_2 particles, two 20mm wide strips
S3F #2	110	-	0.6	93	Attempt to decrease shear modulus, no significant change
S3F #3	118	144	0.9 / 0.45	64	Effort to increase pixel disp., ↓S3F width to 10 mm, ↑Mag factor, ↑S3F thk, S3F extended to C_x = 98% but with T.E. thickness change
S3F #4	100	157	0.9	59	C_x = 42%-98% with uniform thickness, switch to one strip, switch to fluorescent paint markers
S3F #5	37 +/- 10%	145-147 typ.	0.9	32	Fluorescent paint markers
S3F #6	7.7 +/- 10%	156	0.9	16	Fluorescent paint markers

The S3F parameters as well as the carriers were modified in an effort to improve measurements at the low Reynolds numbers and length scale used in the experiments. Creating the S3F and filling the plastic S3F carrier flush to the surface required skill, and often several attempts were made to achieve the desired film properties and fill quality. ISSI Inc. improved the method to generate the S3F at such low shear modulus over the period of the research effort. By the third version (S3F #3) the films were consistently fabricated with shear modulus in the range of 100 Pa.

Initially the width of the S3F strip was 20mm and 0.6 mm thick for both S3F #1 and #2. The width of the S3F set the maximum magnification factor for a given camera and lens combination since part of the S3F carrier above and below the S3F was required in the field of view to correct for airfoil and camera movement. In an effort to increase displacement the width of the S3F was reduced to 10 mm and the thickness increased to 0.9mm. The increase in thickness was at the expense of frequency response, but it remained well above the camera maximum frame rate. By S3F #4 it was realized that the high magnification factors being used required a smaller diameter and denser distribution of markers on the film. In order to increase marker density and decrease marker diameter, fluorescent paint was used rather than titanium oxide particles. A comparison of images of S3F with Titanium Oxide markers versus fluorescent paint markers is shown in Figure 3.24.

a.)   b.)
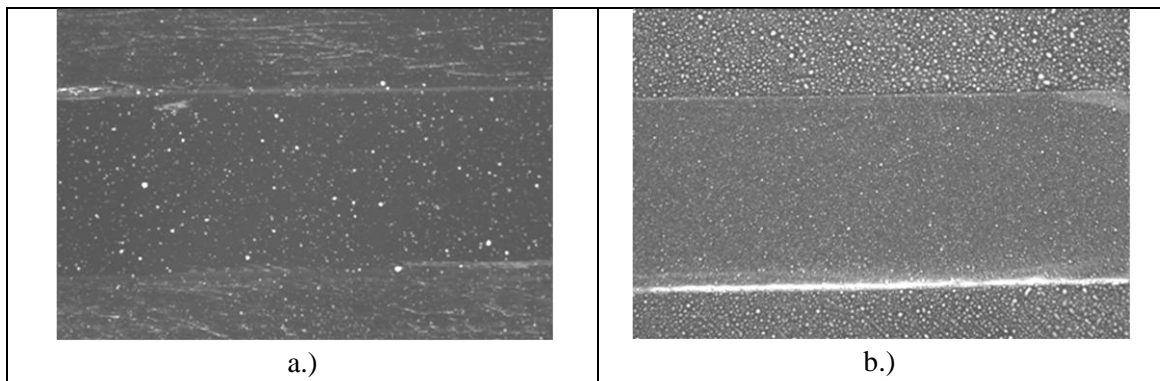
Figure 3.24 Sample images of S3F with different markers: a.) TiO$_2$ particles b.) Fluorescent paint. Nikon 200mm F4 lens, f/32 aperture, 0.6ms exposure, 550 nm long pass filter.

By experimenting with new methods of fabricating S3F, ISSI Inc. was able to produce an even more sensitive film for version #5. This resulted in a significant decrease in shear modulus from 100 Pa to 37 Pa for S3F #5. Film displacement increased and measurements were made at a Reynolds number down to $5\text{x}10^5$. S3F #6 resulted in the lowest shear modulus film tested, having a mean shear modulus of 7.7 Pa along the centerline of the film. ISSI Inc. also observed a larger variation in shear modulus across the film than in previous formulations. Film displacement increased significantly, but frequency response decreased to approximately 16 Hz.

3.4.1. Skin friction

This section discusses the skin friction values inferred from S3F tangential displacement presented in the following sections. Predicting the skin friction on the suction surface of an airfoil with laminar separation and reattachment is difficult in the absence of numerical simulation. Here the discussion is limited to phenomenological and order of magnitude comparisons.

As a laminar boundary layer develops along the surface of an airfoil it will reach a critical point at which it transitions to a turbulent boundary layer. The critical point in which laminar to turbulent transition occurs is strongly dependent on the pressure gradient (Schlichting & Gersten 2000). The boundary thickness increases along the surface of the airfoil and the rate of increase is larger in the turbulent downstream boundary layer than in the laminar boundary layer. As the boundary layer thickness increases, the wall shear stress decreases; however, a turbulent boundary layer has a higher wall shear stress than a laminar boundary layer.

As a rough order of magnitude estimate of skin friction over the E387 airfoil, flat plate estimates of both laminar and turbulent boundary layers are used. The local skin friction in the boundary layer of a flat plate at zero incidences is calculated by solution of the Blasius equation to be:

$$C_f(x) = \frac{0.664}{\sqrt{\text{Re}_x}} \quad (3.1)$$

with boundary layer thickness approximated by:

$$\delta_{99} \approx 5.0 \sqrt{\frac{\upsilon \cdot x}{U_\infty}} \quad . \quad (3.2)$$

The local skin friction and boundary layer height of a flat plate with a turbulent boundary layer can be approximated by the 1/7 power law estimate:

$$C_f(x) \approx \frac{0.027}{\text{Re}_x^{1/7}} \quad (3.3)$$

and

$$\delta_{99} \approx 0.16 \cdot \frac{x}{\text{Re}_x^{1/7}} \quad . \quad (3.4)$$

The boundary layer on the E387 airfoil will differ from the flat plate estimates given in Equations (3.1)-(3.4) due to an adverse pressure gradient on the suction surface beginning at the negative pressure peak. The adverse pressure gradient causes a point of inflection in the boundary layer profile with increasing downstream pressure ultimately leading towards negative flow at the wall and separation (White 1991). Equations (3.1)-(3.4), however, do give an order of magnitude estimate of the shear stress and boundary layer thickness expected over the E387 suction surface.

3.4.2. S3F measurements on airfoil 2

Measurements with S3F #4-#6 are compared in this section at a Reynolds number of 1.0×10^5. These films had shear modulus of 100, 37, and 7.7 Pa which resulted in significant difference in tangential displacement magnitude. Figure 3.25-Figure 3.27 show the mean tangential film displacement at Re = 1.0×10^5 calculated using ISSI Inc.'s hybrid cross correlation/optical flow method (Fonov, 2004). Each plot shows a zero crossing location implying mean boundary layer

reattachment. The zero crossing location is different for each S3F and varies between $C_x = 92\%$ and 96%.
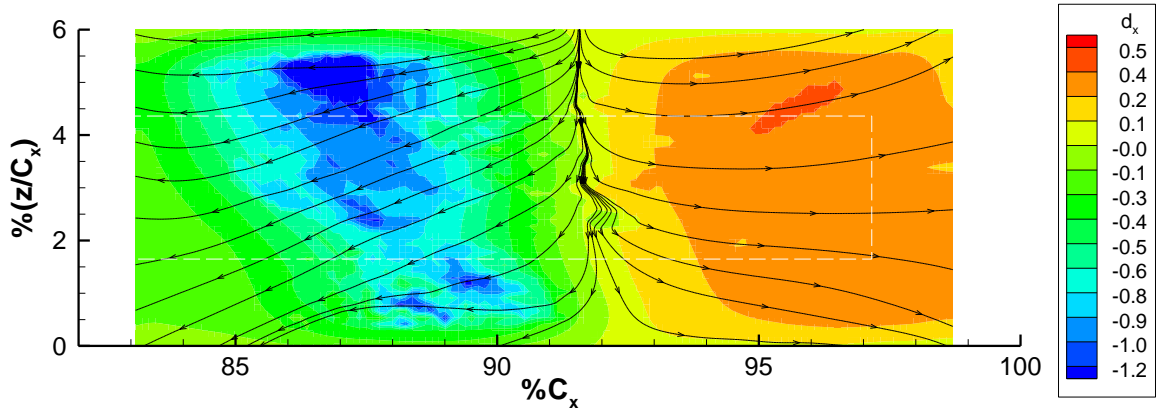
Figure 3.25 S3F #4 mean streamwise displacement in pixels, Re = 1.0x10^5, μ$_m$ = 100 Pa.
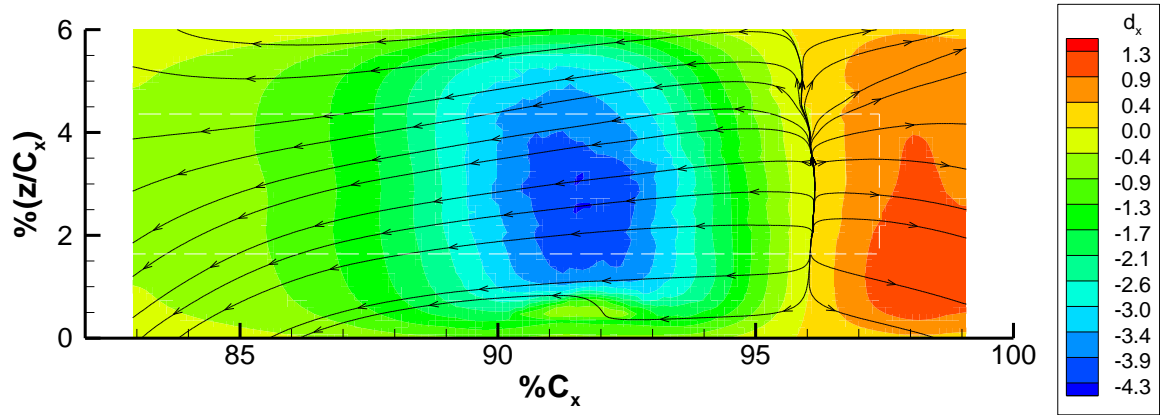
Figure 3.26 S3F #5 mean streamwise displacement in pixels, Re = 1.0x10^5, μ$_m$ = 37 Pa.
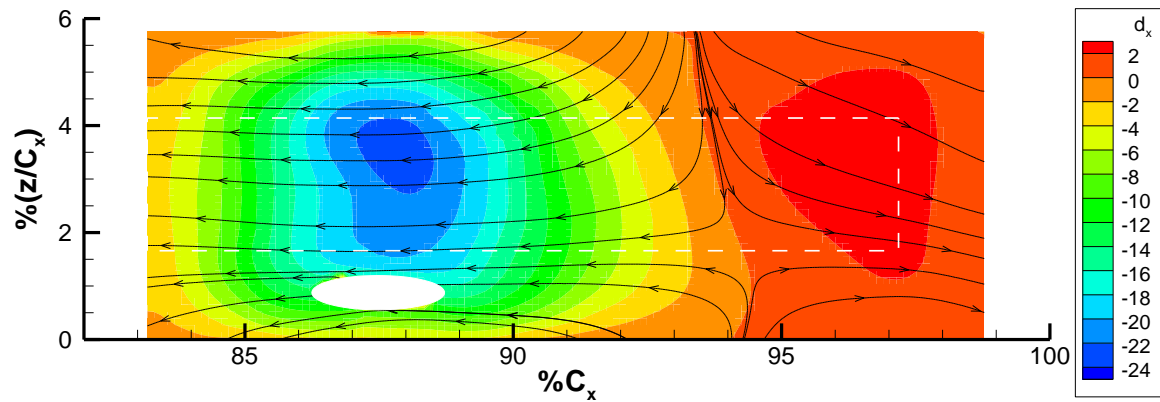
Figure 3.27 S3F #6 mean streamwise displacement in pixels, Re = 1.0x10^5, μ$_m$ = 7.7 Pa.

Figure 3.28 gives estimates of the skin friction coefficient. A word of caution is necessary here when evaluating the skin friction coefficient in Figure 3.28. The skin friction has been calculated assuming shear stress is a linear function of tangential displacement. Crafton et al. (2008) has verified this is true in flow with zero pressure gradients, and this is assumed true in flows with small pressure gradients as well. The E387 suction surface likely has locally high pressure gradients that negate this assumption, especially near the reattachment point.

The minimum skin friction value is nearly identical for S3F #5 and S3F #6, but with different spatial location. S3F #4 has the same shape as the other two films, but with a higher minimum value. The zero crossing location of S3F #4 at $C_x = 91.5\%$ is in very good agreement with PIV data. The estimated turbulent boundary layer skin friction using $1/7^{\text{th}}$ power law is included in the plot for reference. A summary of minimum and maximum S3F tangential displacement, skin friction coefficient, and reattachment location is shown in Table 3.4.

- · - S3F #4   − − S3F #5   —— S3F #6   ····· 1/7th Power Law Estimate
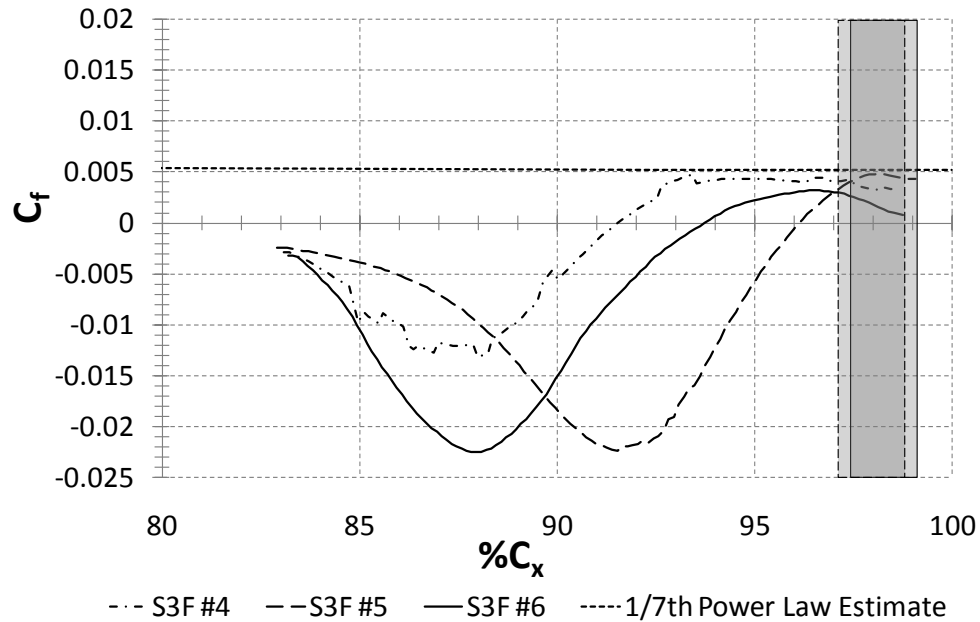
Figure 3.28 Estimate of S3F #6 mean skin friction coefficient, Re = 1.0 x 10^5.

Table 3.4 Summary of mean parameters near the trailing edge region for S3F #4-#6, Re=1.0x10^5.

	$d_{x,max}$ (px)	$d_{x,min}$ (px)	$C_{f,max}$ (estimated)	$C_{f,min}$ (estimated)	%$C_{x,\text{reattach}}$
S3F #4	0.36	-1.02	0.005	-0.013	91.8
S3F #5	0.95	-4.28	0.004*	-0.022	96.2
S3F #6	3.17	-22.62	0.003	-0.023	93.7
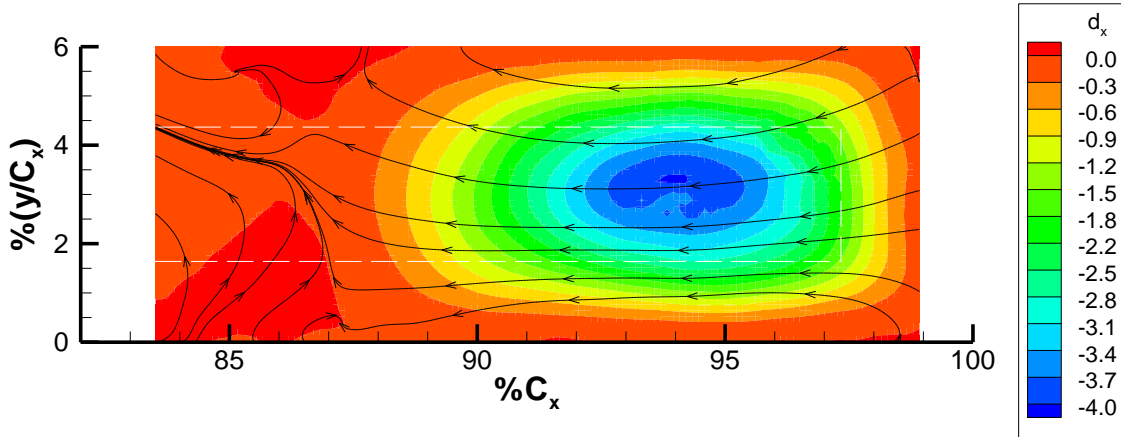
Figure 3.29 S3F #6 mean streamwise displacement in pixels with plasma actuator installed, Re = 6x10^4.

S3F #6 tangential displacement at a lower Reynolds number of 6 x 10^4 is shown in Figure 3.29 and an approximation of skin friction coefficient assuming linear relationship between shear stress and tangential displacement in Figure 3.30. A plasma actuator is installed on the airfoil which is expected to change the boundary layer characteristics compared to a clean airfoil as was discussed in Section 3.3. No zero crossing is indicated in the measurements which would imply that the mean boundary is separated to extent of the S3F near 99% C_x or that the pressure gradient near the trailing edge is large enough relative to shear stress that the tangential displacement is actually a coupled response between pressure gradient and shear stress. PIV data discussed in Section 3.3 showed that a mean reattachment point was in the area of 95% C_x with the plasma actuator installed. There was also a reverse flow vortex in the mean data at Re = 6 x 10^4 centered about 90% C_x. In the absence of simultaneous pressure gradient data it is unclear whether the local minimum in tangential displacement at Re = 6 x 10^4 observed in Figure 3.29 and Figure 3.30 is due primarily to shear stress or a coupling of shear stress and pressure. Regardless of whether the local minimum was created by a coupling of forces or not, it was hypothesized that this minimum would shift spatially depending on reattachment location. This would make the tangential film displacement useful at the lower Reynolds number even if the shift in minimum is due to a coupled forcing affect. Further discussion on the potential impact of ignoring pressure gradient will be discussed in the next section.
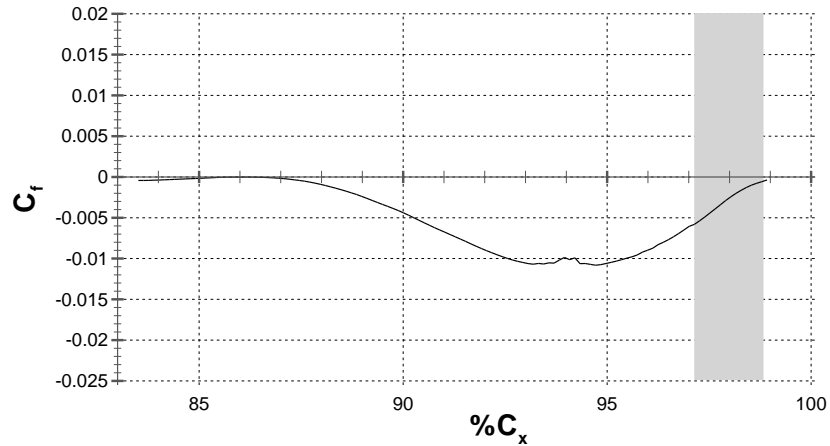
Figure 3.30 Estimate of mean skin friction coefficient measured by S3F #6 with plasma actuator installed, Re = 6x10^{4}.

3.4.3. Assumption of a linear relationship between d_x and C_f

Measurements of S3F #5 tangential displacement in the streamwise direction were obtained with four different overlapping camera views. The S3F midplane, mean streamwise tangential displacements of each individual camera view were assembled into one plot shown in Figure 3.31. Individual images were analyzed using ISSI Inc. image processing software. The combined plot of Figure 3.31 demonstrates that the experimental measurement method was repeatable, as the wind tunnel had to be turned off, the camera repositioned, image view located, and magnification factor calculated for each view. Regions assumed to have edge effects are shaded gray. The shape and direction of S3F displacement is consistent with shear stress magnitude and direction expected along a surface with laminar separation and reattachment. A zero crossing at approximately 52% C_x indicates flow separation and reversal followed by a region of low negative displacement in the separation bubble. The shear stress decreases to a minimum point at approximately 90.5% C_x before increasing to a zero crossing at 96% C_x. The region surrounding the minimum from 82% C_x to 96% C_x is typical of a recirculation area in a laminar separation bubble just upstream from the reattachment point (see Figure 5.15). At the

101

upstream edge of the S3F is actually two zero crossings, the first is on the edge of the region

expected to experience edge effects.
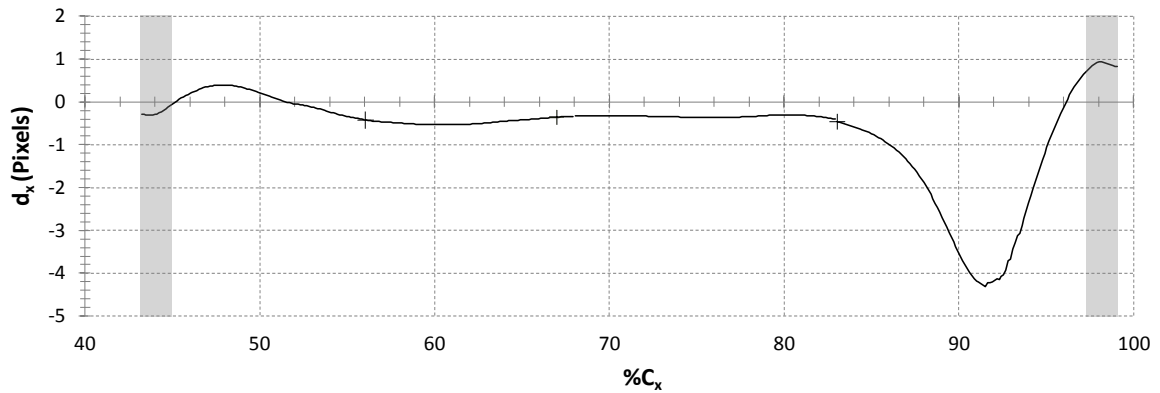
Figure 3.31 S3F #5 streamwise film tangential displacement along the suction surface at Re = 1.0 x 10^5. The plot is a combination of four different views, with division between each view marked with the symbol '+'.

Using S3F tangential displacement directly to indicate suction surface boundary layer

features assumes that the pressure gradient has a negligible effect on S3F tangential displacement.

This assumption may be valid along portions of the S3F and not others depending on the ratio of

pressure gradient to local shear stress. The pressure gradient on the S3F was approximated from

pressure coefficient measurements on Airfoil 2. Equation (2.3) was used to estimate skin friction

coefficient compared to ignoring pressure gradient effects. Pressure tap measurements were

available up to C_x=90%, and the inviscid profile calculated in XFOIL was used to estimate the

pressure coefficient from C_x=90% to the trailing edge of the S3F. Static pressure measurements

were available every 5% C_x to approximate the pressure gradient and linear interpolation was

used to estimate the pressure gradient between pressure tap locations. Pressure distributions used

in the comparison are shown in Figure 3.32. The Airfoil 2 C_p (clean) measurements refer to no

plasma actuator or S3F installed on the airfoil. The measured C_p was also shifted three degrees

downstream in order to understand the effect of the reattachment point shifting downstream. The

inviscid pressure distribution calculated in XFOIL has also been included in the comparison.

An estimation of skin friction coefficient based on Blasius's solution for laminar boundary layer

on a flat plate, and the 1/7th power law estimate of turbulent boundary layer shear stress is plotted in each image.
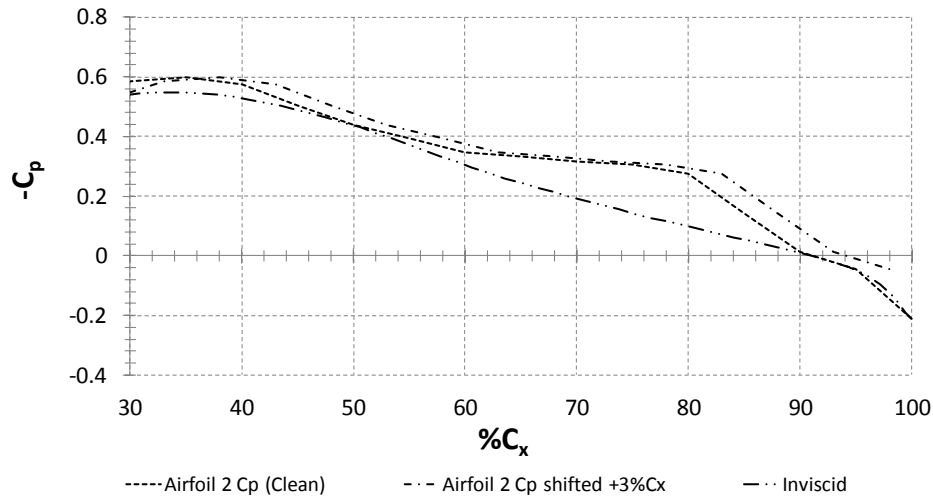
Figure 3.32 C_p profiles at Re = 1.0 x 10^5 used to estimate surface pressure gradient.

The location of highest pressure gradient along the S3F is in the area of the reattachment point, but near the separation point the shear stress is low relative to pressure gradient which can result in a shift in perceived separation point.
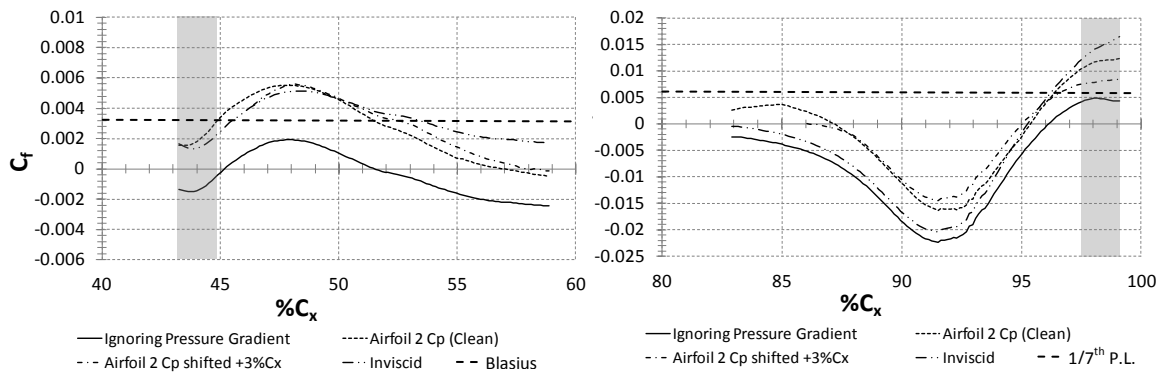
Figure 3.33 Estimation of the effect of pressure gradient on S3F indicated separation and reattachment points, S3F #5, Re = 1.0 x 10^5.

Figure 3.33 shows the potential effect of pressure gradient on the tangential displacement of the S3F near the reattachment and separation points at a Re = 1.0x10^5. Near the separation point the perceived separation point is at 51.5% C_x, but depending on the pressure gradient the separation point could shift in excess of 6% C_x downstream. Both the measured clean Airfoil 2

C_p and the shifted C_p result in a separation point of 57% C_x and 58% C_x respectively. Near the trailing edge of the airfoil each of the pressure gradients shift the reattachment point upstream less than 1% C_x. It is worth noting that when considering pressure gradient in the skin friction estimate upstream of the separation point, the skin friction coefficient is nearly twice as high as Blasius's estimate. Downstream of the reattachment point the estimated skin friction ignoring pressure gradient is within 16% of the $1/7^{th}$ power law estimate, but including pressure gradient in the estimation results in significantly higher skin friction. It is apparent that if the pressure gradient is included in the estimation of skin friction from S3F tangential displacement, the pressure gradient must be accurately located spatially. Pressure gradient location has a large effect on estimated skin friction when using Equation (2.3).

A similar comparison is made at the trailing edge of S3F #6. The perceived reattachment point based on raw S3F tangential displacement is approximately 94% C_x, 2% C_x further upstream than the measurements of S3F #5. The pressure gradients resulted in a larger shift in reattachment point, as much as 2% C_x, and also decreased the minimum skin friction coefficient.
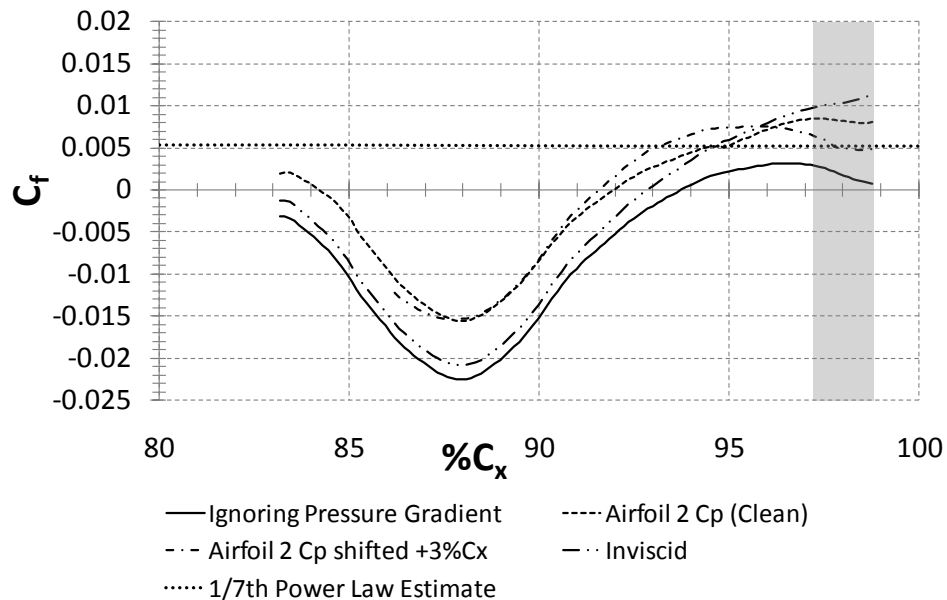
Figure 3.34 Effect of pressure gradient on S3F estimated separation and reattachment points, S3F #6, Re = 1.0 x 10^5.

3.5. **Chapter Summary**

Six different formulations of S3F were tested for use as a separation control sensor on the

E387 at Reynolds numbers below 1.0×10^5. The measured tangential displacement and estimated

skin friction coefficient of the final three films were compared. Each film showed a similar mean

displacement shape, but location of minimum tangential displacement and zero crossing location

varied by as much as 4% C_x at Re $= 1.0 \times 10^5$. At Re $= 6 \times 10^4$ the reattachment point was

indicated by S3F tangential displacement. It is hypothesized that regardless of whether the

minimum in tangential displacement was due to primarily shear stress or a coupled loading with

pressure gradient, the minimum point would shift spatially with reattachment location and still

provide a useful separation control sensor. Estimations of skin friction coefficient that included

pressure gradient showed that the mean separation point could shift spatially in excess 6% C_x

from the perceived separation point based on tangential displacement. Near the reattachment

point the inclusion of pressure gradient only shifted the mean zero crossing 2% C_x.

4. Open Loop Actuator Investigation

The objective of the open loop study was to verify that a plasma actuator could mitigate boundary layer separation on the E387 airfoil and determine an appropriate flow control strategy for the closed loop investigation. Two different plasma actuator electrode arrangements were compared to an asymmetric electrode arrangement that is often used for flow control. The two alternate plasma actuator electrode arrangements were chosen with the intent of generating streamwise vorticity, and improving separation control authority using a DBD plasma actuator. This chapter includes flow visualization of the induced velocity from each actuator configuration, pressure coefficient, profile drag, and flow visualization at various voltage amplitudes.

4.1. Description of Experiment

Three different electrode configurations shown in Figure 4.1were evaluated in an open loop configuration. The first actuator arrangement, DBD-01 was a spanwise array of 11 linear actuators spaced 20.6 mm on center, mounted parallel to the flow. This configuration produced an array of cross stream jets with the intent of generating longitudinal vorticity (Roth et al. 2000). The second actuator, DBD-02 was a spanwise array of linear plasma synthetic vertical jets spaced 23.8 mm on center. Vertical jet arrangements can be created as annular or linear configurations, and operated steady or pulsed (Jacobs et al. 2005, Santhanakrishnan and Jacob, 2007a, 2007b, 2008, 2009). DBD-03 is a single asymmetric electrode across the span of the airfoil centered at 35% C_x. This type of geometry produces a downstream jet along the span of the airfoil.   Figure 4.1 includes a schematic, photograph, and relative length of each discharge compared to the baseline, for each actuator electrode configuration installed in the AFRL/RZ DWT.
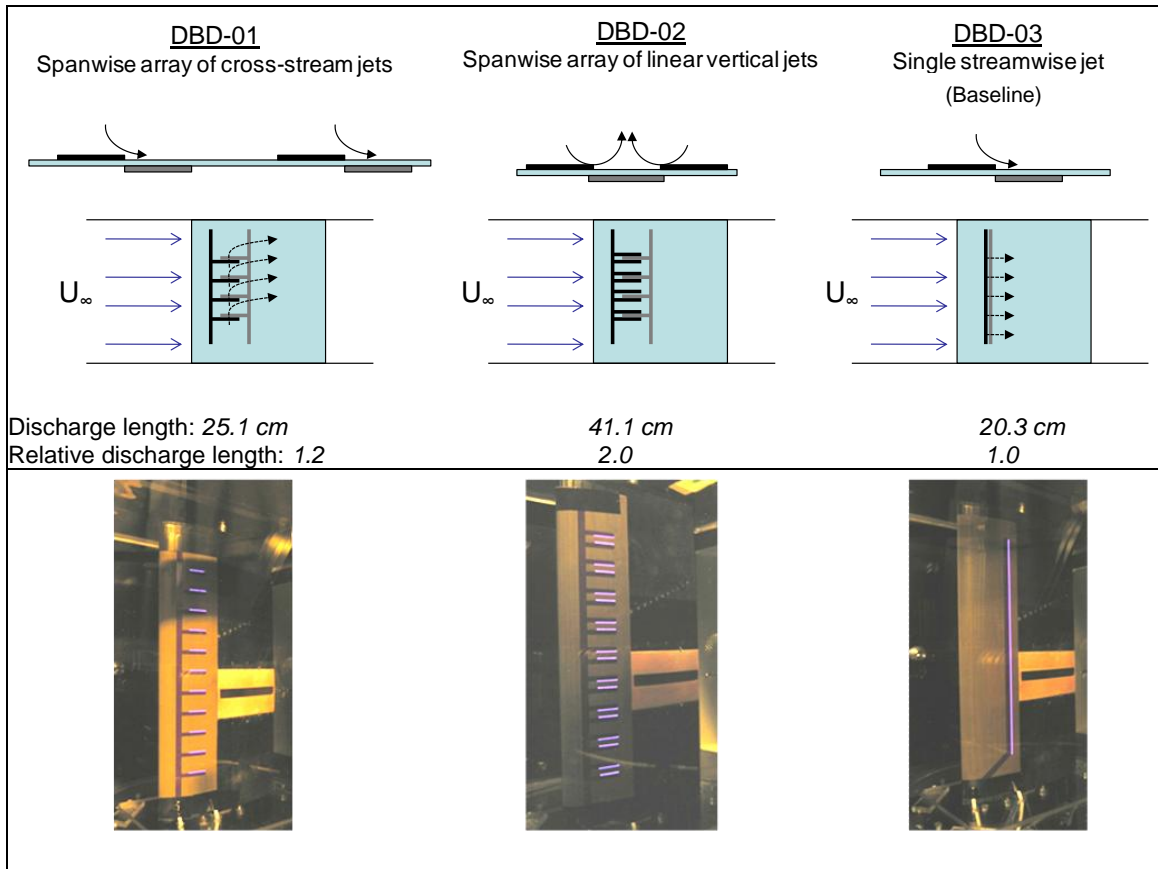
Figure 4.1 Schematic of each plasma actuator electrode configuration and photograph of each actuator installed and powered in the wind tunnel.

S3F #5 was used in the open loop study. In this study the S3F tangential surface displacement was used as a direct indicator of shear stress direction.

A PCO 4000 camera with 4008 x 2672 pixel resolution was used to obtain S3F flow-on and flow-off images. The image field of view was 27.3mm x 18.2 mm with a magnification factor of 146.6 px/mm. Airfoil deformation and motion relative to the camera on the order 25-50 μm (3.5-7 pixels) was corrected for using 2D interpolation using the method discussed in Section 2.6. Displacement maps were calculated using ISSI Inc. hybrid cross correlation/optical flow software. The displacement fields were then corrected for airfoil motion in Matlab.

The plasma actuators were fabricated in the U.S. AFRL Propulsion Directorate's thin film lab by photolithography and etching double-sided copper clad Kapton. The Kapton was 5 mil thick and the copper electrodes were 1.4 mil thick. The top and bottom electrodes were formed flush

107

with each other with no overlap. The plasma actuators were attached to the airfoil suction surface

by 2 mil thick adhesive transfer tape and were wrapped around the entire leading edge of the

airfoil to reduce the chance of tripping the boundary layer.   Surface irregularity added by the

plasma actuators on the suction surface was reduced to a 36 μm (1.4 mil) step up at the exposed

electrode and an approximately 178 μm (7 mil) step down at the trailing edge of the actuator.

Nonetheless, variation in extent of the mean laminar separation bubble was observed between

different installations of the plasma actuators onto the airfoil.

A schematic of the power circuit is shown in Figure 4.2. The electrodes were powered by

two Titan Series power supplies from Compact Power. Each of the power supply output voltages

were increased by an Industrial Test Equipment Co. transformer to kilovolt levels. In this work

the DBD plasma actuators were operated in steady mode with continuous sinusoidal waveforms

at a frequency of 3 kHz. Measurements showed that it took approximately 200ms to achieve

steady state actuator voltage amplitudes.
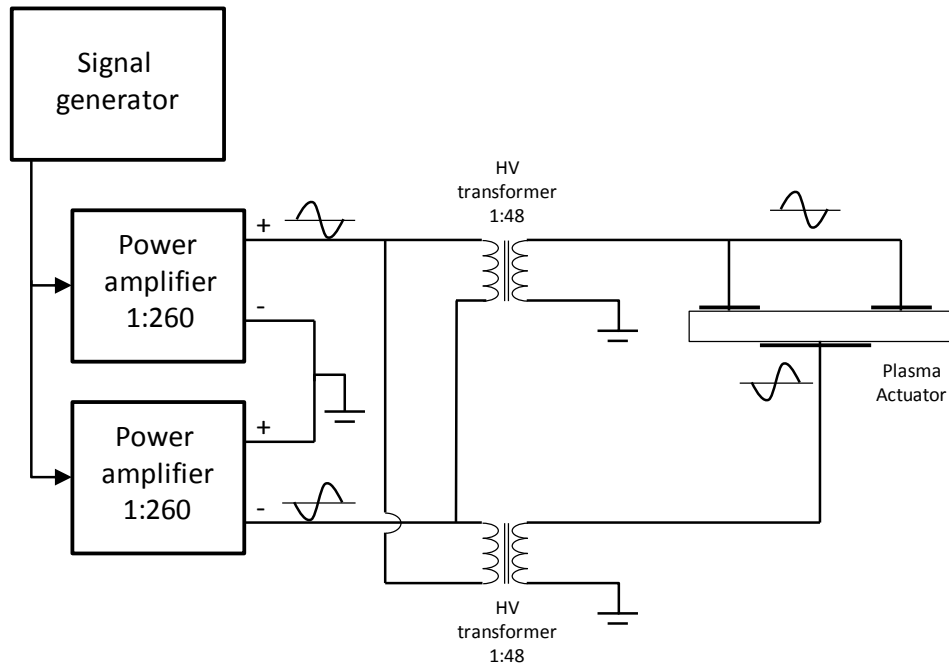
Figure 4.2 Plasma actuator circuit.

The top and bottom electrode voltages were measured using two Northstar PVM-11 high

voltage probes with 1000:1 attenuation. The current was measured using a Pearson Model 4100

current monitor (1 Volt/Amp) placed on the top electrode power lead. The signal from each

probe was measured using a Tektronix TSD 3054B oscilloscope. The power dissipation was

calculated by numerically integrating the product of instantaneous voltage and current:

$$P = \frac{1}{\Delta t} \int_0^T v \cdot i \, dt. \tag{6.1}$$

The average power was obtained by considering the power dissipation over 10 complete periods

of signal history. Figure 4.3 shows a plot of typical power dissipation versus applied voltage for

the plasma actuator. The power dissipation is proportional to $V_{pp}^{3.5}$ and is consistent with the

measurements of other researchers found in literature (Enloe et al. 2004). Figure 4.3 also shows

the power dissipation per meter of discharge. Operation of the plasma actuator permanently

changed the surface of the Kapton dielectric and left an image on the surface that was assumed to

represent the extent of discharge. The image left on the Kapton surface was used to measure the

discharge length. Each buried electrode had two areas of plasma along each spanwise edge

totaling 41.1 cm of discharge length.
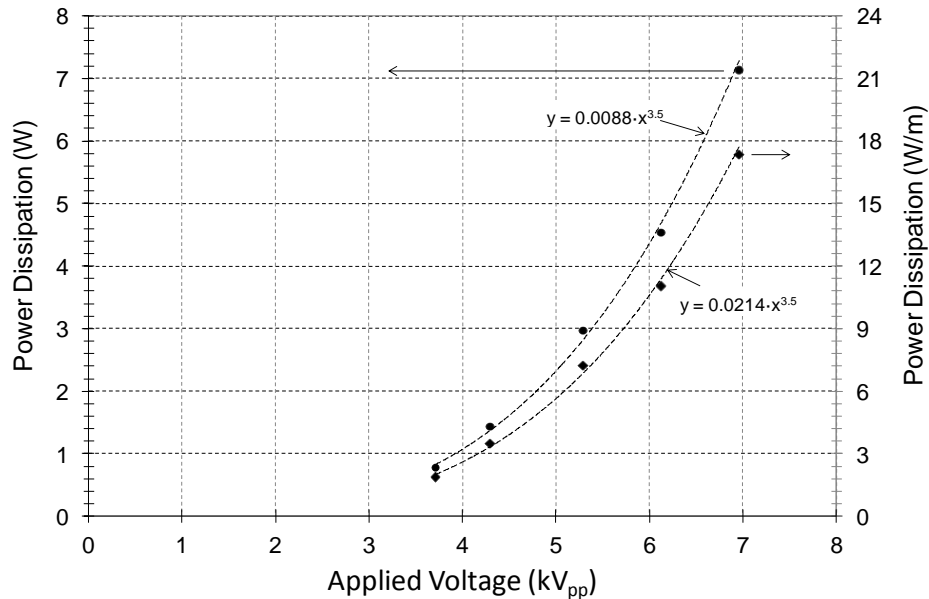
Figure 4.3 Typical actuator power dissipation

4.2. **Open Loop Study Results and Discussion**

4.2.1. Benchtop flow visualization

Flow visualization of the induced velocity generated with each plasma actuator electrode configuration is shown in Figure 4.4-Figure 4.6. In each figure an actuator was fixed to a flat plate with a uniform layer of adhesive transfer tape and placed on a bench top. The flow visualization method was explained in Section 2.3.2.
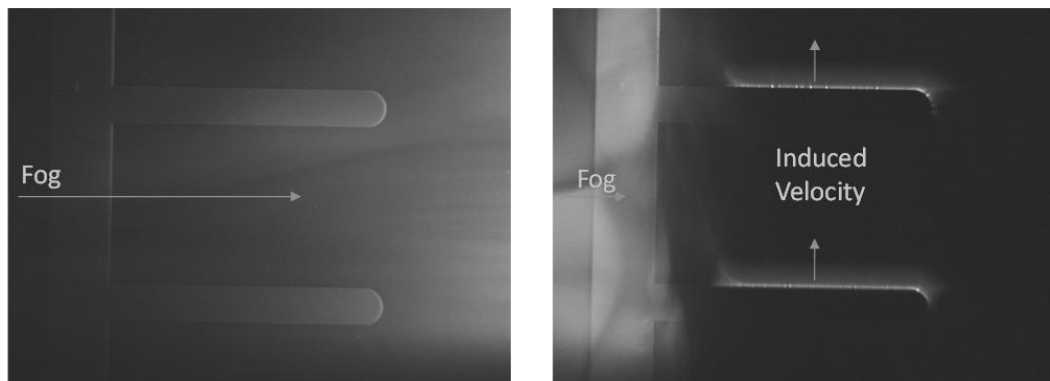
A. Series of lateral jets powered off   B. Series of lateral jet powered on

Figure 4.4 Flow visualization using CO_2 generated fog of the plasma actuator electrode configuration DBD-01. Arrows indicate location of induced velocity from each discharge.
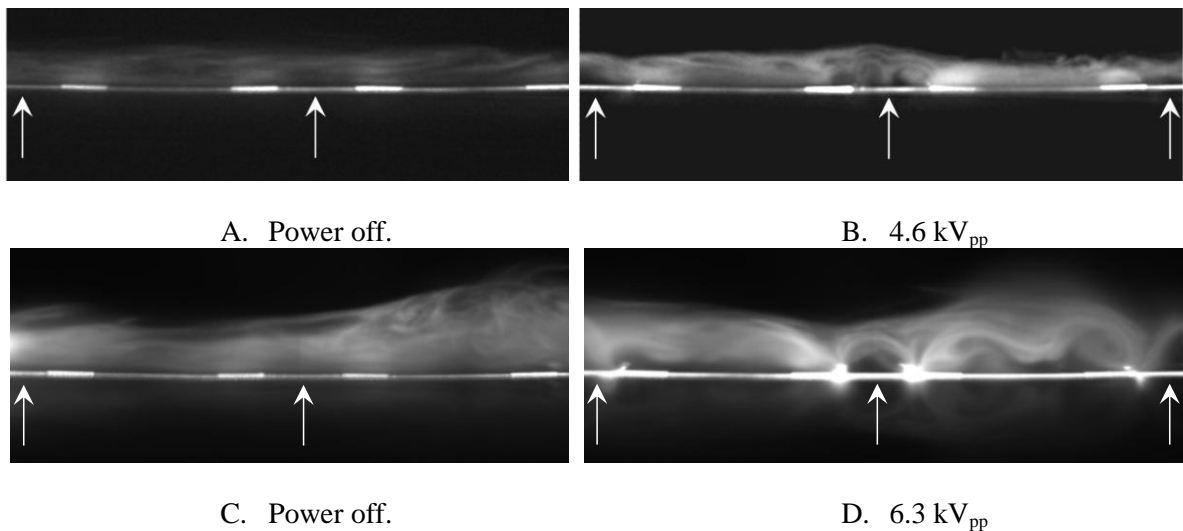
A. Power off.   B. 4.6 kV$_{pp}$

C. Power off.   D. 6.3 kV$_{pp}$

Figure 4.5 Flow visualization using CO_2 generated fog of the plasma actuator electrode configuration DBD-02. Arrows indicate the location of each vertical jet.

actuator

actuator

Asymmetric Electrode Arrangement
Power off

Asymmetric Electrode Arrangement
Power on
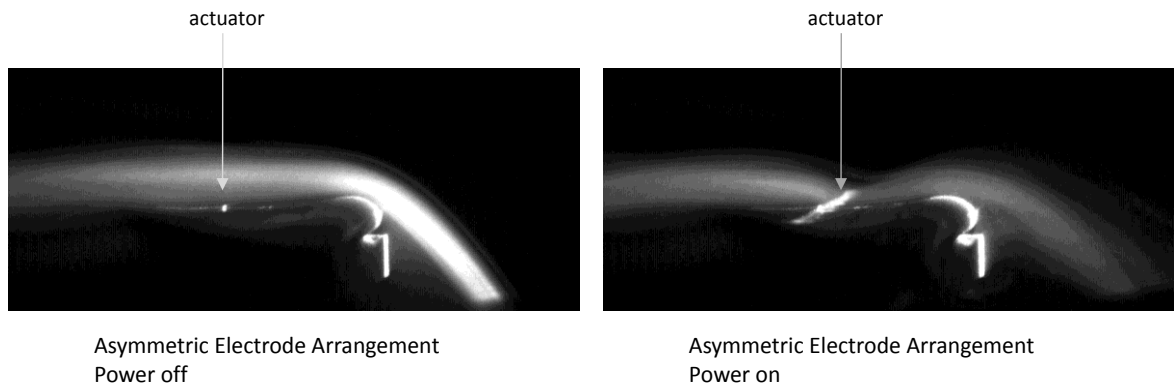
Figure 4.6 Flow visualization using CO_2 generated fog of the plasma actuator electrode configuration DBD-03.

In Figure 4.4 and Figure 4.6 the fog is flowing left to right, and in Figure 4.5 the flow is traveling towards the reader. The image of Figure 4.5 shows a strong jet in the spanwise direction that prevents the fog from reaching the illuminated plane. The potential for streamwise vorticity lies in the interaction between the freestream fluid flow and cross stream wall jets.

In Figure 4.5 two different actuator voltages are shown along with corresponding power off images taken just before each power on image. At the lower voltage vortical structures are observed in the region of the plasma marked by the middle arrow. Induced velocity jets are formed in the region of plasma at the inner edge of the exposed upper electrodes, directed towards each other. At the higher voltage the plasma area at the inner edge of the exposed electrodes looks like a pair of sinks, entraining fluid and drawing it through the plasma region and ejecting it into the vertical jet between electrodes. At the higher voltage an interaction between vertical jets is clearly observed producing streamwise vortical structures in between the vertical jets. No effort to optimize the electrode configuration was made, but this type of spanwise configuration of vertical jets has great potential as a flow effecter due to the potential for generating three-dimensional vorticity and boundary layer instability.

The arrangement of Figure 4.6 produces a tangential wall jet and was discussed in detail in Section 1.4.1.

4.2.2. Flowfield

Data was taken at four different Reynolds numbers with a focus here on performance at Re = 5 x 10^4, and Re = 1.0 x 10^5. At the lower Reynolds number the laminar boundary layer separates and large eddies are formed in the separated shear layer; the flow however, does not fully reattach. At the higher Reynolds number the boundary layer separates then transitions to turbulent and reattaches. The closed separation bubble sheds vortices which travel down the suction surface to the trailing edge. The large scale Kelvin-Helmholtz instabilities that develop in the separated shear layer lead to periodic vortex shedding observed in Figure 4.7. Previous analysis has shown that time averaged measurements of the laminar separation look very similar to measurements of a traditional laminar separation bubble (Lin and Pauley 1996, Selig and McGranahan 2004).
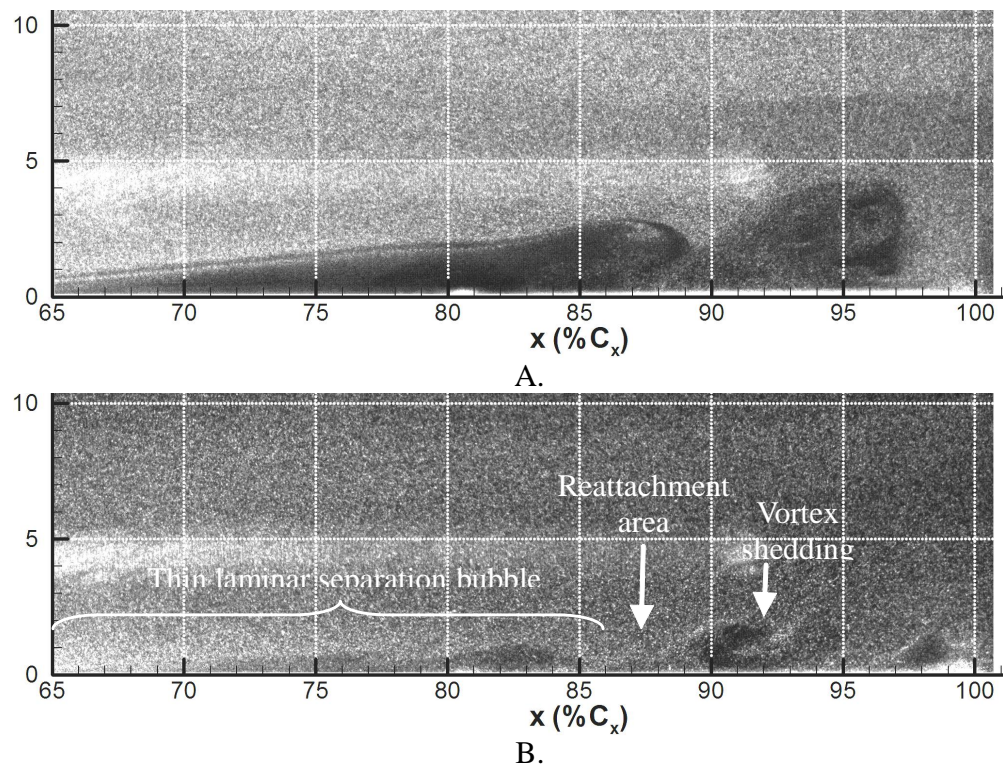
Figure 4.7 Flow visualization over the E387 suction surface from C_x = 67% to trailing edge with DBD-01 installed. Image A is at Re = 5 x 10^4. Image B is at Re = 1.0 x 10^5.

Figure 4.8 shows the suction surface C_p distribution with each plasma actuator installed at each Reynolds number tested along with inviscid results obtained in XFOIL. The C_p distribution is consistent across each plasma actuator installed with regard to the presence of laminar separation without reattachment at Reynolds numbers tested below 6.0×10^4, and laminar separation with reattachment for Reynolds numbers tested equal to 1.0×10^5 and higher. Differences between the C_p profiles include a higher peak C_p for DBD-01 as compared to DBD-02 and DBD-03, with DBD-03 having the lowest peak C_p. In addition,
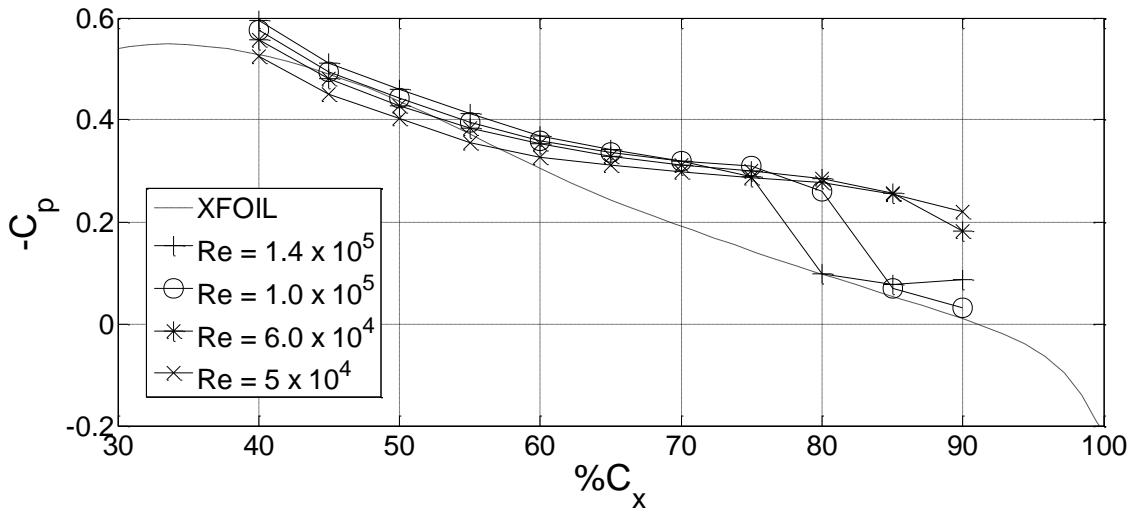
A.
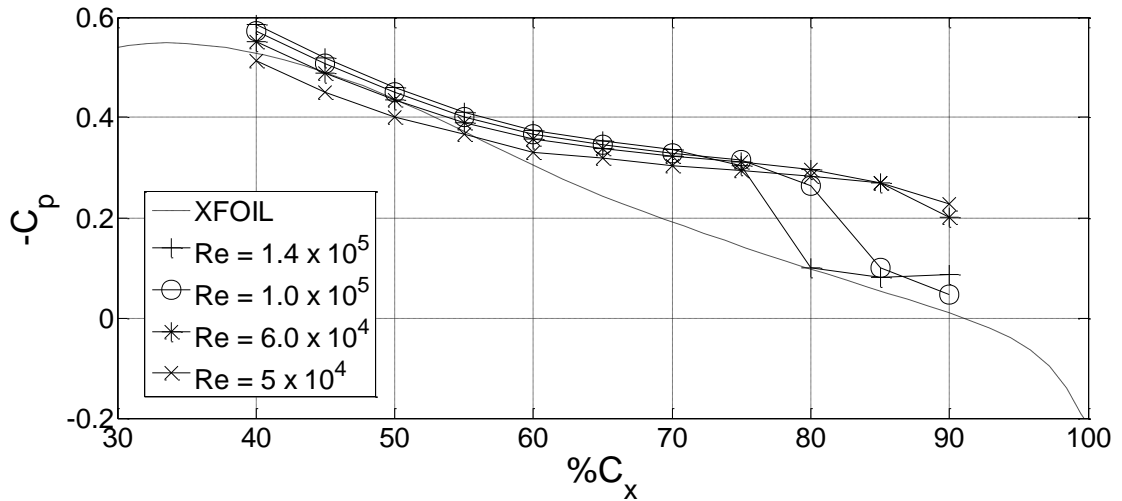
B.
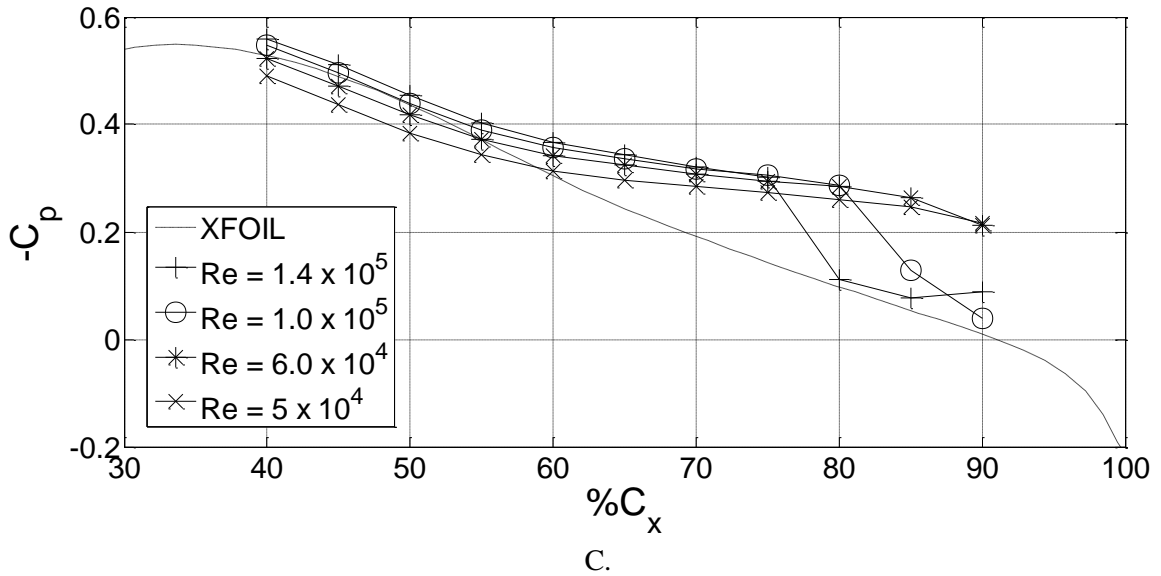
Figure 4.8 Suction surface C_p distribution with plasma actuators powered off. Plot A: DBD-01, B: DBD-02, C: DBD-03.

C_p plots indicate a difference in reattachment location for the three different plasma actuators tested. This difference is most noticeable in the C_p plot of DBD-03 at Re=1.0×10^5 in which the reattachment point noticeably shifts downstream 5% axial chord to $C_x \approx 90\%$. It is important to keep in mind the spatial resolution of C_p data due to the limited amount of pressure taps. The S3F displacement field vector plots of Figure 4.12 indicate that the reattachment point is not uniform along the span, so a discrepancy of several percent axial chord is not unexpected. The difference in max C_p is likely due to the shift in mean reattachment location. The difference in data for each case is presumably due to two things: variation in the quality of installation of each plasma actuator, and the possibility that the electrode geometry caused small scale perturbations in the laminar boundary layer.

A summary of the separation and reattachment locations (extracted from C_p data) is provided in Figure 4.9 for each plasma actuator configuration tested.
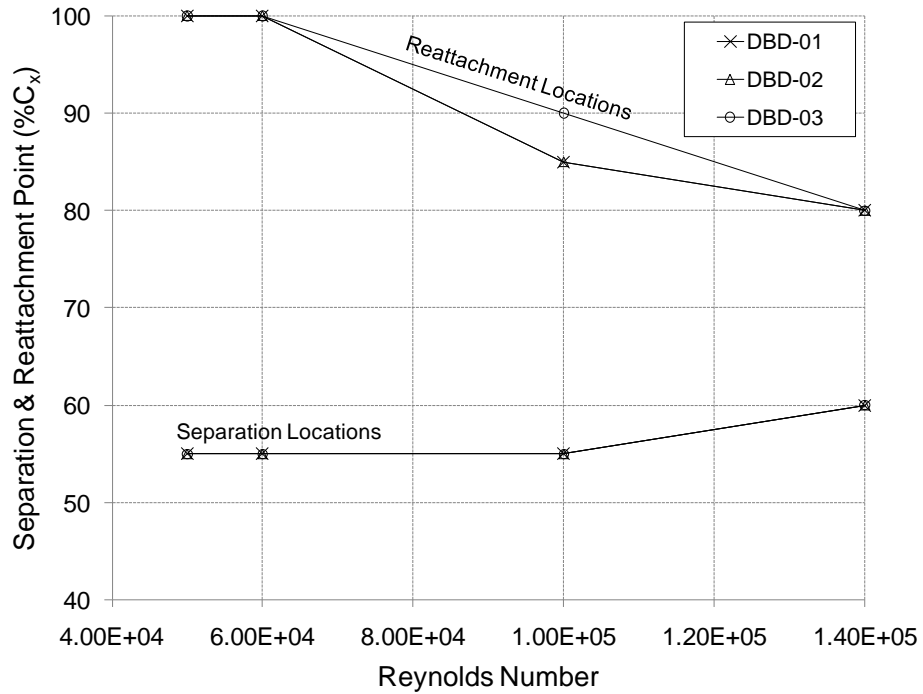
Figure 4.9 Mean suction surface separation and reattachment points for each plasma actuator configuration tested powered off.

4.2.3. Results at Re = 5 x 10⁴

C_p and wake profile plots for each plasma actuator tested at a Reynolds number of 5×10^4 are shown in Figure 4.10 and Figure 4.11 respectively. A range of input voltages are shown in each plot. DBD-01 and DBD-02 drastically improve the surface pressure distribution with the time averaged measurements. With DBD-01 the highest actuator voltage flattened out the pressure plateau indicating a reduction in separation bubble length, but the pressure coefficient near the trailing edge did not recover to the inviscid profile. Operation of the plasma actuator has changed the loading on the airfoil suction surface. A similar trend was observed with DBD-02, except flattening of the pressure coefficient occurred at a lower voltage. Powering on DBD-03 resulted in a movement of the reattachment point upstream, but with a much less significant change in pressure coefficient compared to the first two plasma actuators.

Powering on each actuator resulted in a significant narrowing of the airfoil wake. The wake of DBD-01 decreased in width as input voltage increased to 5.6 kV_{pp}, and then increased width as

voltage was amplified further. As the voltage of DBD-02 was increased beyond 4.2 kV$_{pp}$ the

wake gradually increased in width up to a voltage of 5.6 kV$_{pp}$. At input voltages above 5.6 kV$_{pp}$

the wake began to narrow at its base with a significant increase in peak velocity deficit.

Increasing the voltage of DBD-03 did not decrease the wake considerably beyond the lowest

input voltage applied.

a.) DBD-01

b.) DBD-02

116
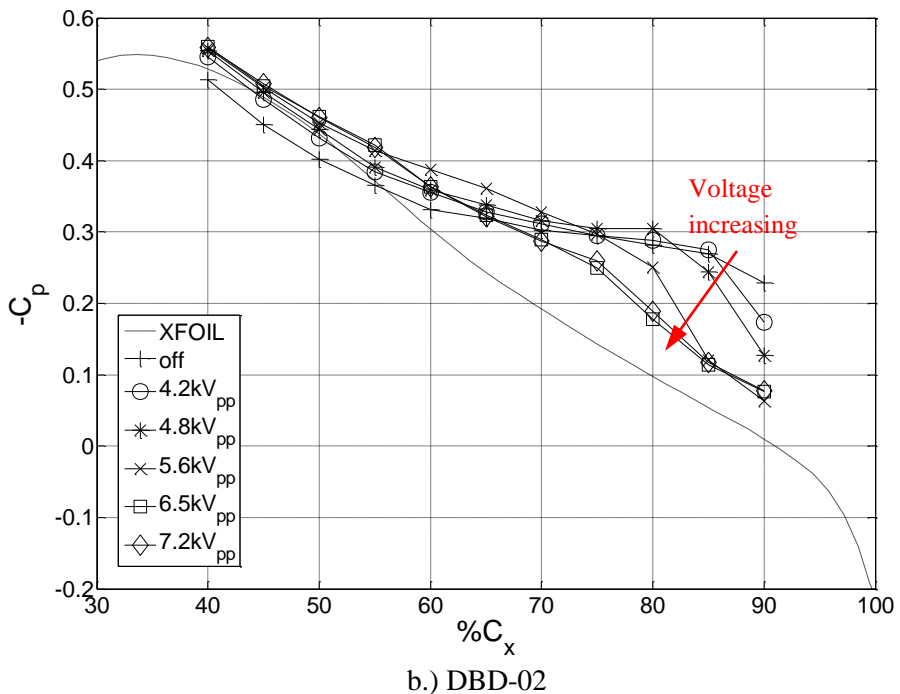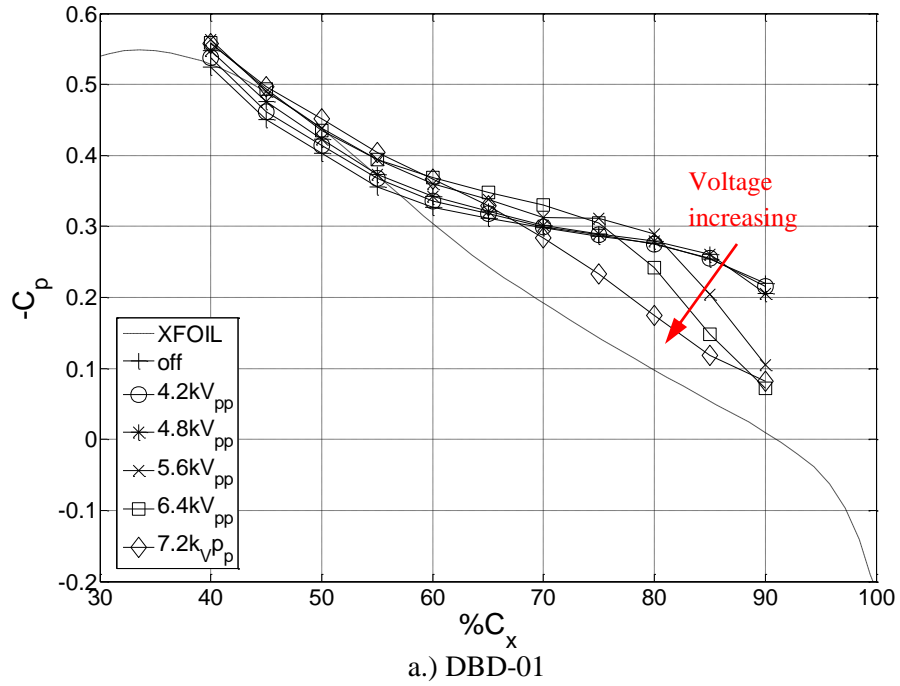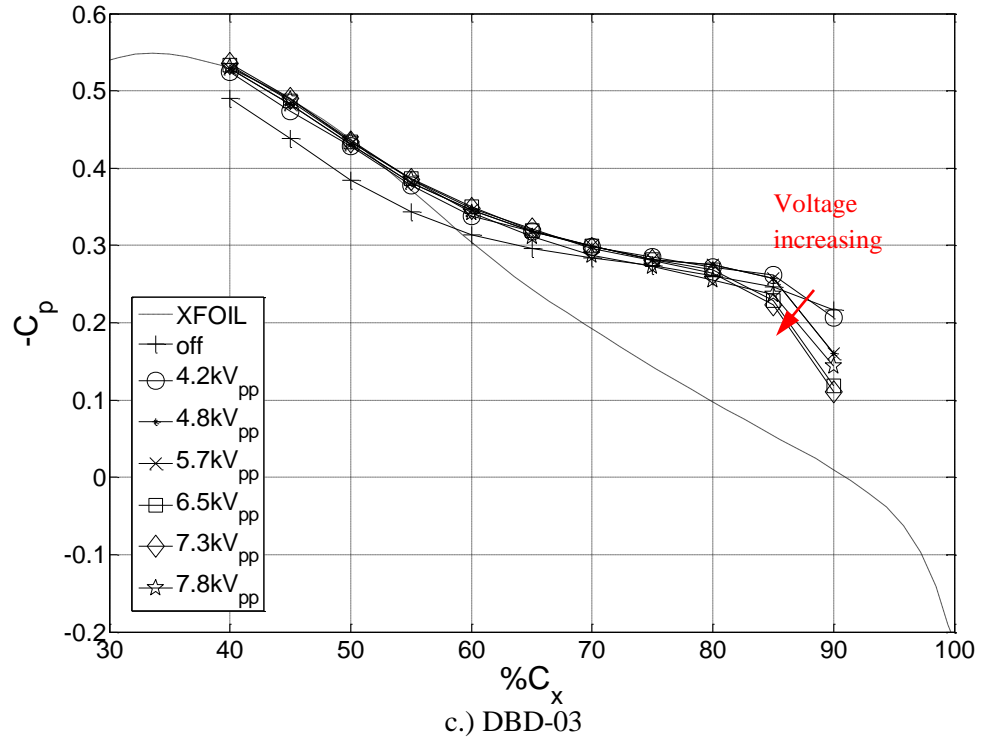
c.) DBD-03

Figure 4.10 Suction surface Cp distribution for each plasma actuator tested at 5 x 10^4.

a.) DBD-01

117
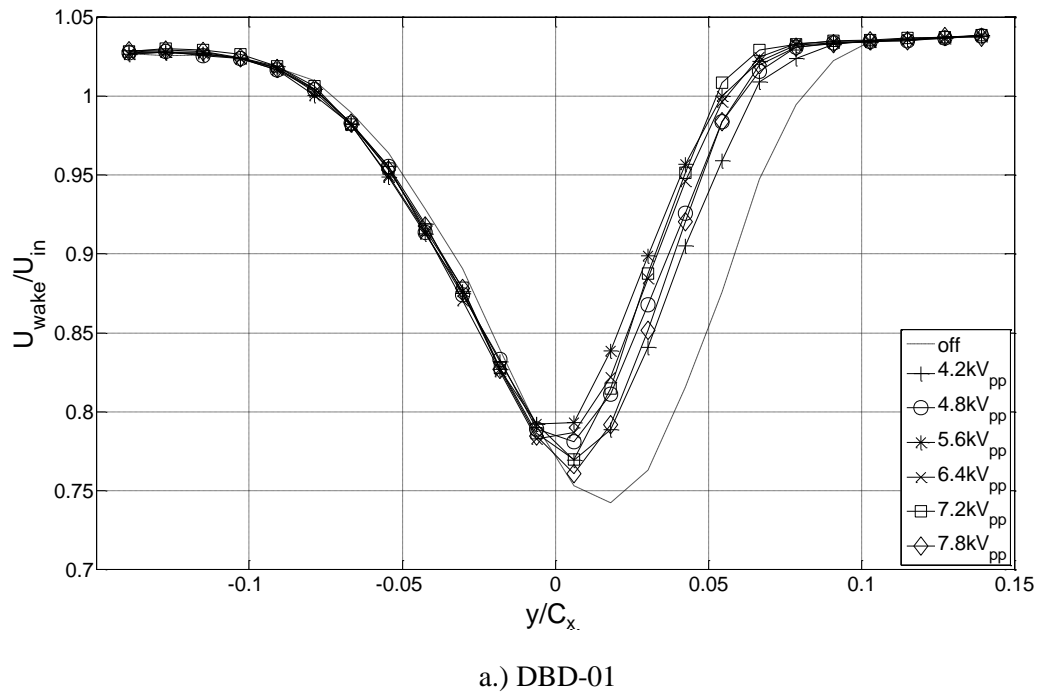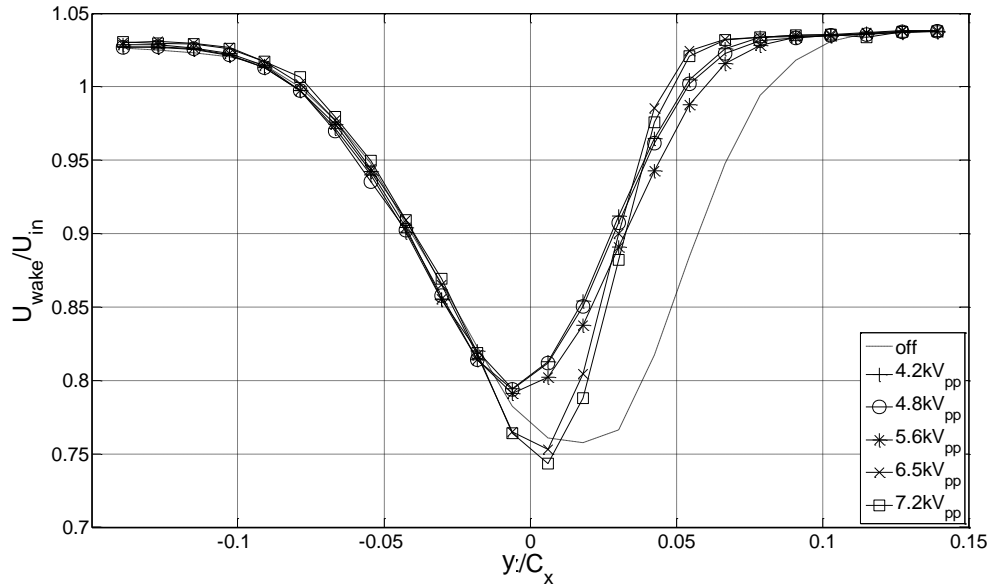
b.) DBD-02
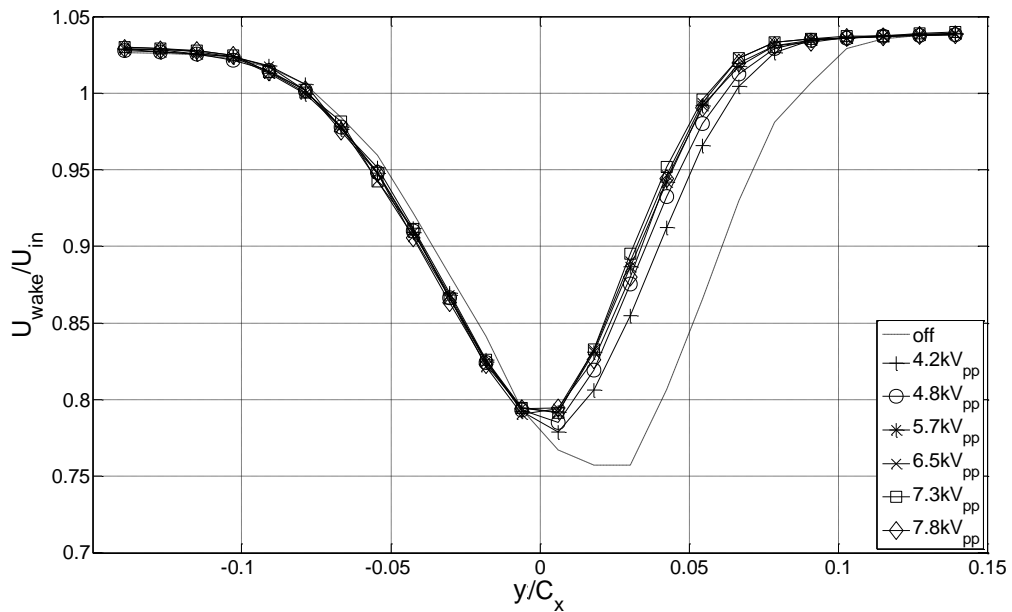
c.) DBD-03

Figure 4.11 Wake profile for each plasma actuator tested at 5 x 10^4.

The use of S3F allows a unique view of the surface tangential displacement which directly corresponds to surface shear stress direction. Figure 4.12 is a series of mean surface tangential displacement vector plots obtained from S3F for DBD-01 actuator off and a range of applied plasma actuator voltage. The plots clearly show the effect of the plasma actuator. For actuator

off conditions a strong reverse flow vortex is present at the trailing edge of the airfoil with a dead air region of separated flow just upstream from the vortex. As the plasma actuator is turned on the reverse flow vortex gradually shifts upstream with increase in voltage. There is a significant upstream shift and movement of the reverse flow vortex out of the view at the highest applied voltage of 7.2 kV_{pp}. At the highest voltage the mean flow appears to be reattached at $C_x \approx 93\%$ indicated by a zero crossing and downstream pointing displacement vectors. Figure 4.13 shows mean S3F tangential streamwise displacement for each plasma actuator tested at a spanwise location at $z = 5.5\% C_x$ (reference views in Figure 4.12).

From data in Figure 4.10 - Figure 4.15 the following conclusions are made for operation at Re=5 x 10^4:

DBD-01 – array of cross stream jets:

- Narrowing of the wake when the actuator is turned on indicates a decrease in drag and decrease in separation angle

- Mean S3F streamwise displacement in Figure 4.12 indicate that boundary layer reattachment and subsequent decrease in separated region does not occur until an applied voltage of 5.6 kV_{pp} and higher.

- C_p measurements agree with S3F in that there is no reattachment and/or minimal shift in reattachment point until higher actuator voltages are applied.

DBD-02 – array of vertical jets:

- C_p, S3F, and wake profile data all indicate that DBD-02 has a much larger effect on the flow at lower applied voltages compared to DBD-01.

- The reverse flow vortex moves upstream several percent chord when the plasma actuator is turned on at the lowest voltage. This is an improvement over DBD-01 and implies that the separated boundary layer is reattached or nearly reattached at the trailing edge at a voltage of 4.2 kV_{pp}. When the voltage is increased to 5.6 kV_{pp} the mean flow is clearly reattached as shown in the C_p and S3F data.
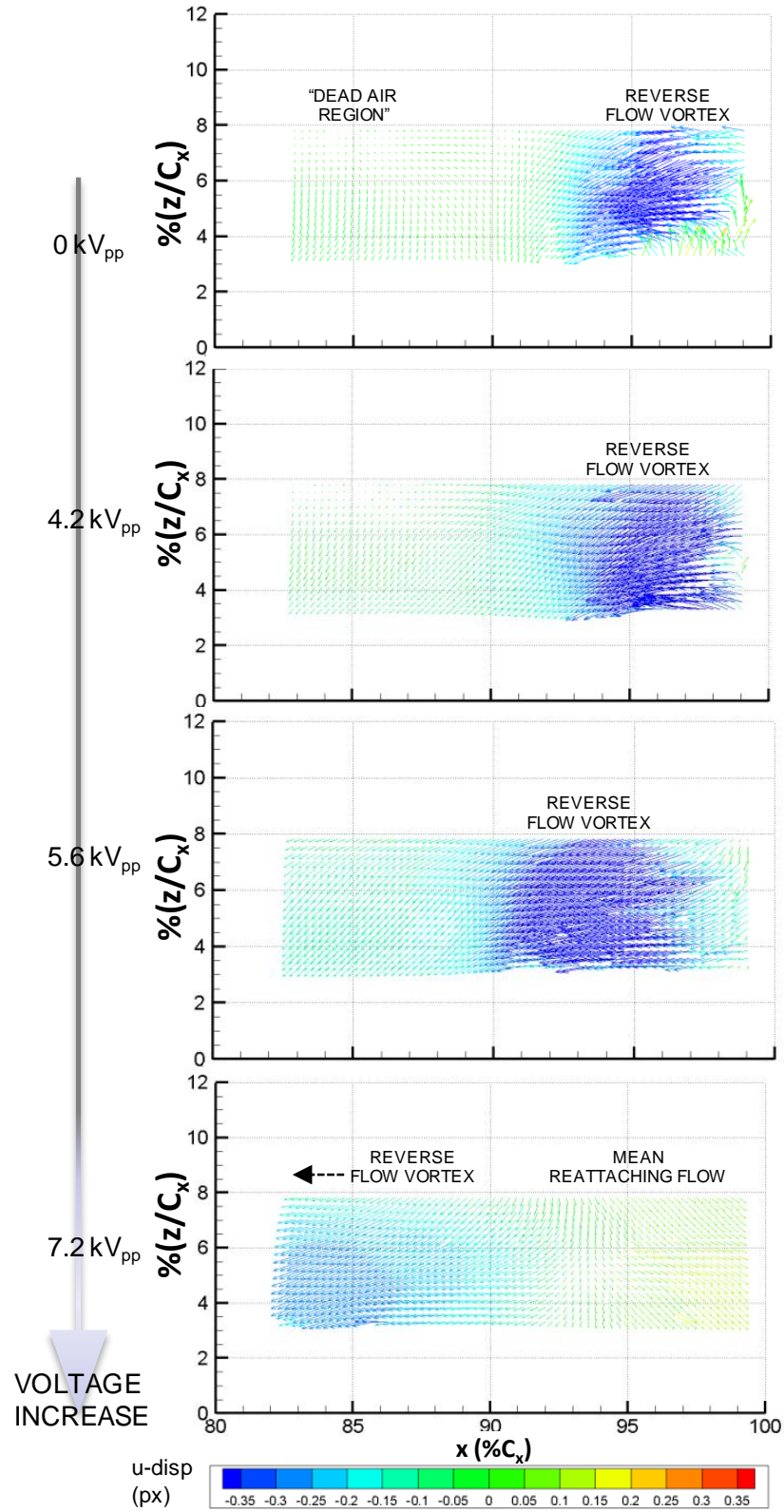
Figure 4.12 S3F measured surface tangential displacement of airfoil with DBD-01 installed. Flow speed is Re = 5 x 10⁴ with various plasma actuator voltages
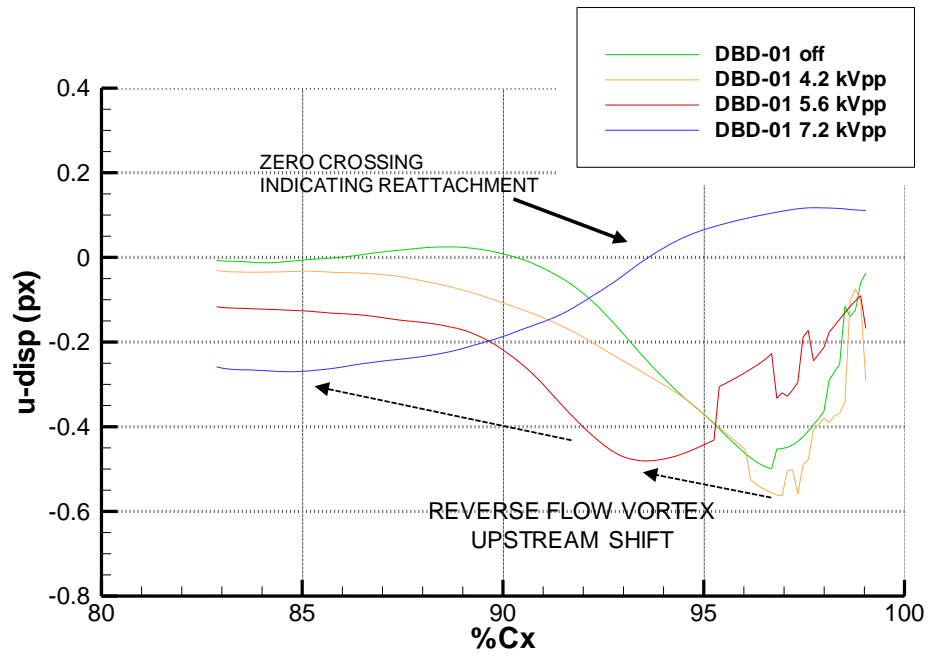
Figure 4.13 S3F streamwise disp. of DBD-01 at Re = 5 x 10^4 & various plasma actuator voltages.
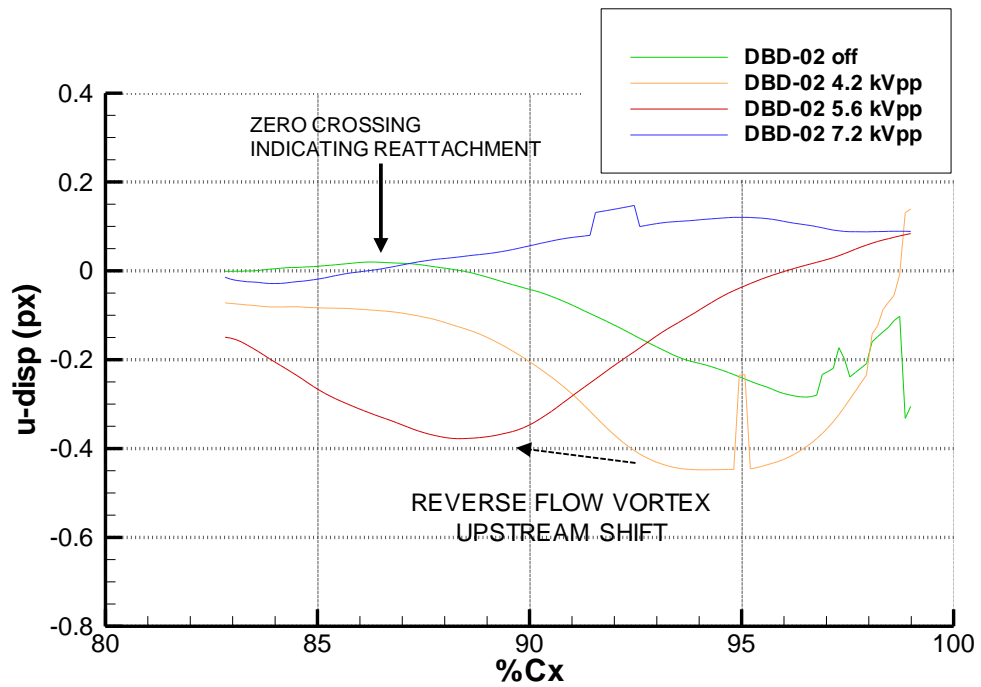
Figure 4.14 S3F streamwise disp. of DBD-02 at Re = 5 x 10^4 & various plasma actuator voltages.

121
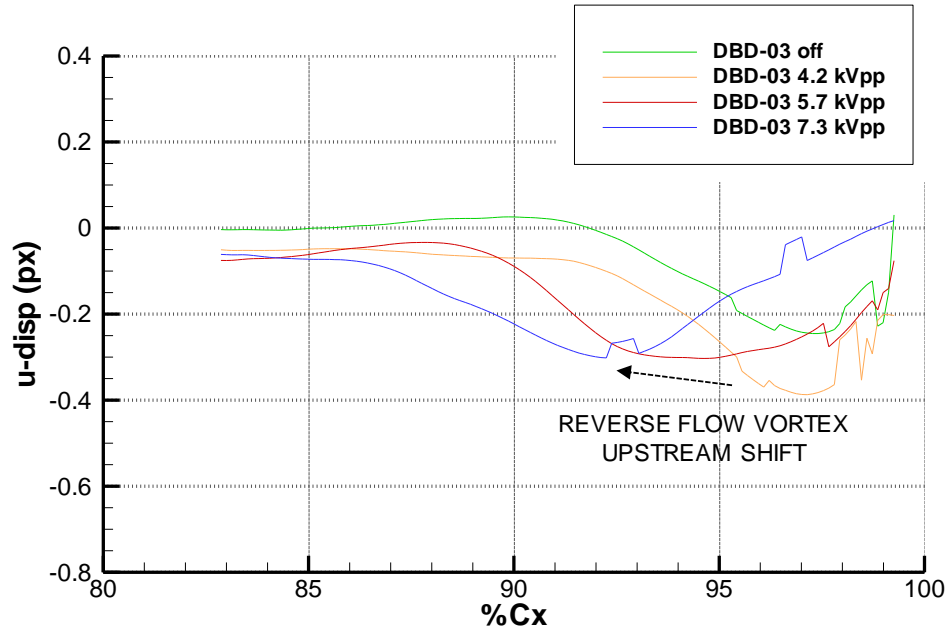
Figure 4.15 S3F streamwise disp. of DBD-03 at Re = 5 x 10^4 & various plasma actuator voltages.

DBD-03 – downstream jet:

- DBD-03 has the least significant change in C_p distribution and S3F streamwise displacement when the actuator is turned on and voltage is increased.

- Decrease in wake profile at the lowest plasma actuator voltage indicates that there is an effect on the separated flow by the actuator.

4.2.4. Results at Re = 1.0 x 10^5

Figure 4.16 shows C_p profiles at Re = 1.0 x 10^5 for which there is laminar separation with reattachment when the actuator is powered off. The C_p profiles for each plasma actuator show an effect on suction surface C_p distribution when the actuator is turned on. The wake profiles (omitted here) however, show no decrease in wake width or depth with actuation; instead they remain constant or grow wider.

When the actuator is powered on the mean reattachment point gradually moves upstream as much as 5%C_x for DBD-01. The plateau region of the C_p distribution is flattened as voltage is

increased for DBD-02 and DBD-03, first with a shift upstream of the reattachment point, then overall smoothing of the pressure gradient. As the pressure coefficient in the separated region is smoothed out the pressure profile does not approach the inviscid profile, instead it is lower. The S3F streamwise displacement in Figure 4.18 agrees with the C_p distributions in that there is a larger shift in reattachment point caused by DBD-02 and DBD-03, than for DBD-01. In fact, based on S3F data at the trailing edge and C_p data, the mean flow reattaches far upstream of C_x=80% for DBD-02 with an applied voltage of 7.3 kVpp. This is a significant decrease in the extent of the mean separation bubble length. Earlier transition to turbulence with less dominance from large scale inviscid type instability and more viscous small scale turbulence in the boundary layer would support the increase in wake velocity deficit seen in DBD-02 at Re=1.0 x 10^5.

a.) DBD-01

123
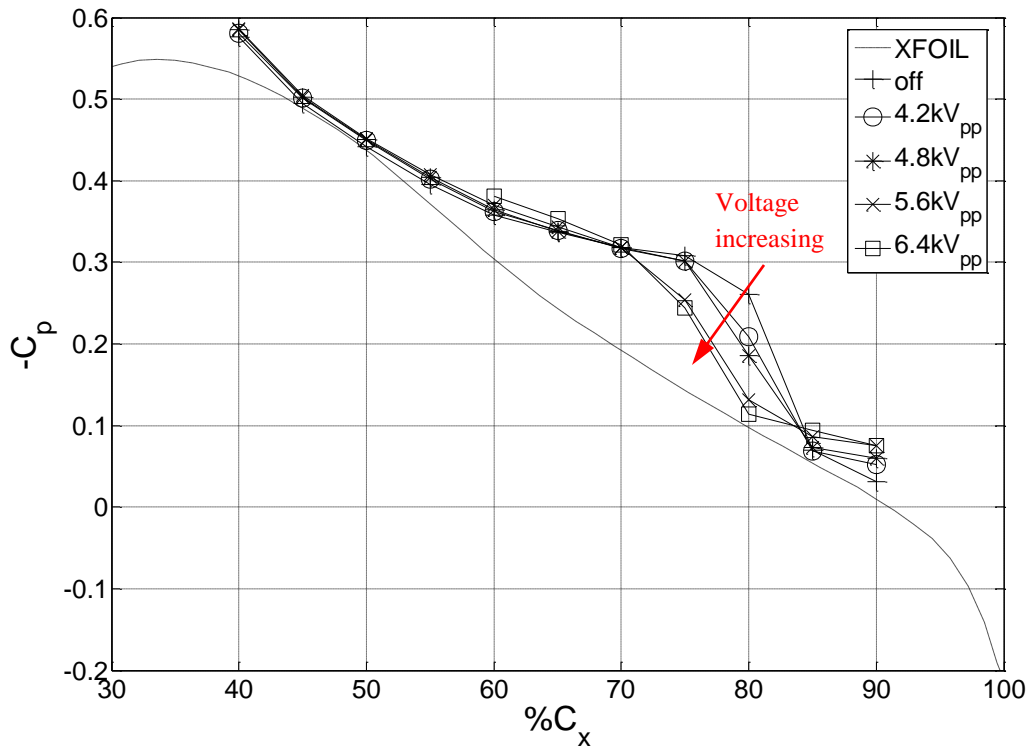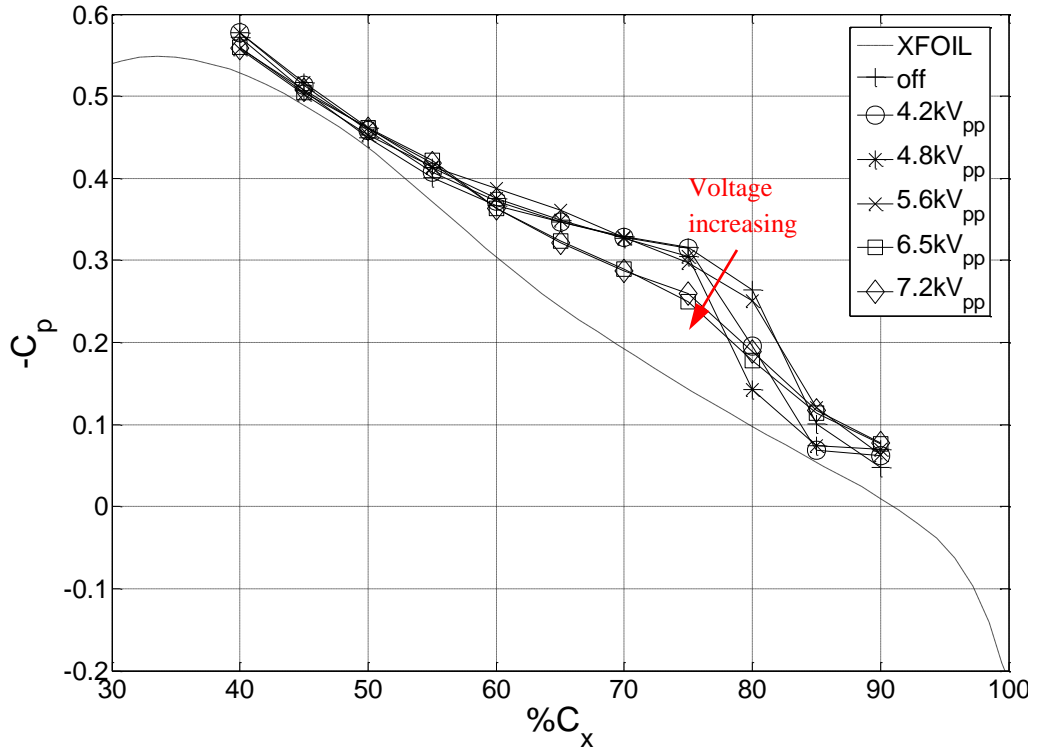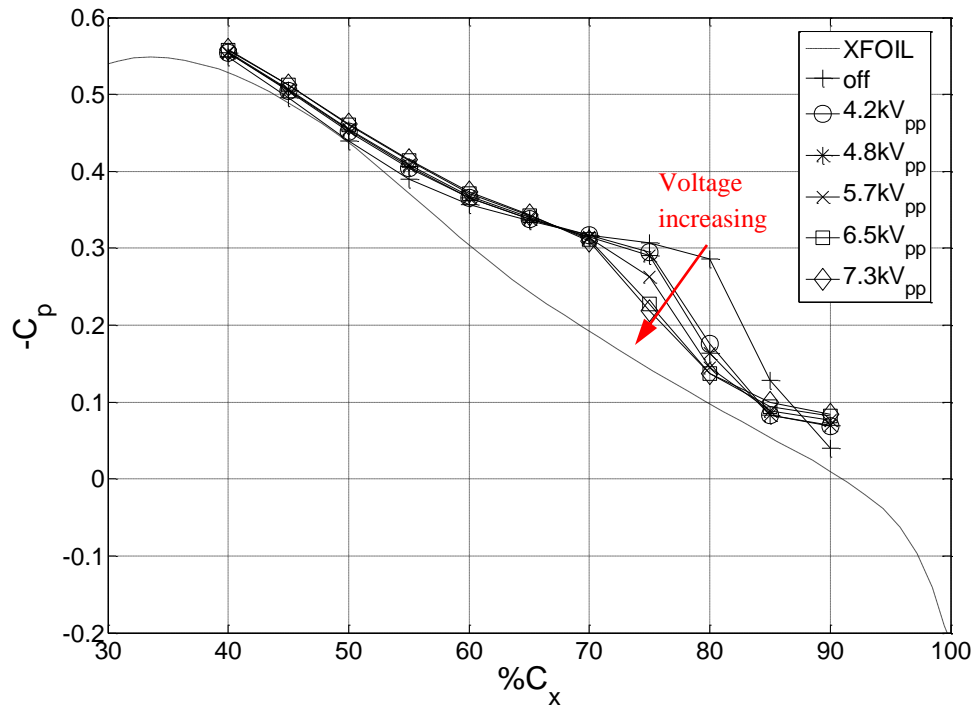
b.) DBD-02

c.) DBD-03

Figure 4.16 Suction surface Cp distribution for each plasma actuator tested at Re = 1.0 x 10^5.
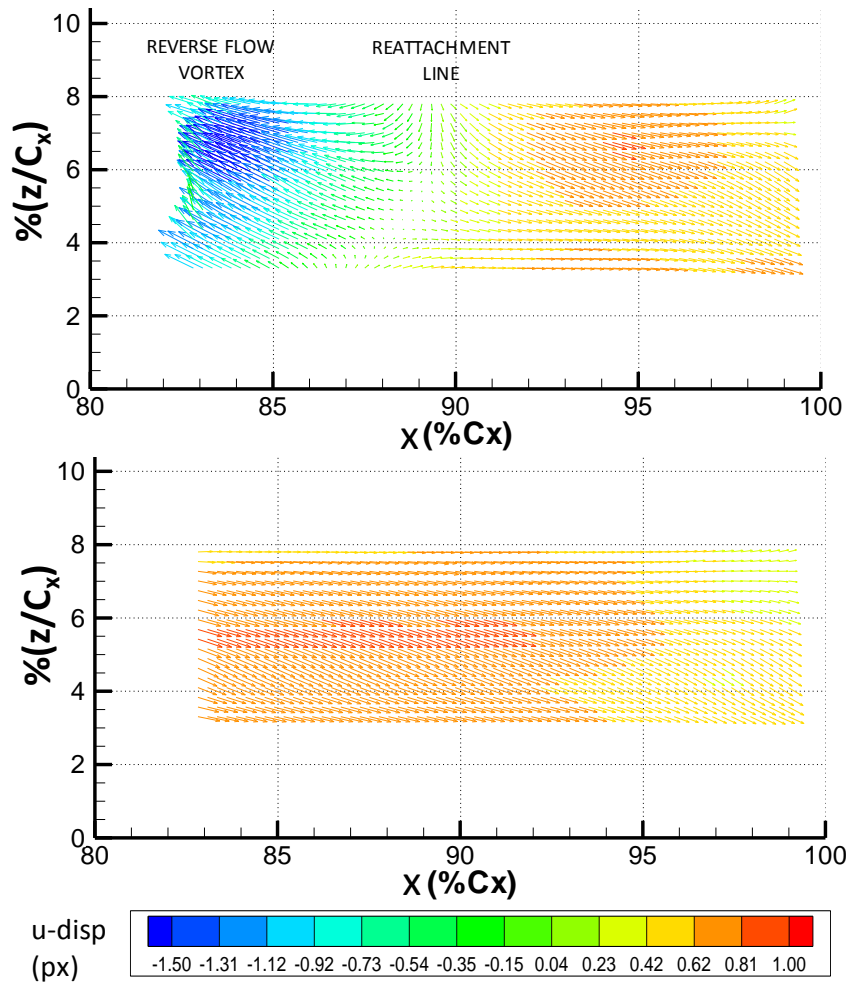
Figure 4.17 S3F tangential displacement of DBD-02 at Re = 1.0 x 10⁵ for Top: Actuator off, Bottom: 7.2 kVpp.

Based on the plots of Figure 4.16 - Figure 4.18 the following conclusions are made for operation at Re = 1.0 x 10^5:

- All three plasma actuators move the mean reattachment point upstream as voltage is increased.

- C_p data indicates an upstream shift in reattachment point for DBD-01 of at least 5% C_x. S3F data indicates an upstream shift in mean reattachment of nearly 4% C_x at the S3F midpoint, but the reattachment point is not uniform along the airfoil span.

- C_p data of DBD-02 shows a significant upstream shift in reattachment location as plasma actuator voltage is increased. The plateau in C_p that marks the separation bubble smoothes out significantly at a voltage of 6.5kVpp and above. The peak velocity deficit in the wake

increases with voltage. S3F data shows a significant upstream shift in mean reattachment location as the voltage is increased culminating with a reattachment point upstream of the view which ends at C_x=83%.

- Powering on plasma actuator DBD-03 shifts the reattachment point upstream with increases in voltage providing further upstream shift in reattachment. S3F indicates a nearly 8% upstream shift in mean reattachment point as voltage is increased to 7.3 kVpp.
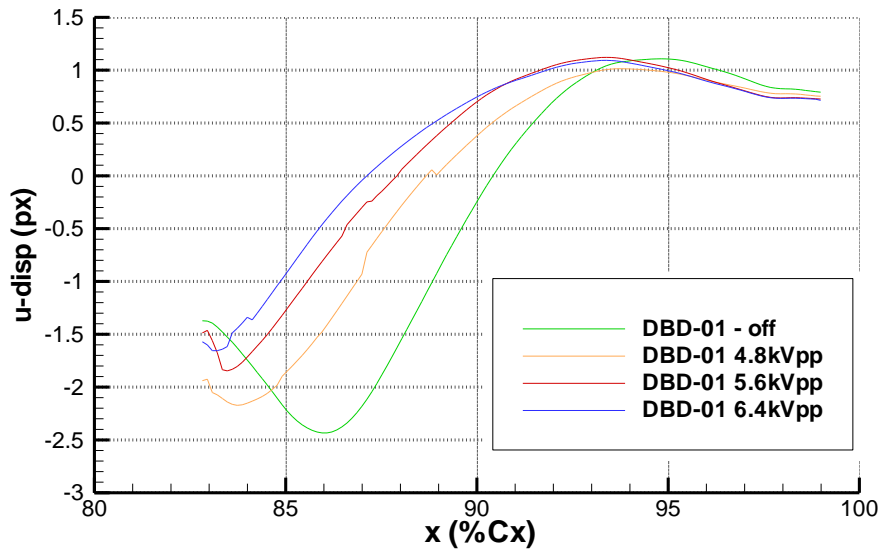
a.) DBD-01
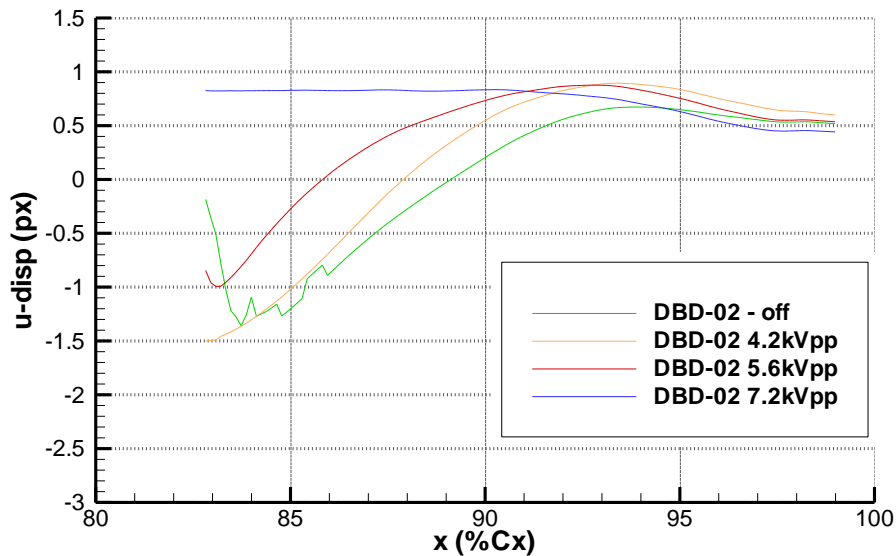
a.) DBD-02
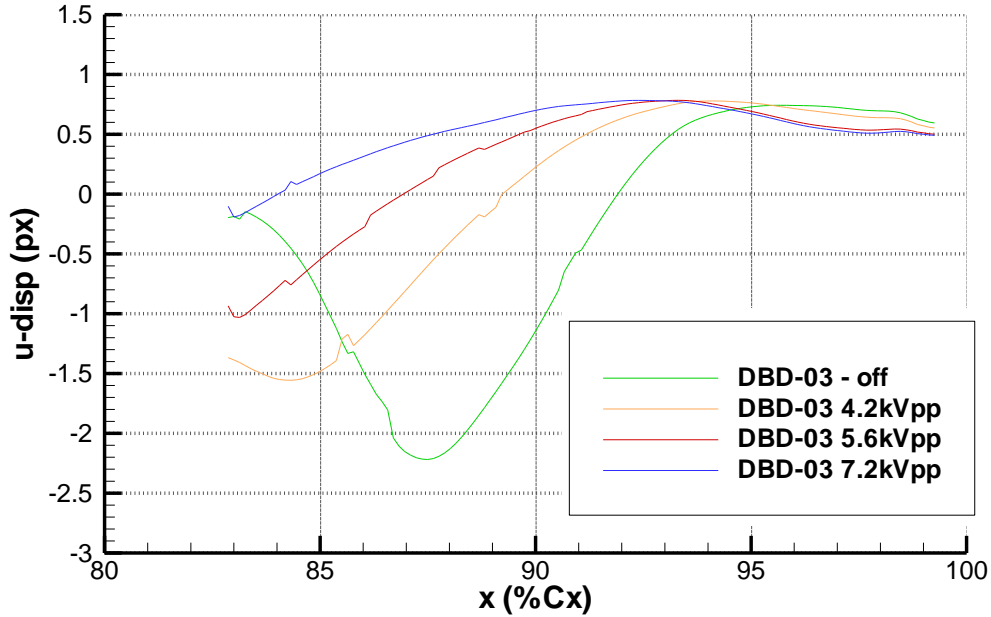
Figure 4.18 S3F tangential displacement at Re = 1.0 x 10^5 and various plasma actuator voltages.

4.2.5. Discussion

Each actuator clearly had an effect on suction surface laminar boundary layer separation as summarized in the plots of Figure 4.19 that show the S3F indicated mean reattachment points. At the lower Reynolds number 5.0x10^4 in which there was laminar separation without reattachment, powering on actuators DBD-01 and DBD-02 clearly resulted in a significant upstream shift in mean reattachment location. Electrode configuration DBD-02, the spanwise array of linear vertical jets led the actuators tested with reattachment at C_x=87%. This is confirmed by C_p data that shows significant smoothing of the plateau in pressure gradient that marked flow separation. DBD-03 did not definitively result in mean reattachment at the highest voltage tested, but did result in a significant decrease in wake width when the actuator was powered.

A. Re= 5×10^4 B. Re = 1.0×10^5
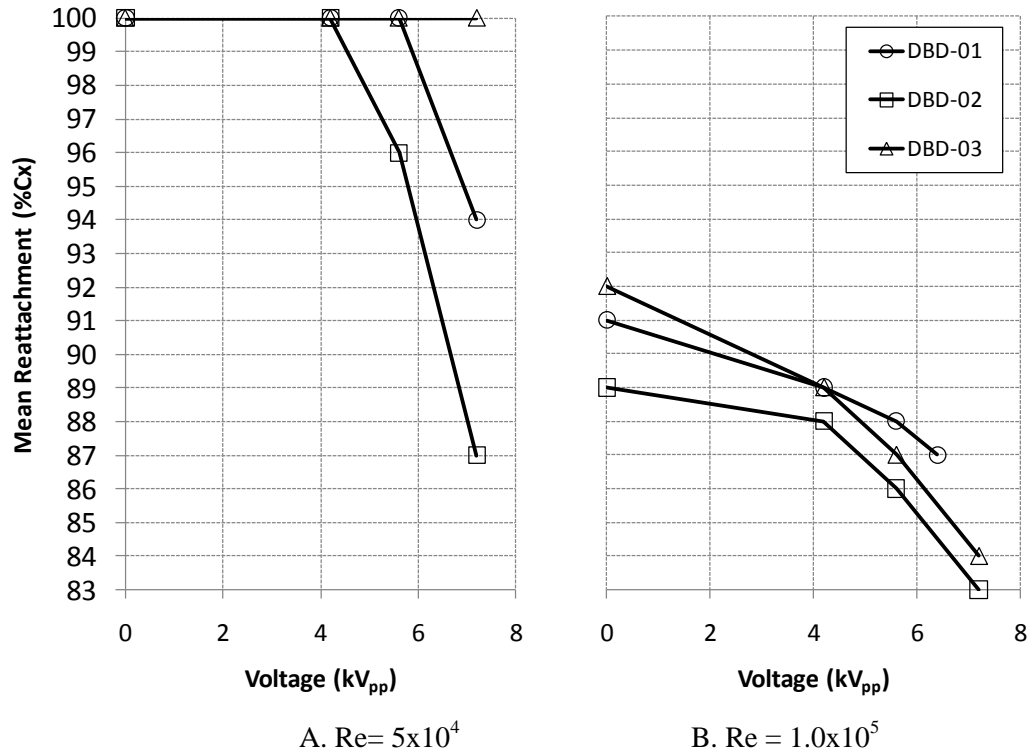
Figure 4.19 S3F indicated shifts in mean reattachment locations with increase in voltage

At the higher Reynolds number, 1.0×10^5, laminar boundary separation with mean reattachment

was present with the plasma actuator off. In these flow conditions powering on DBD-03

significantly shifted the mean reattachment line upstream $8\% C_x$. Less of an upstream shift was

observed for DBD-01, the spanwise array of cross stream jets, however S3F data was not

obtained at 7.2kVpp to compare to the other actuators, and further upstream shift may have

resulted. Electrode configuration DBD-02 had the largest apparent effect with an S3F indicated

shift in mean reattachment point beyond the field of view (reattachment at $C_x < 83\%$).

Drag data is presented in Figure 4.20 for each actuator tested. Powering on each actuator

resulted in a decrease in drag at Re = 5×10^4, with each actuator reaching a minimum drag value.

DBD-02, the spanwise array of linear vertical jets reached its minimum at the lowest plasma

actuator voltage, with a 33% reduction in drag. DBD-03 the downstream facing jet also had a

significant decrease in drag 30% at Re=5.0×10^4. At the Re=1.0×10^5 powering on the actuators did

not result in a decrease in drag. In fact the drag gradually increased with increase in voltage for

128

each actuator. This is most likely due to the increased length of turbulent boundary layer as the separation bubble decreases in length, resulting in no improvement in drag. The drag plot shown in Figure 4.20 also displays the difference in drag due to variation in the quality of installation of each plasma actuator on the airfoil. The airfoil with DBD-03 has the largest initial drag when the plasma actuator is powered off. For a fair comparison of drag reduction between actuators, the power dissipation should be considered. Each actuator configuration had different electrode dimensions, discharge length, and power dissipation across the span. An estimate of the discharge length for each configuration was provided in Figure 4.1. A summary of peak drag reduction and corresponding power dissipation compared to the baseline electrode configuration is listed in Table 4.1.

A. Re = 5 x 10^4

B. Re = 1.0 x 10^5
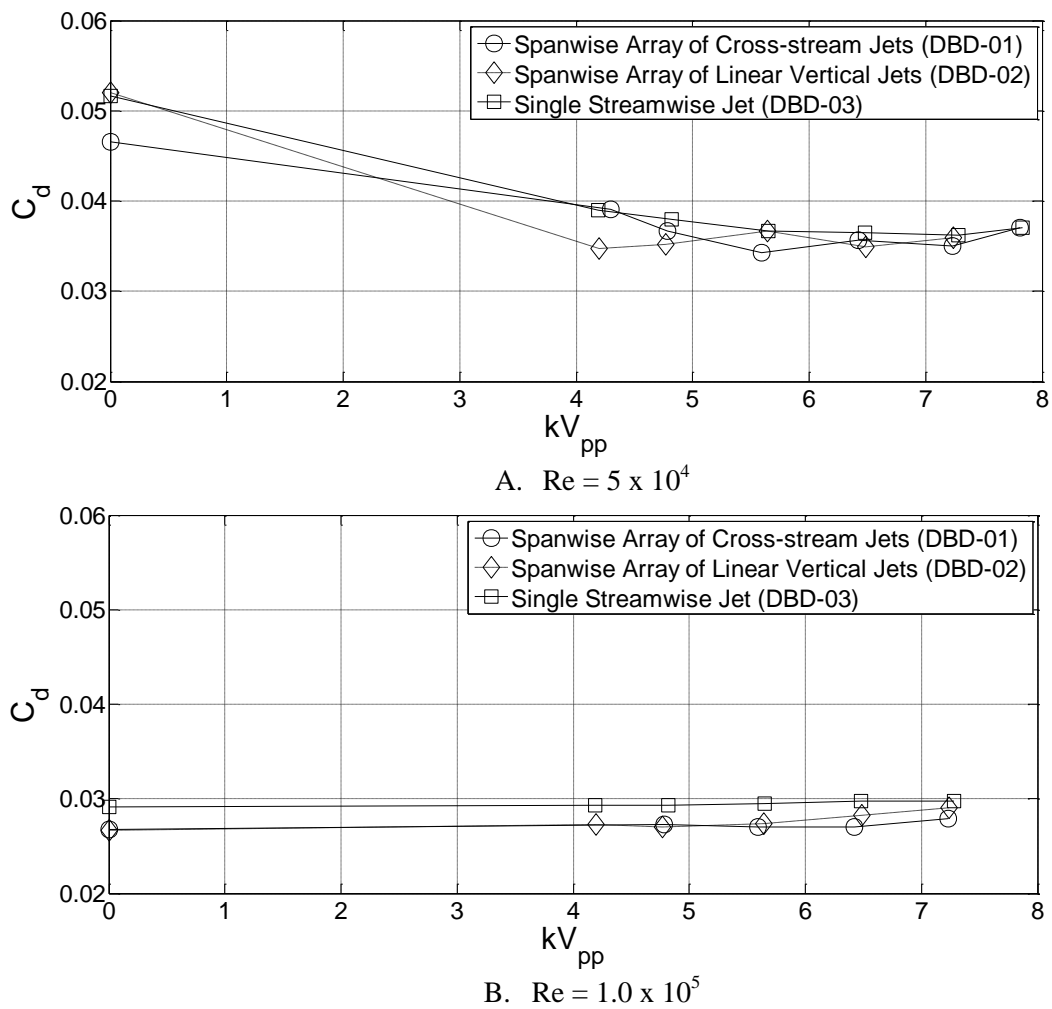
Figure 4.20 Section drag for each plasma actuator tested.

Table 4.1 Comparison of the peak drag reduction of each plasma actuator configuration at Re = 5 x 10⁴.

	Relative length	Voltage (kV$_{pp}$)	Change in C$_d$(%)	Change in Power vs. Baseline (%)
DBD-01	1.2	5.6	-27%	-51%
DBD-02	2.0	4.2	-33%	-70%
DBD-03	1.0	7.3	-30%	0%

Flow visualization images are shown in Figure 4.21-Figure 4.23 in order to further understand the effect of each actuator. Figure 4.21shows a large decrease in separation and boundary layer thickness as the actuator power is increased. At the lower actuator voltage a decrease in separation angle, and smaller, less dominate large scale inviscid structures in the separated shear layer are observed. At the higher voltage a thin separation bubble is formed. This explains the earlier minimum observed in drag. As the voltage increases past 5.6 kV$_{pp}$ and the separated boundary layer reattaches, no additional gains are made in drag due to increased turbulent boundary layer length.

a.)

b.).

c.)
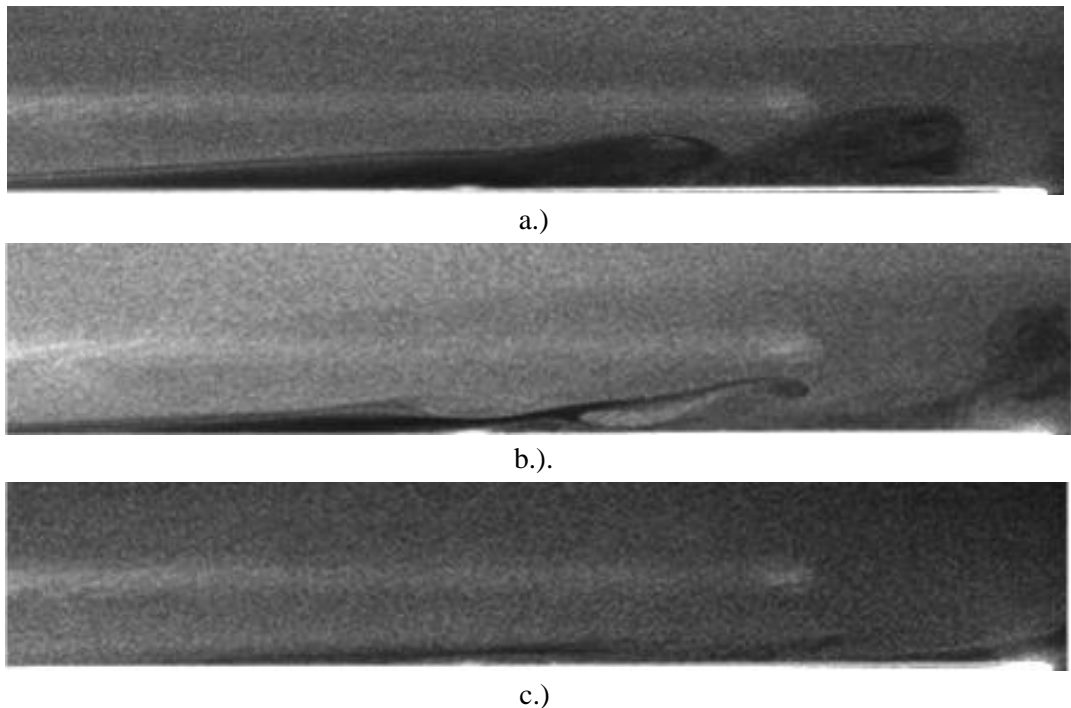
Figure 4.21 Flow visualization of plasma actuator DBD-01 at the trailing edge from C_x=65% to 101% at a Re = 5 x 10⁴. Image A: actuator off, B: 5.6 kV$_{pp}$, C: 7.2 kV$_{pp}$

In Figure 4.22 flow visualization in the area of the plasma actuator and boundary layer separation is shown. The actuator on image is very interesting and shows eddies formed downstream of the actuator. The laser sheet in this case was placed centered with one of the plasma actuator vertical jets. The eddies were only observed at the highest voltage tested 7.3 kV_{pp}. The linear vertical jet is aligned with the streamwise direction and is expected to introduce three dimensional vorticity by creating a local separation region. This bottom image in Figure 4.22 clearly shows that, at the least spanwise coherent eddies form entraining higher momentum flow from the freestream to the wall.
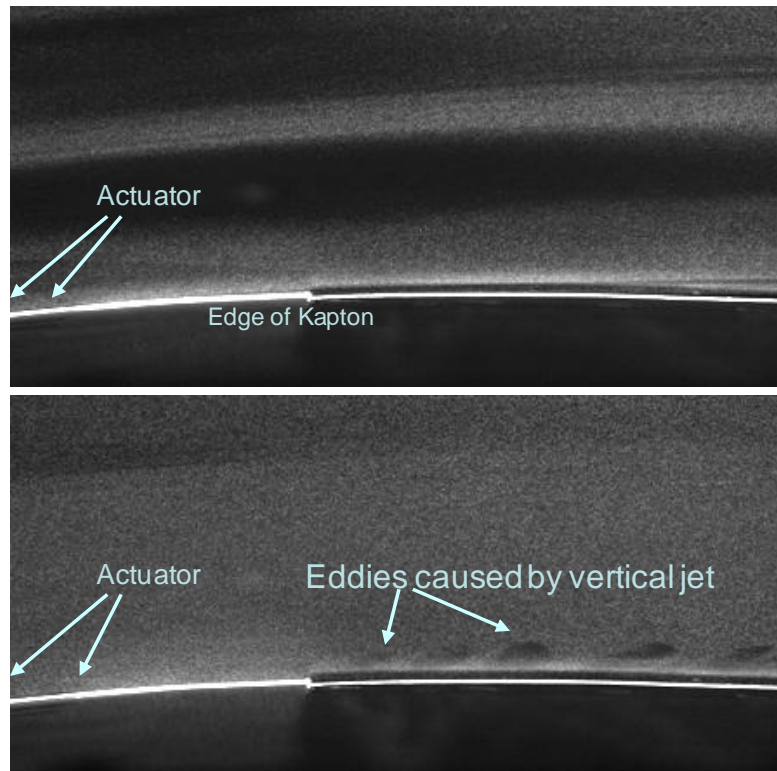
Figure 4.22 Flow visualization showing spanwise coherent unsteadiness generated by the vertical jets of DBD-02 with Re=5x10^4. Top: actuator off, Bottom: actuator voltage 7.2 kVpp. View is from approximately C_x=30% to 60%.
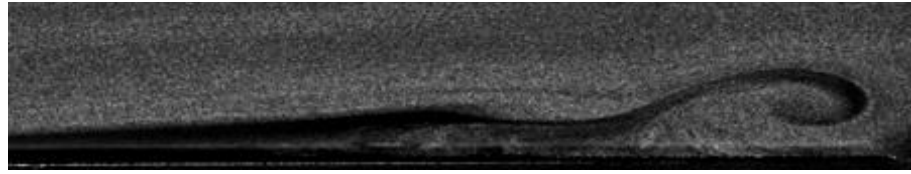
a.)
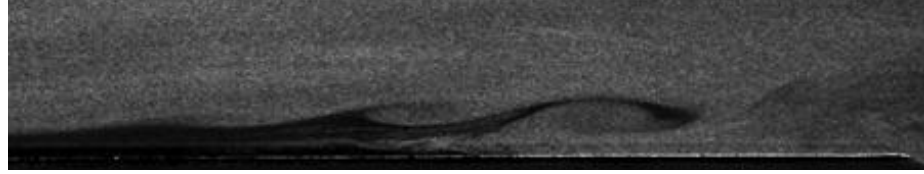
b.)
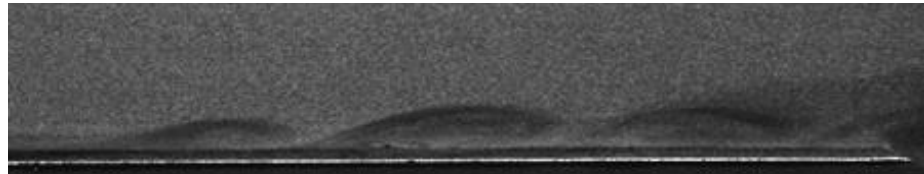
c.)

Figure 4.23 Flow visualization of plasma actuator DBD-03 at the trailing edge from C_x=70% to 101% at a Re = 5 x 10^4. Image A: actuator off, B: 4.8 kV$_{pp}$, C: 7.2 kV$_{pp}$.
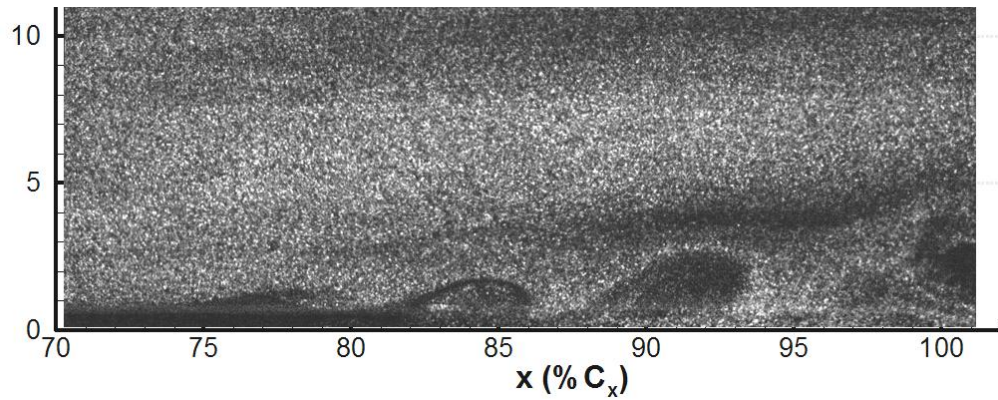
a.)
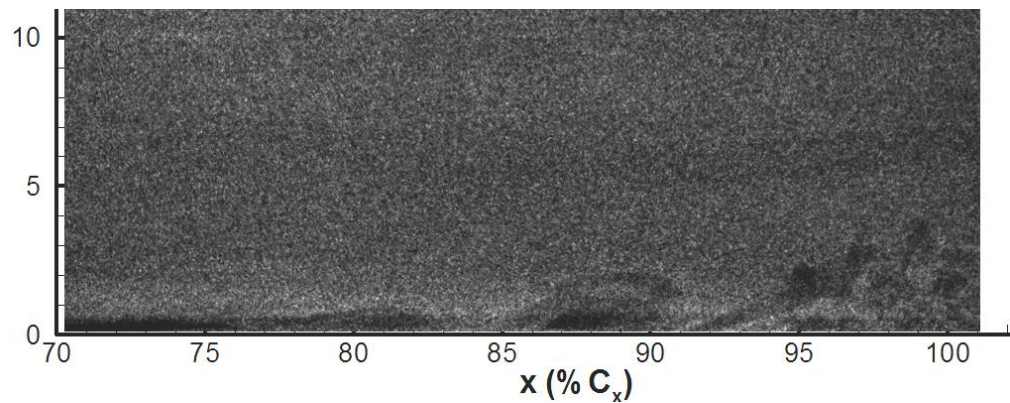
b.)

Figure 4.24 Flow visualization of airfoil with plasma actuator DBD-03 installed. Suction surface near trailing edge is shown at Re=1.0x10^5. Image A: actuator off, B: 7.3 kV$_{pp}$.

The effect of plasma actuator DBD-03 at the trailing edge is shown in Figure 4.23. This

plasma actuator was least effective at the lowest Reynolds number tested. The flow visualization

indicates that as voltage is increased the separated shear layer develops into a boundary layer with

large scale streamwise structures. This orientation acts as a wall jet entraining momentum from

the freestream and adding momentum to the boundary layer. The flow visualization in this study

indicates the configuration was less effective at promoting transition and reattachment of the

boundary layer. The large scale inviscid structures are maintained and do not appear to break up

into small scale structures. It did however, decrease drag by 30%. At the higher Reynolds

number of $Re=1.0x10^5$ in which a mean reattaching separation bubble was present in the actuator

off case, the plasma actuator DBD-03 was very effective at moving the reattachment point

upstream (see Figure 4.24).

5. Closed Loop System

Feedback closed loop separation control experiments are described in this chapter. S3F #6 was used as the separation control sensor, and a spanwise array of linear vertical jets generated by DBD plasma actuator (DBD-04) were used as the flow effecter. The plasma actuator electrode geometry was identical to DBD-02 and mounted at the same location on the airfoil. All data presented in this chapter was taken with the DBD-04 and S3F #6 installed on Airfoil 2. In some situations observations from the experiments presented in this chapter may be compared with measurements from other chapters.

5.1. Boundary Layer Flow Behavior

Examples of instantaneous flow visualization are shown in Figure 5.1 with the plasma actuator and S3F installed.   At a Reynolds number of 1.0×10^5 a laminar boundary layer separates, transitions to turbulent and reattaches. In the area of reattachment vortices are shed from the separation bubble and travel downstream along the boundary layer. The boundary layer reattachment location is approximately 85% C_x and which is further upstream than the measurements in Chapter 3 and 4. This is likely due to variation in the attachment of the plasma actuator to the airfoil.

At Re = 6.0×10^4 and below the boundary layer behavior is complex and very unsteady near the trailing edge as was discussed in detail in Chapter 3. The boundary layer often did not reattach and large coherent eddies were observed convecting down the separated shear layer leading to instances of both reattached and separated boundary layer near the trailing edge.
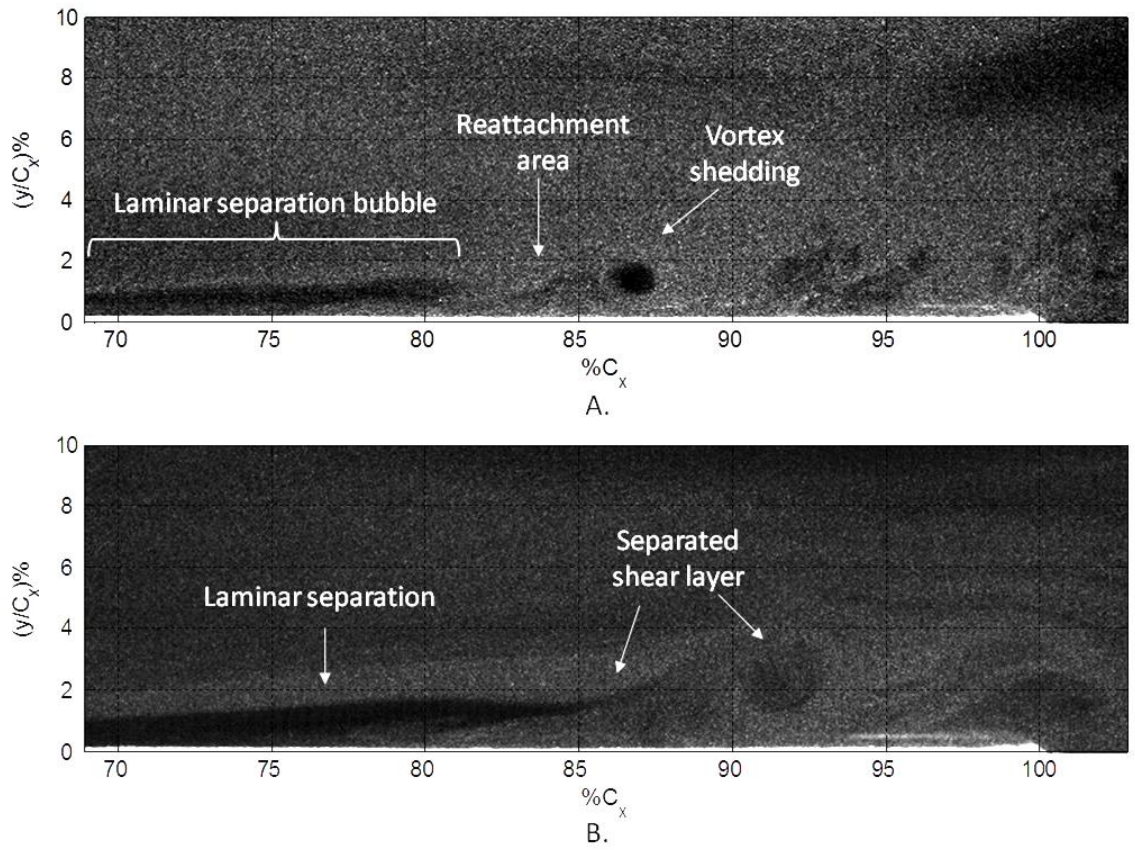
Figure 5.1. Flow visualization over the E387 suction surface trailing edge region with actuator installed and powered off. Image A is at Re = 1.0 x 10^5. Image B is at Re = 6.0 x 10^4.

Mean static pressure across the trailing edge region of the airfoil suction surface with the actuator installed is shown in Figure 5.2 for various Reynolds numbers compared to the inviscid solution calculated in XFOIL. The plateau in suction pressure gradient beginning near C_x=55% is characteristic of boundary layer separation. At a Reynolds number of 1.0×10^5 the pressure recovers in the vicinity of $C_x = 80\text{-}85\%$ which is characteristic of boundary layer reattachment. At the two lower Reynolds numbers, the mean reattachment point moves downstream towards the trailing edge, or does not reattach. The loading on the suction surface of the airfoil increases as Reynolds number increases. The reattachment points have moved upstream significantly compared to the open loop experiments. This is due to variation in attachment of the plasma

actuator. The plasma actuator was wrapped around the leading edge. Any change in the shape at the leading edge or a discontinuity could move the reattachment point upstream.
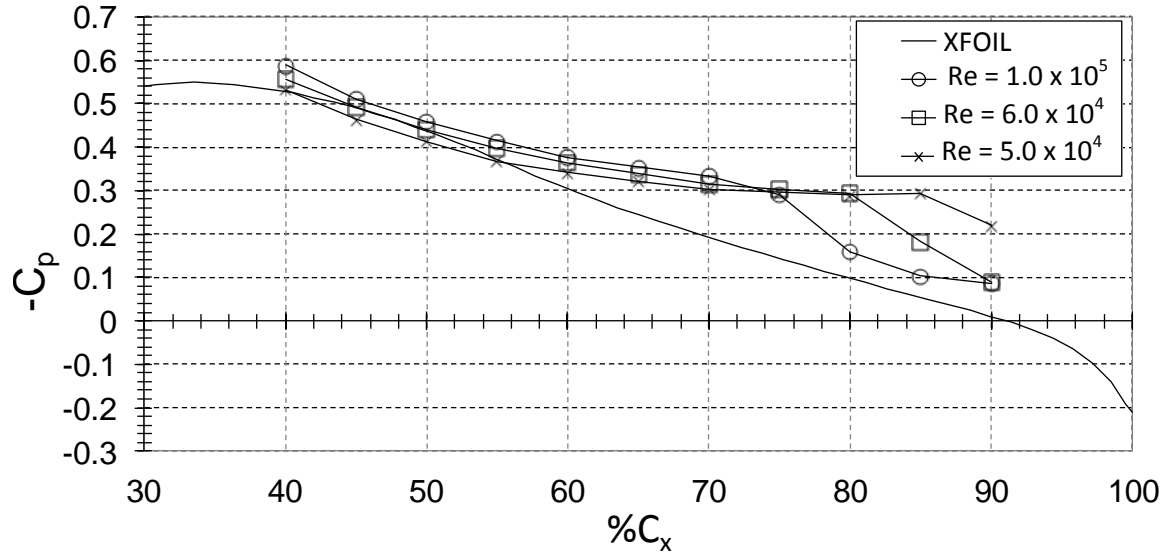
Figure 5.2. Example of Suction Surface C_p in the trailing edge region at various Reynolds numbers with actuator installed.

Mean velocity fields calculated by particle image velocimetry (PIV) are shown in Figure 5.3-Figure 5.4. The laser plane was at the top edge of the S3F. At least 500 images were used to calculate the mean fields. The mean reattachment point at a Reynolds number of 1.0×10^5 is between $C_x = 85$ & 90%. In contrast to observations made using instantaneous flow visualization, the boundary layer reattaches and forms a mean reattaching separation bubble at a Reynolds number of 6.0×10^4 with reattachment between $C_x = 90$ & 95%.
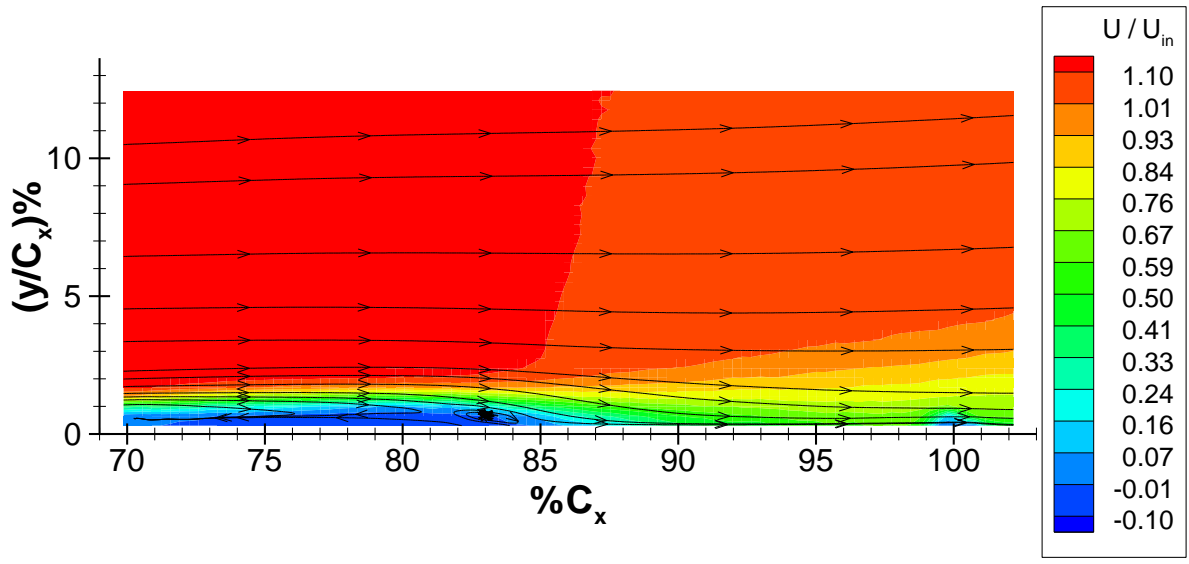
Figure 5.3. PIV mean velocity field at Re = 1.0×10^5 with plasma actuator off.
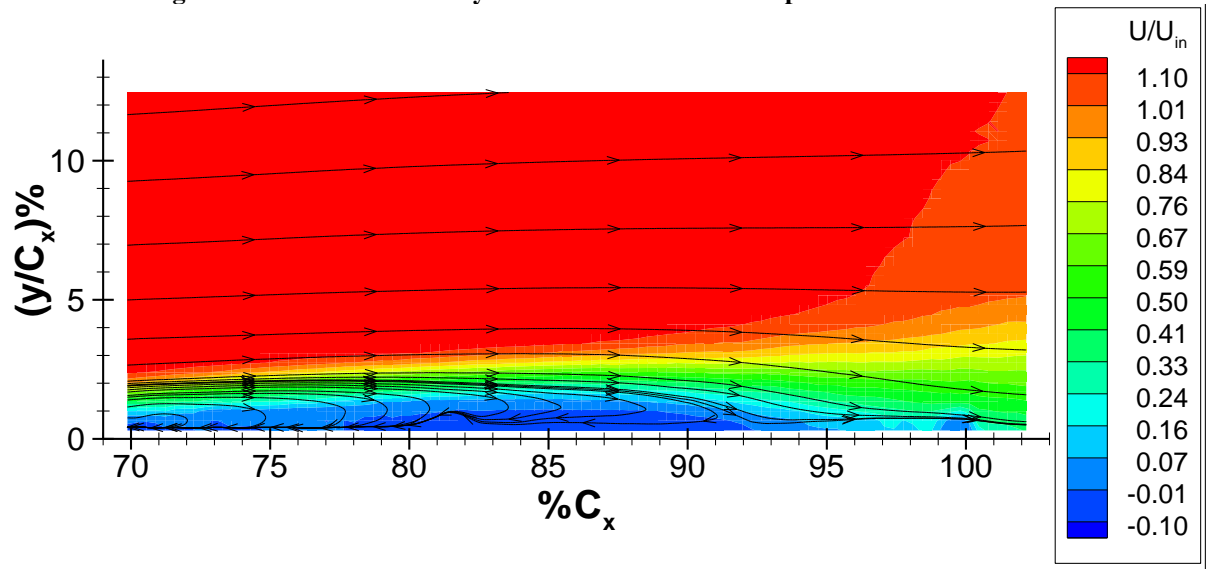
Figure 5.4. PIV mean velocity field at Re = 6.0×10^4 with plasma actuator off.

5.2. **Flow Effecter**

A spanwise array of steady linear vertical jets generated by a DBD plasma actuator was used as the flow effectors based on the results of the open loop control study. The control authority of the spanwise array of linear vertical jets was considered adequate for the current closed loop experiments over the entire Reynolds number range ($1.0 \times 10^5 – 6.0 \times 10^4$) considered here. The

actuator was mounted upstream of the separation point and consisted of 9 linear vertical jets

spaced 23.8mm on center and extending

approximately 20.3mm in the streamwise direction.

The actuator electrode geometry was identical to

DBD-02, and fabricated and installed using the same

method as was described in Chapter 4. For

consistency the data reported in this chapter has been

obtained using the same plasma actuator (DBD-04).

The mean velocity field obtained by PIV with the

actuators on at Reynolds numbers of 1.0×10^5 and

6×10^4 are shown in Figure 5.6 and Figure 5.7.

Comparing the actuator on images with the actuator

off images clearly shows an upstream shift in the mean

reattachment point and significant decrease in the

thickness of the separation bubble. In fact the

separation becomes so thin that it becomes difficult to

Figure 5.5. Plasma actuator configuration mounted in the wind tunnel.

identify a precise mean reattachment point. At a Reynolds number of 1.0×10^5 the plasma actuator

with an applied voltage of 6.4 kV_{pp} moves the mean reattachment point upstream approximately

5% C_x, from 86% to approximately $C_x = 81\%$. At the lower Reynolds number of 6×10^4 the

upstream shift in reattachment point is approximately 10% C_x from $C_x = 93\%$ to $C_x = 83\%$ with a

6.4 kV_{pp} voltage.

Mean boundary layer velocity profiles normal to the airfoil surface with the actuator powered

on and off are shown in Figure 5.8 and Figure 5.9. Mean boundary layer thickness with the

plasma actuator powered on and off are shown in Figure 5.10.

Figure 5.6 PIV mean velocity field at Re = 1.0x10⁵ with plasma actuator on, V = 6.4 kV$_{pp}$
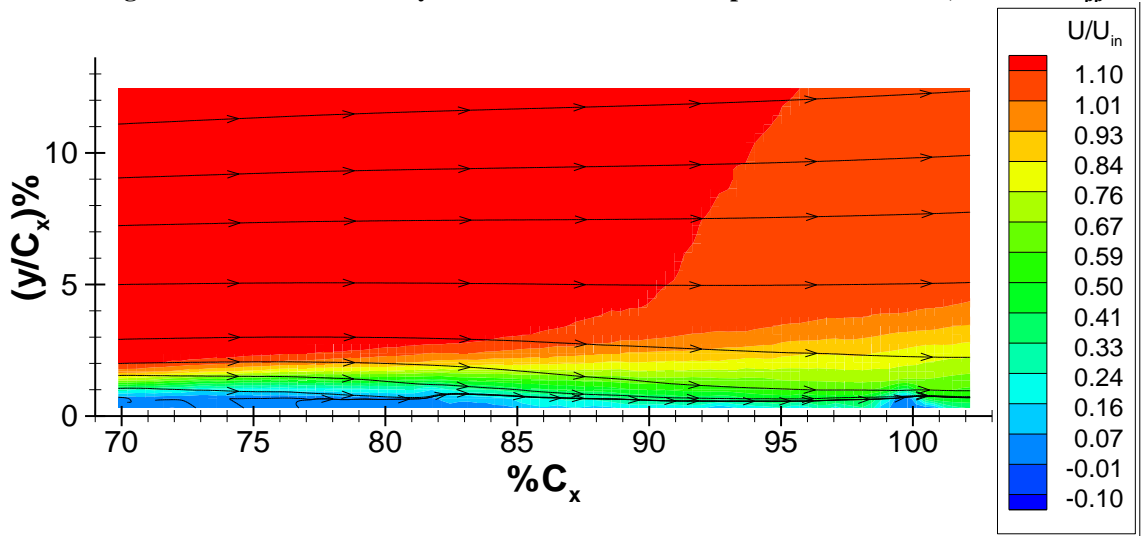
Figure 5.7. PIV mean velocity field at Re = 6.0x10⁴ with plasma actuator on, V = 6.4 kV$_{pp}$.
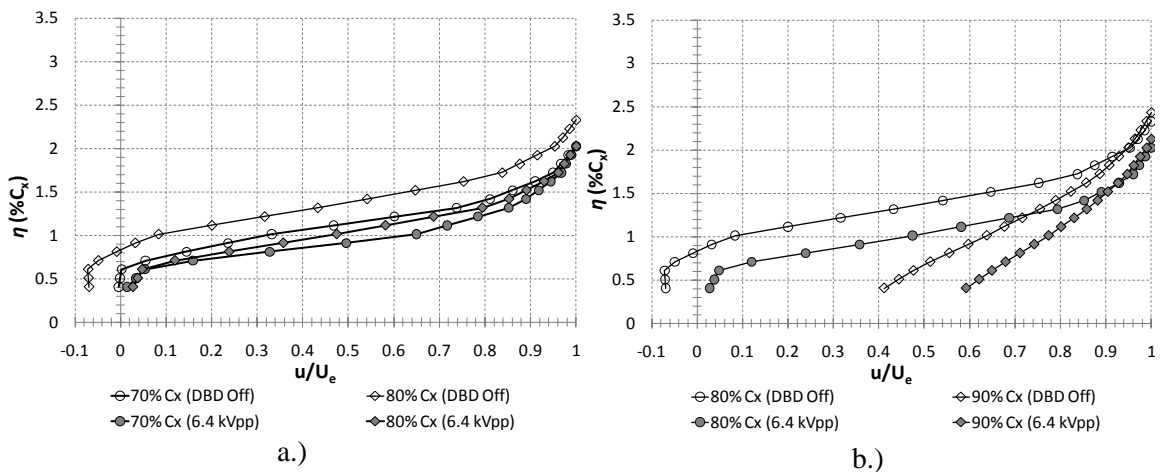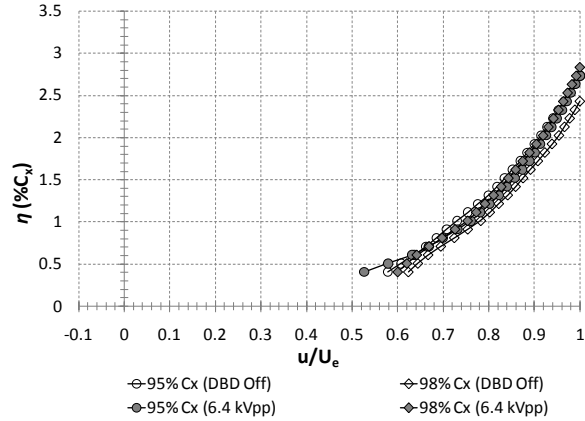
c.)

Figure 5.8 Suction surface PIV velocity profiles near the trailing edge with plasma actuator power on and off, Re = 1.0 x 10⁵.

At a Reynolds number of 1.0×10^5 turning on the plasma actuator results in earlier reattachment and a fuller boundary layer profile at $C_x = 90\%$. The boundary layer thickness is also smaller with the plasma actuator on until the trailing edge of the airfoil where the boundary layer thicknesses are nearly equal.

At the lower Reynolds number of 6×10^4 the boundary layer thickness is significantly reduced, with an approximately 10% upstream shift in reattachment location. Mean boundary layer thickness with the plasma actuator on in Figure 5.10b is very similar to the predicted turbulent boundary layer thickness on a flat plate. In a mean sense, the large scale inviscid structures have broken down into small scale turbulence near the trailing edge of the airfoil as shown in the image of Figure 5.11.
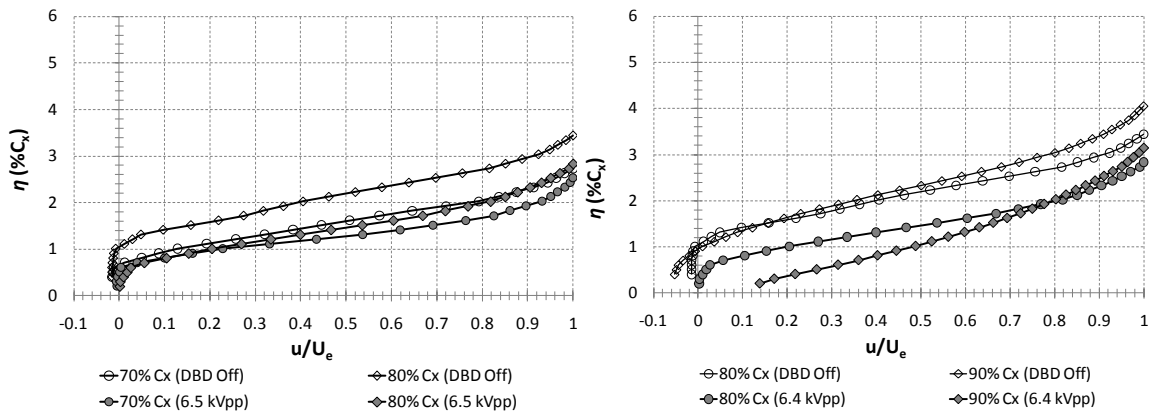
a.)

b.)
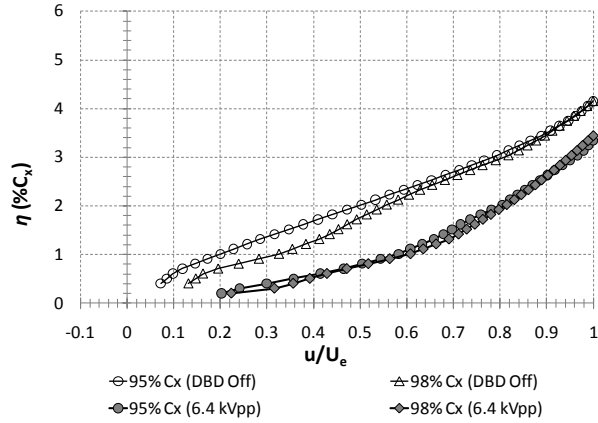
c.)

Figure 5.9 Suction surface PIV velocity profiles near the trailing edge with plasma actuator power on and off, Re = 6 x 10^4.

a.)

b.)
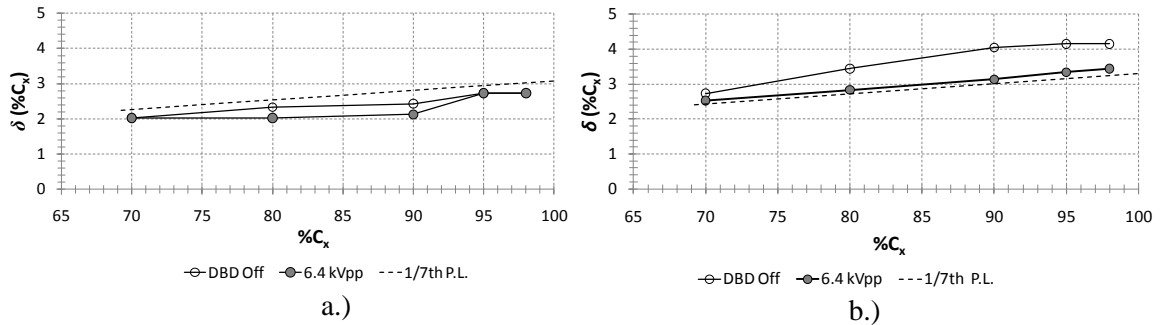
Figure 5.10 Boundary layer thickness with plasma actuator powered on and off at a.) Re = 1.0 x 10^5, and b.) Re = 6 x 10^4.
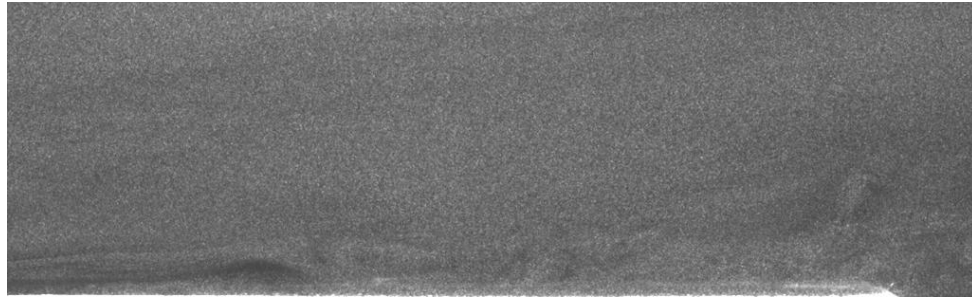
Figure 5.11 Flow visualization over the trailing edge portion of the airfoil with plasma actuator on 6.4 kV$_{pp}$. View is from $C_x \approx 70 - 103$ %

5.3. **Control Method**

A system block diagram of the feedback separation control system is shown in Figure 5.12.

A simplistic approach was taken in this work to develop a simple controller with the objective of

demonstrating that the S3F can be used a separation control sensor. An on/off controller and a PI controller were implemented.

Re, U_∞ change

Error
Detector

d_r + → ( ) d_e → [Controller / *Labview Based*] → [Actuator / *Linear Vertical Jets*] → + ( ) + → [Process / *Fluid Dynamics*] → τ_w

-

d_x [Sensor / *S3F*]
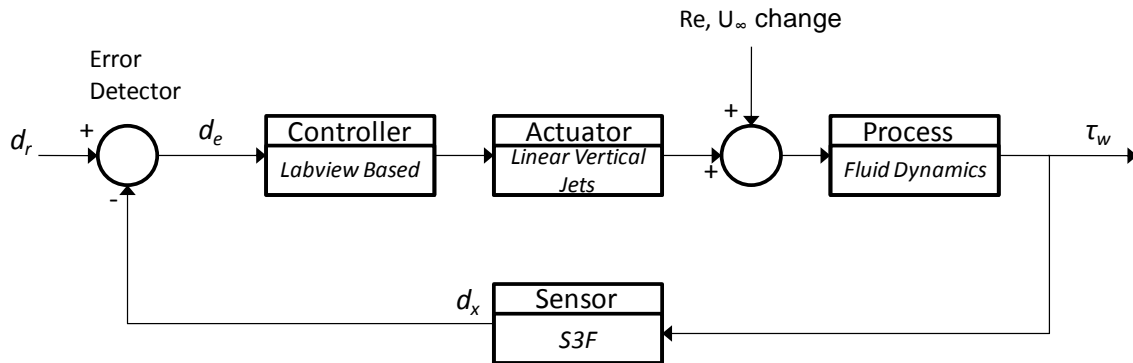
Figure 5.12. Feedback Control System Diagram

5.3.1. System Response

Several measurements were made to understand the sensor response. Mean S3F response at several different plasma actuator voltages is shown in Figure 5.13. Time resolved response at candidate monitoring points is shown in Figure 5.14. The time resolved response of the S3F when the wind tunnel speed is rapidly decreased from a Reynolds number of 1.0×10^5 to 6×10^4 is shown in Figure 5.15.

Figure 5.13 show a mean nonlinear response in tangential displacement at candidate monitoring points, typically located just downstream of the mean reattachment point. Also included in the response plots are mid-S3F line plots across the camera field of view at select plasma actuator voltages. The higher Reynolds number of 1.0×10^5 shows a linear response with increase in actuator voltage until a 5.5 kV_{pp} applied voltage in which a further increase in actuator voltage resulted in little change in shear displacement. The plateau in the response curve is consistent with observations using the same plasma actuator electrode geometry (DBD-02) during the open loop plasma actuator electrode investigation of Chapter 4. This implies there is a threshold voltage of approximately 5.5 kV_{pp} above which there is very little additional decrease in separation length. A maximum upstream shift in reattachment point of 6.1 % C_x was observed at

Re = 1.0 x 10^5 with 7.2 kV$_{pp}$ applied voltage. The reattachment location implied by the S3F

tangential displacement is further downstream than was observed with PIV. With the plasma

actuator off the mean zero crossing location was at 90% C_x with an upstream shift to

approximately 84% C_x with 7.2 kV$_{pp}$ applied voltage.   At the lower Reynolds number the same

linear range is visible but a drop off in shear displacement occurs at the highest plasma actuator

voltage. The mean displacement actually changes to a negative value. Mean reattach point

shifted upstream to as high as 89% C_x with a 6.4 kV$_{pp}$ applied voltage. This is an upstream shift

of approximately 9% C_x. The upstream shift in reattachment point is consistent with PIV

measurements that indicated a 10% upstream shift; however, the location of zero crossing is

nearly 7% further upstream than the reattachment point measured with PIV.
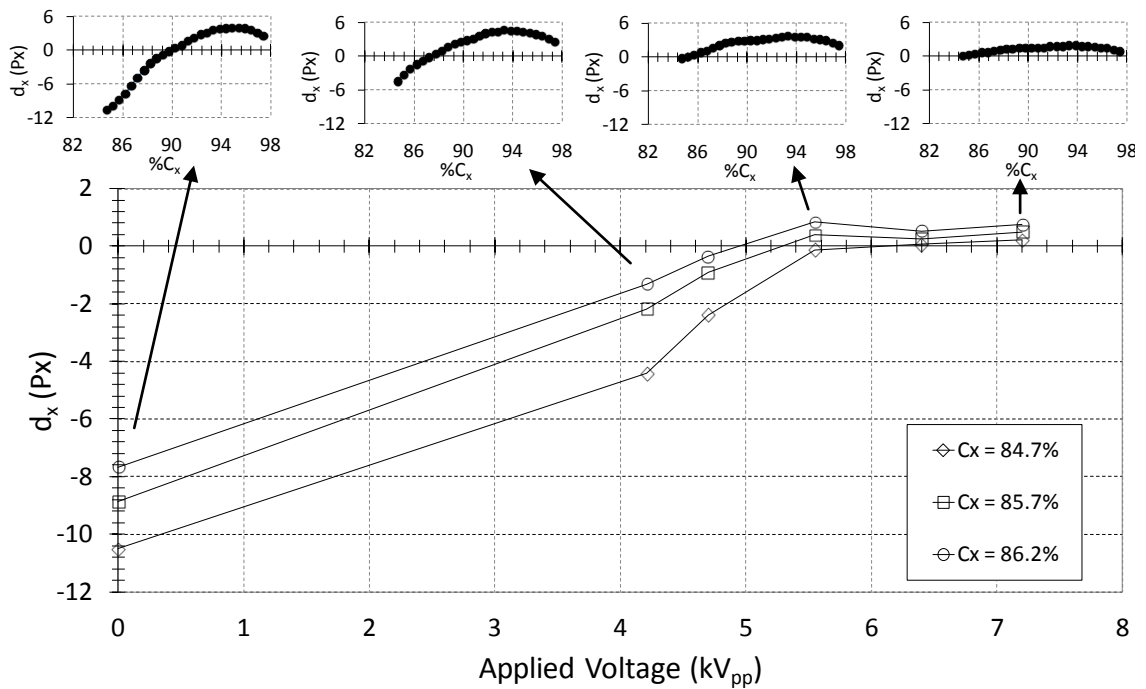
a.)
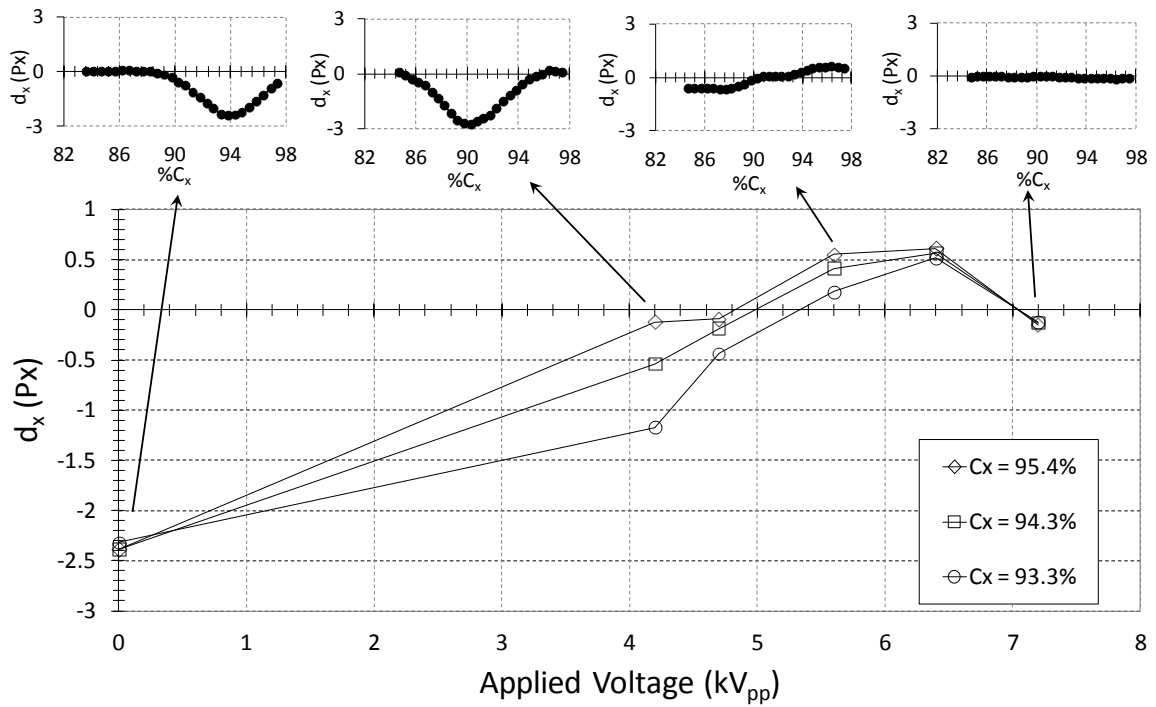
b.)

Figure 5.13 S3F mean response at various sensor locations, a.) Re = 1.0 x 10^5, b.) Re = 6 x 10^4.

Understanding the response of the S3F at a high level of plasma actuator voltage is complicated. Several factors could play a role in the change in S3F tangential displacement: frequency response of the S3F, pressure gradient effects, changes in pressure gradient and shear stress, and uncertainty in the displacement calculation. A mean negative displacement at Re = 6.0×10^4 and the highest actuator voltage could be due to the uncertainty in the single pass cross correlation method as displacement approaches zero.

The time resolved response of the S3F when the plasma actuator is powered on shows that the film responds to load change within 1 second. The response at an applied voltage of 7.2kV$_{pp}$ is interesting since it resembles a damped system, with no oscillation. This could mean that the frequency response characteristics of the film are responsible for the near zero displacement reading.
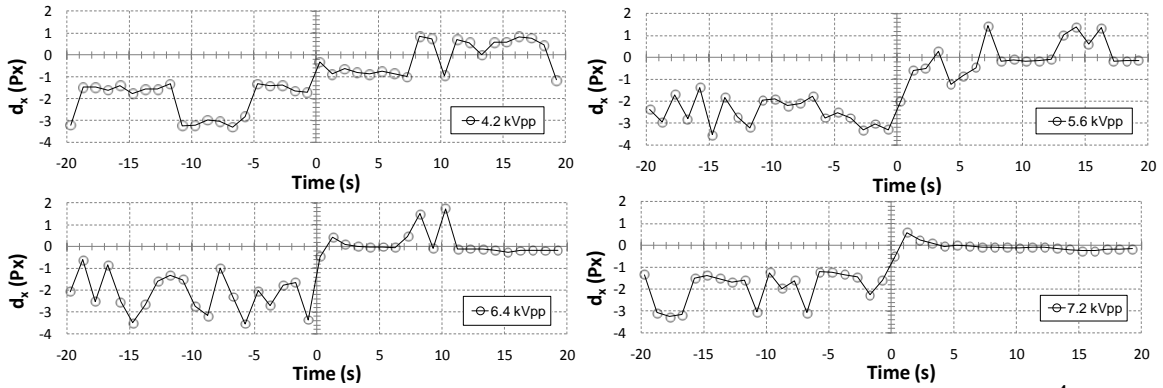
Figure 5.14 S3F time response at various applied voltages, $C_x = 95.4$ %, Re=6 x 10^4.

The response of the highly sensitive, ultra low shear modulus, viscoelastic S3F may require further development and material property testing to fully understand. Nonetheless, the response of the S3F shown in Figure 5.13 makes it useful in a feedback separation control system. With the plasma actuator off the S3F tangential displacement is certainly negative, and when the plasma actuator is turned on the S3F tangential displacement moves positive or towards zero.

The S3F behavior is certainly useful as a sensor for On/off control of the plasma actuator. In order to better understand the time resolved S3F signal response as flow conditions change and separation control is turned on the wind tunnel speed was reduced from a speed at which the S3F displacement was positive and the boundary layer attached to a speed in which the boundary layer is separated over the monitor point. The sampling speed was set to 2.5 Hz and a point at C_x=95.4% was monitored. In one case the actuator was triggered to come on as separation was detected at the S3F monitor point, and the other flow control was left off. The results of both cases are shown in Figure 5.15. At a Reynolds number of 1.0×10^5 the S3F tangential displacement oscillates from just around zero to approximately 3.5 pixels. Oscillation of the signal is consistent with unsteadiness in the boundary layer downstream of the laminar separation bubble observed in the flow visualization in Figure 5.1b. The frequency of oscillation is not accurate due to the low natural frequency of the S3F, and slow sampling speed. For the two cases shown, the magnitude of displacement at a Re = 1.0×10^5 is not the same indicating either error in the measurement, or a small change in the boundary layer behavior between runs due to the

145

sensitivity of the laminar boundary layer to minute changes in freestream unsteadiness. When the tunnel speed is decreased the S3F displacement quickly decreases to a negative displacement implying the reattachment point has moved downstream of the monitor point. There is a 6 second transient response period from the time the tunnel inlet Reynolds number reaches 6×10^4 until the displacement reaches a consistent value centered about approximately -3 px. For the case in which the plasma actuator is triggered on at an S3F filtered displacement of -1 px the boundary layer separation is significantly diminished within approximately 1.5 second. The actuator significantly increases the S3F displacement at the monitor point to a value that fluctuates between positive and negative with a mean value of -0.1 px.

a.) Actuator off

b.) Actuator on, $v = 5.6$ kV$_{pp}$
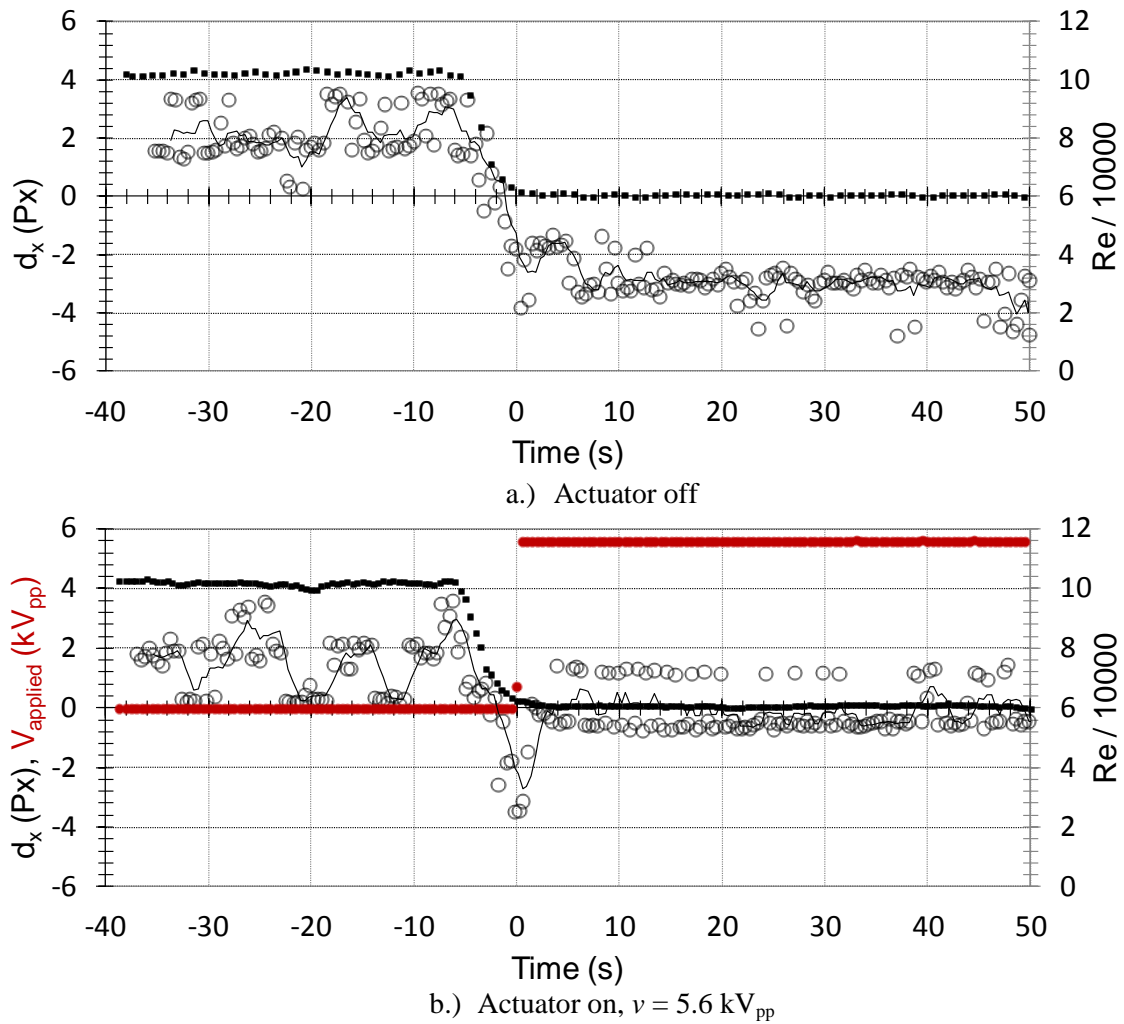
Figure 5.15. Comparison of S3F response for a sudden drop in free stream velocity, with and without flow control. Triggering of plasma actuator at $d_x = $ -1 px, f_s=2.5 Hz, monitor point at 95.4%C_x.

5.3.2. On/off Controller

As a first demonstration of the closed loop system, the S3F sensor signal was used with an on/off controller. This is similar to the stall control system demonstrated by Poggie et al. (2010) using hot film gauges, but with the ability to turn the actuator back off when flow conditions become more favorable. The system used the S3F signal as a trigger to turn on and off the plasma actuator at a predetermined sensor low and high signal level using the logic flow shown in Figure 2.31. If the S3F displacement changed to a value less than the lower set point the actuator would be turned on to a predetermined value. If the displacement increased to a value higher than the upper set point the actuator would be turned off. When the displacement was between the upper and lower set points the actuator would remain at its previous setting. Due to the unsteady signal and latency of the boundary layer response, delay logic was built into the controller. Once the actuator state changed, no control changes could be made for a period of t_d. This assured that the system did not oscillate. The sensor signal was low pass filtered to reduce noise.

Two examples of the on/off controller with different values of actuator voltage are shown in Figure 5.16-Figure 5.17. In both examples the sampling frequency was set to 2.5 Hz and the wind tunnel speed was set to provide a Reynolds number of 1.0×10^5 then decreased to the 6 x 10^4. The sensor location was at $C_x = 95.4\%$. In the first case the actuator was set to 4.7 kV$_{pp}$ and the sensor signal implies that flow separation was removed in under 2 seconds. With the actuator on, the S3F displacement at the monitoring point was 0.1 pixels. As the wind tunnel speed was increased and the controller detected a positive displacement larger than the upper set point the actuator was powered off. After several seconds the displacement begins to oscillate in a similar manner as previous studies.
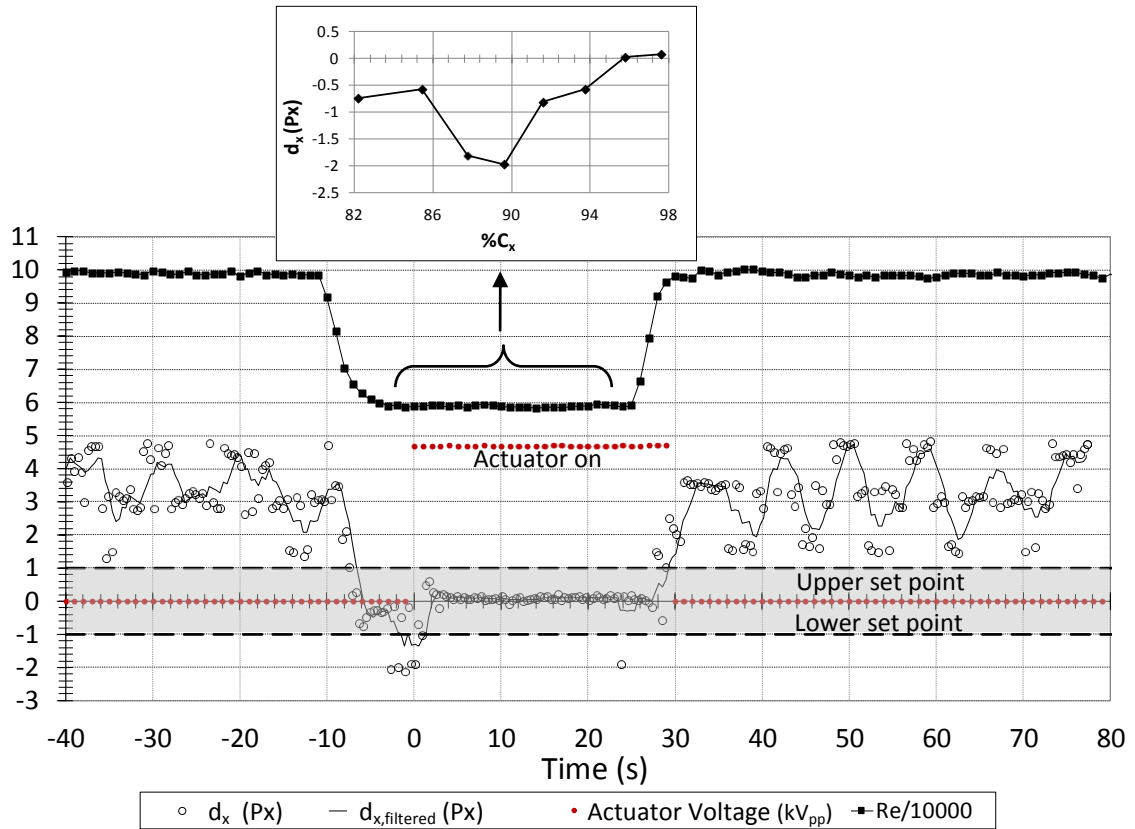
Figure 5.16. On/off controller, f_s = 2.5 Hz, v = 4.7 kVpp.

In the case shown in Figure 5.17 the plasma actuator voltage was set to 5.6kV$_{pp}$ and the upper set point increased to 2 pixels. When the plasma actuator was turned on the displacement reaches a positive value and then oscillates about zero after approximately 10 seconds in a similar manner as was observed in Figure 5.16. The change in S3F displacement after a delay of approximately 10 seconds suggests a difference in boundary layer response between Figure 5.16 and Figure 5.17, even though conditions were the same.

As a final demonstration of the On/off controller, the wind tunnel speed was arbitrarily varied between Re = 1.0 x 10^5 and 5 x10^4 as shown in Figure 5.18.
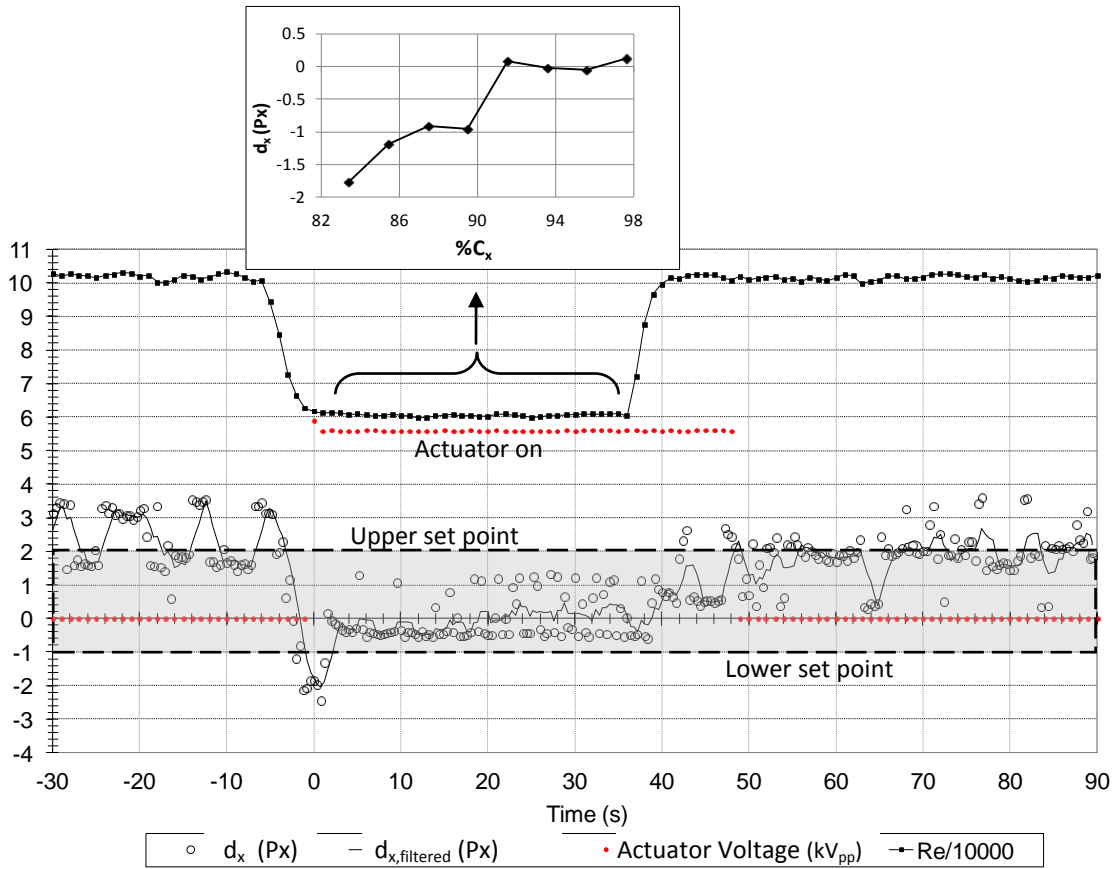
Figure 5.17. On/off controller, f_s**=2.5Hz,** v **= 5.6 kVpp.**
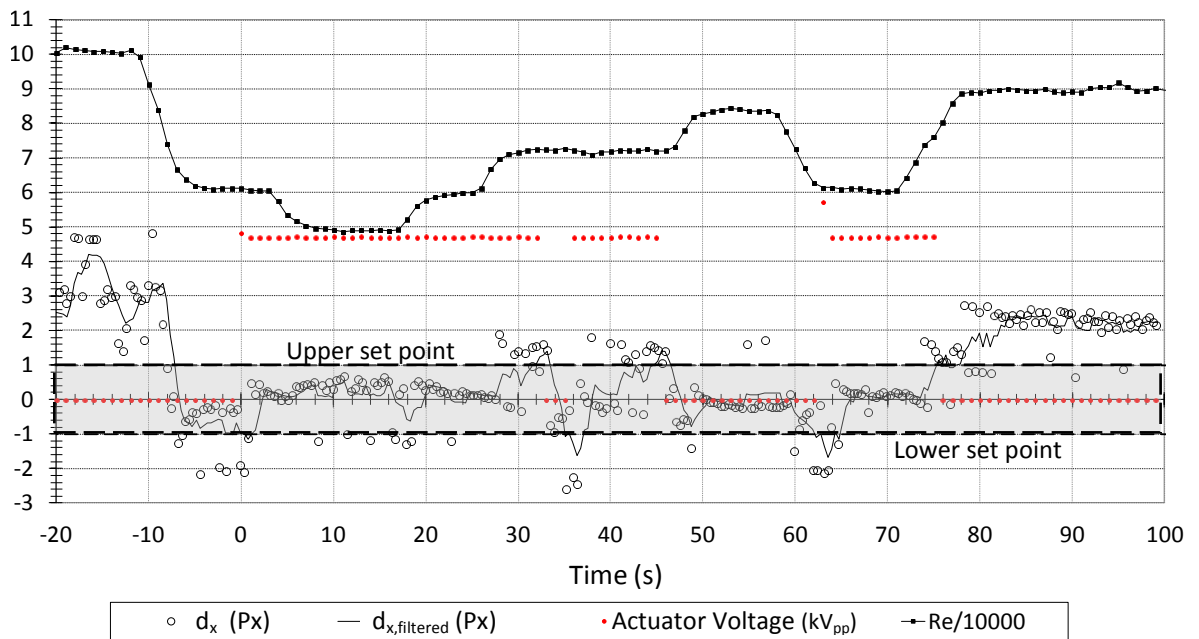
Figure 5.18 On/off controller, f_s **= 2.5 Hz, actuator** v **= 4.7 kV$_{pp}$ with arbitrary tunnel speed.**

5.3.3. PI Controller

A proportional integral (PI) controller was implemented to demonstrate closed loop control with a simple automatic controller. The standard form of a PI controller is given by:

$$u(t) = K_P \cdot d_e(t) + K_I \cdot \int_0^t d_e(\varphi)d\varphi \qquad (5.1)$$

where $u(t)$ is the output signal.

A discrete version of the PI controller was implemented in the control software. First the sensor signal was low pass filtered, compared to the reference value, then PI controller output calculated by:

$$u(t) = K_P \cdot \bar{d}_e(t) + K_I \cdot \sum_{i=1}^{k} \bar{d}_e(t_i) \cdot \Delta t \qquad (5.2)$$

where $\bar{d}_e(t)$ is the low passed filtered error signal calculated by:

$$\bar{d}_e(t) = d_r - \bar{d}(t) \qquad (5.3)$$

$$\bar{d}(t) = \frac{1}{m} \cdot (d(t) + d(t-1) + d(t-2) \cdots d(t-m-1)). \qquad (5.4)$$

The controller gains were manually tuned, first by adjusting the proportional gain, then by adding and increasing the integral gain until a satisfactory response was obtained. It is important to remember that the PI controller used here was un-optimized and a better controller would likely yield better performance. The system sampling rate was typically between 0.5 Hz and 2.5 Hz, which was limited by the hardware available.

Only one interrogation window in the field of view was used to simulate a discrete shear stress sensor. In a first example shown in Figure 5.19 the sampling rate was 0.5 Hz, the reference displacement d_r was 0 pixels at $C_x=96\%$, and the output signal was limited to 0.94 (5.6 kV$_{pp}$). When the control system is turned on the controller commands maximum actuator output and boundary layer separation was eliminated. After approximately 30 seconds from the start of

control the response becomes unsteady and the mean increases slightly resulting in a reduction of the output signal. The reason for the unsteadiness in unknown but assumed to be due to a change in boundary layer behavior. The time resolved reattachment point of the boundary layer with flow control on is spatially unsteady due to the shedding of vortices that form in the separated shear layer as shown in Figure 5.1. The simple un-optimized PI controller used here does a reasonable job at maintaining the set point even with the highly unsteady signal. At t=200s an impulse disturbance is introduced by increasing the flow velocity to a Reynolds number of $1.0x10^5$. At the higher Reynolds number the sensor signal would typically be much higher than zero, but the disturbance happens in too short of a time scale to overcome the inherent damping in the system. At t=230s a step disturbance is introduced for 30 seconds resulting in a significant increase in sensor signal. The controller responds by decreasing the output signal to maintain the set point. As the disturbance is removed the controller increases the output signal. The PI controller response is slow, but necessary due to the unsteady input signal.
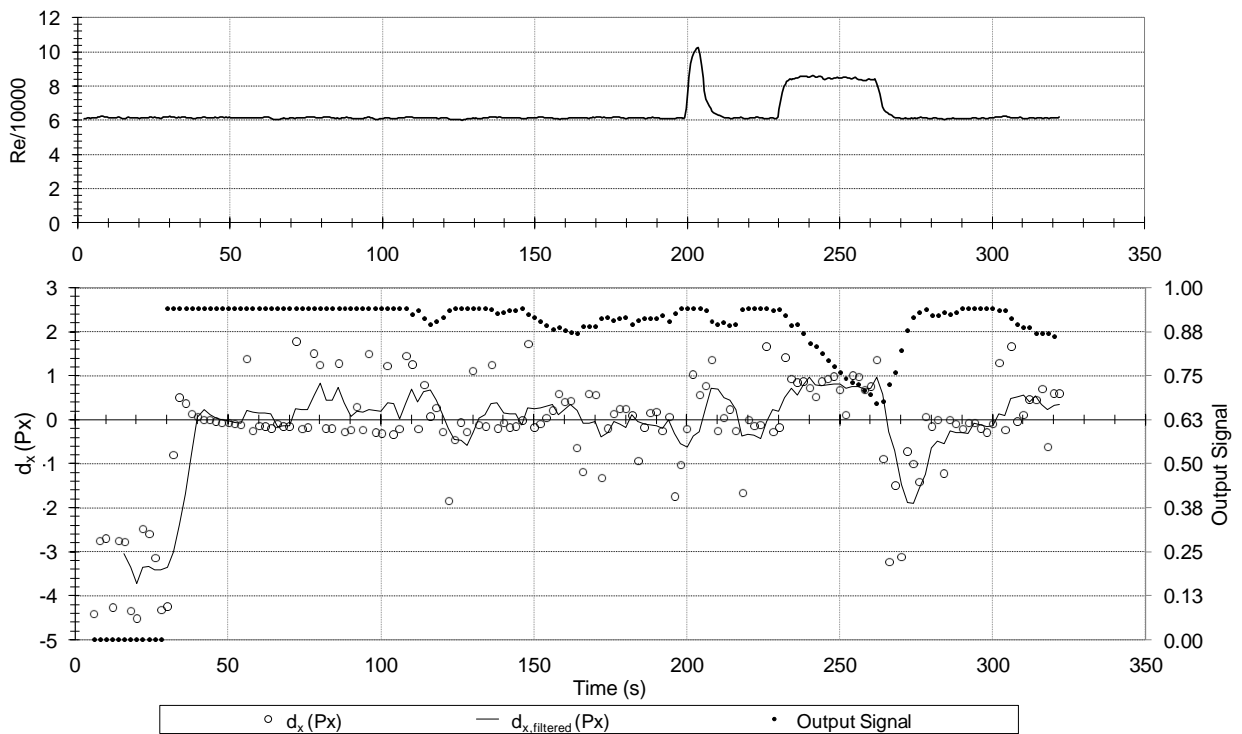
Figure 5.19. Controller response to external disturbances. Set point $d_r = 0$ px at $C_x = 96\%$.

As a second example of the PI controller the wind tunnel was set to a speed providing a Re = 6.0×10^4, and the controller turned on. The output signal was increased over the previous example. Figure 5.20 shows the system response and the top three plots show the mean tangential displacement across the full sensor field of view at three different phases of the run. Three distinct phases of boundary layer response are shown. The first phase is with the feedback control system off. Reverse flow is observed at the trailing edge corresponding to a mean reversed flow vortex inside a separation area. When the control system is turned on the PI controller commands maximum actuator output and the separation is eliminated. After the initial
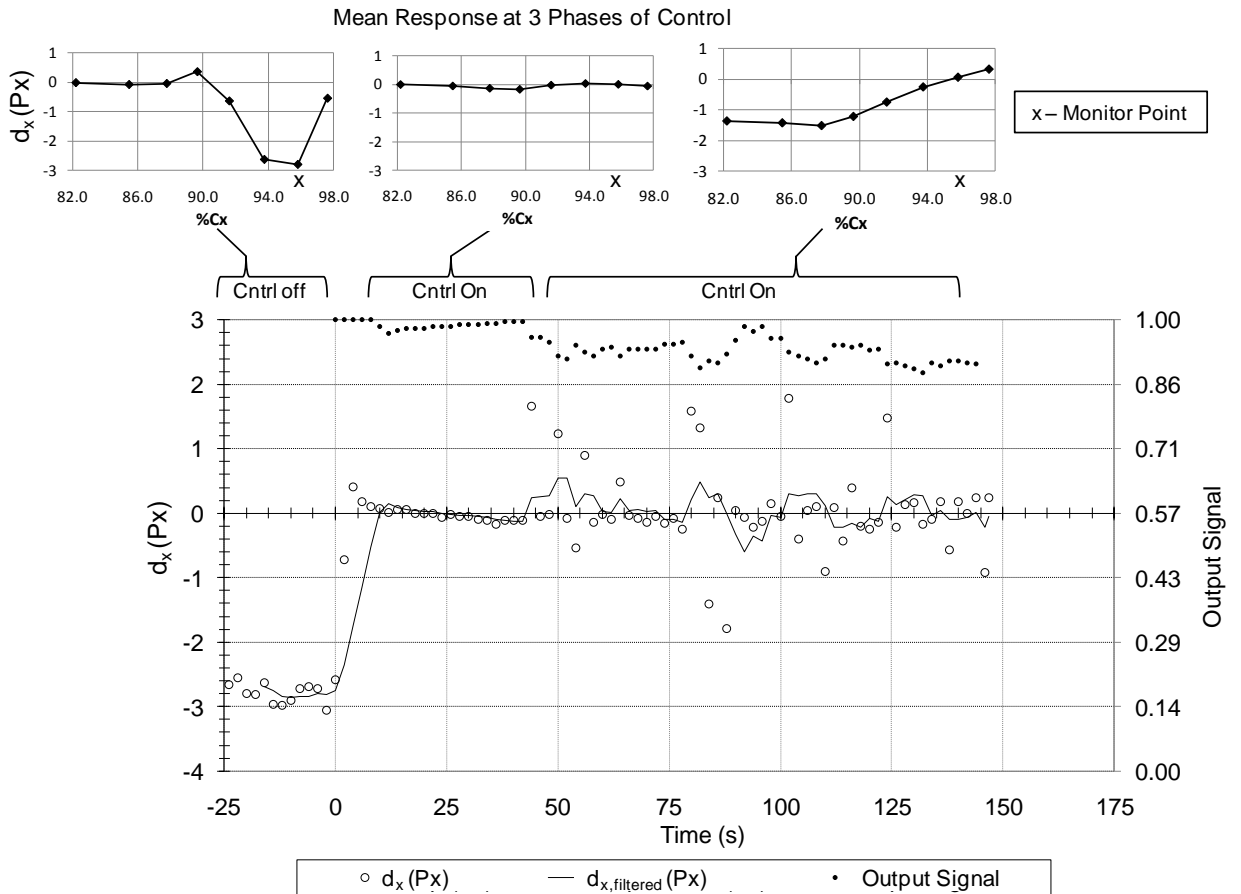
Figure 5.20. Example of separation control using a PI controller at Re = 6.0x10^4, f_s=0.5 Hz.

transient response to the actuator step disturbance, the controller begins to decrease the actuator output signal. As the output signal is adjusted the response begins to oscillate with the controller

trying to respond and maintain the reference value. The response in Phase 3 shows a mean reattachment point in the vicinity of the monitor point. The unsteadiness in the signal is most likely due to shedding of vortices.

The example provided here using a PI controller demonstrates that the S3F sensor signal can be used in a closed loop separation control system. The use of a different type of controller, hardware, and S3F packaging could provide a higher sampling rate, and quicker system response. The system response time using the ultra low S3F in this study are slow and would only make the use of the S3F sensor here useful in a limited number of flight environments. Future efforts should work towards increasing the S3F based sensor sampling speed.

5.3.4. Energy savings

The objective of an active flow control system with feedback is to save energy by turning the actuator off when it is not required, or reducing power when conditions require less control authority. The energy consumption of the two feedback control methods demonstrated here were calculated and compared to simply turning on the plasma actuator at a predetermined condition.

Energy consumption was calculated by numerically integrating the power dissipation of the plasma actuator over time. Instantaneous power dissipation was estimated from the applied voltage using the equation in Figure 4.3. The energy consumption saving is dependent on the profile length. The two different situations were analyzed: On/off controller with arbitrary tunnel speed which was shown in Figure 5.18, and the PI controller experimental run shown in Figure 5.20.

The region used in the calculation of energy consumption without and without the On/off controller is shown in Figure 5.21 and Figure 5.22 respectfully. If the plasma actuator is turned on, and left on, at a predetermined threshold value, 200 J of energy would be used. If an On/off controller is used only 113 J of energy are consumed resulting in a 44% reduction in energy consumption over a 78 second period.
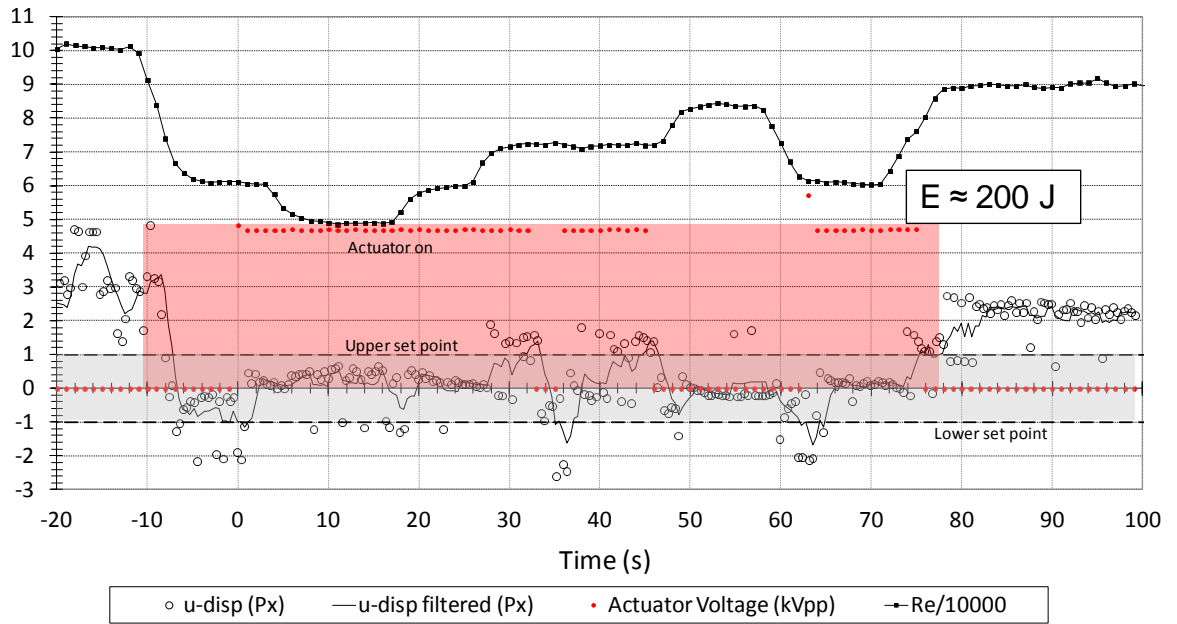
Figure 5.21 Energy consumption calculation without an On/off feedback controller.
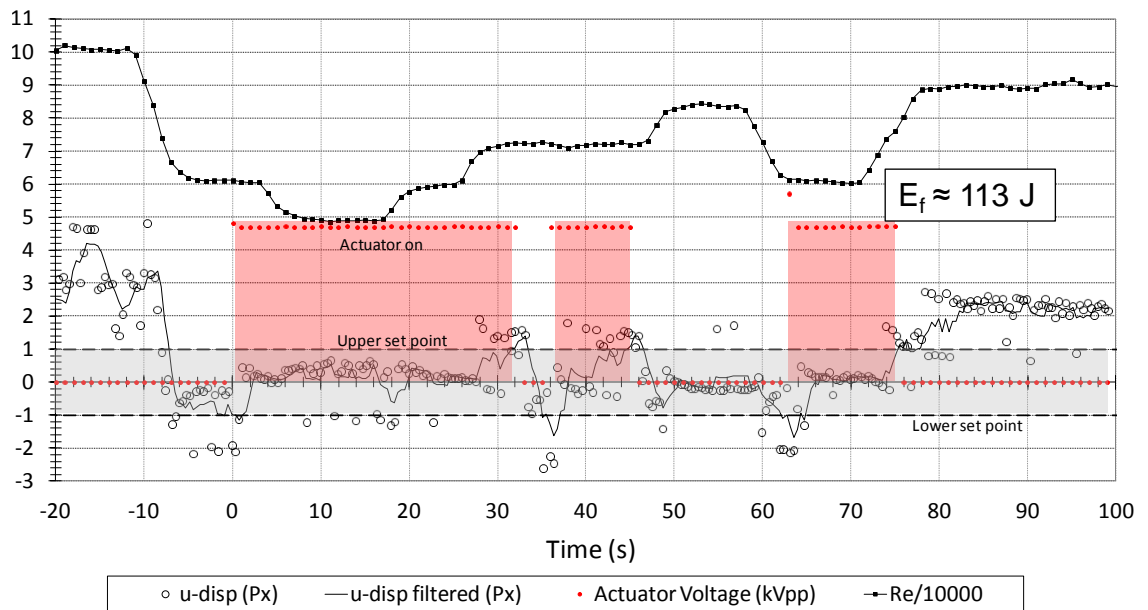
Figure 5.22 Energy consumption calculation with an On/off feedback controller.

In the case of the PI controller, the energy dissipation is shown in Figure 5.23. The use of the PI controller would result in a 34% reduction in energy consumption for 140 seconds of operation. As operation time increases energy consumption will increase. Large savings in energy

consumption can be realized using an automatic controller with a plasma actuator because actuator power dissipation scales proportional to $V^{3.5}$.   The potential for even larger savings are possible if the plasma actuator is operated in an unsteady mode (Huang et al. 2006).
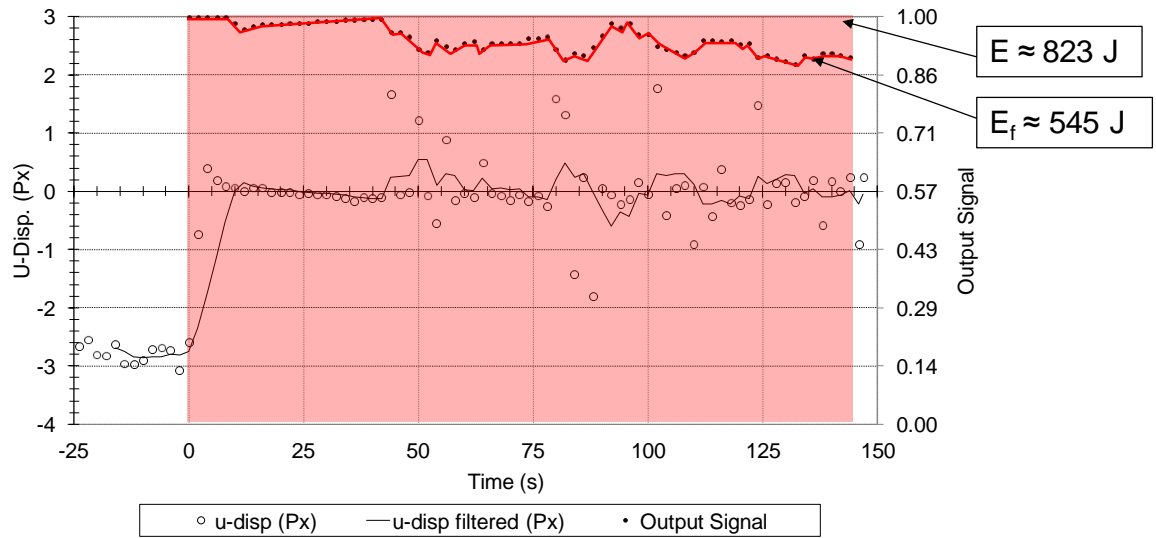
Figure 5.23 Energy consumption calculation using a PI controller.

6. Conclusions

The overall goal of this study was to investigate using the sensitivity of S3F to surface shear stress as a low Reynolds number separation control sensor. Several objectives were listed in the introduction of the document, and they are repeated here with conclusions.

Objective 1: Obtain the experimental suction surface Cp and boundary layer behavior of an Eppler 387 (E387) airfoil model at low Reynolds number over a range of small angles of attack that results in laminar boundary layer flow separation.

The E387 airfoil is a generic representation of a low Reynolds number airfoil and was useful because of laminar flow separation on the suction surface at small angles of attack. E387 suction surface C_p, flow visualization, PIV, and section drag was measured in the AFRL/RZ DWT facility at low angles of attack. This data provided a thorough understanding of the E387 airfoil suction surface boundary layer, and led to a choice of angle of attack and confirmation that the airfoil could be used for a separation control study. The extent of separation could be adjusted by varying the Reynolds number. At a Reynolds number of 1.0×10^5 a mean laminar separation bubble was formed on the suction surface. At Reynolds numbers below approximately 6×10^4 the boundary layer separated and did not reattach.

Objective 2: Study a new method of surface stress sensitive film installation over a curved surface to reduce the effect of the film on boundary layer and surface being studied.

A new method of installing S3F over a curved surface was demonstrated in this study. The new technique originated at ISSI Inc. and uses a thin, flexible S3F carrier. A cavity in the S3F carrier is filled with S3F level and flush to the surface prior to installation on the airfoil. This method simplifies installation of S3F onto a curved surface. Velocity field data were measured

by PIV on the suction surface of the airfoil with the S3F installed, and compared to the velocity field without the S3F installed, and with a plasma actuator installed on the airfoil. The velocity field data indicated that the S3F installation decreased the boundary layer thickness, but not as much as installation of the plasma actuator. The change in the boundary layer was more severe at higher Reynolds numbers.

Objective 3: Compare several different dielectric barrier discharge plasma actuator geometries for low Reynolds number separation control on the E387 airfoil model.

Three different plasma actuator electrode configurations were compared for use in a low Reynolds number separation control system. Two of the actuator configurations were implemented with the intent of generating three-dimensional, or streamwise vorticity to improve momentum entrainment from the freestream into the boundary layer. Operation at two different Reynolds numbers was presented in the study. At the lower Reynolds number of 5×10^4, laminar separation without reattachment was observed with the actuators powered off. At the higher Reynolds number 1.0×10^5 the boundary layer separated and then reattached prior to the trailing edge.

Three parameters were used to compare the performance of each actuator: suction surface C_p profile, S3F streamwise surface displacement, and drag. At the lowest Reynolds number tested, S3F reattachment locations indicated plasma actuator DBD-02, a spanwise distributed array of linear vertical jets, reattached the flow and moved the mean reattachment upstream as voltage was increased to $7.2\mathrm{kV_{pp}}$. The pressure coefficients did not recover to the inviscid profile predicted in XFOIL. This configuration also resulted in the largest improvement in drag at the lowest applied voltage.

At the higher Reynolds number each plasma actuator moved the reattachment point upstream. Plasma actuator configuration DBD-02 shifted the reattachment point upstream in excess of 6% C_x, likely significantly further as the mean reattachment point moved out of the field of view.

157

Plasma actuator configuration DBD-03 shifted the reattachment point upstream 8% C_x. Each actuator tested at Re=$1.0\text{x}10^5$ showed an increase in drag as the separation length decreased with increased voltage. This is considered to be due to an increase in turbulent boundary layer length. Several conclusions can be made from the results of the open loop study:

1. The spanwise distributed array of linear vertical jets (DBD-02) are deemed the most effective in the two flow conditions presented here. However, plasma actuator DBD-01, a spanwise array of cross-stream jet showed promise and it is possible that a different spanwise spacing of the jets would yield better results.

2. Alternative DBD plasma actuator electrode configurations to the standard asymmetric electrode configuration must be considered and studied in more detail as they show potential for performance improvements.

3. The electrode configuration that will provide the most effective separation control at low Reynolds number will likely change with flow conditions. This points towards electrode configurations and power electronics that enable induced velocity jet vectoring. A configuration that uses jet vectoring could create the effects of configurations DBD-01, and DBD-02, and enable switching between jet orientations based on flow condition.

It should be mentioned that the success of the two spanwise distributed arrays, used here in hopes of generating three dimensionality and streamwise vorticity, point towards the conclusion that longitudinal vorticity was generated. However, further study is necessary to verify the control mechanism that led to reattachment.

Objective 4: Develop a first generation closed loop low Reynolds number separation control system using S3F as the separation control sensor.

In order to use S3F as a sensor on the E387 airfoil, an appropriate experimental setup that enabled measurement of low values of film displacement had to be determined. This required the

testing of six different S3F formulations on the E387, and integration of the S3F method into a LabVIEW environment. It was hypothesized that the S3F tangential displacement itself could be used as an input to the separation control system. Calculation of tangential displacement was by single pass cross correlation. The sensitivity of the S3F was significantly increased over time by the manufacturer, but this resulted in a decrease in S3F frequency response. During the course of this work the S3F shear modulus was decreased from approximately 100 Pa to 7.7 Pa. A high speed Cameralink interface was used to transfer images from a high resolution scientific grade camera. A high resolution camera was required to resolve film displacement in the current setup. The use of high resolution camera and the hardware used to calculate S3F displacement set the maximum sampling speed to approximately 3 Hz. Alternate S3F sensor packaging configurations are under development by ISSI Inc. that could potentially increase sampling rate.   A comparison of S3F tangential displacement with Cp and PIV data indicated that tangential film displacement itself could be used to infer reattachment location. At a Reynolds number of 1.0×10^5 a zero crossing was observed that moved upstream in relation to a shift in mean reattachment point. At the lower Reynolds number a strong minimum point was observed that shifted upstream with reattachment point, inferring an upstream shift in reattachment. Examining the mean frequency response of the S3F at two different Reynolds numbers showed a non-linear response curve. Time resolved response of the S3F indicated that the S3F responded in less than 1 second, which was the limit of the sampling rate.   The use of S3F with two different, simple, un-optimized feedback controllers was demonstrated in the AFRL/RZ DWT. An On/off controller and PI controller were used to control boundary layer separation as the inlet Reynolds number was reduced from $Re = 1.0 \times 10^5$ to $Re = 6 \times 10^4$. Decreasing the wind tunnel speed resulted in an increase in the extent of separation. The objective of feedback active control systems over open loop configurations is better control with reduced energy consumption. The energy consumption of two arbitrary experimental runs, one using the On/off controller, and the other using the PI controller was calculated. The On/off controller resulted in a 77% reduction in energy

consumption over a 78 second operating period. The PI controller resulted in a 34% reduction in energy consumption over a 140 second period. The amount of energy savings is directly dependent on the length of the run. The un-optimized PI controller power saving substantially increased over time.

The use of the tangential displacement from an S3F sensor has been used in this study to control Low Reynolds number flow separation over an E387 airfoil. Future work should focus on increasing frequency response, sampling rate, and repackaging the system into an all-in-one discrete sensor that includes S3F and displacement detection system.   This work has demonstrated that a repackaged system, small enough to cleanly integrate into aircraft surfaces, would make a useful flow control sensor for a variety of aerodynamic systems.

References

ALAM, M. AND SANDHAM, N.D. 2000. Direct Numerical Simulation of `Short' Laminar Separation Bubbles with Turbulent Reattachment. *Journal of Fluid Mechanics 403*, 223-250.

AMITAY, M., SMITH, B. L. AND GLEZER, A., 1998. Aerodynamic flow control using synthetic jet technology. *AIAA Paper 98-0208.*

AMITAY, M., KIBENS, V., PAREKH, D. E. AND GLEZER, A., 1999. The Dynamics of Flow Reattachment over a Thick Airfoil Controlled by Synthetic Jet Actuators. *AIAA Paper 99-1001.*

AMITAY, M., PAREKH, D., PITT, D., KIBBENS, V., AND GLEZER, A., 2000. Control of Internal Flow Separation Using Synthetic Jets Actuators. *AIAA Paper No. 2000-0903.*

BARLOW, J., RAE, W., AND POPE, A., 1999. "Low-Speed Wind Tunnel Testing", 3rd Edition, John Wiley & Sons, New York.

BAUGHN, J. W., BUTLER, R. J., BYERLEY, A. R., AND RIVIR, R. B. 1995. An Experimental Investigation of Heat Transfer, Transition and Separation on Turbine Blades at Low Reynolds Number and High Turbulence Intensity. *ASME Paper 95-WA/HT-25.*

BAUGHN, J. W., BYERLEY, A. R., AND GREGORY, J. W. 2006. An Optical Method for Measuring Low Wall Shear Stresses Using Thermal Tufts. *AIAA Paper 2006-0647.*

BECHERT, D. 1996. Calibration of Preston Tubes. *AIAA Journal 34*, 205-206.

BECKER, R., AND KING, R., 2007. Adaptive Closed-Loop Separation Control on a High-Lift Configuration Using Extremum Seeking. *AIAA Journal, 45*, pp 1382-1392.

BOLITHO, M., AND JACOB, J., 2008. Thrust Vectoring Flow Control Using Plasma Synthetic Jet Actuators. *AIAA Paper No: 2008-1368.*

BONS, J., SONDERGAARD, R., AND RIVIR, R., 2001. Turbine Separation Control Using Pulsed Vortex Generator Jets *J. of Turbomachinery 123*, 198-206.

BOWLES, P. AND CORKE, T. 2009. Stall detection on a leading-edge plasma actuated pitching airfoil utilizing onboard measurement. *AIAA Paper 2009-93.*

BREHM, C., GROSS, A., AND FASEL, H. 2006. Closed-Loop Control of Low-Pressure Turbine Laminar Separation. *3rd AIAA Flow Control Conference, 5-8 June, San Francisco, CA.*

BURGMANN, S., BRUCKER, C., AND SHRODER, W. 2006. Scanning PIV Measurements of a Laminar Separation Bubble. *Experimental Fluids 41*, 319-326.

CHENG-YUAN, T., YI-PING, H., ZEN, C. 1998. Robust two-stage approach for image motion estimation. *Electronic Letters, 34*, pp. 1091-1093.

CORKE, T., AND POST, M., 2005. Overview of Plasma Flow Control: Concepts, Optimization, and Applications. *AIAA Paper No. 2005-563.*

CRAFTON, J., FONOV, S., JONES, E., GOSS, L., FORLINES, A., AND FONTAIN, A. 2008. Measurements of skin friction in water using surface stress sensitive films. *Meas. Sci. Technol. 19*, 801-811.

CRAFTON, J., FONOV, S., FORLINES, A., AND GOSS, L., 2010. Skin Friction Measurements Using Elastic Films. *AIAA Paper 2010-42.*

CURTIS, E., HODSON, H., BANIEGHBAL, M., DENTON, J., HOWELL, R., AND HARVEY, N., 1997. Development of Blade Profiles for Low-Pressure Turbine Applications. *J. of Turbomachinery 119*, 531-538.

DRELA, M., AND YOUNGREN, H., 2001. XFOIL 6.9 User Primer. Accessed on January 4, 2009. http://web.mit.edu/drela/Public/web /xfoil/xfoil_doc.txt.

ENLOE, C., MCLAUGHLIN, T., VANDYKEN, R., KACHNER, K., JUMPER, E., CORKE, T. 2004a. Mechanisms and Responses of a Single Dielectric Barrier Plasma Actuator: Plasma Morphology. *AIAA Journal 42,* 589-594.

ENLOE, C., MCLAUGHLIN, T., VANDYKEN, R., KACHNER, K., JUMPER, E., CORKE, T., POST, M., HADDAD, O., 2004b. Mechanisms and Responses of a Single Dielectric Barrier Plasma Actuator: Geometric Effects. *AIAA Journal 42*, 595-604.

ENLOE, C., MCLAUGHLIN, T., BAUGHN, J., 2006. Parameterization of Temporal Structure in the Single-Dielectric-Barrier Aerodynamic Plasma Actuator. *AIAA Journal, 44,* 1127-1136.

FERNHOLZ, H., JANKE, G., SCHOBER, M., WAGNER, P., AND WARNACK, D., 1996. New developments and applications of skin-friction measuring techniques. *Measurement Science Technology 7*, 1396-1409.

FRIDMAN, A., CHIROKOV, A., AND GUTSOL, A., 2005. Non-thermal atmospheric discharges, *Journal of Physics D: Applied Physics, 38*, R1-R24.

FONOV, S., JONES, G., CRAFTON, J., FONOV, V., AND GOSS, L. 2006. The development of optical techniques for the measurement of pressure and skin friction. *Meas. Sci. Technol. 17*, 1261-1268.

FONOV, S., CRAFTON, J., FORLINES, A., GOSS, L. 2010 Demonstration of a Surface Stress Sensitive Films for Skin Friction Measurements in a Variety of Flows. *27th AIAA Aerodynamic Measurement Technology and Ground Testing Conference, AIAA Paper No. 2010-4800.*

FONOV, S., 2011. Personal communication.

FONOV, V., FONOV, S., JONES, G., CRAFTON, J. 2004. Image Processing Technique for Shear-Stress Optical Measurements. *11th International Symposium on Flow Visualization*, University of Notre Dame, USA.

GAD-EL-HAK, M. 2000. Flow Control Passive, Active, and Reactive Flow Management 1-2. Cambridge University Press.

GAD-EL-HAK, M. 2001a. Flow Control: The Future. *Journal of Aircraft 38*, 402-418.

GAD-EL-HAK, M. 2001b. Micro-Air-Vehicles: Can They Be Controlled. *Journal of Aircraft 38,* 419-429.

GLAUSER, M., HIGUCHI, H., AUSSEUR, J., AND PINIER, J. 2004. Feedback Control of Separated Flows. AIAA Paper 2004-2521.

GLEAZER, A., AND AMITAY, M. 2002. Synthetic Jets. *Annu. Rev. Fluid Mech. 34*, 503-529.

GNANAMANICKAM, E. P., AND SULLIVAN, J. P. 2008. Image Based Sensor for Distributed Wall Shear Stress Measurement. *46th AIAA Aerospace Sciences Meeting and Exhibit, 7-10 January 2008, Reno, NV.*

GOETT, H., 1939. Experimental Investigation of the Momentum Method for Determining Profile Drag. NACA Report No. 660.

GROSS, A., AND FASEL, H. 2007. Self-Adaptive Closed-Loop Control of Low-Reynolds Number Laminar Separation. *25th AIAA Applied Aerodynamics Conference*, 25-28 June 2007, Miami, FL.

GREGORY, J. W., BAUGHN, J. W., PORTER, C. O, AND BYERLEY, A. R. 2008. Optical Method for Measuring Low Wall Shear Stresses Using Thermal Tufts. *AIAA Journal 46*, 1088-1095.

GROBE, S., AND SCHRODER, W. 2008. Mean wall-shear stress measurements using the micro-pillar shear-stress sensor MPS^3. *Measurement Science and Technology 19*, 1-12.

GROBE, S, SCHRODER, W., AND BRUCKER, C., 2006. Nano-Newton drag sensor based on flexible micro-pillars. *Measurement Science and Technology 17,* 2689-97.

GUNES, H., AND RIST, U., 2004. Proper orthogonal decomposition reconstruction of a transitional boundary layer with and without control. *Physics of Fluids 16,* 2763-2784.

HALL, J., AND MOHSENI, K., 2007. Numerical simulation of an airfoil at Low Reynolds number. *45th AIAA Aerospace Sciences Meeting,* 8-11 January, Reno, NV. AIAA Paper 2007-1269.

HART, D. (2000). PIV error correction. *Exp. Fluids 29*, 13-22.

HEADLEY, J. 1968. Skin Friction Balance. Journal of Scientific Instruments (Journal of Physics E) 2, 360.

HENNING, L., AND KING, R. 2007. Robust Multivariable Closed-Loop Control of a Turbulent Backward-Facing Step Flow. *Journal of Aircraft 44,* 201-208.

HORTON, H.P. 1968. Laminar Separation in Two and Three-dimensional Incompressible Flow. *PhD Dissertation*, University of London.

HORTON, H.P. 1969. A Semi-empirical Theory for the Growth and Bursting of Laminar Separation Bubbles. C.P. No. 1073.

HUANG, H., DABIRI, D., GHARIB, M., 1997. On errors of digital particle image velocimetry. *Measurement Science Technology*, *8*, pp. 1427-1440.

HUANG, J., CORKE, T., AND THOMAS, F., 2003. Plasma Actuators for Separation Control of Low Pressure Turbine Blades. *AIAA Paper 2003-1027.*

HUANG J., CORKE, T., AND THOMAS, F. 2006. Unsteady Plasma Actuators for Separation Control of Low-Pressure Turbine Blades. *AIAA Journal 44*, 1477-1487.

JACOB, J., RAMAKUMAR, K., ANTHONY, R., RIVIR, R. 2005. Control of Laminar and Turbulent Shear Flows using Plasma Actuators. *4th International Symposium on Turbulence and Shear Flow Phenomena,* June 27-29 2005, Williamsburg, VA.

JACOBSON, S. A. 1995. An Experimental Investigation Towards the Active Control of Turbulent Boundary Layers. Ph.D. Thesis, Stanford, CA, 1995.

JIANG, F., LEE, G., TAI, Y., HO, C., 2000. A flexible micromachine-based shear-stress sensor array and its application to separation-point detection. *Sensors and Actuators 79*, 194-203.

JOHNSTON, J., AND NISHI, M., 1990. Vortex Generator Jets – Means for Flow Separation Control. *AIAA Journal, 28*, pp. 989-994.

KAHNG, S., SCOTT, M., BEELER, G., BARTLET, J., AND COLLINS, R., 2000. An Integrated MEMS Sensor Cluster System for Aerospace Applications. NASA Langley Research Center, Doc ID: 20040086577.

KING, R., BECKER, R., FEUERBACH, G., HENNING, L., PETZ, R., NITSCHE, W., LEMKE, O., NEISE, W. 2006. Adaptive Flow Control Using Slope Seeking. *14th Mediterranean Conference on Control and Automation, IEEE*.

KUMAR, S. M., REYNOLDS, W. C., AND KENNEY, T. W. 1999. MEMS Based Transducers for Boundary Layer Control. *IEEE Proceedings of the 12th International Workshop on Micro Electro Mechanical Systems – MEMS*, 17-21 Jan. 1999, Orlando, FL.

LAKE, J., KING, P, AND RIVIR, R., 1999. Reduction of Separation Losses on a Turbine Blade with Low Reynolds Number. *AIAA Paper 99-0242.*

LIN, J. C., AND PAULEY, L. L., 1996. Low-Reynolds-Number Separation on an Airfoil. *AIAA Journal 34*, 1570-1576.

LISSAMAN, P. B., 1983. Low-Reynolds-Number Airfoils. *Ann. Rev. Fluid Mechanics 15*, 223-239.

LIU, K., YUAN, W., DENG, J., MA, B., AND JIANG, C. 2007. Detecting boundary-layer separation point with a micro shear stress sensor array. *Sensors and Actators A 139*, 31-35.

LIU, T., WOODIGA, S., NOTEFORT, J., CONN, K., AND SHEN, L. 2008. Mapping Skin Friction Fields in Complex Flows Using Luminescent Oil. *46th AIAA Aerospace Sciences Meeting and Exhibit*, Reno, NV. AIAA Paper 2008-267.

LUMLEY, J. 1967. The structure of inhomogeneous turbulence. In A. M. Monin and V. I. Tatarski (Eds.), *Atmospheric Turbulence and Wave Propagation*, pp. 166-178. Moscow: Nauka.

MAYLE, R. E., 1991. The Role Laminar-Turbulent Transition in Gas Turbine Engines. *J. of Tubomachinery 113*, 509-531.

MCGHEE, R. J., WALKER, B. S. AND MILLARD, B. F. 1988. Experimental Results for the Eppler 387 Airfoil at Low Reynolds Numbers in the Langley Low-Turbulence Pressure Tunnel. *NASA Technical Memorandum 4062,* NASA Langley Research Center.

MCMASTER, J. H., AND HENDERSON, M. L., 1980. Low Speed Single Element Airfoil Synthesis. *Technical Soaring 6,* 1-21.

MCQUILLING, M. W. 2007. Design and Validation of a High-Lift Low-Pressure Turbine Blade. *PhD Dissertation*, Wright State University.

MCQUILLING, M., WOLFF, M., FONOV, S., CRAFTON, J., SONDERGAARD, R., 2008a. An Experimental Investigation of a Low-Pressure Turbine Blade Suction Surface Using a Shear and Stress Sensitive Film. *Experiments in Fluids 44*, 73-88.

MCQUILLING, M., WOLFF, M., FENOV, S., CRAFTON, J., AND SONDERGAARD, R., 2008b. An Experimental Investigation of Suction Surface Flow Features on a High-Lift LPT. *AIAA Paper No. 2008-79*.

MOREAU, E., 2007. Airflow control by non-thermal plasma actuators. *Journal of Physics D: Applied Physics 40*, 605-636.

MONTELPARE, S., AND RICCI, R. 2004. A Thermographic Method to Evaluate the Local Boundary Layer Separation Phenomena on Aerodynamic Bodies Operating at Low Reynolds Number. *International Journal of Thermal Sciences 43*, 315-329.

MUELLER, T. J., POHLEN, L. J., CONIGLIARO, P. E., AND JANSEN, B. J., JR. 1983. The Influence of Free-Stream Disturbances on Low Reynolds Number Airfoil Experiments. *Experiments in Fluids 1,* 3-14.

MUELLER, T. J. 1985. Low Reynolds Number Vehicles. AGARD-AG-288.

NESSLER, C., MARKS, C., SONDERGAARD, R., AND WOLFF, M., 2009a. An Investigation of Losses on a Highly Loaded Low Pressure Turbine Blade with Unsteady Wakes. *47th AIAA Aerospace Sciences Meeting*, Orlando, FL.

NESSLER, C., MARKS, C., SONDERGAARD, R., AND WOLFF, M., 2009b. PIV Investigation of Periodic Unsteady Wakes over a Highly Loaded Low Pressure Turbine Blade. *AIAA Joint Propulsion Conference*, Denver, CO.

PADMANABHAN, A., GOLDBERG, H., BREUER, K., SCHMIDT, M., 1995. A Silicon Micromachined Floating-Element Shear-Stress Sensor with Optical Position Sensing by Photodiodes. *IEEE 8th International Conference on Solid State Sensors and Actuators, and Eurosensors IX.* Stockholm, Sweden, Jun 25-29, 1995.

PATEL, M. P. TILMAN, C. P., NG, T. T., 2003. Active Transparent Stall Control Systems for Air Vehicles. *Journal of Aircraft, 40*, pp. 993-997.

PATEL, M. P., SOWLE, Z. H., CORKE, T. C., HE, C., 2007. Autonomous Sensing and Control of Wing Stall Using a Smart Plasma Slat. *Journal of Aircraft, 44*, pp 516-527.

PINIER, ,J., AUSSEUR, J., GLAUSER, M., AND HIGUCHI, H. 2007. Proportional Closed-Loop Feedback Control of Flow Separation. *AIAA Journal 45,* 181-190.

POGGIE, J., TILMAN, C., FLICK, P., SILKEY, J., OSBORNE, B., ERVIN, G., MARIC, D., MANGALAM, S., MANGALAM, A., 2010. Closed-Loop Stall Control System. *Journal of Aircraft, 47*, pp. 1747-1755.

PONS, J., MOREAU, E., AND TOUCHARD, G., 2005. Asymmetric surface barrier discharge in air at atmospheric pressure: electric properties and induced airflow characteristics, *Journal of Phy. D: Appl. Phys.,38*, 3635-3642.

POPE, S., 2008. *Turbulent Flows*. Cambridge University Press, New York.

PORTER, C., ABBAS, A., COHEN, K., MCLAUGHLIN, T., AND ENLOE, C., 2008. Spatially Distributed Forcing and Jet Vectoring with a Dielectric Barrier Discharge Plasma Actuator. *AIAA Paper No. 2008-1374*.

PORTER, C., ABBAS, A., COHEN, K., MCLAUGHLIN, T., ENLOE, C., 2009. Spatially Distributed Forcing and Jet Vectoring with a Plasma Actuator. *AIAA Journal, 47,* pp. 1368-1378.

PRESTON, J. 1954. The Determination of Turbulent Skin Friction by Means of Pitot Tubes. *Journal of the Royal Aeronautical Society 58,* 109-121.

RAFFEL, M., WILLERT, C., WERELEY, S., AND J. KOMPENHANS, 2007. Particle Image Velocimetry: A Practical Guide. Springer.

REEDER, M., CRAFTON, J., ESTEVADEORDAL, J., DELAPP, J., MCNIEL, C., PELTIER, D., AND REYNOLDS, T., 2009. Clean seeding for flow visualization and velocimetry measurements. *Exp. Fluids,* DOI:10.1007/S00348-009-0.

RIVIR, R. B., BAUGHN, J. W., BUTLER, R. J., BYERLEY, A. R., AND TOWNSEND, J. L. 1999. Thermal Tuft Fluid Flow Investigation Apparatus with a Color Alterable Thermally Responsive Liquid Crystal Layer. *U.S. Patent No. 5963292*.

RIZZETTA, D.P. AND VISBAL, M.R., 2007b. Numerical Simulation of Plasma-Based Flow Control for Transitional Highly Loaded Low-Pressure Turbine. *AIAA Journal 45*, 2554-2564.

ROTH, J., SHERMAN, D., AND WILKINSON, S., 2000. Electrohydrodynamic Flow Control with a Glow-Discharge Surface Plasma. *AIAA Journal, 38*, p. 116.

ROY, S., AND WANG, C. 2009. Bulk flow modification with horseshoe and serpentine plasma actuators. *J. Phys. D: Appl. Phys. 42*, DOI:10.1088/0022-3727/42/3/032004.

SAHIN , M., HALL, J., MOHSENI, K. 2008. Direct Numerical Simulation of Separated Low-Reynolds Number Flows around an Eppler 387. *46th AIAA Aerospace Science Meeting*, 7-10 January, Reno, NV. AIAA Paper 2008-422.

SANTHANAKRISHNAN, A., AND JACOB, J., 2007a. Flow Control with Plasma Synthetic Jet Actuators. *J. Phys. D: Appl. Phys. 40,* pp 637-651.

SANTHANAKRISHNAN, A., AND JACOB, J., 2007b. Effect of Plasma Morphology on Flow Control Using Plasma Synthetic Jet Actuators. *AIAA Paper No. 2007-783*.

SANTHANAKRISHNAN, A., AND JACOB, J., 2008. Charactarization of Linear Plasma Synthetic Jet Actuators. AIAA Paper No. 2008-538.

SANTHANAKRISHNAN, A., REASOR, J., AND LEBEAU, R. 2009. Characterization of linear plasma synthetic jet actuators in an initially quiescent medium. *Physics of Fluid 21.* DOI:10.1063/1.3097004.

SCHLICHTING AND GERSTAN, 2000. Boundary Layer Theory. Springer.

SCHMIDT, M., HOWE, R., SENTURIA, S., AND HARITONIDIS, J., 1988. Design and Calibration of a Microfabricated Floating-Element Shear-Stress Sensor. *IEEE Transactions on Electron Devices 35*, 750-757.

SEIFERT, A. AND PACK-MELTON, L. 2004. Control and Identification of Turbulent Boundary Layer Separation, NASA Langley Research Center Doc ID: 20040111309.

SELIG M. S. AND MCGRANAHAN, B. D. 2004. Wind Tunnel Aerodynamic Tests of Six Airfoils for Use on Small Wind Turbines. National Renewable Energy Laboratory Subcontractor Report, NREL/SR-500-34515.

SHARMA, O., 1998. Impact of Reynolds Number on LP Turbine Performance. *Proceedings of 1997 Minnowbrook II Workshop on Boundary Layer Transition in Turbomachines*, NASA/CP-1998-206958.

SHERMAN, D. M. 1998. Manipulating Aerodynamic boundary layers using an electrohydrodynamic effect generated by a One Atmosphere Uniform Glow Discharge Plasma, August 1998, *Master's Thesis, University of Tennessee, Knoxville*.

SMITH, D., AMITAY, M., KIBENS. K., PAREKH, D., AND GLEZER, A., 1998. Modification of lifting body aerodynamics using synthetic jet actuators. *AIAA Paper 98-0209.*

SONDERGAARD, R., RIVIR, R., AND BONS, J., 2002. Control of Low-Pressure Turbine Separation Using Vortex-Generator Jets. *J. of Propulsion and Power 18*, 889-895.

TANI, I., 1964. Low-Speed Flows Involving Bubble Separations. *Progress in Aerospace Sciences 5*, 70-103.

WHITE, F., 1991. *Viscous Fluid Flow,* 2nd ed., McGraw-Hill, Inc., Boston.

WILLERT, C., AND GHARIB, M., 1991. Digital particle image velocimetry. *Exp. Fluids, 10*, pp 181-193.

WINANT, C. D., AND BROWAND, F. K., 1974. Vortex Pairing: The Mechanism of Turbulent Mixing-Layer Growth at Moderate Reynolds Number. *Journal of Fluid Mechanics, 63, Pt. 2,* pp. 237-255.

WRIGHT, K. D., WASHBURN, A. E., JORDAN, J. D., LEIGHTY, B. D., WALTKINS, A. N., INGRAM, J. L., OGLESBY, D. M., FLEMING, G. I., SCOTT, M. A., BALLA, R. J., HART, R. C., HERRING, G. C., FLETCHER, M. T., SCHWARTZ, R. J., 2002. Measurement Technology for Use in Active Flow Control. *22nd AIAA Aerodynamic Measurement Technology and Ground Testing Conference,* 24-26 June 2002, St. Louis, MO.